Dynamics of the membrane potential

Studies of the membrane potential of Jurkat cells using wavelet and wavelet bispectral analysis

Author:
Aleksandra Pidde, MSc

*A thesis submitted in fulfillment of the requirements
for the degree of Doctor of Philosophy*

in the

Department of Physics
Lancaster University
Lancaster, UK

Department of Information and
Communication Technologies
Universitat Pompeu Fabra
Barcelona, Spain

August 16, 2020

Complex Oscillatory Systems:
Modeling and Analysis
Innovative Training Network
European Joint Doctorate

Declaration of Authorship

I, Aleksandra Pidde, MSc, declare that this thesis titled, "Dynamics of the membrane potential" and the work presented in it are my own. I confirm that:

- This thesis is my original work and has not been submitted, in whole or in part, for a degree at this or any other university.

- Nor does it contain, to the best of my knowledge and belief, any material published or written by another person, except as acknowledged in the text. All quotations have been distinguished by quotation marks and the sources of information specifically acknowledged.

- This thesis is submitted for the degree of Doctor of Philosophy undertaken at Lancaster University (Lancaster, UK) and at the Universitat Pompeu Fabra de Barcelona (Barcelona, Spain).

List of Publications

Published

- G. Lancaster, D. Iatsenko, A. Pidde, V. Ticcinelli, and A. Stefanovska. "Surrogate data for hypothesis testing of physical systems". *Phys. Rep.*, 748:1 – 60, 2018. (5-Year Impact Factor: 23.715). Work on bispectra and Monte Carlo eigenspectrum mostly not presented in the thesis, some points discussed in Chapters 3 and 4.

- J. P. Roach*, A. Pidde*, E. Katz, J. Wu, N. Ognjanovski, S. J. Aton, and M. R. Zochowski. "Resonance with subthreshold oscillatory drive organizes activity and optimizes learning in neural networks", *Proc. Nat. Acad. Sci. USA*, 115(13):E3017–E3025, 2018. *authors contributed equally. (5-Year impact factor: 10.600). Work not presented in the thesis.

Under revision

- J. Newman, A. Pidde, and A. Stefanovska. "Defining the Wavelet Bispectrum". under revision for publication in *Appl. Comput. Harmon. A.* Work from Chapter 4.

In preparation

- A. Pidde, S. Patel, M. Eissa, J. Owen-Lynch, S. Roberts, A. Stefanovska. "Dynamics of the free-running membrane potential of Jurkat cells". Work from Chapter 5.

Conferences

- A. Pidde, A. Stefanovska, "Dynamics of membrane potential oscillations in biological cells", *COSMOS final conference*, Novo Mesto, Slovenia, September 2018, oral presentation.

- A. Pidde, A. Stefanovska, "Coupling in the signal without the distinctive dominant frequency band? Study of the membrane potential", *Physics of Biological Oscillations Conference*, Chicheley Hall, UK, November 2018, poster and poster-preview presentation.

- A. Pidde, A. Stefanovska, "Fluctuations in the free-running membrane potentials of non-excitable cells – Study of the Jurkat cells membrane potential", *Electrical Cell Biology Workshop*, University of Warwick, Coventry, UK, March 2019, poster presentation.

- A. Pidde, A. Stefanovska, "Wavelet bispectral analysis: a robust tool for characterising coupling in time-varying dynamical systems", *Predicting Transitions in Complex Systems Workshop*, Dresden, Germany, April 2018, poster presentation.

- A. Pidde, J. Newman, A. Stefanovska, "Characterising coupling in time-varying dynamical systems with wavelet bispectral analysis" *Analysis and Modeling of Complex Oscillatory Systems (AMCOS)*, Barcelona, Spain, March 2018, poster presentation.

- P. Clusella, M. Lucas, A. Pidde, C. Zankoc, "Effects of noise and (non-) stationarity", COSMOS workshop, Amsterdam, Netherlands, December 2016, oral presentation group work summary.

- A. Pidde, "Introduction to perforated patch clamp experiment", *COSMOS meeting*, Wittenberg, Germany, March 2017, oral presentation.

- A. Pidde, A. Stefanovska, "Fluctuations in the membrane potential of a biological cell?", *19th IUPAB congress and 11th EBSA congress, (European Biophysical Societies' Association)*, Edinburgh, UK, July 2017, poster presentation.

- A. Pidde, A. Stefanovska, "Progress on my PhD", *2nd COSMOS school*, Aberdeen, June 2016, oral presentation.

- A. Pidde, M. L. Barabash, S. Patel, J. Owen-Lynch, S. Roberts and A. Stefanovska, "Why do we observe fluctuations in membrane voltage of a cell?", *8th Cell Model Systems Summer School*, Rome, Italy, 2016, poster presentation.

- *A. Pidde, M. L. Barabash, S. Patel, J. Owen-Lynch, S. Roberts and A. Stefanovska, "Membrane potential of a biological cell: Stochastic or deterministic?", *International Conference on Biological Oscillations (ESGCO 2016)*, Lancaster, UK, April 2016, poster presentation. *received prize for "Best posters on fundamentals of biological oscillations".

- A. Pidde, and A. Stefanovska, "Dynamics of cell membrane potential oscillations", *Lancaster University Christmas Conference*, December 2015, poster presentation.

Abstract

Fluctuations are fundamental for living organisms. They arguably result from inter-actions with the complex, and unpredictable environment, and can often be mani-fested as temporal variability. Let us consider the smallest representative of living organisms, the cell. It must continually resist the external perturbations, such as variations in the electrochemical gradient induced by changes in the extracellular ionic concentrations. To avoid the rise in osmotic pressure, that drives the water into the cell and could result in the cell bursting, the cell carefully adjusts the con-centration of permeable ions. Those continuous adjustments can be achieved only through a highly specialised network of membrane transporters, both passive, ion channels, and active, ion pumps. The collective activity of the membrane trans-porters is manifested in the dynamics of the membrane potential – very often viewed as fluctuations, seemingly without a preference for any particular frequency band. The aim of the work presented here is to provide understanding and insight into the dynamics of the free-running membrane potential in non-excitable cells, based on experimental data from Jurkat and smooth muscle cells. In order to achieve this, first the quantitative comparisons of the average values of the membrane potential and their standard deviations recorded in various extracellular solutions are made. The analysis is further extended through the use of the wavelet transform to investi-gate the time and frequency components of the signal. This work is the first to report an intermittent oscillation in smooth muscle cell, around 0.008 Hz in the membrane potential recorded with the free-running voltage perforated whole-cell patch clamp method. Additional activities around frequencies of 0.03, 0.05 or 0.09 Hz can be also observed. These appear as intermittent behaviour. To further understand this dy-namics from univariate time series, two methods were applied: wavelet-bispectrum and time-reversibility. The wavelet-bispectral density was developed. An appropri-ate normalisation for the wavelet bispectrum, that allows for a formal quantitative, not merely qualitative interpretation of the results of wavelet-bispectral analysis, was proposed. The practical aspects of the bispectral analysis were discussed using numerical examples. Finally, the newly developed auto-wavelet-bispectral analysis was applied to the recordings of the membrane potential. These indicated possible nonlinear couplings between different oscillatory modes in the cellular membrane potential.

Acknowledgements

First and foremost, I am sincerely grateful to my supervisors: Prof. Aneta Stefanovska and Assoc. Prof. Ernest Montbrió for the opportunity of doing my PhD and their support throughout this journey. I would like to thank Aneta for her time, her passion, her continuous support and unwavering willingness to share her research approach with me, and her patience and persistence when reading my thesis. Without her help I would not be able to reach this stage. I would like to thank Ernest for his time, his kindness and introduction to the Catalan spirit.

I would like to thank me committee Prof. Peter V. E. McClintock, Prof. Krasimira Tsaneva-Atanasova and Prof. Robert Young for the insightful discussions and truly positive *viva voce* examination experience.

Thanks to Prof. Peter V. E. McClintock for his kindness during my first conversations in "English", his patience and persistence when reading my thesis, his positive energy during my appraisals and his entertaining jokes. Thanks to Prof. Ralph Andrzejak for his time, his advices and for making me feel a part of his group in Barcelona. Thanks to Assoc. Prof. Vladimir Matchkov for dedicating his time and sharing his expertise with me. Without his positive energy and patience I would not be able to perform the experiment. Thanks to Prof. Christian Aalkjær for the useful discussions and for welcoming me in his group in Aarhus. Thanks to Prof. Michał Żochowski for his kind and unconditional support, his passion, his great sense of humour and useful career advices.

Sincerest thanks to Dr William Gibby for his advices on my thesis, his kindness when correcting my English language, our scientific discussions and great banters. Thanks to Dr Julian Newman for fruitful discussions and his patience in communicating research. Many thanks to Dr Gemma Lancaster for her kindness and for supervising me during my first scientific projects in Lancaster. Thanks to Dr Miraslau Barabash for introducing me to the project during my first months and sharing his results with me. Thanks to Dr Shakil Patel for sharing his data with me and explaining his experiment. Thanks to Dr Olena Fedorenko for showing me her experiment. Thanks to Dr Mahmoud Farout for his time to discuss the results included in the thesis. Thanks to Dr James Roach for his great ability to make the discussions humorous, his patience and inspiring attitude.

Thanks to Lancaster University Physics Department and Department of Information and Communications Technologies, Universitat Pompeu Fabra for hosting and supporting me during my PhD. Thanks to European Union's Horizon 2020 research and innovation programme No 642563 for funding my PhD.

Great thanks to my officemate in Lancaster: Max, Will, Ticci, Miraslau, Yunus, Julian, Zhenia, Fede, Basti, Matteus, Vamsi, Hala, Mahmoud and my officemate in Barcelona: Irene, Fede, Minia, Giulia, Cristina, Marc, Anais, Paola, Angela, Mario for creating a great atmosphere in the office and providing entertainment during lunch-breaks.

Contents

List of Figures

List of Tables

Glossary, abbreviations, and notations

Glossary and abbreviations

Adenosine triphosphate (ATP) Molecule that provides energy to drive many processes in living cell.

Aliasing A distortion of a signal during the sampling process due to insufficient sampling frequency.

Amplitude adjusted Fourier transform (AAFT) Algorithm to generate surrogate signal, preserving the exact amplitude distribution of the original signal and similar power spectrum.

Averaged wavelet power (AWP) Wavelet power averaged over time and integrated over the selected frequency range.

Bispectral density (BD) Dimensionless quantity allowing for quantitative measure of bispectrum content by integrating around the areas of interest.

Cell cycle The sequence of events when a cell is stimulated to grow and divide. It can be triggered either through fertilisation or proliferation.

Cohort Here it relates to separation of the cells into groups based on dominant permeability for K^+, Na^+ and Cl^-.

Confidence level, γ The probability that the true value of the unknown parameter lies within the confidence interval associated with this confidence level. It is related to the level of significance α by $\gamma = (1 - \alpha) \times 100\%$.

Cytosol The aqueous component of the cytoplasm of a cell, within which various organelles and particles are suspended.

Discrete Fourier transform (DFT) Transform describing the distribution of the signal energy in the frequency domain for discretely sampled signals.

Endoplasmatic reticulum (ER) A type of organelle in a eukaryotic cell. One of its functions is to store the intracellular Ca^{2+}.

Equilibrium (eq) Here used to refer to system's state of the lowest energy.

Fourier transform (FT) Transform describing the distribution of the signal energy in the frequency domain.

Goldman-Hodgkin-Katz (GHK) GHK potential describes the equilibrium potential for K^+, Na^+ and Cl^- ions.

Hodgkin & Huxley (HH) Here used to refer to HH mathematical model of action potential.

Iterative amplitude adjusted Fourier transform (IAAFT) Algorithm to generate surrogate signal, preserving the exact amplitude distribution or power spectrum, while keeping the very close approximation of the other one.

Jurkat cell Immortalised T-lymphocytes cell line, here used as a non-excitable cell model.

Level of significance, α Probability of the rejection the null hypothesis when it is true, also known as false-positive or type I error.

Membrane potential (MP, V_m) Difference between intra- and extracellular potential.

Nernst potential (V_K) Equilibrium potential, there is no current across the membrane for a certain ion, e.g. K^+.

Osmotic pressure The minimum pressure which needs to be applied to a solution to prevent the inward flow of its pure solvent across a semipermeable membrane.

Ordinary differential equation (ODE) Mathematical framework used to model the evolution in time.

Oxidative phosphorylation (OXPHOS) Part of cellular metabolism that produces the most ATP.

Proliferation The process whereby cells reproduce themselves by growing and then dividing into two equal copies. A cell in the resting state, stimulated to proliferation, enters the cell cycle.

Proton pumps Pump that transports the H^+ ion from one to another side of a membrane against its concentration gradient using the energy. Here, it refers to the proton pumps that use the energy stored in the ATP molecules.

Scale (s) In wavelet analysis can be understood as the scaling factor along the time axis for the mother wavelet. For a wavelet with unimodal Fourier transform the reciprocal relationship between the scale and frequency is assumed.

Time-averaged wavelet power (TAWP) Wavelet power averaged over time.

Turnover time Mean time over which the pool of a given metabolite will be replaced due to the rates of production and utilization.

Wavelet iterative amplitude adjusted Fourier transform (WIAAFT) Algorithm to generate surrogate signal, preserving the discrete time-averaged wavelet power.

Wavelet transform (WT) Transform describing the distribution of the signal energy in time-frequency space.

Physical Constants

Electron charge, $e = 1.602\,176\,634 \times 10^{-19}\,\text{C}$

Faraday constant, $F = 96\,485.3329\,\text{s}\,\text{A}\,\text{mol}^{-1}$

Ideal gas constant, $R = 8.314\,462\,618\,153\,24\,\text{J}\,\text{K}^{-1}\,\text{mol}^{-1}$

Symbols

C_ψ	wavelet-power normalisation	
dH_2O	distilled water	
$D_\psi(\lambda)$	wavelet-bispectrum normalisation	
f	frequency	Hz
g	conductance	mS/cm^2
I	current	µA
$[\text{K}]$	concentration of K^+	mM
$\log$	logarithm e	
p	permeability	
Q	electric charge	C
T	temperature	K
V	membrane potential	mV
$W_{\psi,x}$	wavelet transform of the signal x and wavelet ψ	units of x
z	valence	

Chapter 1

Introduction

Interactions are essential in life. Fluctuations may reflect the living organisms' ability to interact because they often result from interactions with the complex and unpredictable environment. Systems, whose behaviour is inherently deterministic, arguably have a much smaller capacity to cope with new conditions. Fluctuations are often a key to understand the living organisms [20], because they are frequently an essential ingredient in providing order to the living system [211], e.g. oscillations. Oscillations are an inseparable element of living organisms [202, 201, 86, 25, 41, 88]. For example the organisation of the sequential reactions of Krebs cycle has puzzled the scientists for many years. Finally, turning the sequential processes into a loop had lead to the solution of the problem [157, 20]. Oscillatory processes have an ability to interact, e.g. synchronise [84], co-depend on each other [156]. Collective, synchronous activity of many units can result in oscillations, measurable at macroscopic level, e.g. [38].

Life emerges from events happening in the right time and place. Matter can be organised in many ways and have various physical and chemical properties, yet only specific properties of matter, e.g. reaction rates, make life possible. According to the second law of thermodynamics, matter should tend to a state of bigger disorder, however the living systems seem to stay in ordered states. This apparent paradox has puzzled the great minds, including Schrödinger's [216]. In his monograph, *What is life?*, he proposed a solution involving the *openness of the system*: the living matter takes the negative entropy from the environment, in the form of organised complex molecules and in return decomposes it to simpler ones, at the same time dissipating heat. By increasing the entropy of their surroundings, living organisms avoid a quick decay to equilibrium. Relentless processes are pushing an organism back towards thermodynamic equilibrium with its environment. Therefore, every organism needs to be endogenously active by regularly performing the activities that keep it in the appropriate non-equilibrium relation with its environment [20]. This is one way to see the inherent fluctuations in a living organisms. Another possibility is to verify if the fluctuations act as a trade-off between the robustness and efficiency [233, 43]. In any case, a special framework when dealing with living system is needed. The pioneering contribution to the field of open systems far from thermodynamic equilibrium was made by Haken [96] and Prigogine [76]. Despite progress in this

field many problems remain open and unsolved [118]. In modern science, probably the best way to take thermodynamic openness into account, is to explicitly consider spatial and temporal dynamical variability. Living organisms are unique in terms of their robustness and also the ability to adapt to their environment [21, 62]. Needless to say, turning this beautiful ideology into well-defined workflow is an incredible challenge. Here, some of my steps undertaken to understand the dynamics of the membrane potentials of the cell are described.

1.1   Outline of the thesis

Chapter 2 defines the membrane potential, explains its origin and reviews the most important contributions to the field. A membrane potential cannot exist in isolation, therefore, the most important cellular rhythms, such as metabolism, cell cycle, pH, Ca^{2+} oscillations are also reviewed and their links to the membrane potential discussed. Particular attention is paid to metabolism, as to the best of my knowledge it has not been explicitly considered in the dynamics of the membrane potential. In addition the patch clamp method is described as it is the approach used to collect the data which are analysed later in the thesis.

Chapter 3 introduces and reviews the time-series analysis methods, used in the thesis. The chapter is organised as follows: first the motivation behind time-series analysis is introduced; then a description of the Fourier transform and its analysis is provided; then the extension to wavelet analysis is introduced; and finally the concept of using surrogates as a statistical method is introduced.

Chapter 4 introduces the wavelet bispectral density. Previous definitions of wavelet bispectrum allow for merely qualitative interpretation of computational results. A suitable normalisation is provided, allowing for treatment of the bispectrum formally as a bispectral density over time-frequency-frequency space. This wavelet bispectral density allows for a quantitative interpretation of the results of wavelet bispectrum analysis over time-frequency-frequency space. Therefore, it becomes well-suited to the investigation of nonlinear time-varying dynamics. The definition and justification are followed by numerical examples testing the approach. The later section introduces more of the practical issues and surrogates application.

Chapter 5 presents the results and analysis of the membrane potential recorded using the free-running voltage patch clamp technique. The recordings taken of the smooth muscle dataset using the perforated whole-cell patch clamp technique were collected as part of my industrial internship under the supervision of V. Matchkov in Aarhus. However, the recordings taken on the Jurkat cell line (JC) were collected erlier [192]. The JC results include investigating the effect of extracellular ion concentration and addition of intracellular Ca^{2+} or/and ATP. The results include the analysis of average values, standard deviations and wavelet analysis. Finally, a design for future experiments is suggested.

Chapter 6 presents the analysis of the cellular membrane potential using time reversibility and wavelet-bispectral density analysis outlined and developed in Chapter 4. This analysis is combined with surrogates testing, and it indicates significant bispectral peaks possibly due to self-coupling in the recordings of membrane potential. The temporal dynamics of the coupling is investigated with biamplitudes and biphases. The membrane potential recordings indicate significant time-irrevesibility on the fast timescales.

Finally, Chapter 7 gives a summary of the previous chapters and original contribution of the thesis.

Chapter 2

Membrane potential and various cellular rhythms

2.1 Introduction

All living organisms function according to their own internal clocks, which can themselves be influenced by various external factors, e.g. the environment. Well-defined rates and time delays of biochemical reactions make life possible. The rhythmic behaviours in humans are present in various time scales, nevertheless their origins probably lie in cellular oscillators and their interactions. Some of the human organism rhythms are presented in Fig. 2.1.

The membrane potential is an important element of the cellular rhythms. Yet, the membrane potential cannot exist in isolation. This chapter introduces various cellular rhythms that affect and are affected by the membrane potential. Moreover the chapter reviews the membrane transport options for the Jurkat cell (this cell type is used later in Chapter 5 as a model of a non-excitable cell). In Sec. 2.2 a glimpse of the transport across the membrane is given and the origin of the membrane potential is explained, in Sec. 2.3 a glance at the cellular metabolism is presented, in Sec. 2.4 the cell cycle and its interaction with the membrane potential is discussed, in Sec. 2.5 cellular pH is described and in Sec. 2.6 Ca^{2+} oscillations are introduced. Sec. 2.7 describes the methods that were used to collect the data (which is further discussed and analysed in Chapter 5) and eventually Sec. 2.8 describes the membrane transport in Jurkat cells. In summary all the most important cellular rhythms are combined together. Further insight into cellular oscillations can be found in [25, 252, 201].

2.2 The membrane potential

The membrane potential (V_m) is the difference in electric potential between the interior and the exterior of a cell. The membrane serves as both an insulator and a diffusion barrier to the movement of ions, letting selected ion types to pass across. This is reflected in the fluctuations in the membrane potential. Fluctuations in the membrane potential play an important role in neuroscience, e.g. information processing of the visual [140, 7] and rat barrel cortex [174], a memory formation [205],

SPONTANEOUS RHYTHMS

period duration (log)

seasonal growth, involution	1 year	10^8 sec — annual solar cycle
reproduction	1 month	10^7 — lunar cycle
		10^6
sleep-wakefulness autonomous equilibrium	1 day	10^5 — earth rotation
sleep cycles smooth muscle tone	1 hour	10^4
		10^3
blood distribution	1 min	10^2
peristalsis blood pressure respiration heart beat	1 sec	10^1
EEG nerval action	0.1 sec	10^{-1}
	0.01 sec	10^{-2}
	0.001 sec	10^{-3}

metabolic system

rhythmic transport and distribution systems

informational system

period duration (log)

Figure 2.1: Some of the rhythms of human organism and their approximated timescales. The oscillations interact with each other, the collective dynamics of many oscillators contribute to the rhythm measured microscopically, e.g. synchronous activity of many neurons could be measured in EEG. Cellular oscillators are arguably at the base of all the other human rhythms. Modified with permission from [176].

neostriatal spiny cells [264] or corticostriatal and striatal neurons [234], and other fields [122]. There is no clear distinction between fluctuations and oscillations in the membrane potential. Oscillations may result from synchronous activity of various membrane transporters or from resonance effect of the cellular transporters with the input delivered to the cell. Tab. 2.1 presents examples of oscillations in the membrane potential recorded with electrophysiology techniques.

2.2.1 Transport across the membrane

The living cell maintains a certain electrolyte state, which on the one hand secures the particular conditions for all enzymatic reactions, and on the other accumulates potential energy in the form of electrochemical gradients. This requires a highly specialised, enzymatically controlled system of membrane transporters. The membrane transporters can be classified according to the role of energy:

freq. (Hz)	experimental technique	cell type	ref.	note
0.0038 ±0.0011	patch-clamp	β-cells	[167]	simultaneous recordings of MP and metabolism; Ca^{2+} entry into β-cells influences metabolism
0.017– 0.15 **0.067**	electrophysiology	L cells	[183] [184]	spontaneous osc. of the MP between -15 and -40 mV, strongly sensitive to temperature
0.08–0.17	electrophysiology	cultured epithelial intestine cells	[268]	three patterns of osc.: transient, burst and continuous for more than 1h
0.16–0.25	electrophysiology	mamm. intestinal	[121] [55]	Na^+/K^+ pumps are considered as generator of this osc.
0.5–2	two-microelectrode method	cardiac Purkinje fibers	[124]	possibly arises from oscillatory variations in intracellular free Ca^{2+}
3–7	patch-clamp	LTS interneuron	[226]	osc. depend on voltage-gated calcium channels
20–100	sharp micropipettes	ganglia neurons	[155]	subthreshold oscillations frequency was dependent on the average MP
30–60	*in vivo* whole-cell patch-clamp	cat visual cortex	[112]	synchronization most likely due to rhythmic synaptic inputs

Table 2.1: Examples of membrane potential (MP) oscillations (osc.) from the literature observed in experiments using electrophysiology methods.

- Passive (diffusion) – ions move according to their electrochemical gradient, this class includes both pores and channels. Water pores are always open while ion channels have the vitally physiologically important ability to close.

- Passive (co-transport) – this is known also as secondary active transport and relies on the correlation between ions. A transporter protein couples the movement of an ion down its electrochemical gradient to the uphill movement of another molecule or ion against an electrochemical gradient. In this way, energy stored in the electrochemical gradient of an ion is used to drive the transport of another solute against an electrochemical gradient.

- Active – pumps transport ions or small molecules against their electrochemical gradients, using metabolic energy, most commonly in the form of ATP.

Tab. 2.2 summarises and provides some example of the classification detailed above. Ionic pumps play an important role in various cellular processes:

- They control and regulate intracellular environment, creating and maintaining the steep ionic gradients across the membrane.

- They control the osmotic pressure within the cell (by taking part in regulatory volume decrease, see Secs. 2.2.4 and 2.2.5), which is probably the primordial function of the pumps [232].

- They provide very efficient signalling systems by maintaining the intracellular concentrations several order of magnitude smaller than the extracellular one, e.g. calcium signalling.

- In addition some of pumps directly contribute to the membrane potential.

type	passive				active	
	diffusion		**co-transport**		**transport ATPase**	
	pore	channel	symport	antiport	one ion	two ions
no charge	H_2O		Na^+/Cl^-	Na^+/H^+		K^+/H^+
charge	K^+, Na^+	K^+, Na^+	gluc.-Na^+	$3Na^+/Ca^{2+}$	H^+-ATPase, PMCA	$2\,K^+/3Na^+$

Table 2.2: Classification of the membrane transport with examples, modified from [83].

2.2.2 Equilibrium and Nernst potential

One of the most important equations in electrophysiology is the Nernst equation. This relates differences in ionic concentration on either side of the membrane to the potential difference across the membrane. Suppose there are two reservoirs containing the same salt AB (where A^{z+}, B^{z-}, z valence of the ion), but at different concentrations. The reservoirs are separated by a semipermeable membrane, which is permeable to A^{z+} but not B^{z-}. The initial solutions in both reservoirs are assumed to be electrically neutral, and thus each ion A^{z+} is balanced by another B^{z-} ion. If the membrane is permeable to A^{z+} but not B^{z-}, then the concentration difference across the membrane results in a net flow of A^{z+}, down its concentration gradient. However, because B^{z-} cannot diffuse through the membrane, the diffusion of A^{z+} causes a buildup of charge across the membrane. This charge imbalance, sets up an electric field that opposes the further net movement of A^{z+} through the membrane. Equilibrium is reached when the electric field exactly balances the diffusion of A^{z+}. One may immediately notice that there are more A^{z+} ions than B^{z-} ions on one side and fewer A^{z+} ions than B^{z-} ions on the other. Hence neither side of the membrane is *exactly* electrically neutral. However, because the force from the charge accumulation is very strong only a small number of A^{z+} ions move across the membrane. Consequently the concentrations of ions are usually assumed unchanged. An estimation of ionic concentration change as a function of change in the membrane potential for an example cell is presented in appendix A.1. The electrochemical potential of A^{z+} on the inside of the membrane is

$$\mu_{A,x} = \mu_{0A} + RT \log([A]_x) + zFV_x,$$

where x denotes *in* or *out*, which correspond to two reservoirs, μ_{0A} is the chemical potential of the pure substance, R the ideal gas constant, T the temperature (K), z the valence of the ion, F Faraday constant, $[A]$ the concentration of the ion, log the natural logarithm. At equilibrium there is no electrochemical potential difference, $\Delta\mu_A$, between the two sides of the membrane, thus

$$\Delta\mu_A = \mu_{A,in} - \mu_{A,out} = 0.$$

This is only true when the membrane potential equals

$$V_{eq} = \frac{RT}{zF} \log \left(\frac{[A]_{out}}{[A]_{in}} \right),$$
(2.1)

called the *Nernst* potential for an ion A. This equilibrium potential describes a single-ion system only. In case of a multiple-ion system, each ion type has an individual Nernst potential. Reaching the Nernst (or in other words equilibrium) potential for multiple ions at the same time is not possible. Therefore, the cellular membrane potential constantly fluctuates, being limited by the equilibrium potentials of the dominant ions, K^+, Cl^-, Na^+.

2.2.3 Electrodiffusion: the Nernst–Planck equation

The flow of ions through the membrane is driven by both the concentration gradient and electric field gradient. If the flow of ions and the electric field are transverse to the membrane, the flow of ions J can be obtain from

$$J = -D \left(\frac{dc}{dx} + \frac{zF}{RT} c \frac{d\phi}{dx} \right),$$
(2.2)

which is the one dimensional *Nernst–Planck equation*. Here: D is a diffusion constant, ϕ is an electrical potential, and $\frac{d\phi}{dx}$ the corresponding electric potential gradient.

Steady-state: the Goldman–Hodgkin–Katz equation

If there are several types of ions, e.g. K^+, Na^+, Cl^- each with different concentrations on either side of the membrane, then the flow of each of these is governed separately by its own current–voltage relationship. In general, there is no potential at which these currents are all individually zero. However, the potential at which the net electrical current is zero is called the Goldman–Hodgkin–Katz (GHK) potential [89]

$$V_{GHK} = \frac{RT}{F} \log \left(\frac{p_K[K^+]_o + p_{Na}[Na^+]_o + p_{Cl}[Cl^-]_i}{p_K[K^+]_i + p_{Na}[Na^+]_i + p_{Cl}[Cl^-]_o} \right).$$
(2.3)

Here, p_X is the membrane permeability for ion X, and $[X]_{i/o}$ the concentration of ion X inside and outside the cell respectively. V_{GHK} can be derived from the Nernst–Planck equation under the assumption of constant electric field and no net electrical current [89].

2.2.4 Osmosis and reasons why the membrane potential is created

The cell has only a thin lipid bilayer and hence lacks a rigid structure. Therefore, it is capable of resisting only very small hydrostatic pressure differences. Yet, a certain number of intracellular proteins and ions are required inside the cell for cell staying alive. However if their concentrations become too large, osmosis causes the

entry of water into the cell, causing it to swell and burst. Thus, in order to survive the cell must regulate its intracellular ionic composition [164, 126]. If a cell was not full of proteins or intracellular organelles, mostly negatively charged, the excessive osmotic pressures could be avoided simply by allowing ions to cross the plasma membrane freely. The more negatively charged organelles and proteins inside, the more negative the membrane potential that is generated. For example, the membrane potential of the red blood cell, which does not posses either nucleus or mitochondria is much less negative at around -10 mV compared to other cells [83, 26]. Therefore, the red blood cells do not need metabolic systems as efficient as other cells, and obtain their entire ATP by glycolysis. In other mammalian cells glycolysis produces only around 7% of the total ATP, which is further discussed in Sec. 2.3. The impermeant molecules make a substantial contribution to the osmotic concentration within a cell, representing about one third of the total osmotic concentration [125]. Various models incorporating the membrane potential and osmotic pressure were proposed [126, 113, 10, 270] in which the important role of Na^+/K^+ pumps in osmotic regulation, and the membrane potential maintenance is emphasised. One of the conclusions from these models [126, p. 88–97] is that there is no benefit from increasing the pumping reaction rate because the cell naturally optimises it by minimising the energy expenditure to form the right osmotic pressure. This optimum also corresponds to the most negative membrane potential.

2.2.5   Volume regulation

The osmotic pressure is proportional to the molar concentration of the solutes, [83, eq. 3.99], [126, eq. 2.138] and cell volume primarily represents the amount of water in a cell [210]. The cell adjusts the concentrations of various ions and organic molecules. Water tends to move across a membrane from a solution of low solute concentration to one of high. Therefore, as a result, the generated osmotic concentration gradient drives the water by diffusion across the lipid bilayer or through aquaporins. The cell adjusts the volume by adjusting the ionic concentrations via two mechanisms: regulatory volume increase (RVI) and regulatory volume decrease (RVD). The schematic picture with the ion channels involved is presented in Fig. 2.2.

Volume regulation plays a crucial role in apoptosis, typically paralleled with cell shrinkage [271], and necrosis, typically co-occurring with the cell swelling [186]. In a living cell, both the osmotic pressure and the cell volume are continuously regulated. This process results in a dynamical variation of the membrane potential, i.e. of the potential difference between the interior and the exterior of the cell.

2.2.6   Membrane potential dynamics, Hodgkin & Huxley model

Probably the most popular model of the temporal dynamics of the membrane potential was introduced by Hodgkin & Huxley (HH) [100]. The model was originally used to represent the neural action potential of a squid axon. The general aim of their
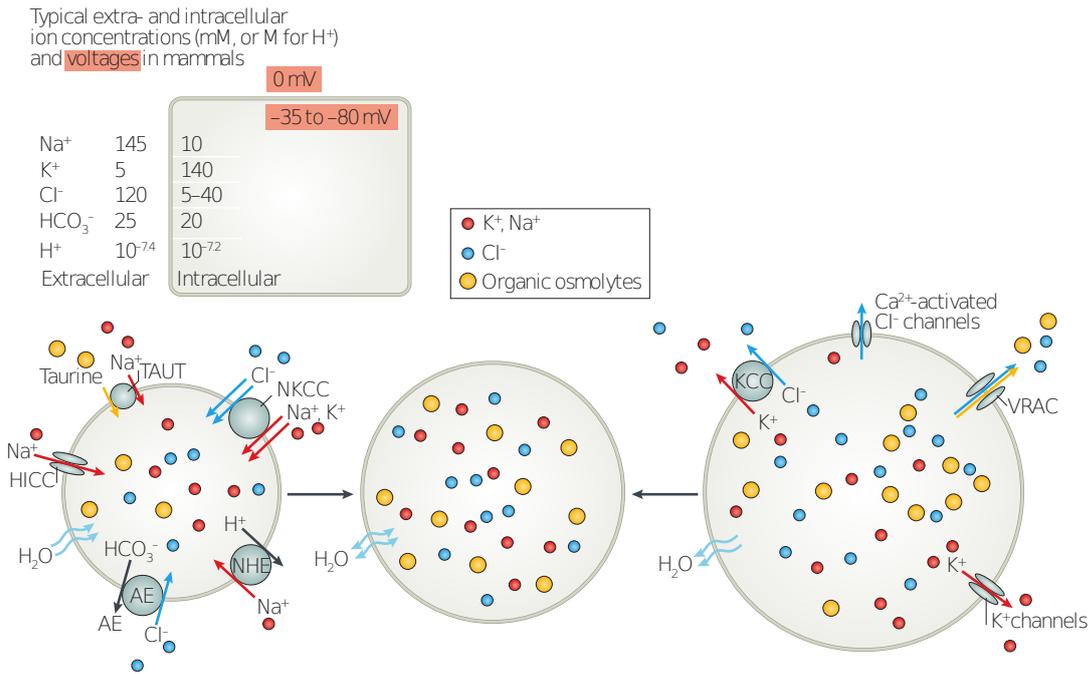
Figure 2.2: Plasma membrane channels and transporters involved in cell volume regulation. The cell adjusts its volume by regulating the concentrations of various ions, e.g. K^+, Na^+. The generated osmotic gradient drives water across the membrane. (left) Shrunken cells returns back to the normal volume via regulatory volume increase (RVI). The process differs from one cell to another, nonetheless mainly involves simultaneous activation of Na^+/H^+ exchangers (NHEs; mainly NHE1) and Cl^-/HCO_3^- anion exchangers (AEs; mainly AE2), or the stimulation of $Na^+/K^+/2Cl^-$ cotransporters (NKCCs; mainly NKCC1). Both processes increase cytoplasmic Na^+ and Cl^- concentrations. In some cells, the activation of hypertonicity-activated, non-selective cation channels (HICCs) can also be involved and mainly leads to Na^+ influx. In cases mentioned earlier, the Na^+/K^+-ATPase will systematically replace intracellular Na^+ with K^+. Na^+-coupled uptake of taurine by taurine transporter TAUT (also known as SLC6A6) rather takes part in long-term RVI. Swollen cells recover their volume through regulatory volume decrease (RVD; right). One of the possible mechanisms is extruding K^+, Cl^- and organic osmolytes, e.g. taurine. The cell may lose either through K^+/Cl^- cotransporters (KCCs; mainly KCC1, 3 or 4) or through parallel Cl^- and K^+ channels. Pivotal role in RVD is being played by volume-regulated anion channels (VRACs), conducting not only Cl^-, but also organic osmolytes. Inset presents typical extra- and intracellular concentrations of ions involved in mammalian volume regulation. The direction of passive ion transport depends not only on the concentration difference, but also on the voltage across the plasma membrane (the electrochemical gradient). The intracellular Cl^- concentration shows substantial variation between cell types. In most cells, except neurons, the Cl^- exit (e.g. through VRACs) will be favoured. Figure reprinted with permission from [119].

series of papers ([104, 101, 102, 103, 100], summarised in [100]) was to determine the laws which govern movements of ions during the generation of the action potential. They measured current-voltage relationship and proposed a model, which was also shown with its electrical circuit equivalent, as presented in Fig. 2.3. The energy stored in the electrochemical gradients of the ions can be represented by the batteries, the ion channels by variable conductances. HH noticed that a significant role in the membrane potential and its dynamics is played by K^+ and Na^+ ion channels. In the initial model, the pumps were not explicitly included but they would work as

a chargers, turning the energy stored in ATP into energy stored in the electrochemical gradients. Mathematically, the model can be expressed via the following set of equations. The current flowing through the lipid bilayer can be written as

$$I_c = C_m \frac{dV_m}{dt}, \tag{2.4}$$

here, C_m is the membrane capacitance. The current of each ion type is given by

$$I_i = g_i(V_m - V_i), \tag{2.5}$$

g_i is the conductance for each ion, V_i equilibrium (Nernst) potential for each ion. Thus, for the cell where a crucial role is played by K$^+$ and Na$^+$ currents, the total current is given by

$$I = C_m \frac{dV_m}{dt} + g_K(V_m - V_K) + g_{Na}(V_m - V_{Na}) + g_l(V_m - V_l). \tag{2.6}$$

Here, g_l represents the leak conductance. Importantly, they conducted the series of experiments and proposed the form of g_K and g_{Na} conductances. Based on measured sodium and potassium currents they proposed

$$\begin{aligned} g_K &= \bar{g}_K n^4, \\ g_{Na} &= \bar{g}_{Na} m^3 h, \end{aligned} \tag{2.7}$$

where $\bar{g}$ describes the maximal conductance for each channel type and n^4, $m^3 h$ a fraction of the ion channels in the open state for K$^+$ and Na$^+$ respectively. They described the dynamics of $x = n, m, h$ with equations of the form

$$\frac{dx}{dt} = \alpha_x(V_m)(1 - x) - \beta_x(V_m)x, \tag{2.8}$$

that provided the best fit to the experimental results. Here, $\alpha_x(V_m)$ and $\beta_x(V_m)$ are voltage-dependent reaction rates of ion channels getting open and getting closed respectively. The work was awarded the Nobel Prize in 1963 and is probably the most used model of the action potential [42].

2.3 Cell metabolism

2.3.1 Link to the membrane potential

As already mentioned in Secs. 2.2.4 and 2.2.6, Na$^+$/K$^+$ pumps play a crucial role in maintaining the ionic gradients, and thus maintaining the correct osmotic pressure. Nevertheless the pumps need a source of energy to function, which is where metabolism plays a role. The direct role of the membrane potential in cellular metabolism is only well known for β-cells. β-cells have ATP-sensitive K$^+$ channels that are the natural sensors of the ATP/ADP ratio. The channels are spontaneously active

Extracellular Medium

Intracellular Medium
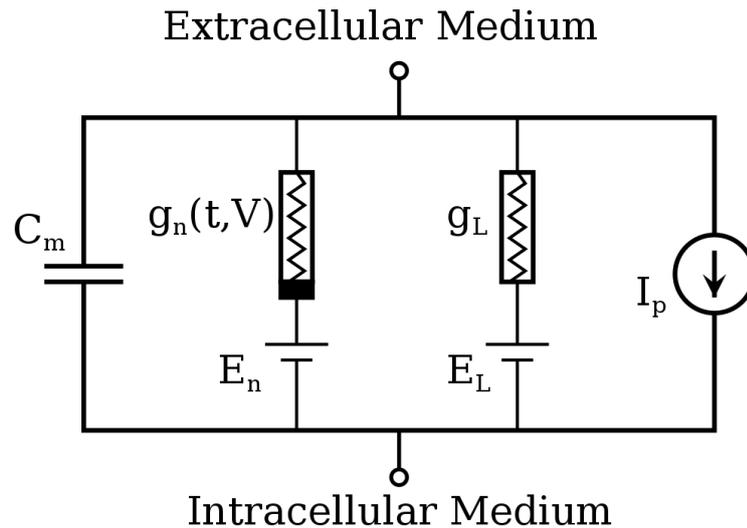
Figure 2.3: Schematic picture of the electric circuit representing a cell. The electrochemical gradients of the ions K^+ and Na^+ are represented by the battery (E_n) the varying conductance ($g_n(t, V)$) represents the collective activity of K^+ and Na^+ channels, lipid bilayer by membrane capacitance (C_m) and ion channels by variable conductances. For the mathematical description see the main text. Figure taken from [51].

(open), and when the ratio of ATP/ADP rises, they close. As a result the membrane depolarises, activating the voltage-gated calcium channel. Ca^{2+} promotes the release of insulin, which controls the energy conservation and utilization. Consecutively, the insulin decreases the level of glucose, which is a main molecule required for metabolism.

2.3.2 Catabolism

Metabolism is arguably one of the most important processes in living organism, because it produces energy from glucose molecules. Metabolism can be divided into two separate parts; catabolism – the breakdown of compounds, e.g. the breaking down of glucose to pyruvate by cellular respiration; or anabolism – the build-up (synthesis) of compounds, such as proteins, carbohydrates, lipids, and nucleic acids. The main attention will be now focused around the first part. The catabolic part of cellular metabolism comprises many biochemical reactions, ultimately resulting in the production of adenosine triphosphate (ATP).

Living systems obtain energy in a relatively complex, yet tightly controlled way. If a supply molecule, such as glucose is oxidised in a single step, as it happens in nonliving systems, then the amount of released energy would be many times larger than any carrier molecule could capture [4]. Cellular respiration consists of four essential parts: glycolysis, pyruvate oxidation, the citric acid cycle and oxidative phosphorylation. This section summarises only the essential events. An important review providing insight into the oscillatory nature of the metabolism and its associated phase relations can be found in [30]. A simplified schematic model of cellular metabolism can be found in Fig. 2.4. Effectively, ATP is produced in glycolysis (2

molecules) and oxidative phosphorylation (26 or 28 molecules): the later part requires the availability of O_2. Tab. 2.3 summarises the effective product in the form of NADH/ATP of each part of catabolism, a place where the process takes place and the amount of energy stored in the form of electrons. The table also presents the turnover times for selected metabolites. The turnover time corresponds to the mean time over which the pool of a given metabolite will be replaced due to the rates of production and utilization. The turnover time for ATP and ADP is much shorter than for the citric acid cycle. About 93-95% of the total ATP is produced in mitochondria and requires the availability of oxygen. It was observed that in the absence of pathology, glucose metabolism is predominantly governed by oxygen concentrations. Thus, high-efficiency oxidative phosphorylation (even up to 36 ATP/glucose) is a default source of ATP under normal concentrations of oxygen, whereas in the fermentative pathway (without the need of oxygen), glycolysis (glucose metabolised to lactate yielding 2 ATP/glucose), is an emergency ATP source only if oxygen is deficient [260]. Normal differentiated cells rely primarily on oxidative phosphorylation, as opposed to cancer or proliferative cells that use glycolysis [255]. Glycolysis was shown to be an emergency source of ATP responding to fluctuating energy demand, for example a sudden rise in Na^+/K^+ pumps activity, or a rise in osmotic pressure in both normal and cancer cells [65, 193].

Glycolysis

Glycolysis is a metabolic pathway that converts glucose ($C_6H_{12}O_6$) into pyruvate $CH_3COCOO^- + H^+$. One cycle effectively produces 2 molecules of ATP and converts 2 molecules of NAD^+ into NADH (by redox reaction). This NADH will be converted later to ATP. This process takes place in the cytosol.

While glycolysis is a necessary step for any cell to obtain energy, in a number of experiments mainly in yeast and muscle cells, the concentration of metabolites was reported to repeatedly fluctuate [43, 81, 64]. This phenomenon is called glycolytic oscillations. The occurrence of the oscillations was explained as a trade-off between efficiency and robustness using control system theory [43]. In this simple model, oscillations are neither directly profitable, nor have an evolutionary character but are a necessary consequence of autocatalysis and hard trade-offs between stability (the need to stabilise the coupled system) and efficiency (the need to maintain high energy charge). The energy charge is an index used to measure the energy status of biological cells. It is defined as (ATP + 0.5 ADP)/(AMP + ADP + ATP), and it was proposed as a fundamental metabolic control parameter [13]. Drop in the energy charge is associated with more rapid loss of cellular viability.

Pyruvate oxidation

The next step requires the pyruvate to enter mitochondria. Then pyruvate is turned into acetyl-CoA, producing CO_2 and NADH.

part	effective (net) products	where?	electrons
glycolysis	2 ATP, 2 NADH	cytozol	2 electrons bounded
pyruvate oxidation	2 NADH	mitochondrial matrix	2 electrons bounded
citric acid cycle	6 NADH, 2 ATP, 2FADH$_2$	mitochondrial matrix	6 (NADH) + 4 (2FADH$_2$) electrons bounded
oxidative phosphorylation	26 (or 28) ATP	mitochondrial membrane	uses all electrons bounded earlier (in NADH and FADH$_2$) to produce ATP

(a) The energetic gain, O_2 demand, electron pathway for converting one molecule of glucose.

metabolite	turnover time (s)	
	S. cerevisiae	*E. coli*
ADP	0.3	0.8
ATP	1.4	2
pyruvate	1.7	1.5
TCA cycle	4–30	0.7–9

(b) The turnover time for selected metabolites for *S. cerevisiae* and *E. coli* cells taken from [171, p. 276].

Table 2.3: Summary of cellular respiration for converting one molecule of glucose and turnover time for selected metabolites.

Citric acid cycle

The citric acid (TCA) cycle, also known as the Krebs cycle, is a metabolic pathway that connects carbohydrate, fat, and protein metabolism. The produced acetyl-CoA combines with a four-carbon molecule and goes through a cycle of reactions. The ultimate products are ATP, NADH and FADH$_2$. Morover CO_2 is released. Both pyruvate oxidation and the citric acid cycle take place in a mitochondrial matrix.

Oxidative phosphorylation

Oxidative phosphorylation, also known as the electron transport chain, takes place within the mitochondrial inner membrane. It is powered by the movement of electrons through a series of proteins embedded in the inner membrane of the mitochondria. The NADH and FADH$_2$ deposit their electrons and convert them into NAD$^+$ and FAD, respectively. As the electrons pass through the electron transport chain, the protons are pumped out of the mitochondrial matrix into the mitochondria intra membrane space, forming a gradient. As they passively move back to the mitochondrial matrix, their energy is used to create ATP. This hypothesis, proposed by Mitchell (chemiosmotic theory) [173], initially not well accepted, was later awarded the Nobel Prize in 1978.

Isolated mitochondria display a range of oscillatory activity [30, 87, 29]. Yet, mitochondrial activity is sensitive to both internal and external input. Therefore it is not clear, whether they are driven by oscillatory input of pyruvate, resulting from
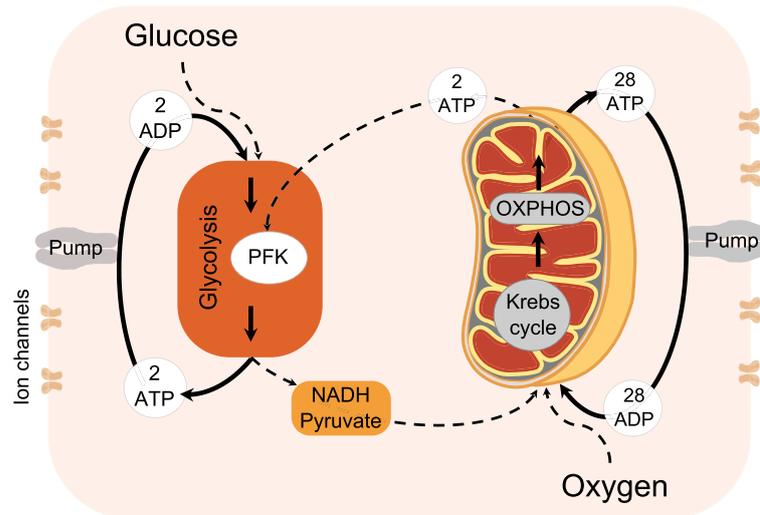
Figure 2.4: Schematic picture representing the cell metabolism as a system of self-sustained coupled oscillators. Glycolysis, as the only part of cellular metabolism that proceeds without mitochondria was represented as a single oscillator, while remained parts: pyruvate oxidation, the citric acid cycle, and oxidative phosphorylation that take place in mitochondria were combined together and represented as a another oscillator, OXPHOS. Schema indicates the ion pumps utilising the ATP produced in the process. Figure reprinted under a Creative Commons Attribution 4.0 International License from [142].

glycolytic oscillations, or there is an intrinsic mechanism to generate oscillations, or both. The observed ATP/NADH oscillations frequencies are spanning from around 1.67×10^{-4} Hz [190] to 0.026 Hz [188].

2.4 The cell cycle

In this section, the cell cycle is introduced and the links with cellular metabolism and the membrane potential are made. The cell cycle is a sequence of actions that the cell needs to perform in order to duplicate its DNA, split the organelles, and divide into two daughter cells. The process is regulated and controlled by several checkpoints. Four distinct phases make up the eukaryotic cell cycle:

- G_1 phase: increase in size.

- S phase (synthesis): replication of the DNA.

- G_2 phase (or interphase): cell growth continuation.

- M phase: division into two daughter cells, nucleus division (mitosis) and cytoplasm division (cytokinesis).

For a human cell line the whole process takes about 20 h. The fraction of time dedicated to each phase is shown in Fig. 2.5. Cells that have temporarily or reversibly stopped dividing are said to have entered a state of quiescence known as the G_0 phase.
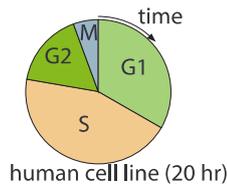
Figure 2.5: The fraction of time dedicated to each phase of the cell cycle for human cell line. The full cycle takes around 20 h. Modified from [171, p. 329].

2.4.1 Link to metabolism

The mechanism of interaction between the cell cycle and metabolism was investigated by Papagiannakis et. al [190]. They concluded that the cell cycle is a higher-order function, which emerges from the collective synchrony between a metabolic oscillator, and a biomass segregation oscillator. They summarised that metabolic cycles are an intrinsic and independent from the growth conditions. Moreover, they are characteristic for single cells, rather than the collective behaviour of many cells.

2.4.2 Link to the membrane potential

The link between the cell cycle and the membrane potential was suggested in the late 1950s [26]. However pioneering work was done by Cone Jr. who was first to observe that the membrane potential varied through the cell cycle and directly related it to progression through G_1/S and G_2/M transitions in proliferating cells [53]. Later showed that DNA synthesis and mitosis were evoked in fully differentiated neurons, by exposing the cell to sustained elevated level of intracellular Na^+ and decreased intracellular K^+ [52].

Ionic regulation of cellular behaviour has been found to play a critical role in proliferation [238]. Yet it it is known that the relationship between the membrane potential (V_m) and proliferation is not simple, as V_m illustrates the collective activity of various ion channels, transporters or pumps. Fig. 2.6 illustrates the membrane potential changes during the cell cycle. The membrane potential has been examined as a key regulator of proliferation in a number of cell types, suggesting that modulation of the membrane potential is required for both the G_1/S phase and the G_2/M phase transitions [27]. Progression from G_1 to S coincides with membrane hyperpolarisation, while during the G_2/M transition membrane depolarisation is typically observed.

2.5 pH

One of the important parameters controlled by the cell is the concentration of hydrogen ions. Physiologically normal intracellular pH is most commonly between 7.0 and 7.4, however, there is variability between tissues, e.g. mammalian skeletal muscle tends to have a pH of 6.8-7.1. There is also pH variation across different organelles, which can span from around 4.5 to 8.0.

$$V_{GHK} = \frac{RT}{F} \log \left(\frac{p_K[K^+]_o + p_{Na}[Na^+]_o + p_{Cl}[Cl^-]_i}{p_K[K^+]_i + p_{Na}[Na^+]_i + p_{Cl}[Cl^-]_o} \right)$$
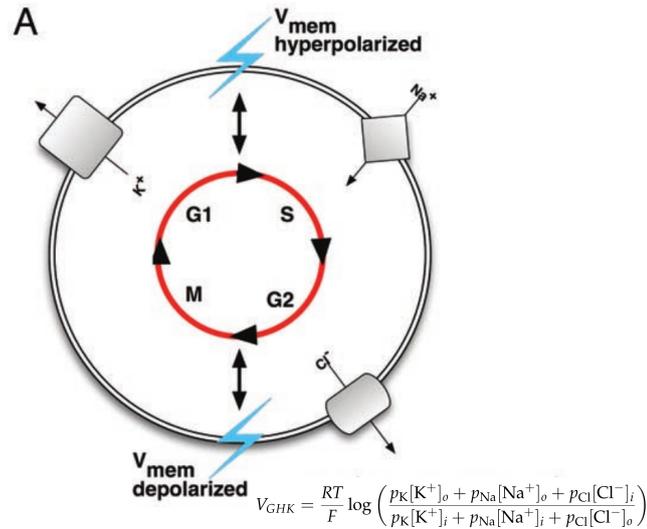
Figure 2.6: Bioelectric signals influence the cell cycle via V_m changes. Figure illustrating the membrane potential changes due to the ion channel dynamics during the cell cycle. During G_1/S transition, V_m becomes hyperpolarised due to potassium efflux from the cell, sodium channels also become activated. While the G_2/S progression the membrane is depolarised, potassium channels activity decreases. During G_2/M transition chloride channels become activated, chloride flows out of the cell. All K^+, Na^+ and Cl^- ions are involved during the cell cycle. Modified from [27].

2.5.1 Link to the membrane potential (volume)

The Na^+/H^+ exchanger (NHE), which is present in most animal cells, merits particular attention when considering pH and the membrane potential. Despite being electroneutral, NHE affects the intracellular concentrations of the ions. Under physiological conditions and at neutral pH, it is inactive. However, it becomes activated by acidic intracellular pH. It plays an important role in regulatory volume increase. There are examples of potassium ion channels with a pH-dependent conductivity [175, 245]. In particular, intracellular acidification blocks the K^+ conductance and depolarises the membrane. While considering intracellular pH, just as important is exchanger Cl^-/HCO_3^-, activated by alkaline pH. Similarly to NHE, it also plays a role in volume regulation. Cl^-/HCO_3^- transports extracellular Na^+ and HCO_3^- into cells in exchange for intracellular Cl^- and H^+, thus raising the intracellular pH [259]. The transport is electroneutral. In some of the cellular membranes the presence of H^+ translocating ATPases was reported. They utilise energy stored in ATP to build up a proton gradient across a biological membrane. Proton pumps are electrogenic, but are coupled to other channels to counterbalance the membrane potential drop: either to an anion channel (symport) or K^+ channels (antiport) [166]. Even if the proton pumps are not located at the plasma membrane they can actively remove H^+ ions from the cytosol.

2.5.2   Link to metabolism and the cell cycle

Small variations in pH strongly influence phosphofructokinase, the enzyme playing an important role in glycolysis [158, 71, 253]. DNA, RNA but also protein synthesis are affected by pH. The synthesis of DNA and RNA increase with increasing intracellular pH within the physiological range (as discussed in [158]).

pH is also well known to play a role in cell proliferation. Proliferation of mammalian cells is dependent on a permissive pH in the slightly alkaline range (7.0-7.2), as reviewed in [73].

2.6   Ca^{2+} oscillations

Ca$^+$ is known as a universal signalling molecule, playing a critical role in diverse processes such as fertilization, proliferation, development, learning and memory, contraction and secretion [24, 48]. Having an excess of Ca^{2+} is highly toxic and dangerous. Exceeding its normal spatial and temporal boundaries can result in cell death through either necrosis or apoptosis. Ca-ATPase together with various Ca^{2+} channels and sarcoplasmatic reticulum (SR) Ca^{2+} storage establishes an effective signalling system. The Ca-ATP pump creates an extremely low calcium level in the cytoplasm which is of the order of 10^4 times lower than the concentration in the extracellular fluid. In this way an important membrane transport and signal transduction pathway is established, which can be triggered even by a minimal increase in the Ca-permeability of the membrane or a release of Ca^{2+} from SR.

2.7   Experimental method – patch-clamp technique

This section introduces the patch-clamp method – an experimental technique that was used to collect the data that are analysed in Chapter 5. Patch clamp is a technique employed in electrophysiology [258]. Patch clamping can be performed using the voltage clamp technique (or current clamp), together with micropipettes. The technique was developed by E. Neher and B. Sakmann in the late 1970s/early 1980s, and was awarded the Nobel Price in Physiology or Medicine in 1991. The patch-clamp technique allowed for the recording of single ion channel current for the first time. Importantly the pipette, which has a relatively large tip diameter, is sealed onto the surface of the cell membrane, rather than inserted through it. There are several modes of patch-clamp recordings, presented in Fig. 2.7. Firstly, one should achieve so-called a giga-seal, or in other words electrical isolation between the membrane and the pipette, known as cell attached. The most common type of patch-clamp is whole-cell, where the membrane needs to be ruptured and thus an access to the interior of the cell is achieved. Alternative to rupturing the cell is to apply small amounts of an antifungal or antibiotic agent, such as amphothericin-B and after achieving the cell attached mode, and then wait until the pores will be formed. This is known as

perforated patch. Other modes appropriate to measure single channel(s) activity in isolation from the cell are outside-out and inside-out.
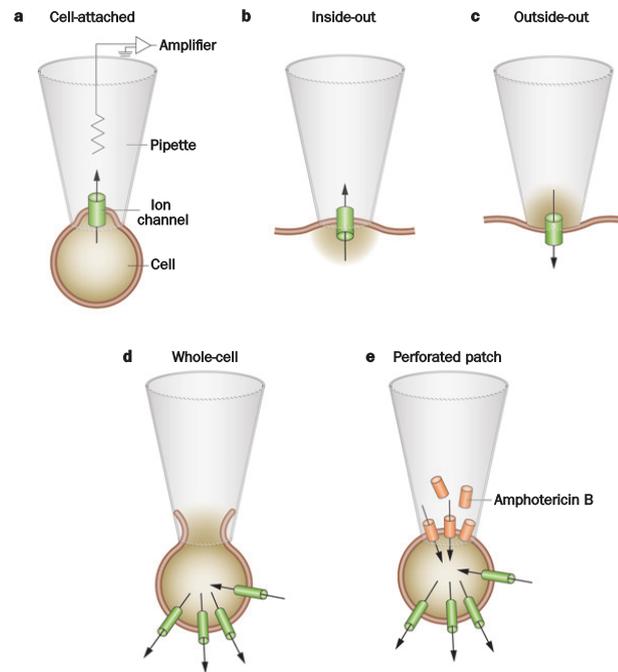
Figure 2.7: Different modes of the patch-clamp technique. First part common for all the modes is achieving so-called giga-seal, or in other words electrical isolation between the membrane and the pipette, known as cell-attached, on cell (a). Most common mode of patch-clamp is whole-cell patch-clamp (d), where the membrane needs to be ruptured and thus an access to the interior of the cell is achieved. From there, it is possible to measure single channel(s) activity in isolation from the cell, where the outside of the channel faces the extra-cellular solution, also known as outside-out (c). Alternatively, from the cell attached mode, the patch of the membrane can be detached, by pulling the pipette. This may lead to the possibility of measuring single ion channel activity, separated from the cell, where the interior of the channel faces extracellular solution, also called inside-out (b). Another option is to apply small amounts of an antifungal or antibiotic agent, such as amphothericin-B and after achieving the cell-attached mode, and then wait until the pores will be formed. This is known as perforated patch (e). Picture reprinted with permission from [11].

2.7.1   Perforated patch-clamp technique

The whole-cell patch-clamp technique allows for measuring the collective electric activity of all the membrane transporters. This represents the collective current crossing the membrane or the collective membrane potential change. Nevertheless because of the need to rupture the membrane, there is no guarantee that the cell will stay functional. This means that small organelles, like mitochondria, may diffuse to the pipette rather than stay inside the cell. One possible solution is to avoid breaking the membrane by instead forming small pores that allow only small ions to freely diffuse between pipette and the cell. This is possible by applying tiny amount of an antifungal or antibiotic agent, such as amphothericin-B, nystatin, or gramicidin into the pipette solution. After achieving the gigaohm seal, the agent will slowly

form the pores, providing electrical access to the interior of the cell. Many studies on amphotericin-B have confirmed the existence of monovalent cation over anion selectivity [98].

2.8 Membrane transport in Jurkat cells

Many ion channels, transporters and pumps interplay resulting in rich dynamics of the membrane potential. Here, the selected membrane transporters that may contribute to the membrane potential in Jurkat cells are reviewed. Jurkat cells are the immortalised line of human T lymphocyte cells.

2.8.1 Potassium transport

Kv1.3 and voltage-gated K$^+$ current

The voltage-dependent K$^+$ current is activated when the cell membrane is depolarised, and K$^+$ ions passively move outwards from the cell along its electrochemical gradient. If the membrane remains depolarised channels are slowly closing (inactivating). Efflux of K$^+$ ions causes the membrane potential to decrease. Typically human peripheral blood T cells have approximately 300-500 functional Kv1.3 channels [40, 39]. Only a small fraction of those channels (1-2 channels [44]) is involved in maintaining the resting potential which is around -50 mV in physiological conditions. However, when the membrane becomes depolarised, the Kv1.3 channels' conductance increases more than 10 times. This prohibits additional depolarisation even after an influx of Ca^{2+} ions [39]. However Ca^{2+} was also reported to block the voltage-gated K$^+$ channels in the whole-cell configuration, (when [Ca^{2+}]$_i$ was elevated from 10 nM to 1μM) [33]. Interestingly, voltage-gated K$^+$ channels in squid giant axons have been directly shown to be permeable to Ca^{2+} in experiments using high Ca^{2+} concentrations, passing about 1% as much Ca^{2+} as K$^+$ current [44]. Intracellular ATP (up to 1 mM) was reported to have no influence on activity of voltage-sensitive K$^+$ channels [33].

KCa3.1 and Ca^{2+}-activated K$^+$ current

The properties of Ca^{2+}-activated channels found in T-cells are well distinguishable from those of voltage-gated K$^+$ channels. The KCa3.1 channel is naturally closed and opens rapidly when cytosolic Ca^{2+} rises effectively up to 300 nM. The channel is voltage independent and activated by Ca^{2+} binding to calmodulin, which is connected to the C terminus of the channel [66]. The channel opening allows for K$^+$ efflux preventing membrane depolarisation, and thus maintaining the favourable (more negative) potential for sustained Ca^{2+} entry ([39] and ref. therein). Grinstein et al. [91] summarised evidence of their presence in T lymphocytes. Nevertheless another group using fluorescence measurements indicated that they are unlikely to

contribute to the averaged membrane potential [265]. Channels were well characterised later, using the patch-clamp technique [94]. The resting T lymphocytes revealed around 20 conducting channels, noting that this number increases even up to 500 in activated T cells.

2.8.2 Calcium transport

Calcium is a universal second messenger involved in the regulation of many cellular processes, including ion transport, proliferation, motility and secretion. Second messengers are intracellular signalling molecules released by the cell in response to exposure to extracellular signalling molecules–the first messengers. Intracellular free Ca^{2+} is being maintained at a very low level (about 10^4 times lower than in the extracellular space), so that any small changes in concentration bring drastic and rapid consequences. This allows for a very efficient communication.

STIM1 and Orai1, CRAC current

Calcium currents in T-lymphocytes were explored using different techniques but successful recordings were only made after combining the perforated patch-clamp technique together with careful monitoring of intracellular Ca^{2+} [149]. The tiny inward Ca^{2+} current was connected to the T cell receptor (TCR) stimulation. The perforated patch-clamp technique, based on permeabilising the membrane with pore-forming antibiotics, allows for preserving the signal transduction pathways. Studies reveal inwardly rectifying Ca^{2+}-selective current. In normal conditions the concentration of cytosolic free Ca^{2+} is very low, therefore a few picoampere current already causes a substantial rise in Ca^{2+}. This current is activated by depletion of ER luminal Ca^{2+}. When the ER Ca^{2+} store is depleted, STIM proteins transduce the signal from ER to the plasma to activate the CRAC channels formed by Orai1 proteins [69]. STIM triggers CRAC channels to open [272, 191].

Voltage-gated Ca^{2+} channels (VGCC)

Ca_V channels are highly selective to Ca^{2+}. Their role in Ca^{2+} influx is well investigated in neurons, cariomyocytes, and other excitable cells. The role of Ca_V channels in TCR-induced Ca^{2+} influx was confirmed in experiment with genetically modified mice, lacking the typical expression of Ca_V [185, 16, 120]. All experiments resulted in reducing the Ca^{2+} influx. However there is a major gap in understanding how Ca_V1 channels are activated in immune cells [70]. In excitable cells, typically a channel's voltage sensor is sensitive to depolarisation of the plasma membrane. At physiologic or resting membrane potential, VGCCs are normally closed. They are activated (i.e., opened) at depolarised membrane potentials and this is the source of the "voltage-gated" epithet. Meanwhile most of the studies on T cells indicated the opposite

effect: TCR-induced Ca^{2+} influx is reduced, rather than increased, under the membrane depolarisation because of the reduced electrical driving force for Ca^{2+} influx through CRAC channels.

Great attention has been paid to mechanism of Ca^{2+} entry to the cell. However the mechanism of removing the Ca^{2+} from the plasma membrane is nevertheless important.

Ca^{2+}-ATPase

Plasma membrane Ca^{2+}-ATPases (PMCA) provide the dominant mechanism for Ca^{2+} clearance in human T cells and Jurkat cells [148]. In comparison to the Na^+/Ca^{2+} exchanger, which is believed to be an another important mechanism of Ca^{2+} exclusion [60, 17, 61], PMCA has a high affinity for intracellular Ca^{2+} and low transport capacity [91]. The reported transport rates of Ca^{2+} (in vesicular systems) were very different spanning from 0.08 [15] to 2.4 pmol $\cdot \mu$g protein$^{-1} \cdot$ min^{-1} [152]. This transport was reported to be Mg^{2+}-dependent and insensitive to ouabain or changes in K^+ or Na^+ concentrations [152]. Ca^{2+}-ATPase activity was enhanced by ATP concentrations up to 1 mM, (nevertheless further increase in Ca^{2+} uptake was observed with increase in ATP concentration up to 4mM [152]).

A second, nonetheless important, mechanism for removal of Ca^{2+} from the intracellular space, is the SERCA pump clearing the Ca^{2+} from the cytosol into the endoplasmic reticulum (ER). Its contribution in human T cells to the rate of clearance of cytosolic Ca^{2+} is small [148]. However, SERCA plays an important role in the Ca^{2+} signaling network in T cells by accumulating Ca^{2+} in the ER and controlling store-operated Ca^{2+} entry [59].

A large number of Ca^{2+} sources and sinks interact with each other, creating a variety of complex Ca^{2+} responses, e.g. isolated transients, sustained oscillations or elevated intracellular Ca^{2+} concentrations [148, 24, 48].

2.8.3 Chloride transport

There are large discrepancies in the values of total chloride concentration in lymphocytes reported by different groups spanning from 82-87 mM [273] to significantly lower concentrations estimated later [92]. The conductive permeability of the lymphocyte membrane to Cl^- is considered as very low. Moreover, cells rendered permeable to cations by means of the conductive ionophore gramicidin fail to swell osmotically, indicating that anion Cl^- conductance is negligible. Finally, the rate of $^{36}Cl^-$ transport was found to be unaffected by changing the membrane potential, as would be expected for a conductive pathway [92].

Swelling-activated Cl⁻ current: volume regulation

At least three different of osmotically activated Cl⁻ channels were reported in the 1990s in human T lymphocytes [39, 150, 209]. Although Cl⁻ conductance is negligible in lymphocytes suspended in isotonic media, a marked change has been reported when the cells are subjected to hypotonic stress therefore they were named volume-regulated anion channels (VRAC) or swelling-activated Cl⁻ channels (Cl_{swell}) [150, 209]. Alternatively, addition of ATP to the pipette makes the solution hypertonic, which implies the influx of water and the cell swelling [39]. Consequently outwardly rectifying Cl⁻ channels are activated. The Cl⁻ current is induced about 1 min after the cell starts swelling. For many years the molecular identity of VRAC had been unidentified. Relatively recently two studies identified a four transmembrane domain proteins (LRRs) called LRRC8A or SWELL1 as a presumed pore-forming subunit of VRAC channel [257, 198]. In the whole-cell patch-clamp recordings the capability to induce the Cl⁻ current decreased a few minutes after achieving the whole-cell configuration, unless intracellular ATP was added or the experiment was performed in perforated patch mode, when current can be observed for at least 30 min [150]. ATP may be required for phosphorylation or allosteric activation, or as an energy source for ion pumping or reorganization of cytoskeletal filaments. This channel did not indicate any voltage-dependence. Based on current variance analysis [223] during the osmotic activation of Cl⁻ current, it was estimated that each cell contains on the order of 10^4 activatable Cl⁻ channels, making it the most abundant ion channel in lymphocytes yet described [150]. This number very much differs for different cells, dependent on their function.

   Cl_{swell} and Kv1.3 channels interplay in regulatory volume decrease (RVD). Cl⁻ channels are activated by volume increase, efflux of Cl⁻ ions depolarises the membrane, which directly activates voltage-activated K⁺ channels. The membrane potential stays between the equilibrium potentials for Cl⁻ and K⁺ but the concentrations of Cl⁻ and K⁺ decrease. Volume regulation was found to be generally associated with a loss of cellular K⁺, with little change in Na⁺ content [37, 92, 207]. As a result, water molecules leave the cell, and after few minutes the cell shrinks back to its original size. Consequently, Cl⁻ channels close.

   In physiological conditions (pig) lymphocytes were reported to lack active Cl⁻ transport mechanisms. However, studies using fluorescence, have indicated their existence in an extremal environment [68].

2.8.4   Sodium transport

In the pioneering studies on Jurkat cells a very small fraction of human T cells exhibited voltage-gated Na⁺ activity [40], yet later studies confirmed their absence from T cells [256]. However, other research reported Na_V currents in 10% of Jurkat T

cells [75, 105], indicating their role in the invasive capacity of T cells [44]. In T lymphocytes sodium reaches equilibrium very quickly [93, 153]. This suggests the presence of effective transport mechanisms [91]. Despite the isotopically measured large permeability to Na^+, the Na^+ conductance is comparatively low [93]. This can be explained by the existence of robust electroneutral transport pathways [91].

The essential contribution to Na^+ transport in lymphocytes is done by Na^+/K^+ ATPase. Three independent studies, using ouabain, drew similar conclusions, finding 32,400–44,000 ouabain binding sites per cell (but the cells from chronic lymphocutic leukemia patients indicated significantly fewer pumps [263], as reviewed in [91]). In the other studies, using radioactive probes, Na^+/K^+ pumps were shown to modify the membrane potential by 7 mV, with the average membrane potential -56 mV [68]. The membrane potential of lymphocytes measured with an electrophysiology method was reported to be significantly higher. Nonetheless an important contribution to Na^+ transport, found in the plasma membrane of various types of lymphocytes, is done by the Na^+/H^+ exchanger (NHE). This transporter is known to be a major carrier involved in regulating both cytosolic pH and the cell volume [93, 91]. The stimulation of NHE leads to alkalisation of plasma membrane and/or the cell swelling, and its inhibition leads to acidification and contributes to apoptosis [143]. Moreover, the decline of ATP is known to inhibit Na^+/H^+ exchangers.

Some studies reported the presence of $Na^+-K^+-2\,Cl^-$ cotransporters in the lymphocyte plasma membrane [14, 93] but later studies did not manage to confirm it [93]. It was concluded that $Na^+-K^+-2\,Cl^-$ cotransporters, if present, contribute very little to membrane transport in T cells. Similarly, the role of Na^+/Ca^{2+} exchangers can be omitted in T cells [61].

TRPM4, TRPM7 and MIC current

TRPM4 has been described as a calcium-activated nonselective (CAN) cation channel that mediates membrane depolarisation. It belongs to the family of transient receptor potential (TRP) channels. TRPM4 indicates higher permeability to Na^+ than to Ca^{2+} [70, 144, 145] and can be activated by Ca^{2+} influx following antigen receptor stimulation, resulting in Na^+ influx and membrane depolarisation. Consequently, the driving force for Ca^{2+} is reduced. TRPM4b may interplay with K^+ and Cl^- channels to control intracellular Ca^{2+} oscillations through oscillatory changes in the membrane potential [145]. TRPM4 was reported to regulate Ca^{2+} oscillations after T cell activation [144]. Another outward rectified channel transporting monovalent and divalent cations non-specifically should be mentioned, known as Mg^{2+}-inhibited Ca^{2+}-permeable (MIC) current exhibits the time course similar to the CRAC channel and higher conductance [39].

With the use of atomic absorption spectrophotometry, the estimated value of total cellular magnesium in porcine mesenteric lymphocytes was 12 mM [204]. The

MIC-TRPM7 channel is also permeable to Mg^{2+} ions, and therefore can play a role in Mg^{2+} homoeostasis.

2.9 Summary

This chapter describes the various cellular processes and quantities that may influence and also be influenced by the membrane potential. A summary of these is presented in Fig. 2.8. Arguably the central point of cellular oscillators is metabolism. This is influenced by pH or glucose availability but may also be influenced by the ionic composition of the cell [126, eq. (2.169)] (either directly or by the cascade of processes like in β-cells), or the instantaneous demand for ATP and energy charge of the cell [12]. ATP is mostly utilised to maintain the ionic concentration gradients and consequently the negative membrane potential. The progression of the cell cycle is influenced by the ionic composition (the membrane potential is a function of the charge distribution) and metabolism. The cell volume is directly proportional to the amount of water in the cell, while the flux of water through the membrane is proportional to the osmotic pressure difference. The osmotic pressure is determined by the number of particles per unit volume of fluid. Therefore, the cellular volume is another function of ionic composition. Ca^{2+} oscillations, not included in the figure, establish a very efficient information transmission system because they can evoke cascades of other process. Ca^{2+} oscillations can be considered as a special class of oscillations in the ionic composition. When designing experiments the interactions within the cell should be carefully taken into account. "Fixing" or even perturbing one of the parameters may unnaturally affect the others. Unfortunately this takes place to some extent, in every experiment. However, the importance of cellular interactions is to be considered. The final section introduces the membrane transport specific to Jurkat cells used in experiments that data are analysed in Chapter 5.
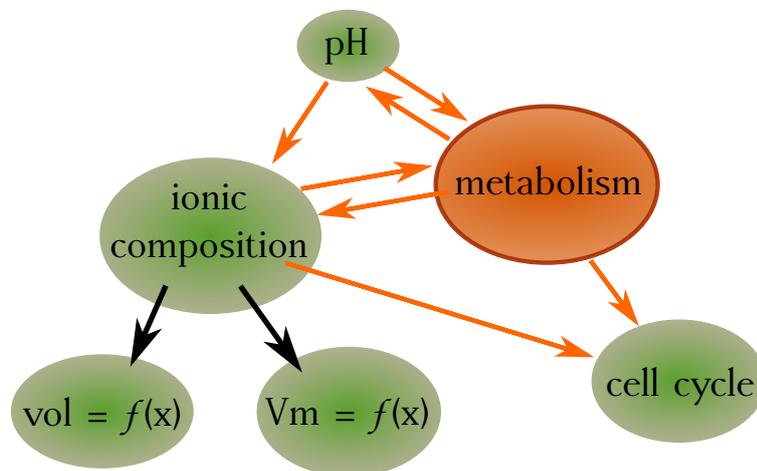
Figure 2.8: The summary of some of the interactions between cellular oscillators. In the central part should be metabolism, bidirectionally coupled to ionic composition and pH. The cellular volume and the membrane potential are directly dependent on ionic composition. Cell cycle is influenced by metabolism and ionic composition. More details *how they interact?* are written in the main text.

Chapter 3

Tackling the complex dynamics with time-frequency analysis

3.1 Introduction

Remarkable complexity can be found in the recordings originating from living systems. Therefore they require very careful and subtle treatment. Assumptions such as stationarity, linearity or time-invariance are invalid in numerous cases. This chapter reviews and discusses selected methods that have been applied to the analysis of the complex dynamics in general. In addition, it provides a more detailed insight into the methods that have been used to analyse the recordings of membrane potential in Chapters 5 and 6. Sec. 3.2 introduces dynamical systems in general. Sec. 3.3 introduces methods operating directly in the time domain, while Sec. 3.4 is focused on the frequency domain. In Sec. 3.5 methods combining both the time and frequency domains are presented. Sec. 3.6 provides an outlook into the methods appropriate for investigating the coupling between interacting oscillatory systems. Finally, in Sec. 3.7 selected statical techniques for dynamical testing of hypotheses using surrogate data are presented.

3.2 Dynamical systems

Dynamical systems theory describes the evolution over time and phase space of the system under consideration. Let $\mathbf{x}$ be a d-dimensional vector, describing the state of the system. Considering continuous time, the evolution of the system is described by *differential equations*. An important example of such equations are *ordinary differential equations* (ODE), which concern the time evolution of the system. Therefore, the time evolution of $\mathbf{x}$ is described by

$$\dot{\mathbf{x}} = \mathbf{f}(\mathbf{x}). \tag{3.1}$$

Here the overdot denotes differentiation with respect to time, t. Thus $\dot{\mathbf{x}} \equiv \frac{d\mathbf{x}}{dt}$. The state of the system (3.1) depends only on the evolution function $f(x)$ and its current state but not on time. This class is called *autonomous dynamical systems*.

3.2.1 Nonlinearity

One of the properties characterising complex systems is nonlinearity. Nonlinearity is a relationship which cannot be explained as a linear combination of its variable inputs. The term *nonlinear dynamics* refers to a system described by the set of nonlinear differential equations. Typical nonlinear terms are products, powers, and functions of the x_i, such as $x_i x_j$, $(x_i)^3$, $\cos(x_j)$, where i denotes i-th coordinate of $\mathbf{x}$ [235, p. 6]. Nonlinear systems attract a lot of interest, despite the fact that the majority of them are impossible to solve analytically. The essential difference is that linear systems, as opposed to nonlinear, can be broken down into parts. Subsequently, each part can be solved separately and finally recombined to solve the problem. In many cases this simplification does not work in real-life systems. Whenever parts of a system interfere, cooperate, or compete, nonlinear interactions must be involved [235, p. 9].

3.2.2 Non-autonomous systems

There is a class of systems whose evolution law explicitly depends on time, called *non-autonomous systems*, which can be generally defined as

$$\dot{\mathbf{x}} = \mathbf{f}(\mathbf{x}, \mathbf{t}). \tag{3.2}$$

The state of the system depends on the evolution function $f(x, t)$ and time but also on the initial conditions of both $\mathbf{x}$ and time.

3.2.3 Phase oscillator

Particularly interesting, when thinking about the systems in nature are *self-sustained oscillatory systems* [194]. Those oscillators are characterised by the following: they maintain their oscillations even if isolated; the form of the cycle, and hence the form of oscillation is entirely determined by the internal parameters of the system; and eventually the oscillations are stable against (small) perturbations. Such systems can be formally described as *limit-cycle oscillators*, where the limit-cycle is the curve in state space associated with the oscillation. It is convenient to represent a self-sustained oscillator as a single variable, namely the phase. This type of oscillator is called a *phase oscillator*, formally denoted as

$$\dot{\phi} = \omega. \tag{3.3}$$

Here, more useful will be to introduce *non-autonomous phase oscillator*, defined as

$$\dot{\phi} = \omega(t). \tag{3.4}$$

In the following sections, various systems such as frequency modulated or amplitude modulated are used to visualise the performance of the introduced methods.

Meanwhile, the following oscillator with a varying frequency is given as an example

$$\dot{\phi} = \omega_0(1 + k\sin(\omega_m t)),$$
$$r = 1.$$
(3.5)

Here, $\omega_0 = 2\pi f_0$ is the main frequency, $\omega_m = 2\pi f_m$ is a frequency of slow variation, and k is the amplitude of variability $[0, 1]$. The signal $s = r\sin\phi$ was simulated for time T with the sampling frequency $F_s = 1/dt$.

3.3 Time domain

Living systems are rarely isolated from their surroundings; instead they interact and adapt to the dynamically changing environment. This adaptation is pronounced in time-variability. Therefore, when one tries to understand the dynamics of an open system, the importance of time must be stressed and explicitly considered. In this section time domain methods that could aid in the understanding of the membrane potential dynamics are introduced.

3.3.1 Time-reversibility

Living systems are rarely linear. A very powerful indicator of nonlinearity in a time series is the change of statistical properties introduced by a reversal of the time direction [242, 213, 58, 215]. For discretely sampled time series, $\vec{S} = \{s_1, ... s_N\}$, the quantity

$$\alpha_{rev} = \frac{1}{N} \sum_{n=1}^{N-1} (s_{n+1} - s_n)^3,$$
(3.6)

is a one of the simplest measure of the asymmetry of a series under time reversal. Linear stochastic processes do not contain any information about the direction of time. Therefore the time-irreversibility implies the nonlinearity, but the nonlinearity does not imply time-irreversibility. An example of this is the fact that the measure, from Eq. (3.6) is not able to distinguish nonlinearity in the Lorenz system [213].

3.3.2 Moving average

One of the preprocessing routines in signal analysis is filtering out the "background noise". However deciding which part of the signal should be considered as meaningless noise is one of the greatest challenges. The moving average is a smoothing filter that uses the idea of averaging within the segments (windows) of the signal and replacing the middle point of each segment with the average value. The window is shifted along the time series. There are a few variations: simple, cumulative, or the weighted forms but the simple version is commonest. Mathematically, the i-th element of the discrete time series $\vec{S} = \{s_1, ... s_N\}$, smoothed with the function

f_n, where n is the length of the smoothing window, can be defined as

$$s'_{\vec{S},f_n}(i) = f_n(\{s_{i-n/2},...s_{i+n/2}\}),\tag{3.7}$$

where the most commonly f denotes the average. The moving average removes short-term fluctuations (i.e. the high frequency component) and highlights longer-term trends or cycles. A common use of the moving average, as in the following chapters, is to downsample a time series [50]. Finally it is also important to note that the moving average enables to smooth-out the high frequencies from the time series in order to avoid *aliasing*.

3.4   Frequency domain

Analysis exclusively in the time domain is quite limited and usually ends up not to be very informative. A typical way in time series analysis is to use the frequency domain to demonstrate how the signal energy is distributed over the frequency range.

3.4.1   Fourier transform

The Fourier transform decomposes the function in time, $f(x)$ into its constituent frequencies. Mathematically it can be written

$$\hat{f}(\xi) = \int_{-\infty}^{\infty} f(u)e^{-2\pi i u \xi}du,\tag{3.8}$$

where ξ is a real number. If we restrict the consideration to periodic functions with period T, fulfilling Dirichlet conditions, then each function can be represented as a Fourier series

$$f(x) = \sum_{n=-\infty}^{\infty} c_n e^{-i\frac{2\pi t}{T}n},$$
$$c_n = \frac{1}{T}\int_0^T f(t)e^{\frac{2\pi i n t}{T}}dt.\tag{3.9}$$

In practice signals are never continuous or infinite. Therefore the discrete Fourier transform (DFT) is used,

$$X_f = \sum_{n=0}^{N-1} x_n e^{-\frac{2\pi i}{N}kn}.\tag{3.10}$$

The gap between analytic continuous formulas and their actual numerical implementations is typically not discussed, but the exact derivation of the DFT from the FT can be found in [79]. The frequency interval for the DFT is restricted to $1/T = F_s/N$ (low) and $F_s/2$ (high frequency), where T (in sec) and N (in points) is the length of time series and F_s sampling frequency. The frequency resolution of DFT is equal to F_s/N.

Now, the DFT will be tested on the signal with time-variability introduced in Eq. (3.5). The results of the DFT can be seen in Fig. 3.1. The amplitude spectrum

consists of discrete harmonics like peaks, also from beyond the range of variability of the main frequency (0.4–1.6 Hz). The highest peaks are around the frequencies that are the extremes of the range of variability. To investigate whether this effect is entirely numerical or has an analytic origin, the analytic formula was expanded in Appendix B.1. From this form it is clear that discrete peaks are to be expected, and are neither the numerical effect of under-sampling or finite length of the time series, nor the effect coming from the DFT instead of (continuous) Fourier transform. Importantly, this representation, perfectly correct and real, does not bring much of an insight into the nature of oscillations. For oscillations with sinusoidally-varying frequency, it was possible to find another analytic form; nevertheless real life signals often have more complicated forms.
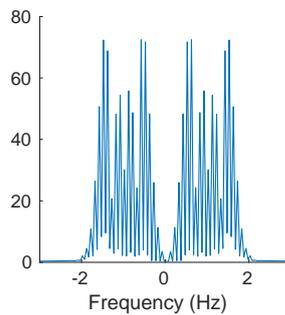
Figure 3.1: Amplitude spectrum of DFT of the signal with time-varying frequency, Eq. (3.5). The spectrum consists of discrete peaks. This representation, although perfectly in agreement with the theoretical predictions (see the main text for the details), does not provide much information about the original dynamics. The simulation parameters were: $k = 0.6$, $T = 20$ sec, $F_s = 20$ Hz, $f_0 = 1$ Hz, $f_m = 0.1$ Hz.

3.5   Time-frequency domain

It was shown above that signals exclusively in the time domain or exclusively in the frequency domain are not very informative when it comes to oscillations with complex forms. Time-frequency representations allow for simultaneous insight into both the time and frequency dynamics. Thus, combining the two domains can give great advantages.

3.5.1   Short-time window Fourier transform

The very first method to include both the time and frequency domains was named the short-time window Fourier (WFT). It uses the Fourier transform applied to the short-time-window of the time series, defined as

$$\tilde{f}(\omega, t) = \int_{-\infty}^{\infty} e^{-2\pi i \omega u} \overline{g}(u - t) f(u) du. \tag{3.11}$$

Here, g is a function of a window in time, while $\overline{g}$ its complex conjugate. The function g can be arbitrary with finite energy [108]. Nevertheless well justified and common choice is the Gaussian window

$$g(u) = \frac{1}{\sqrt{2\pi f_0}} e^{-(u/\sigma)^2/2}. \tag{3.12}$$

Its Fourier transform is then given by

$$\hat{g}(\xi) = e^{-2(\pi \sigma \xi)^2}. \tag{3.13}$$

The Gaussian window provides the optimal joint time-localisation and frequency resolution [159, 123, 168]. The width of the window is determined by the resolution parameter σ. Shorter time windows provide a better localisation in time, but unfortunately a worse resolution in frequency. Correspondingly longer time windows provide a better resolution in frequency, but a worse localisation in time. This property is defined by the *Heisenberg-Gabor uncertainty principle*, which states that sharp localizations in time and in frequency are mutually exclusive [123].

3.5.2   Wavelet transform

One way to minimise the impact of the above uncertainty principle, rather than sticking to the fixed window length for all the frequencies (as in WFT), is to fix the number of cycles for each frequency. Principally, this means that the window length must be adaptive and must depend on the frequency. This idea is implemented in the continuous wavelet transform (WT), defined as

$$W_{\psi, x}^{[p]}(f, t) = \left(\frac{f}{\kappa}\right)^p \int_{\mathbb{R}} x(\tau) \overline{\psi\left(\frac{(\tau - t)f}{\kappa}\right)} d\tau. \tag{3.14}$$

Here, is the $W_{\psi,x}$ wavelet transform of signal x, given the wavelet function ψ, $\overline{\psi}$ denotes its complex conjugate, p is the normalisation constant, f is a frequency and t time. The alternative choice of p is discussed in Chapter 4, meanwhile $p = 1$ will be assumed unless otherwise stated. κ is where the Fourier transform of the wavelet function $\hat{\psi}$ is maximised. For the lognormal wavelet, defined in Sec. 3.5.2, κ is equal to 1. It is always possible to rescale ψ such that κ becomes 1 without any loss of generality. However, in practice, the conventional formulations of some wavelets (such as Morlet wavelets) do not have their Fourier transform $\overline{\psi}$ maximised at or near 1. Because of this fact, the presence of κ is retain in the definitions.

In real-life time series analysis it is reasonable to assume only non-negative frequencies. Therefore, only the analytic wavelet functions with non-negative-valued Fourier transform are used here. A detailed discussion regarding this point and why negative valued FTs should be used can be found in [108, supplementary]. Typically wavelet analysis is defined in terms of scales s; however, in practice it is more intuitive to work directly with frequencies f ($f = \frac{\kappa}{s}$). Therefore, all functions and variables are transformed with respect to the frequencies. In general, a simple reciprocal relationship between scale and frequency is not always guaranteed to be appropriate. However, the wavelet of the unimodal Fourier transform is a natural choice [177, 170].

Practical remark   Practically, in numerical analysis the wavelet transform takes a different form to Eq. 3.14, due to its computational cost. Typically the convolution theorem is applied and the form

$$W_{\psi,x}^{[p]}(f,t) = \left(\frac{f}{\kappa}\right)^{p-1} \int e^{2\pi i \xi t} \hat{x}(\xi) \hat{\psi}\left(\frac{\kappa\xi}{f}\right) d\xi \qquad (3.15)$$

is implemented instead. $\hat{x}(\xi)$ stands for the Fourier transform of x. This substantially speeds up the computations [3].

Wavelet energy density

To allow for quantitative wavelet analysis over time-frequency space, a suitable measure must be introduced. This measure is known as wavelet energy density (WED, $\rho_{\psi,x,x}^{I}$), and it can be defined as (transformed from [123, p.69])

$$\rho_{\psi,x,x}^{I}(f,t) = (C_\psi \kappa)^{-1} f^{1-2p} |W_{\psi,x}^{[p]}(f,t)|^2. \qquad (3.16)$$

Here, C_ψ is called the admissibility constant and it can be defined as

$$C_\psi = \int_0^\infty \frac{\hat{\psi}(r)^2}{r} dr. \qquad (3.17)$$

The wavelet energy over region of interest A, in time-frequency space is then defined as

$$p_{\psi,x,x}^I(A) = \int_A \rho_{\psi,x,x}^I(f,t)d(f,t). \tag{3.18}$$

Defining the wavelet function

A wavelet function must fulfil the admissibility condition $\int_0^\infty \frac{\hat{\psi}(r)}{r}dr < \infty$, which implies having a vanishing expected value in the time domain. Particular attention is paid to the lognormal wavelet, also known as the log Gabor wavelet [132, 72, 154, 108]

$$\hat{\psi}_\sigma = e^{-2(\pi\sigma\log r)^2} = \frac{1}{\sqrt{2\pi}\sigma}f_{1/(2\pi\sigma)}(\log r) = \hat{f}_\sigma(\log r), \tag{3.19}$$

for $r > 0$. Here, f_σ is the probability density function of a normal distribution of mean zero and variance σ^2. σ is a parameter that corresponds to frequency resolution discussed later in this section. The justification of the choice of the wavelet function can be found in Appendix B.2. Intuitively, the lognormal wavelet is represented by the Gaussian window in both the time and log-frequency domains, which according to the uncertainty principle, ensures the optimal time localisation and frequency resolution. All the further calculations and analyses are done using this wavelet.

Finite signal length effect, cone of influence

Theoretically, one integrates over an infinite time, but in practice the signal has a finite time duration. Therefore a problem appears near the signal's time borders, because of the convolution operation, where the dot product of the time-shifted wavelet function and the signal is calculated and assigned to the value of time-shift. If the time-shift is too small (or too big) a substantial part of the wavelet function goes beyond the signal end points, see Eq. (3.14). There are several ways to tackle this issue: one can use padding. This fills the signal with chosen values at both ends, and then the subset of values that corresponds to the original length of the time series in the WT can be selected. The most common padding scheme are: filling with zeros, symmetric/periodic and predictive padding [249, 108]. However, regardless of the scheme, padding may introduce discontinuities and distortions into the WT. For better accuracy it is advisable to rely on the time-frequency region where boundary distortions are negligible. This is known as the cone-of-influence (COI). The reliable region in time-frequency space is given by $\left[0 + \frac{\Delta}{f}, L - \frac{\Delta}{f}\right]$ where

$$\int_\Delta^\infty |\psi(r)|dr \simeq \int_\Delta^\infty f_\sigma(r)dr = 0.025\int_{-\infty}^\infty |\psi(r)|dr. \tag{3.20}$$

The number 0.025 is estimated using the properties of the Gabor window and setting the "cut-off" at 2 standard deviations.

There are exceptional circumstances, e.g. extracting the oscillatory modes from the time frequency representation [109], where removing the cone of influence is not advisable [108].

Selection of frequency resolution

Dependent on the underlying dynamics One of the most important, and non-trivial parameters to select in wavelet analysis is the frequency resolution (σ). The optimal choice of σ depends on the properties of the dynamics that generate the time series and the information that one is trying to obtain. The following signals are considered as examples: two-cosine signal presented in Fig. 3.5, frequency modulated signal presented in Fig. 3.6, and amplitude modulated one shown in Fig. 3.7. Four types of behaviour of their time-frequency representation can be indicated [108], namely:

I. All tones are fully resolved – the signal is represented as a sum of sinusoidal components, the amplitudes are constant over time and there is no time variability.

II. Tones are partially resolved and interfere with each other, nevertheless on time-averaged WT several distinct peaks can be indicated.

III. Tones strongly interfere with each other, some of them merge on a time-averaged WT.

IV. Signal is represented as one mode with time-varying frequency, and one distinct peak on time-averaged WT can be indicated.

The behaviour depends on the timescales of the dynamics and the selected frequency resolution, for example for signal from Eq. (3.5), this would be two variables, $\sigma f_m / f_0$ and k. The idea and the signals with their parameters are adapted from [108] and the idea is illustated in Figs. 3.5– 3.7.

Independent of the underlying dynamics The reasonable σ range discussed in this paragraph is entirely methodological and independent of the underlying dynamics of the analysed system. For σ larger than 0.7, the lognormal wavelet can be approximated by the Gabor function, $\phi_\sigma(r) \simeq f_\sigma(r)e^{2\pi ir}$. Fig. 3.2 shows the numerically generated lognormal wavelets in the time domain and the corresponding Gabor functions. For a given σ, the number of oscillatory cycles within one wavelet window is fixed and independent of the frequency, as explained earlier.

- *Low limit of σ*
  From the properties of a Gaussian window it is known that so-called "2 standard deviations", corresponds to $\simeq 95\%$ of the wavelet integral. Consequently $4 \times \sigma$ cycles of oscillations can be fitted independently of the frequency. Therefore in practice, the lowest σ used is 0.5, allowing for fitting $4 \times 0.5 = 2$ cycles of

the oscillations. This property is presented in Fig. 3.3. Computing the WT with a value of σ lower than 0.5 produces meaningless results. On the other hand, in the frequency domain, 95% of wavelet integral centred around f_x would be limited by $f_x \exp(\mp \frac{1}{2\pi\sigma})$. This implies that given a time series of length L in s and sampling frequency F_s in Hz, the reliable frequency interval is limited by $\left[\frac{1}{L} \exp\left(\frac{1}{2\pi\sigma} \right), \frac{F_s}{2} \exp\left(-\frac{1}{2\pi\sigma} \right) \right]$.

- *High limit of σ*

  When the σ is large, a longer time window, and thus bigger region of time frequency at the end of time series is unreliable. This is due to finite time of the time series.

  If one wishes to preserve m cycles of oscillations after removing the unreliable region (Eq. 3.20), then the lowest frequency (f_{min}) that one can use is given by $f_{min} = \frac{4\sigma+m}{L}$, where L is the length of the original time series.

Summarising the discussion above, given the reasonable choice of σ (> 0.5), one obtains

$$
\begin{aligned}
f_{min} &= \frac{4\sigma + m}{L}, \\
f_{max} &= \frac{F_s}{2} \exp\left(-\frac{1}{2\pi\sigma} \right)
\end{aligned}
\tag{3.21}
$$

Frequency discretisation

Another parameter that one needs to select when computing the wavelet transform is the frequency discretisation. On a logarithmic frequency scale, the frequency discretisation $\Delta F_{\log(\text{freqs})}$ can be formulated as

$$
\Delta F_{\log(\text{freqs})} = \frac{1}{nv.}
\tag{3.22}
$$

Here, nv is the parameter telling how many frequency bins are between two neighbouring powers of e, namely e^k and e^{k+1}. Here, the convention to use base e because it simplifies integration over the log-scale, as discussed in Chapter 4. However, in some cases base 2 may be more suitable. Frequency discretisation should depend on the real frequency resolution determined by the span of the wavelet function in the frequency domain, Eq. (3.19). Insufficient frequency discretisation could result in a misleading representation of the two independent frequency modes. However, too high frequency discretisation will unnecessarily increase the computation burden. The lognormal wavelet is represented by the Gaussian window in the frequency domain Eq. (3.19), with standard deviation $\tilde{\sigma}_{\log(\text{freqs})} = \frac{1}{2\pi\sigma}$. Therefore, the window should be represented by a certain number of points, $N_p > 1$. From the properties of Gaussian window it is known that so-called "1 standard deviation" corresponds to $\simeq 68\%$ of the wavelet integral. Therefore, 68% of the wavelet integral, represented by N_p points would correspond to $\Delta F_{\log(\text{freqs})} = \frac{2\tilde{\sigma}}{N_p}$. The corresponding nv can be

found using

$$nv = \pi\sigma N_p. \tag{3.23}$$

$N_p = 1$ is an absolute theoretical minimum: typically greater values, e.g. 8-10 are considered as sufficient.
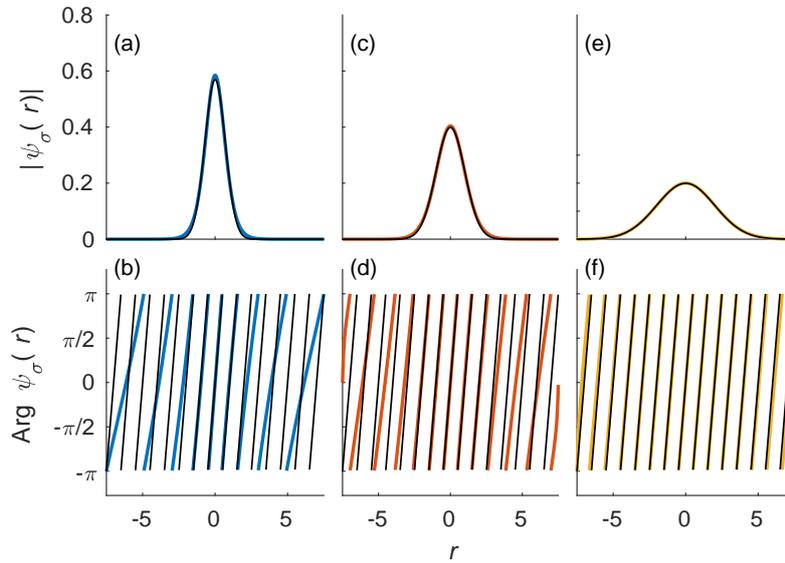
Figure 3.2: Lognormal wavelet function ψ_σ for (a, b) $\sigma = 0.7$, (c, d) $\sigma = 1$, (e, f) $\sigma = 2$. In (a, c, e) the modulus $|\psi_\sigma(r)|$ is shown in colour, against which $f_\sigma(r)$ is shown in black. In (b,d,f) the argument of $\psi_\sigma(r)$ is shown in colour, against which the wrapped angle $2\pi r$ is shown in black. It can be seen that $|\psi_\sigma(r)|$ is approximately equal to $f_\sigma(r)$, and that, where $f_\sigma(r)$ is not very small (compared to its maximum value $\frac{1}{\sqrt{2\pi}\sigma}$), the argument of $\psi_\sigma(r)$ is approximately equal to $2\pi r$ modulo 2π.

3.5.3 Extraction of the oscillations

After observing oscillations of non-trivial form in the time-frequency representation, one aims to extract them from their background. Here, extraction refers to knowing the exact time-dependent phase and amplitude. Typically, dynamical signals are a mixture of complex oscillations, rather than simple sines. Nonlinear mode decomposition is a method that combines time-frequency analysis and surrogate testing to decompose a signal that consists of oscillations of arbitrary form [110]. The method uses the ridge extraction [109] from the time-frequency representation and therefore the results of the reconstruction are dependent on the results of the earlier analysis. Similar ideas were later developed in different groups [197, 165], however, nonlinear mode decomposition provides the full algorithm, including time-shifted surrogate testing [8, 199] and detection of harmonics [219].
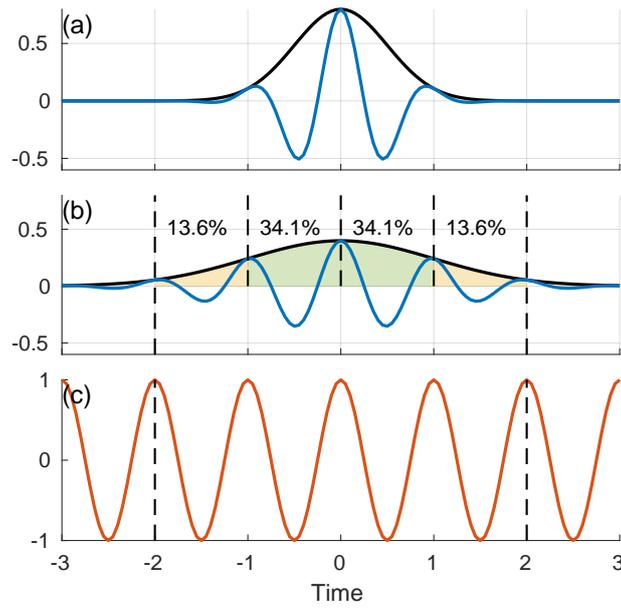
Figure 3.3: Properties of lognormal wavelet in time. Gabor functions $f_\sigma(r)$ for (a) $\sigma = 0.7$, (b) $\sigma = 1$. In (a, b) the modulus $|f_\sigma(r)|$ is shown in black, while the real part of $f_\sigma(r)e^{2\pi i r}$ is shown in blue. In (b), additionally, the properties of a Gaussian window are presented; the integral indicated by the green and yellow areas together corresponds to about 95% of the wavelet integral, and captures $4 \times \sigma$ cycles of oscillations, which for $\sigma = 1$ equals to 4, as discussed in the main text. (c) presents the $\cos(2\pi t)$ function in time.
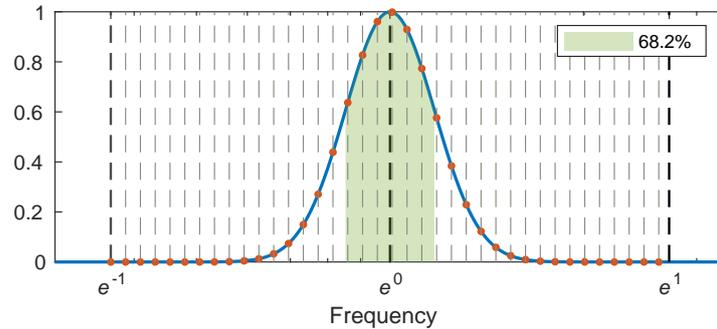
Figure 3.4: The discretisation in the frequency domain of the wavelet function necessary for computations. Figure presents graphically what is discussed in the main text. In blue $\hat{\psi}_\sigma$ as defined in Eq. (3.19). The green area spans between $\exp(\mp\frac{1}{2\pi\sigma})$ along the frequency axis. From the properties of a Gaussian window it corresponds to 68.2% of the wavelet integral. The orange dots correspond to estimated computations points, for $N_p = 6$ and $\sigma = 1$. f_{k+1} dot is in the position $f_k \times \exp(1/nv)$.

3.6 Coupling

An inherent element of life is an ability to interact. Because most of these interactions have a non-trivial form, they require careful treatment. Ideally, applied methods should address not only the questions of whether the coupling exists, or what is its directionality, but also what is the form of coupling. A lot of attention was paid to this topic in recent decades [266, 97, 194, 236], many methods for investigation specific forms of coupling were developed [229]. The reconstruction within
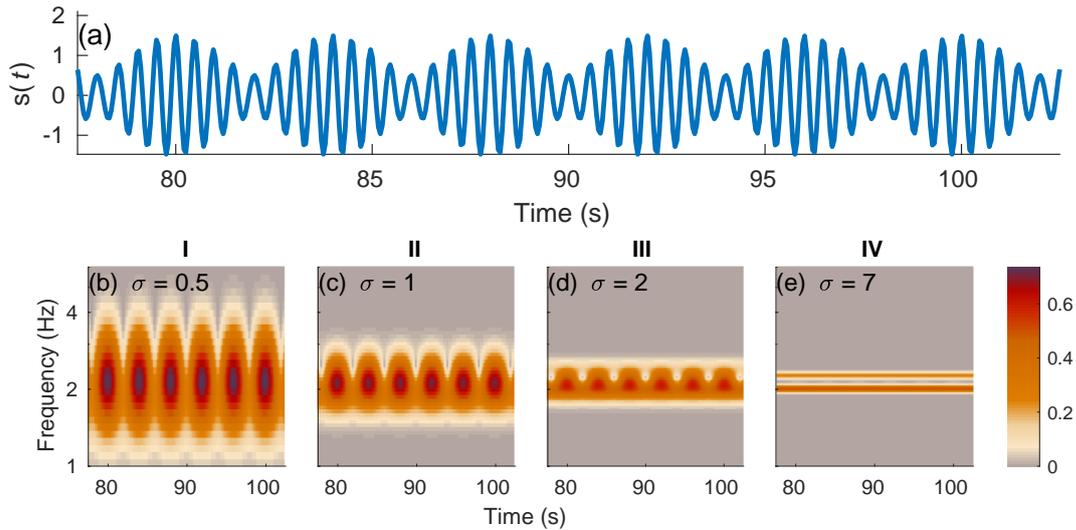
Figure 3.5: Possible behaviour of the wavelet transform for two-cosines signal for different values of σ. (a) Two-cosine signal $s(t) = \cos(2\pi 2t) + 0.5\cos(2\pi 2.25t)$, simulated for 500 sec at sampling frequency Fs = 20 Hz. (b-e) Amplitudes of the wavelet transform for different values of σ. The explanation for the types of behaviour I-IV in the main text.
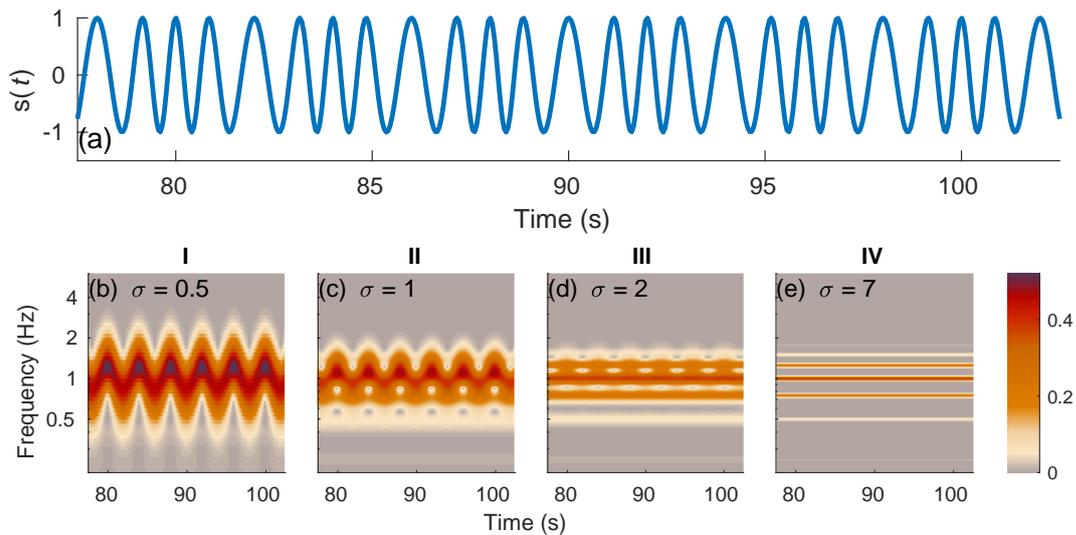
Figure 3.6: Possible behaviour of the wavelet transform for frequency modulated signal for different values of σ. (a) Frequency modulated signal $s(t) = cos(2\pi t + sin(2\pi t/4))$, simulated for 500 sec at sampling frequency Fs = 20 Hz. (b-e) Amplitudes of the wavelet transform for different values of σ. The explanation for the types of behaviour I-IV in the main text.

these methods is based on a variety of inference techniques, e.g. least-squares and kernel smoothing fits [208, 134], dynamical Bayesian inference [228], maximum likelihood (multiple-shooting) methods [247], stochastic modeling [217], and the phase resetting [78, 246, 147].
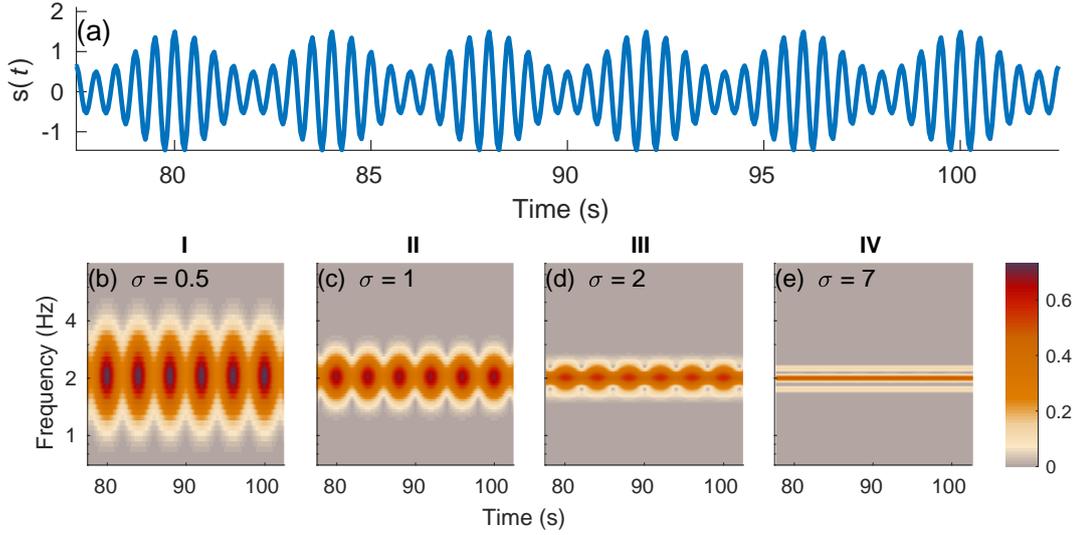
Figure 3.7: Possible behaviour of the wavelet transform for amplitude modulated signal for different values of σ. (a) Amplitude modulated signal $s(t) = (1 + 0.5\cos(2\pi 0.25t))\cos(4\pi t)$, simulated for 500 sec at sampling frequency Fs = 20 Hz. (b-e) Amplitudes of the wavelet transform for different values of σ. The explanation for the types of behaviour I-IV in the main text.

3.6.1   In the time-frequnecy domain

In this subsection selected methods based on the time-frequency analysis will be introduced. These allow for further insight into concurrent phases and amplitudes without the need for explicit extraction. This gives a great advantage, when it comes to analysing oscillations with non-trivial forms, which are masked by background noise.

Wavelet coherence

We say that two wave sources are perfectly coherent if they have a constant phase difference, the same frequency, and the same waveform. To investigate the temporal evolution of coherence the wavelet cross-energy spectrum can be used. The wavelet phase coherence measures were shown to be equivalent to the Hilbert transform [146]. Mathematically wavelet and Fourier coherence approaches are also equivalent [36]. There are two possible quantities that can be referred to as coherence, or more precisely "phase coherence". The first is known as *wavelet coherence*. This is defined in Eq. (3.24) and was introduced in [250]. It is defined with respect to the angle between the time frequency smoothed versions of the wavelet transforms between the two signals,

$$c_{\psi,xy}^{(1)}(f,t) = \frac{\left| \int_{\mathbb{R}^2} S_f(\zeta, \tau - t)\zeta^{1-2p} W_{\psi,x}^{[p]}(\zeta,\tau)\overline{W_{\psi,y}^{[p]}(\zeta,\tau)}\, d(\zeta,\tau) \right|^2}{\int_{\mathbb{R}^2} S_f(\zeta, \tau - t)\zeta^{1-2p} |W_{\psi,x}^{[p]}(\zeta,\tau)|^2\, d(\zeta,\tau) \int_{\mathbb{R}^2} S_f(\zeta, \tau - t)\zeta^{1-2p} |W_{\psi,y}^{[p]}(\zeta,\tau)|^2\, d(\zeta,\tau)}.$$

$$(3.24)$$

$S_f(\zeta,t)$ is a smoothing window. The second is known as wavelet phase coherence and will be discussed below.

Wavelet phase coherence

Another possible form of coherence can be found by reversing the order of the "smoothing" and the "angle extracting" operations. Here, the wavelet amplitudes do not play any role. In the previous approach, the measure of coherence between phases is weighted over time in proportion with the instantaneous wavelet amplitudes. The amplitude-invariant (currently described) approach was originally introduced in [139], and also independently developed in [18]. The later applications can be found in [219, 220]. Originally, temporal smoothing with rectangular windows was applied. However, more generally, one can smooth using smoothing window S_f in time-frequency space:

$$c^{(2)}_{\psi,xy}(f,t) \;=\; \frac{\left| \int_{\mathbb{R}^2} S_f(\zeta, \tau - t) \langle\, W_{\psi,x}(\zeta, \tau)\overline{W_{\psi,y}(\zeta, \tau)}\,\rangle\, d(\zeta, \tau) \right|}{\int_{\mathbb{R}^2} S_f(\zeta, \tau)\, d(\zeta, \tau)}, \qquad (3.25)$$

where $\langle v \rangle := v / |v|$. The most reasonable dependence of S_f on f should be as given by

$$\int_{\mathbb{R}^2} S_f(\zeta, \tau)\, d(\zeta, \tau) \;=\; \frac{1}{f} \int_{\mathbb{R}^2} S(\zeta, \tau)\, d(\zeta, \tau).$$

Nevertheless, the other selections could be also justified.

Wavelet bispectrum

Bispectral analysis belongs to a group of techniques based on higher-order statistics [178, 179, 239]. One can apply it to detect Gaussianity [133], but more importantly bispectrum may be used to study couplings between interacting oscillatory processes, or to investigate phase relations [106].

First introduced by Hasselmann [99] to study ocean waves, bispectral analysis was originally applied in oceanography [269], but it also gained popularity in biomedical sciences, (e.g. in EEG analysis [19, 63, 180, 222, 261, 212], cardio-respiratory interactions [114], abnormalities in respiration [241]), geophysics [227], turbulence analysis [267, 170, 80], astrophysics [133], plasma physics [200], machine engineering [46], economics [85] and seismology [162].

In this section, the well-known methodology is discussed and a new approach is introduced in Chapter 4.

The bispectrum can be derived from the Fourier spectrum as the third-order moment $M(f_1, f_2)$ [179], namely

$$M(f_1, f_2) = F(f_1)F(f_2)\overline{F(f_3)}, \qquad (3.26)$$

where F corresponds to the Fourier transform of the time series, $\overline{F}$ its complex conjugate, f_1, f_2 pair of frequency of interest and $f_3 = f_1 + f_2$. However, there are some examples in the literature of modifying f_3 according to the research hypothesis, e.g. $f_3 = 2f_1 - f_2$ [116]. In order not to overlook time-dependent effects, the signal can

be partitioned into K consecutive time-windows. Then, the average bispectrum over these windows is defined as

$$\tilde{B}(f_1, f_2) = \frac{1}{K} \sum_{k=1}^{K} M_k(f_1, f_2). \tag{3.27}$$

Alternatively, the time-frequency representations can also be applied. Typically the short-time Fourier or wavelet transform can be used but also, less commonly, the Wigner-Ville transforms may also be used [74, 28]. The wavelet bispectrum can be calculated as follows

$$B(s_1, s_2) = \int_0^T W_{\phi,x}(s_1, t) W_{\phi,y}(s_2, t) \overline{W_{\phi,z}(s_3, t)} \, dt, \tag{3.28}$$

where T is the time length of the signal, s_i are wavelet scales with $\frac{1}{s_3} = \frac{1}{s_1} + \frac{1}{s_2}$ and $\overline{W}$ denotes a complex conjugate of W. Importantly, the original definition of bispetrum was expressed in terms of scales.

The bispectrum lacks appropriate normalisation and is directly dependent on the amplitude of the component in the time series. To overcome this problem and at the same time give a measure of the relative strength of coupling, one can use the normalised version of the bispectrum–*bicoherence*:

$$b(f_1, f_2) = \frac{|M(f_1, f_2)|}{\sqrt{|F(f_1)F(f_2)|^2 |F(f_3)|^2}}, \tag{3.29}$$

and the corresponding wavelet bicoherence:

$$b_{xyz}(s_1, s_2) = \frac{|B_{xyz}(s_1, s_2)|}{\sqrt{\int_0^T |W_x(s_1, t) W_y(s_2, t)|^2 dt \int_0^T |W_z(s_3, t)|^2 dt}}. \tag{3.30}$$

The bispectrum allows for identification of either cross-coupling between different signals (x, y, z), but more importantly self-coupling (x, x, x), between different oscillatory modes within one time series. The method is capable of detecting any type of coupling between f_1 and f_2 that would result in occurrence of the frequency $f_1 + f_1$, e.g. some types of nonlinear coupling, quadratic, phase-amplitude coupling but not phase locking. Some particular examples are given in Chapter 4. The quadratic phase coupling (QPC) and quadratic frequency coupling (QFC) are discussed in [218]. QPC and QFC both result in occurrence of the third mode with the frequency $f_{3(QPC/QFC)} = f_1 + f_1$. Importantly, in QPC the phase of the third mode is equal to the sum of the coupled modes $\phi_{3(QPC)} = \phi_1 + \phi_2$, as opposed to QFC where this is not the case $\phi_{3(QFC)} \neq \phi_1 + \phi_2$.

3.6.2 Information theory approach

Another approach to detect coupling is based on using the statistics of information theory, e.g Granger causality, transfer entropy, etc. This approach does not require prior extraction of the phase and amplitude but is applied directly to the time series. In short, it addresses the question of how much information in a single time series can be predicted by the past information of another one. This approach does not allow for the investigation of the dynamical properties of the coupling, yet combining it with methods searching for dynamical properties of the coupling may give promising results, e.g. [117].

3.7 Statistical testing

In this section statistical methods are described. The first part presented in Sec. 3.7.1 is focused on the surrogates testing – the method suitable for testing the hypothesis involving the complex dynamics. The second part presented in Sec. 3.7.2 introduces the Wilcoxon method for individual comparisons.

3.7.1 Surrogates testing

Motivation

Surrogate data testing is an essential part of the data analysis process. It allows for the statistical evaluation and verification of obtained results to a selected level of confidence. Hence observed results can be sorted into either coincidental or true characteristic of the underlying dynamics in the system. Many processes in nature appear very unlikely *a priori* to be linear, yet the possible nonlinearity might not be obvious because it can be hidden in particular aspects of the dynamics. The methods of surrogate data testing, gained popularity in the early 1990s after the work of Theiler et al., who presented it as a test for nonlinearity [242]. As the new methods were developed, additional issues have arisen together with the need for an additional review of the field [215]. Together with the growing interest in time varying dynamics, and the development of various methods appropriate for nonlinear dynamics, the approaches used inevitably evolve. The concept of surrogate data testing has been expanded up to date to test, not only for nonlinearity, including chaos, but also for oscillations in noisy data, for nonlinear coupling between two systems or synchronisation between two or many systems and several more applications [141].

Parameters of the test

There are two important parameters which characterize the performance of a statistical test. The first one is the level of significance α, which is the probability that the null hypothesis is rejected, although it is in fact true. It is known as a false positive or type I error. The α corresponds to the confidence level $(1 - \alpha) \times 100\%$. A

test is called one-sided if the null hypothesis is rejected only if the data deviate from the surrogates in a specified direction. In this case and at a given α, one creates $K = m/\alpha - 1$ surrogate datasets, where m is the chosen natural number and also the second parameter. Choosing $m = 1$ does not put unnecessary computational burden, nevertheless may be insufficient in some cases [141]. Then the test is computed on the original data set and on each of the surrogates. If the total of $1/\alpha$ sets are available, the probability for each of them to have the smallest (or biggest) value of the calculated statistic by chance is just α, as desired. For two-sided tests, one generates $K = 2m/\alpha - 1$ surrogates. For $m = 1$, the probability for any of the $2/\alpha$ sets to have either the smallest or largest value of the statistic is then again α.

Surrogates types

The aim of surrogates is to preserve all the properties of the original data, except the one that is being tested. There are two approaches to generate the surrogates. In the first one a pre-existing model is used to generate the surrogates, e.g. the autoregressive (AR) model [5]. This approach assumes a priori the properties of the system and the model must be known beforehand. This approach is called *typical* [243]. Another group of methods uses the inverse approach to extract the information from the data. This approach is known as *constrained*. Within this class the choice of the method would strongly depend on the null hypothesis. Some examples of this class will now be introduced.

Random permutation surrogates   The random permutation (RP) of the time series in the time domain is taken. The shuffling in the time domain destroys any time dependency or temporal correlations. The null hypothesis of the observed data being fully described by independent and identically distributed (IID) random variables is tested when applying those surrogates.

Fourier transform surrogates   The Fourier transform (FT) surrogates test the null hypothesis that the data were generated by some linear stochastic process with Gaussian increments. In other words, all structures in a time series could be modelled by computing first and second order quantities, namely the mean, the variance and the auto-covariance function, or equivalently, the data do not contain any nonlinear structure. The surrogates satisfy the null hypothesis if they have the same power spectrum as the original data. To create the realisation of the surrogates, typically the amplitude Fourier spectrum of the original data is used, while the Fourier phases are randomised. FT surrogates do not preserve the amplitude distribution of the original dataset.

Amplitude adjusted Fourier transform surrogates   The amplitude adjusted Fourier transform (AAFT) surrogates test the null hypothesis that the observed time series is a monotonic, nonlinear transformation of a linear Gaussian process. The origin of

the nonlinearity is not dynamical but static, i.e. introduced into the system during the measurement [242]. To create the realisation of the AAFT surrogates the following steps are taken. A realisation of Gaussian noise is generated and reordered to match the rank of the original time series; this means if in the original time series $s(i)$ is the n-th smallest element, then in the reordered Gaussian noise $g(i)$ is the n-th smallest too. Consequently, the FT surrogates of the reordered Gaussian signal are generated, called G_s. Eventually, the original time series is reordered to match the rank of the G_s; this means if in the $G_s(i)$ is the n-th smallest element, then in the reordered time series $s'(i)$ is the n-th smallest too. In this way the amplitude distributions of the original data and the surrogates are identical. The main issue with this type of surrogates is that spurious flatness is introduced into the Fourier spectrum.

Iterative adjusted Fourier transform surrogates The issue with the bias in the Fourier spectrum of AAFT surrogates can be bypassed using iterative steps. The iterative adjusted Fourier transform surrogates (IAAFT) surrogates were introduced by Schreiber & Schmitz [214]. The iterative steps lead towards maintaining one property, either power spectrum or amplitude distribution, and keeping the close match with the other one. The null hypothesis is the same as in the case of AAFT surrogates, but theoretically the transformation function does not need to be monotonic [135], namely the observed time series is a nonlinear transformation of a linear Gaussian process. Due to preservation of very specific constraints, the variance in the IAAFT surrogates is relatively small, which means that the number of realisations needed will be smaller than in case of the other surrogate types [141]. This comes at the expense of affecting the outcome of the test. IAAFT surrogates may fail to reject the null hypothesis when it is false, but the number of false rejections of the null hypothesis is smaller than for AAFT [214, 135]. Rath et. al [203] investigated the phase correlations in FT, AAFT and IAAFT surrogates, concluding that the presence of phase correlations is a generic property of AAFT and IAAFT surrogates. Therefore those surrogates may fail to reject the null hypothesis in case of weak nonlinearity. They concluded that surrogate algorithms aiming at testing both static and dynamic nonlinearities cannot reproduce both the power spectrum and the amplitude distribution while preserving the randomness of the Fourier phases.

Wavelet surrogates Fourier surrogates are the most commonly used type of surrogates when testing for nonlinearity. However, one may wish to address more specific questions such as: correlations between particular frequency modes in the oscillations or between the individual cycles, i.e. whether there is any long term determinism. In this case one of the possible choices could be wavelet surrogates in which typically the discrete wavelet transform is used. Breakspear et al. [32] introduced a method based on the resampling of wavelet coefficients. The data within each scale could be resampled in the following ways:

- shuffling of wavelet coefficients within each scale,

- cyclic rotation of coefficients within each scale (time-shifting),

- block resampling of wavelet coefficients within each scale, in which blocks of coefficients are shuffled in time.

Keylock [128] proposed the IAAFT algorithm as a resampling method for the coefficients within each scale; thus the power spectrum and amplitude distributions are better preserved within each scale. This method is called wavelet iterative amplitude adjusted Fourier transform (WIAAFT). In wavelet surrogates there is no stationarity requirement.

Time-shifted surrogates   Surrogate testing in addition to allowing for the investigation of underlying dynamics in a single time series can also be an essential part of the investigation of interactions between systems, when given two or more time series. One of the possibilities for interdependence testing is the application of time-shifted surrogates. First proposed in [199], time-shifted surrogates were further developed in [8]. The idea is to use the original time-shifted signals, and thus preserve all the properties of the original data. They test the null hypothesis of two processes with arbitrary linear or nonlinear structure but without nonlinear interdependence or significant linear cross-correlation. In many cases, the circular shift is used.

Other   There are many other and typically more specific surrogate types. Some that are worth naming are intersubject surrogates/mismatched [248, 107, 219], the method-specific analytically derived confidence intervals, e.g. [220], method-specific randomisations, e.g. [131, 151]. The analytically derived confidence intervals are especially useful when it comes to computational cost.

Nonstationarity

Nonstationarity has been excluded by many surrogate types, e.g. FT, AAFT, IAAFT by the requirement of a null hypothesis that is constant in time. The important consequence of this is the possibility of rejection of the null hypothesis due to the fact that it is false indeed, or alternatively due to the occurrence of nonstationarity. Fortunately, some surrogate types explicitly address this issue [215, 141].

3.7.2   Wilcoxon test

The Wilcoxon test is a nonparametric test of the null hypothesis that two populations have the same probability distribution [262]. There are two variations of the test: signed-rank test and rank-sum test.

Signed-rank test

The Wilcoxon signed-rank test can be applied to the comparison of two groups of two related, matched samples. This means that there are two nominal variables

and one measurement variable [163]. In the case of the cellular data analysis from Chapter 5 this means, that each cell was exposed to two different conditions, such as "standard bath" and "non-standard bath". The null hypothesis is that the median difference between pairs of observations is zero.

Rank-sum test

The Wilcoxon rank-sum test (also called the Mann–Whitney U test or the Wilcoxon–Mann–Whitney test) can be applied to test, whether a *randomly* selected value from one sample will be less than or greater than a *randomly* selected value from a second sample. This test can be used to determine whether two independent samples were selected from populations having the same distribution. In the case of cellular data analysis from Chapter 5 this means that different cells were exposed to two different conditions, such as "standard pipette" and "Ca^{2+} pipette".

3.8 Summary

The growing availability and abundance of data coming from various sources has led to an increased demand for methods that reveal certain dynamical properties of the underlying system that generated the data. This chapter has introduced and discussed some of the key methods, and the majority of them have been applied to the recordings of the membrane potential in Chapter 5. The methods can be categorised in various ways, e.g. as in this chapter, with respect to the domain they operate on, e.g. time, frequency or time-frequency. The complex dynamics is defined as a temporal evolution; therefore only methods that explicitly take time into account allow one to gain insight into the underlying dynamics. Time-frequency methods may give some advantages in understanding the complex, oscillatory dynamics, nevertheless they are not the exclusive approach. Methods based on the phase space or complexity analysis should not be overlooked. While working with the data, a crucial part of the process is verifying which parts of the data correspond to meaningful values. Here, the key role in determining this is statistical testing and the use of surrogates. The surrogate method has evolved significantly from its initial introduction, and this chapter has reviewed selected contribution to the field.

Chapter 4

Wavelet bispectral density, wavelet bispectrum

4.1 Introduction

The wavelet bispectrum, which was already introduced in Chapter 3 (in Sec. 3.6.1), is an effective tool to study nonlinear coupling, or some forms of nonlinearities in the time series. Nevertheless, in its current form it does not allow for quantitative but merely qualitative evaluation over the frequency-frequency or rather scale-scale space. This chapter introduces work done jointly with Julian Newman and Aneta Stefanovska, which was submitted in the manuscript [177]. The key result of this work was identifying a suitable normalisation to allow for the treatment of the bispectrum formally as a bispectral density, over the time-frequency-frequency space. Wavelet bispectral density allows for a quantitative interpretation of the results of wavelet bispectrum analysis over time-frequency-frequency space, *ipso facto* becoming a well-suited method to investigate nonlinear time-varying dynamics.

4.1.1 Background

Wavelet bispectral or rather wavelet bicoherence analysis was first proposed by van Milligen et al. [170, 254]. The formulas persisted for many years since their pioneering work in 1995. However, several important questions remained unaddressed until recently. Namely because of the Gabor-Heisenberg uncertainty principle (Sec. 3.5.1), the quantification of the bispectral content of any given region in frequency-frequency space was not possible in time-localised manner. In addition the choice of *wavelet normalisation* (refers to p as in Sec. 3.5.2) is crucial and this point was identified in [170, 115, 141], but remained unsolved. However, the choice of wavelet normalisation issue was usually overcome by using bicoherence, as in Eq. (3.30).

4.1.2   Current definition and its limitations

Needless to say, the inability to quantify the bispectral content of a region in scale-scale space also implies the inability to describe quantitatively how bispectral content is distributed across different regions in scale-scale space. The problem is illustrated in Fig. 4.1, where the instantaneous wavelet bispectrum, $b_{xyz}^{\tau}(s_1, s_2)$, is presented. The instantaneous wavelet bispectrum, i.e. the product of the wavelet transform terms at a fixed time τ, is defined as

$$b_{xyz}^{\tau}(s_1, s_2) \; := \; W_x(s_1, \tau) W_y(s_2, \tau) \overline{W_z(s_3, \tau)}, \tag{4.1}$$

where $\frac{1}{s_3} = \frac{1}{s_1} + \frac{1}{s_2}$, using the conventional wavelet normalisation, $p = 1/2$, as used in [170, 254], for signals of the form

$$\begin{cases} x(t) &= \cos(2\pi \nu_1 t) \\ y(t) &= \cos(2\pi \nu_2 t) + \cos(2\pi \nu_3 t) \\ z(t) &= \cos(2\pi(\nu_1 + \nu_2)t) + \cos(2\pi(\nu_1 + \nu_3)t - \theta). \end{cases} \tag{4.2}$$

For this particular choice of signals and parameters, the dependence on the fixed time τ is negligible, so the results are essentially identical to averaging over a time-interval.

(a) $\sigma = 1$ (b) $\sigma = 4$
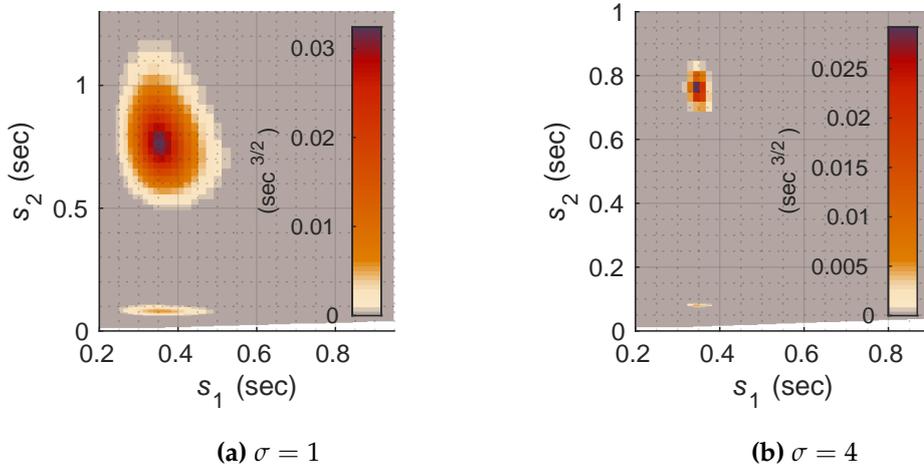
Figure 4.1: Wavelet bispectrum according to the current standard definition, Eq. (4.1). Plots show magnitude $|b_{xyz}^{\tau}(s_1, s_2)|$ of the instantaneous wavelet bispectrum Eq. (4.1) in units of $\text{sec}^{3/2}$ for the signals x, y, z in Eq. (4.2) with $\nu_1 = 2.8$ Hz, $\nu_2 = 1.3$ Hz, $\nu_3 = 12$ Hz and $\theta = \frac{\pi}{3}$, using conventional $p = \frac{1}{2}$ definition of the wavelet transform, with a lognormal mother wavelet (Sec. 3.5.2) with frequency resolution parameter (a) $\sigma = 1$ and (b) $\sigma = 4$. Scale s and frequency f are here related by $f = \frac{1}{s}$. The signals are simulated over a time-interval $[0\,\text{s}, 60\,\text{s}]$ and the time-instant τ is taken at $\tau = 30$ s.

In Fig. 4.1 (both (a) and (b)), a bispectral contribution from the frequency pair (ν_1, ν_2) and (ν_1, ν_3) can clearly be seen, both appearing as blurs. Yet, it is not straightforward to compare, or even quantify the two bispectral contributions. The two

peaks do not appear to be equal, but they represent the equal coupling indeed. In both cases the three contributing components have amplitudes equal to 1.

4.1.3 Approach to solving the wavelet bispectrum normalisation problem

The fundamental part of finding a suitable wavelet analogue to the Fourier bispectrum is to identify that: by the analogy of second-order spectra describing a distribution of energy over the frequency axis, the bispectra represent a density of a distribution over the frequency-frequency space. However, this requires including a suitable pre-factor, such that the results are really the density of a bispectral distribution over time-frequency-frequency or time-scale-scale space. Consequently, the quantitative measure of coupling can be obtained by integration. Here, for the first time the wavelet bispectral density is proposed. This allows one to obtain a correct wavelet bispectrum formula by integrating the wavelet bispectral density.

4.2 Appropriate wavelet normalisation, p

The most common convention for wavelet normalisation is $p = \frac{1}{2}$. This can be justified by preservation of the L^2 norm independently from the wavelet scale s, and consequently the fact that the square of the wavelet transform provides a suitable definition of wavelet power [123, 108]. However, choosing $p = 1$ has significant advantages, e.g.

- for a sinusoidal signal the maximal amplitude in wavelet transform corresponds exactly to the frequency of input,

- two sinusoidal modes with the same amplitude are represented by peaks of the same height, and also have equal spread when viewed with a logarithmic-scale frequency axis, as shown in Fig. 4.2,

- when integrating with respect to a logarithmic scale and $p = 1$, (not $p = \frac{1}{2}$), the total signal energy is preserved,

- when considering the third-order spectral density, as further shown, $p = 1$ *remains* the most appropriate choice when integrating with respect to a logarithmic frequency scale.

Therefore, the normalisation $p = 1$ is selected as the most appropriate and used for the further analysis, unless stated otherwise. Other choices such as $p = \frac{1}{2}$ are also possible; however, in the case of bispectral density, modification of the formula would be required. The wavelet transform, initially defined in Eq. (3.14), can now be defined using the normalisation $p = 1$,

$$W_{\psi,x}(f,t) = \frac{f}{\kappa} \int_{\mathbb{R}} x(\tau) \overline{\psi\left(\frac{(\tau-t)f}{\kappa}\right)} d\tau. \tag{4.3}$$

Here, $W_{\psi,x}$ is the wavelet transform of signal x given the wavelet function ψ, $\overline{\psi}$ denotes its complex conjugate, p is the normalisation constant, f is a frequency and t time. κ is where the Fourier transform of the wavelet function $\hat{\psi}$ is maximised, typically equals to 1. In Fig. 4.2 the wavelet transforms of signals x, y, z, with $\sigma = 1$ are presented. It should be noted that the wavelet transform provides a mean of *time-localised frequency analysis*. From Eq. (3.15), in the case that $x(t) = A\cos(2\pi \nu t + \phi)$ with $\nu > 0$, it can be immediately seen that

$$W_{\psi,x}(f,t) = \tfrac{1}{2}\hat{\psi}\left(\tfrac{\kappa \nu}{f}\right) A e^{i(2\pi \nu t + \phi)} \tag{4.4}$$

for all $f > 0$ and $t \in \mathbb{R}$.
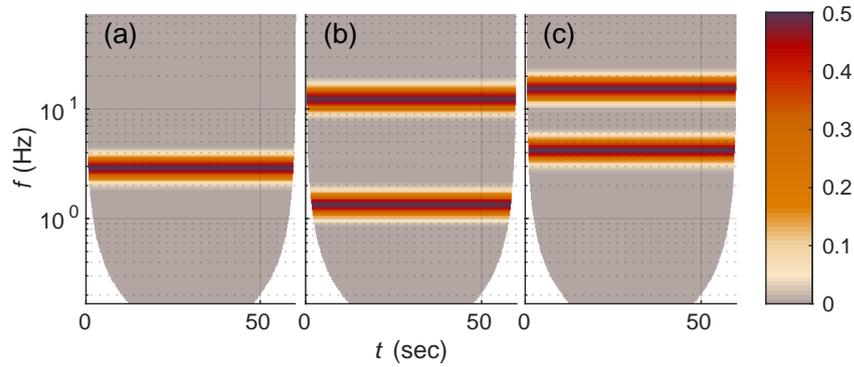
Figure 4.2: Wavelet transforms for fixed-frequency oscillatory components. Plots show wavelet amplitudes $|W_{\psi,x}(f,t)|$, $|W_{\psi,y}(f,t)|$ and $|W_{\psi,z}(f,t)|$, respectively in (a), (b) and (c), for the signals x, y, z defined in Eq. (4.2) with $\nu_1 = 2.8$ Hz, $\nu_2 = 1.3$ Hz, $\nu_3 = 12$ Hz and $\theta = \frac{\pi}{3}$, using a lognormal mother wavelet with $\sigma = 1$.

4.3　Wavelet energy spectral density

In Chapter 3 the wavelet energy spectral density was introduced within the framework of the most common convention of linear frequency approach, see Eq. (3.16). In this chapter an alternative, logarithmic frequency approach is presented, which is more natural and suitable for wavelet analysis using its current definition. The wavelet spectral energy density with respect to the logarithmic frequency scale is defined as

$$\rho_{\psi,xx}(f,t) := C_{\psi}^{-1}|W_{\psi,x}(f,t)|^2 \tag{4.5}$$

where C_{ψ} is first defined in Eq. (3.17) except that now the logarithmic frequency scale definition is also provided

$$C_{\psi} = \int_0^{\infty} \frac{\hat{\psi}(r)^2}{r}\,dr = \int_{-\infty}^{\infty} \hat{\psi}(e^r)^2\,dr. \tag{4.6}$$

Here, $\hat{\psi}$ corresponds to the Fourier transform of the wavelet function. Consequently, the *wavelet energy spectrum* of x is given by

$$p_{\psi,xx}(A) \;=\; \int_{\mathbb{R}^2} \mathbb{1}_A(e^{\zeta}, t) p_{\psi,xx}(e^{\zeta}, t)\, d(\zeta, t), \tag{4.7}$$

where A indicates the region of interest in time-frequency space and $\mathbb{1}_A(e^{\zeta}, t)$ is equal to 1, where e^{ζ} and t are included in A. $p_{\psi,xx}(e^{\zeta}, t)$ as defined in Eq. (4.5). Note, that the *logarithmic frequency scale* implies a logarithm of base e; however transformation to a different base is straightforward.

4.4 Wavelet bispectral density

4.4.1 Normalisation

The aim of this section is to propose a third-order normalisation, analogous to C_ψ. The combination of the logarithmic-frequency nature of the wavelet transform with the linear-frequency sum involved in bispectral analysis creates difficulty in defining the wavelet bispectrum in analogy to wavelet energy spectral density. The details are shown in Appendix B.3. Therefore, instead of being a single value, like C_ψ, the bispectral normalisation depends on the frequencies or rather their ratio, $\lambda = \frac{f_1}{f_1+f_2}$. The following normalisation, given a wavelet function ψ, for each $\lambda \in [0, 1]$, is proposed

$$D_\psi(\lambda) \;:=\; \int_0^\infty \int_0^\infty \frac{\hat{\psi}\big(\frac{f_1}{\xi_1}\big)\hat{\psi}\big(\frac{f_2}{\xi_2}\big)\hat{\psi}\big(\frac{f_1+f_2}{\xi_1+\xi_2}\big)}{\xi_1\xi_2}\, d\xi_1 d\xi_2. \tag{4.8}$$

$$= \int_0^\infty \int_0^\infty \frac{\mathring{\psi}(r_1)\mathring{\psi}(r_2)\mathring{\psi}(\lambda r_1 + (1-\lambda)r_2)}{r_1 r_2}\, dr_1 dr_2 \tag{4.9}$$

$$= \int_{-\infty}^\infty \int_{-\infty}^\infty \mathring{\psi}(e^{r_1})\mathring{\psi}(e^{r_2})\mathring{\psi}(\lambda e^{r_1} + (1-\lambda)e^{r_2})\, dr_1 dr_2, \tag{4.10}$$

where $\mathring{\psi}(x) := \hat{\psi}(\frac{1}{x})$. Note that $D_\psi(\lambda) = D_\psi(1-\lambda)$. D_ψ is not a "perfect" third-order analogue of Eq. (4.6) because it depends on the ratio of the frequencies as represented by λ. Yet, D_ψ serves as a reasonable third-order analogue of C_ψ. Given a wavelet ψ and signals

$$
\begin{aligned}
x(t) &= A_1 \cos(2\pi\lambda\nu t + \phi_1) \\
y(t) &= A_2 \cos(2\pi(1-\lambda)\nu t + \phi_2) \\
z(t) &= A_3 \cos(2\pi\nu t + \phi_1 + \phi_2 - \theta)
\end{aligned}
$$

with $\nu > 0$, it is true that

$$\tfrac{1}{8}A_1 A_2 A_3 e^{i\theta} \;=\; \frac{1}{D_\psi(\lambda)} \int_{\mathbb{R}^2} W_{\psi,x}(e^{\zeta_1}, t) W_{\psi,y}(e^{\zeta_2}, t)\overline{W_{\psi,z}(e^{\zeta_1} + e^{\zeta_2}, t)}\, d(\zeta_1, \zeta_2) \tag{4.11}$$

for any $t \in \mathbb{R}$. This fact is immediate from Eq. (4.4). It is also shown in [177] that, in the limit as $\sigma \to \infty$,

$$\sigma^2 D_{\psi_\sigma}(\lambda) \;\to\; \frac{1}{\pi\sqrt{8(1 - \lambda + \lambda^2)}},$$

for which the range is between $(\sqrt{8}\pi)^{-1} \approx 0.1125$ and $(\sqrt{6}\pi)^{-1} \approx 0.1299$. Fig. 4.3 illustrates the dependence of $D_{\psi_\sigma}(\lambda)$ on λ for the lognormal wavelet function ψ_σ defined by $\hat{\psi}_\sigma(r) = e^{-2(\pi\sigma \log r)^2}$ on $r > 0$, where the parameter σ is taken over the range $[0.5, 3]$. From Fig. 4.3 it is also clear that the suggested approximation holds fairly well also for smaller σ.
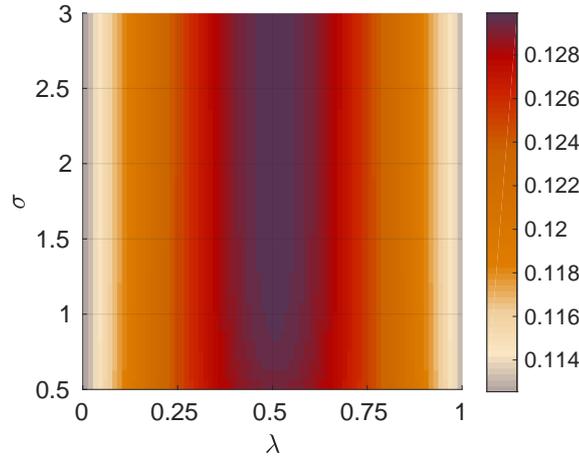
Figure 4.3: Depedence of $D_{\psi_\sigma}(\lambda)$ on λ for the lognormal wavelet function ψ_σ, across varying σ. The plot specifically shows $\sigma^2 D_{\psi_\sigma}(\lambda)$ as a function of σ and λ. For each σ, $D_{\psi_\sigma}(\lambda)$ ranges from about $0.11\sigma^{-2}$ to about $0.13\sigma^{-2}$.

4.4.2 Definition

Given a wavelet ψ and functions x, y, z, the *logarithmic-frequency wavelet bispectral density (BD)* $b_{\psi, xyz}$ is defined by

$$b_{\boldsymbol{\psi}, xyz}(f_1, f_2, t) \;=\; D_\psi\left(\tfrac{f_1}{f_1 + f_2}\right)^{-1} W_{\boldsymbol{\psi}, x}(f_1, t) W_{\boldsymbol{\psi}, y}(f_2, t) \overline{W_{\boldsymbol{\psi}, z}(f_1 + f_2, t)}. \tag{4.12}$$

In particular, $b_{\psi, xxx}$ is referred as the *logarithmic-frequency wavelet autoBD* of x, while BD $b_{\psi, uvw}$ for which it is *not* the case that $u = v = w$ is referred to as a *cross-BD*.

4.5   Examples

In this section selected numerical examples are presented. The proposed normalisation gives good results for fixed-frequency components and for phase-coupled oscillators, as illustrated below.

4.5.1 Sinusoidal components

To begin with, the sinusoidal components are investigated. In this section, the "instantaneous wavelet bispectral content" of a set A, indicating the subset in frequency-frequency space at a time t is defined by

$$\mathfrak{b}^{\text{inst}}_{\psi,xyz}(A,t) := \int_{\mathbb{R}^2} \mathbb{1}_A(e^{\zeta_1}, e^{\zeta_2}) b_{\psi,xyz}(e^{\zeta_1}, e^{\zeta_2}, t) \, d(\zeta_1, \zeta_2). \quad (4.13)$$

Here, $\mathbb{1}_A(a,b) = 1$, where $a,b \in A$ or 0 otherwise, $b_{\psi,xyz}$ is a logarithmic-frequency wavelet bispectral density, as defined in Eq. (4.12). All the signals in this section are simulated over a time interval $[0 \text{ s}, \ 60 \text{ s}]$, and instantaneous wavelet bispectral results are considered at $\tau = 30$ s to avoid any effect of the cone of influence, discussed in Sec. 3.5.2.

To begin with, exactly the same signals as in Eq. (4.2) are considered. The parameters are $\nu_1 = 2.8$ Hz, $\nu_2 = 1.3$ Hz, $\nu_3 = 12$ Hz and $\theta = \frac{\pi}{3}$ (as in the caption of Fig. 4.1). The wavelet bispectral density $b_{\psi_\sigma,xyz}(f_1, f_2, \tau)$ is shown in Fig. 4.4, using $\sigma = 1$ and $\sigma = 4$ just as in Fig. 4.1.

(a) $\sigma = 1$ **(b)** $\sigma = 4$
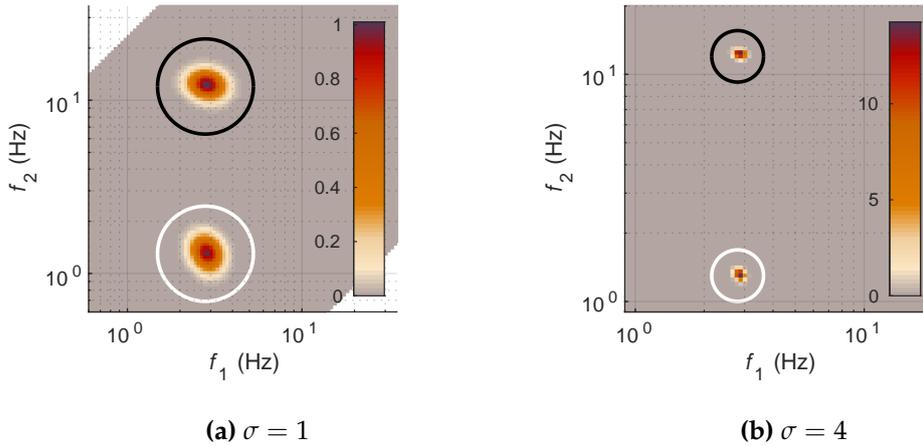
Figure 4.4: Wavelet bispectral density according to the definition in Eq. (4.13), for the signals considered in the Eq. (4.2). Plots show magnitude of the logarithmic-frequency wavelet bispectral density $b_{\psi_\sigma,xyz}(f_1, f_2, \tau)$ for the signals x, y, z in the Eq. (4.2) with $\nu_1 = 2.8$ Hz, $\nu_2 = 1.3$ Hz, $\nu_3 = 12$ Hz and $\theta = \frac{\pi}{3}$, with (a) $\sigma = 1$ and (b) $\sigma = 4$. In (a), the white circle marks the boundary of S_1 and the black circle the boundary of S_2. In (b), the white circle marks the boundary of S_3 and the black circle the boundary of S_4.

A blurry peak around (ν_1, ν_2) and (ν_1, ν_3) for both $\sigma = 1$ and $\sigma = 4$ can be seen. For $\sigma = 1$, a region S_1 containing the visible blur around (ν_1, ν_2) is marked and a region S_2 containing the visible blur around (ν_1, ν_3), both indicated in Fig. 4.4. A numerical computation yields

$$\mathfrak{b}^{\text{inst}}_{\psi,xyz}(S_1, \tau) \approx 0.1251 \quad \text{and} \quad \mathfrak{b}^{\text{inst}}_{\psi,xyz}(S_2, \tau) \approx 0.1249 e^{0.3333\pi i}.$$

Likewise, for $\sigma = 4$, a region S_3 containing the visible blur around (ν_1, ν_2) is marked

and a region S_4 containing the visible blur around (ν_1, ν_3), again both indicated in Fig. 4.4. A numerical computation yields

$$\mathfrak{b}^{\text{inst}}_{\boldsymbol{\psi},xyz}(S_3, \tau) \approx 0.1250 \quad \text{and} \quad \mathfrak{b}^{\text{inst}}_{\boldsymbol{\psi},xyz}(S_4, \tau) \approx 0.1250e^{0.3333\pi i}.$$

So all four of these regions have instantaneous bispectral content equal in magnitude to approximately $\frac{1}{8}$, which is to be expected immediately from Eq. (4.11). In particular, for both frequency resolutions it is possible to show that the two bispectral contributions are of essentially the same magnitude, which could not be seen from the current standard definition of wavelet bispectra as described in Sec. 4.1.

Even considering the lower frequency resolution, the novel wavelet bispectrum definition gives good results. Fig. 4.5(a) shows $b_{\boldsymbol{\psi}_\sigma,xxy}(f_1, f_2, \tau)$ with $\sigma = 0.5$ for the pair of signals

$$\begin{cases} x(t) & = & \cos(2\pi\nu t) \\ y(t) & = & \cos(4\pi\nu t) \end{cases} \tag{4.14}$$

with $\nu = 2.8$ Hz. The instantaneous wavelet bispectral content of the white-circled region in Fig. 4.5(a) is approximately 0.1255, again remarkably close to the ideal value of $\frac{1}{8}$. Likewise Fig. 4.5(b–c) shows $b_{\boldsymbol{\psi}_\sigma,xxy}(f_1, f_2, \tau)$ with $\sigma = 0.5$ for signals x, y, z of the form presented in Eq. (4.2), with $\theta = 0$. The instantaneous wavelet bispectral content of the white-circled region and the black-circled region in Fig. 4.5(b) are approximately $0.1260 + 0.0002i$ and $0.1254 - 0.0002i$ respectively. The instantaneous wavelet bispectral content of the white-circled region and the black-circled region in Fig. 4.5(c) are approximately $0.1253 + 0.0001i$ and $0.1250 - 0.0001i$ respectively. These values are very close to $\frac{1}{8}$, as desired. It can also be seen in the remaining plots of Fig. 4.5 how the size of the blurs in frequency-frequency space decreases with increasing σ.

Autobispectra

Now, autobispectra for example sine signals are illustrated. Tested signals have the form

$$x(t) = 2\cos(2\pi\nu t) + \cos(4\pi\nu t) \tag{4.15a}$$

$$x(t) = \cos(2\pi\nu t) + \cos(3\pi\nu t) + \cos(4\pi\nu t) \tag{4.15b}$$

$$x(t) = \cos(2\pi\nu t) + \cos(4\pi\nu t) + \cos(6\pi\nu t). \tag{4.15c}$$

The wavelet autobispectra are diagonally symetrical. Fig. 4.6 shows $b_{\boldsymbol{\psi}_\sigma,xxx}(f_1, f_2, \tau)$ with $\sigma = 3$ for each of the three signals $x(t)$ in Eq. (4.15). For Eq. (4.15a), the instantaneous wavelet bispectral content of the circled region in Fig. 4.6(a) is approximately 0.5001. For Eq. (4.15b), the instantaneous wavelet bispectral content of the circled region in Fig. 4.6(b) is approximately 0.1250. For Eq. (4.15c), the instantaneous wavelet bispectral content of each of the circled regions in Fig. 4.6(c) is approximately 0.1250.
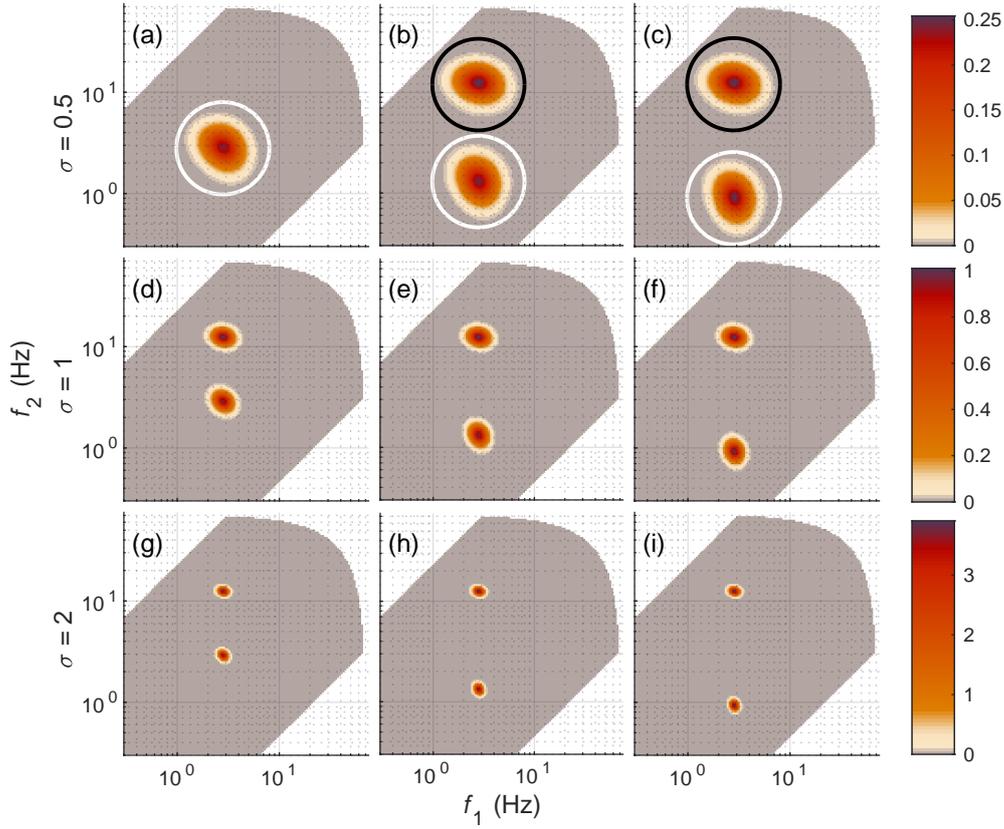
Figure 4.5: Wavelet bispectra for fixed-frequency oscillatory components. In (a), $|b_{\psi_\sigma,xxy}(f_1, f_2, \tau)|$ is shown for x, y as in Eq. (4.14) with $\nu = 2.8$ Hz, with $\sigma = 0.5$. In (d,g) is shown, respectively with $\sigma = 1$ and $\sigma = 2$, $|b_{\psi_\sigma,xyz}(f_1, f_2, \tau)|$ for x, y, z as in Eq. (4.2) with $\nu_1 = \nu_2 = 2.8$ Hz, $\nu_3 = 12$ Hz and $\theta = 0$. In (b,e,h) is shown, respectively with σ equal to 0.5, 1 and 2, $|b_{\psi_\sigma,xyz}(f_1, f_2, \tau)|$ for x, y, z as in Eq. (4.2) with $\nu_1 = 2.8$ Hz, $\nu_2 = 1.3$ Hz, $\nu_3 = 12$ Hz and $\theta = 0$. In (c,f,i) is shown, respectively with σ equal to 0.5, 1 and 2, $|b_{\psi_\sigma,xyz}(f_1, f_2, \tau)|$ for x, y, z as in Eq. (4.2) with $\nu_1 = 2.8$ Hz, $\nu_2 = 0.9$ Hz, $\nu_3 = 12$ Hz and $\theta = 0$. All nine plots use the same frequency axes. The instantaneous wavelet bispectral content of the circled regions (numerical integration values) in (a–c) are given in the text.

4.5.2 Coupled phase oscillators

In this section the "time-marginalised bispectral density" is discussed, which can be defined as

$$b^I_{\psi,xyz}(f_1, f_2) := \int_I b_{\psi,xyz}(f_1, f_2, t)\, dt.$$

Here, $I \subset \mathbb{R}$ indicates the time interval. Except where stated otherwise, the signals in this section are simulated over a time interval $[0\,\text{s}, 500\,\text{s}]$, and bispectral results are considered over the central time-subinterval

$$I_0 := [233\tfrac{1}{3}\,\text{s}, 266\tfrac{2}{3}\,\text{s}]$$

of duration $33\tfrac{1}{3}$ s. This corresponds to one time period of the frequency modulation that will be introduced below.
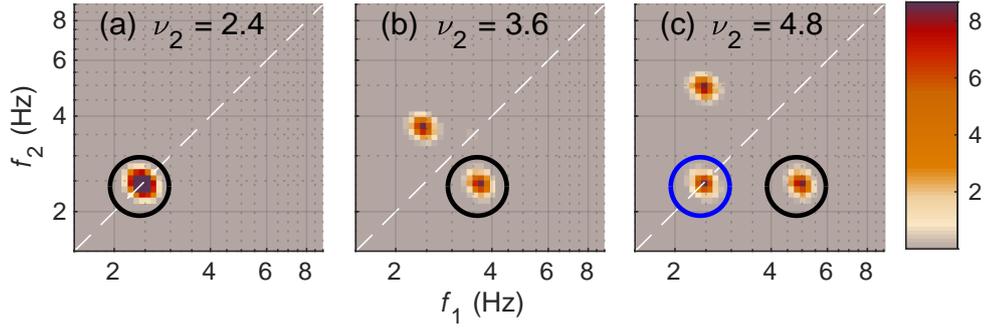
Figure 4.6: Wavelet autobispectra for signals with fixed-frequency oscillatory components. In (a), (b) and (c) are shown $|b_{\psi_\sigma,xxx}(f_1,f_2,\tau)|$ for $x(t)$ as in Eqs. (4.15a), (4.15b) and (4.15c) respectively, with $\nu = 2.4$ Hz, with $\sigma = 3$. Shown in dashed white is the diagonal. The instantaneous wavelet bispectral content of the circled regions (numerical integration values) are given in the text.

One form of interaction between oscillators that bispectral analysis is likely to detect is *dynamical coupling* in the form of added coupling terms in the differential equations of motion [170, 116]. Here, Kuramoto-type symmetric coupling between two phase oscillators is considered. The simplest scenario would be to introduce the coupling between two linear phase oscillators, as in the usual Kuramoto model; however, as explained later in Sec. 4.5.3, bispectral analysis is probably unable to detect such coupling between two linear phase oscillators. Therefore, the Kuramoto coupling between two highly nonlinear phase oscillators is considered instead.
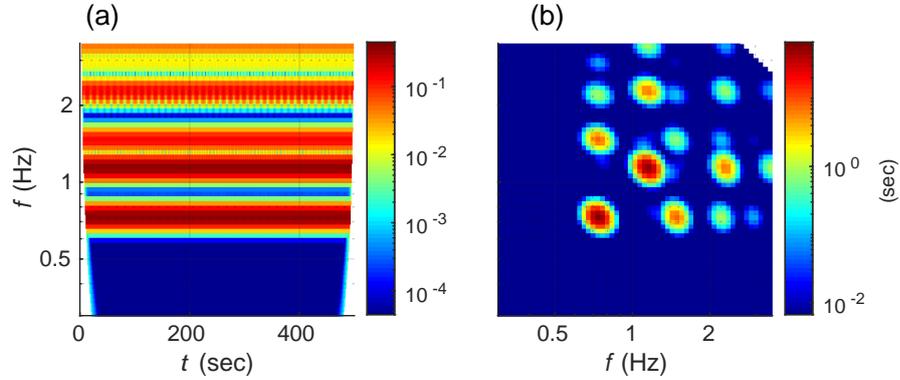
Figure 4.7: Wavelet and wavelet-bispectral representation of a linear superposition of two non-interacting nonlinear oscillators. In (a) and (b) are shown respectively $|W_{\psi_\sigma,x}(f,t)|$ and $|b^{I_0}_{\psi_\sigma,xxx}(f_1,f_2)|$ (the latter in units of seconds), for the fixed-frequency uncoupled oscillators as in Eq. (4.16), with $\sigma = 3$.

Two phase oscillators $\theta_1(t)$ and $\theta_2(t)$ and the signal

$$x(t) = \cos(\theta_1(t)) + \cos(\theta_2(t))$$

on which autobispectral analysis will be carried out are considered. In the first

instance, uncoupled phase oscillators with a fixed basic frequency are considered; specifically, they follow the system of differential equations

$$\begin{cases} \dot{\theta}_1(t) &= 2\pi\nu_1(1+0.6\cos(\theta_1)) \\ \dot{\theta}_2(t) &= 2\pi\nu_2(1+0.6\cos(\theta_2)) \end{cases} \tag{4.16}$$

with $\nu_1 = 0.9$ Hz and $\nu_2 = 1.4$ Hz. The oscillator θ_1 is strictly periodic with frequency $\tilde{\nu}_1 := 0.8\nu_1 = 0.72$ Hz, and the oscillator θ_2 is strictly periodic with frequency $\tilde{\nu}_2 := 0.8\nu_2 = 1.12$ Hz. For this case, Fig. 4.7(a) shows the wavelet transform of x and Fig. 4.7(b) shows $b^{I_0}_{\psi_\sigma,xxx}(f_1,f_2)$, both with $\sigma = 3$. The six most prominent bispectral contributions can be seen in Fig. 4.7(b). Those are: the diagonal contribution around $(\tilde{\nu}_1,\tilde{\nu}_1)$, and the off-diagonal around $(2\tilde{\nu}_1,\tilde{\nu}_1)$ and its mirror-reflection around $(\tilde{\nu}_1,2\tilde{\nu}_1)$; and likewise, the diagonal contribution around $(\tilde{\nu}_2,\tilde{\nu}_2)$, and the off-diagonal around $(2\tilde{\nu}_2,\tilde{\nu}_2)$ and its mirror-reflection around $(\tilde{\nu}_2,2\tilde{\nu}_2)$. These bispectral contributions are simply due to the nonlinearity of the two individual oscillators. Hence, they do not signify any kind of interaction between the oscillators.

However, introducing coupling results in new peaks that indicate interaction. Now the coupled system

$$\begin{cases} \dot{\theta}_1(t) &= 2\pi\nu_1(1+0.6\cos(\theta_1)) + K\sin(\theta_2 - \theta_1) \\ \dot{\theta}_2(t) &= 2\pi\nu_2(1+0.6\cos(\theta_2)) + K\sin(\theta_1 - \theta_2) \end{cases} \tag{4.17}$$

is considered with ν_1 and ν_2 as defined before, and $K = 0.2$ rad/s. This coupling is not very strong, but it has a significant effect. Once again, Fig. 4.8(a) shows the wavelet transform of x and Fig. 4.8(b) shows $b^{I_0}_{\psi_\sigma,xxx}(f_1,f_2)$, both with $\sigma = 3$. In Fig. 4.8(b) prominent bispectral contributions can be seen around roughly the same points as in Fig. 4.7(b), plus some new peaks, the most prominent being a bispectral contribution roughly around $(\tilde{\nu}_2,\tilde{\nu}_1)$ as well as its mirror-reflection roughly around $(\tilde{\nu}_1,\tilde{\nu}_2)$.
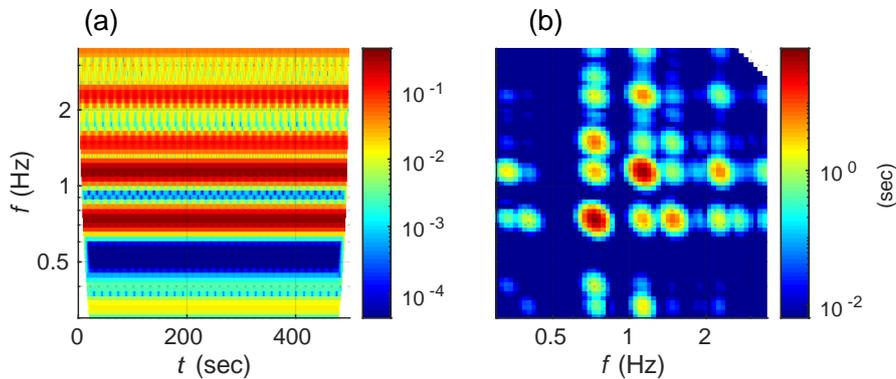
Figure 4.8: Wavelet and wavelet-bispectral representation of a linear superposition of two interacting nonlinear oscillators. In (a) and (b) are shown respectively $|W_{\psi_\sigma,x}(f,t)|$ and $|b^{I_0}_{\psi_\sigma,xxx}(f_1,f_2)|$ (the latter in units of seconds), for the coupled fixed-frequency oscillators as in Eq. (4.17), with $\sigma = 3$.
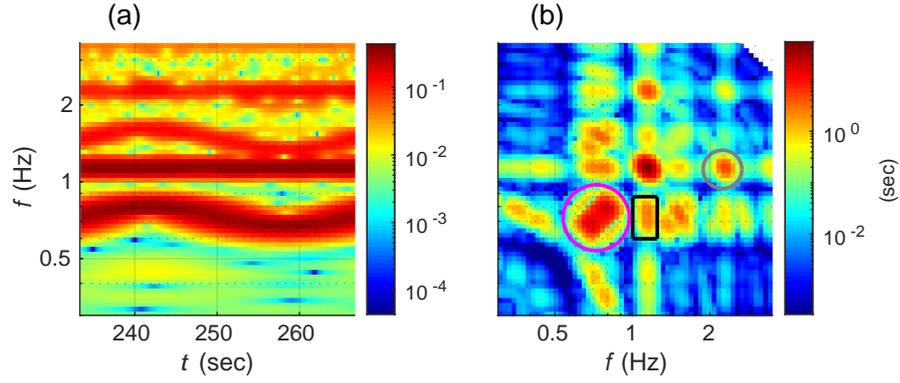
Figure 4.9: Wavelet and wavelet-bispectral representation of a linear superposition of two interacting nonlinear oscillators, with one having slowly time-varying inherent frequency. In (a) and (b) are shown respectively $|W_{\psi_\sigma,x}(f,t)|$ and $|b^{I_0}_{\psi_\sigma,xxx}(f_1,f_2)|$ (the latter in units of seconds), for the coupled oscillators as in Eq. (4.18), with $\sigma = 3$. The bispectral content associated to the three marked frequency-frequency regions over the time interval I_0 are given in the text. Peak around $(\tilde{v}_1,\tilde{v}_1)$ is now bimodal as opposed to unimodal. This is because the sinusoidal temporal variation of $v_1(t)$ spends more time near its extreme values 0.81 Hz and 0.99 Hz than it does around each value in between.

It is clear that the bispectrum can detect the interaction between oscillators. But this detection is not new and could have been achieved using the more traditional non-time-evolving Fourier bispectral analysis. A major improvement of bispectrum can be seen when slow frequency modulation is introduced. For simplicity, the modulation is sinusoidal in shape, but any shape of slow frequency modulation can be used. The used system was

$$\begin{cases} \dot{\theta}_1(t) &= 2\pi v_1(t)(1+0.6\cos(\theta_1)) + K\sin(\theta_2-\theta_1) \\ \dot{\theta}_2(t) &= 2\pi v_2(1+0.6\cos(\theta_2)) + K\sin(\theta_1-\theta_2) \end{cases} \tag{4.18}$$

with v_2 and K as previously defined, and

$$v_1(t) \;=\; 0.9\,\text{Hz} \,\times\, (1+0.1\sin(2\pi f_m t)),$$

where $f_m = 0.03$ Hz. The parameter θ_1 has now a slowly varying inherent frequency, approximately of the sinusoidal shape $0.8v_1(t)$, and the time interval I_0 corresponds exactly to one time period of $v_1(t)$. Fig. 4.9(a) shows the wavelet transform of x over I_0 and Fig. 4.9(b) shows $b^{I_0}_{\psi_\sigma,xxx}(f_1,f_2)$, both with $\sigma = 3$. Some bispectral contribution ensures that around $(\tilde{v}_1,\tilde{v}_1)$ is now bimodal as opposed to unimodal. This is because the sinusoidal temporal variation of $v_1(t)$ spends more time near its extreme values 0.81 Hz and 0.99 Hz than it does around each value in between.

In the example shown in Figs. 4.7–4.9 it is clear that the new definition of wavelet bispectrum allows for the quantification and comparison of bispectral contributions over given time intervals or across different parts of frequency-frequency space. This

was not previously possible.

In Fig. 4.9(b) regions R_{purple}, R_{grey} and R_{black} are marked respectively around the blurry peaks containing frequency pairs $(\tilde{\nu}_1, \tilde{\nu}_1)$, $(2\tilde{\nu}_2, \tilde{\nu}_2)$ and $(\tilde{\nu}_2, \tilde{\nu}_1)$ respectively. Once again, the first two regions contain contributions due to the nonlinearity of the individual oscillators, while the third represents the interaction that has been introduced between the oscillators. The bispectral content associated with each of the three indicated contributions is:

$$
\begin{aligned}
\mathfrak{b}_{\psi,xxx}(R_{\text{purple}} \times I_0) &\approx 0.976 e^{0.08\pi i} \text{ s} \\
\mathfrak{b}_{\psi,xxx}(R_{\text{grey}} \times I_0) &\approx 0.097 e^{0.03\pi i} \text{ s} \\
\mathfrak{b}_{\psi,xxx}(R_{\text{black}} \times I_0) &\approx 0.086 e^{-0.45\pi i} \text{ s.}
\end{aligned}
$$

Moreover, one can actually track over time the motion of the peaks and associated bispectral content. Each of the time intervals $I_1, I_2, I_3 \subset I_0$ is a 5-second interval centred on $7.25 f_m^{-1}$, $7.5 f_m^{-1}$ and $7.75 f_m^{-1}$ respectively. The intervals are marked in Fig. 4.10. In Fig. 4.11 are shown $b_{\psi_\sigma,xxx}^{I_1}(f_1, f_2)$, $b_{\psi_\sigma,xxx}^{I_2}(f_1, f_2)$ and $b_{\psi_\sigma,xxx}^{I_3}(f_1, f_2)$; and on these plots are marked respectively the regions $R_{\text{black}}^{(1)}$, $R_{\text{black}}^{(2)}$ and $R_{\text{black}}^{(3)}$ which help to trace over time the bispectral contribution to the green-marked region in Fig. 4.9(b). Again, the new definition of the wavelet bispectrum enables quantification of the time-evolving bispectral contributions:

$$
\begin{aligned}
\mathfrak{b}_{\psi,xxx}(R_{\text{black}}^{(1)} \times I_1) &\approx 0.008 e^{-0.52\pi i} \text{ s} \\
\mathfrak{b}_{\psi,xxx}(R_{\text{black}}^{(2)} \times I_2) &\approx 0.017 e^{-0.47\pi i} \text{ s} \\
\mathfrak{b}_{\psi,xxx}(R_{\text{black}}^{(3)} \times I_3) &\approx 0.011 e^{-0.45\pi i} \text{ s.}
\end{aligned}
$$

Here, three time-subintervals are sampled. A more continuous-time tracking of bispectral content can be achieved by following the frequency variation of oscillatory components of interest directly from the wavelet transforms themselves via "ridge-extraction" methods, as described in Sec. 3.5.3.
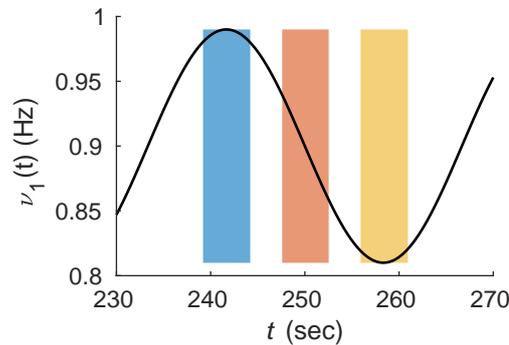
Figure 4.10: Graph of $\nu_1(t)$ over I_0, on which are marked the time intervals I_1 (blue), I_2 (orange) and I_3 (yellow).
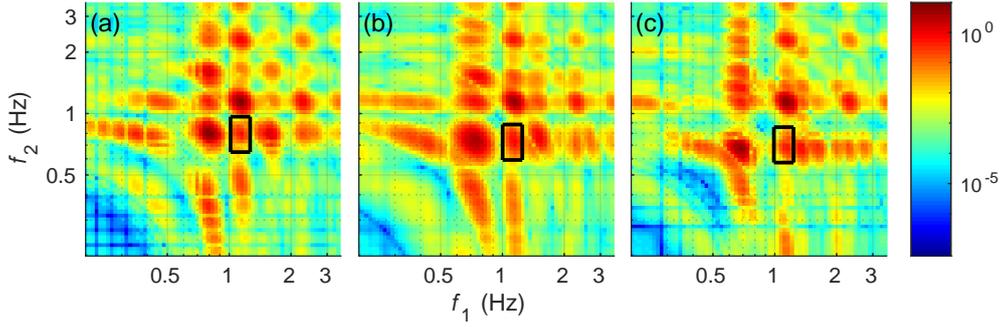
Figure 4.11: Tracing a bispectral contribution over time. In (a), (b) and (c) are shown respectively $|b^{I_1}_{\psi_\sigma,xxx}(f_1,f_2)|$, $|b^{I_2}_{\psi_\sigma,xxx}(f_1,f_2)|$ and $|b^{I_3}_{\psi_\sigma,xxx}(f_1,f_2)|$ (all in units of seconds), for the coupled oscillators as in Eq. (4.18), with $\sigma = 3$. The bispectral content associated to the marked regions of frequency-frequency over the respective time-intervals are given in the text.

4.5.3 The bispectrum and the coupling for linear phase oscillators

The phase oscillator model selected earlier is very specific and describes a narrow class of oscillators. In this section the signal $x(t) = \cos(\theta_1(t)) + \cos(\theta_2(t))$ and the Kuramoto model

$$\begin{cases} \dot{\theta}_1(t) &= 2\pi\nu_1 + K\sin(\theta_2 - \theta_1) \\ \dot{\theta}_2(t) &= 2\pi\nu_2 + K\sin(\theta_1 - \theta_2) \end{cases} \tag{4.19}$$

are considered with $\nu_1 = 0.9$ Hz, $\nu_2 = 1.4$ Hz and $K = 0.2$ rad/s. The signal $x(t)$ was simulated over the time interval $[0\text{ s}, 10^4\text{ s}]$. Fig. 4.12 shows the magnitude of $X(\cdot)$ defined as the result of taking the Fourier transform of x restricted to the interval $[200\text{ s}, 10^4\text{ s}]$ and dividing by the time-duration 9800 s. (The first 200 seconds were removed to avoid any possible transient dynamical behaviour of the system from Eq. (4.19).)
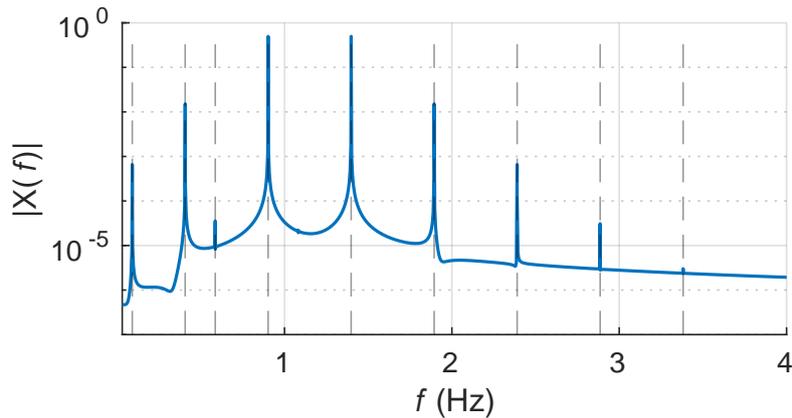
Figure 4.12: The Fourier components of $x(t)$. Here, $|X(f)|$ as plotted on the vertical axis is the Fourier amplitude associated with f, normalised by the duration of the signal. The frequency-values $|0.406 + 0.496n|$ Hz are marked with the respective vertical grey dashed lines for integers n ranging from -2 to 6. The value 0.4959 corresponds to a beat frequency that can be found using Eq. (7.34) from [194].

It can be seen in Fig. 4.12 that the Fourier components of $x(t)$ have frequencies

that all lie within a set of the form $\{|\xi_1 + n\xi_2| : n \in \mathbb{Z}\}$. If ξ_1 and ξ_2 are rationally independent, then no two frequencies in this set can have a sum that also lies in this set. Thus, bispectral analysis would not be able to detect the coupling. Instead, at least some kind of trispectral (i.e. fourth-order spectral) analysis would be needed: perhaps the simplest and most direct approach, as proposed in [116], would be to investigate the presence of frequency triplets with equal spacing between the two consecutive pairs of frequencies, using a time-evolving version of the "modified" Fourier bispectrum

$$\mathcal{T}_{xxx}(f_1, f_2) = \frac{\hat{x}(f_1)^2 \overline{\hat{x}(f_2)\hat{x}(2f_1 - f_2)}}{|\hat{x}(f_1)|}$$

on $\Gamma_{1-} := \{0 < f_2 < f_1\}$ or equivalently on $\{0 < f_1 < f_2 < 2f_1\}$.

4.6 Uncertainty principle again

The new tool, bispectral density, allows for a quantitative evaluation of the bispectral content over time-frequency-frequency space, which establishes a milestone in higher-order analysis. Hence, it is truly suitable for application to complex dynamics. However, it is still not clear what can be concluded about the underlying dynamics based on this approach. In this section some warnings related to the selection of appropriate σ are presented. The whole point of the correct bispectral normalisation is that for fixed frequency components the value of the integral under the patch that corresponds to the "real" effect does not depend on σ. This is presented in Fig. 4.5 where the value of the integral is not affected by σ.

4.6.1 Fixed frequency components

The ability of the wavelet transform to resolve two sinusoidal components depends only on the ratio between the two frequencies f_1 and f_2, (let $f_2 \geq f_1$). Multiplying the frequencies by the same factor c would shift the entire diagram along the frequency axes by an amount proportional to log(c). Nevertheless, it is not well defined what "resolvability" means; more detailed discussion can be found in [108]. Now, the signal of the two uncoupled fixed-frequency components of the form

$$x = \sin(2\pi\nu_1 t) + \sin(2\pi\nu_2 t) \tag{4.20}$$

is considered, where $\nu_2 \neq n\nu_1$, $n \in \mathbb{N}$. It is immediately obvious that the coupling should not be indicated. Fig. 4.13 shows the wavelet transforms and wavelet auto-bispectra integrated over the time interval $[20, 40]$ s for different values of σ. The values of $|W_{\psi_\sigma, x}(f, t)|$ and $|b_{\psi_\sigma, xxx}^{I_0}|$ are shown in upper and lower row respectively. I_0 indicates integration over the interval $[20, 40]$ s. The signal was simulated for $T = 60$ s with sampling frequency $F_s = 50$ Hz. For low σ values, $\sigma < 2$, and fixed frequency components, $\nu_1 = 0.9, \nu_2 = 1.4$, a spurious peak is generated centred

around $(0.84, 0.84)$ and was found empirically. The value could be found explicitly from Eq. (4.4), by adding the wavelet transforms, applying the bispectrum formula, Eq. (4.4.2), and finding the pair for frequencies for which the absolute value of bispectrum is maximised. The values of the integrals over $I_0 = [20, 40]$ s are marked by white circles in frequency-frequency space and are respectively

$$
\begin{aligned}
\mathfrak{b}_{\psi_{\sigma=0.5}, xxx}(R_{(b)} \times I_0) &\approx 0.0060 e^{-0.5154\pi i} \text{ s} \\
\mathfrak{b}_{\psi_{\sigma=0.7}, xxx}(R_{(d)} \times I_0) &\approx 0.0034 e^{-0.5123\pi i} \text{ s} \\
\mathfrak{b}_{\psi_{\sigma=1}, xxx}(R_{(f)} \times I_0) &\approx 0.0016 e^{-0.5093\pi i} \text{ s} \\
\mathfrak{b}_{\psi_{\sigma=2}, xxx}(R_{(h)} \times I_0) &\approx 0.0001 e^{-0.5080\pi i} \text{ s} \\
\mathfrak{b}_{\psi_{\sigma=3}, xxx}(R_{(j)} \times I_0) &\approx 0.0000 e^{-0.5080\pi i} \text{ s}.
\end{aligned}
$$

The values of the integrals are relatively small when compared with the values of the integrals from Fig. 4.5; however in Fig. 4.13(b, d, f) the integral gives a non-zero contribution.

Minimal frequency resolution

Now, the general recipe of "safe" σ selection in case of fixed frequency components will be formulated. It is straightforward from Eq. (3.19) that the lognormal wavelet can be represented by a Gaussian window in the frequency domain, with standard deviation $\dfrac{1}{2\pi\sigma}$. For simplicity it is now assumed that two modes are resolvable if they are separated by m standard deviations. Minimal frequency resolution, σ_{min}, needed to resolve two fixed frequency components is given by

$$
\sigma_{min}^{-1} = \frac{2\pi}{m} \min \left\{ \log \left(\frac{f_2}{f_1} \right), \log \left(\frac{f_1 + f_2}{f_2} \right) \right\}. \tag{4.21}
$$

From this equation, one can easily check that if $f_2 \gg f_1$, and $\frac{f_1 + f_2}{f_2} \to 1$ then $\sigma \to \infty$. This is one of the reasons why investigating the interactions between modes whose frequencies are too far apart, does not give meaningful results when applying bispectral analysis. It will be advisable after identifying the coupled modes, to go back to the wavelet transform and check whether this effect could be due to the insufficient frequency resolution.

4.6.2 Time-varying basic frequency

So far, fixed frequency components were discussed in the context of selecting the most appropriate σ. Of course, in this particular case, the higher the frequency resolution the better the coupling will be resolved because there is no time variability. In case of fixed frequency components the Fourier bispectrum is sufficient. The next step is to investigate dynamics that can change over time. Hence, the easiest way to approach the time variability is by introducing strictly periodically-varying
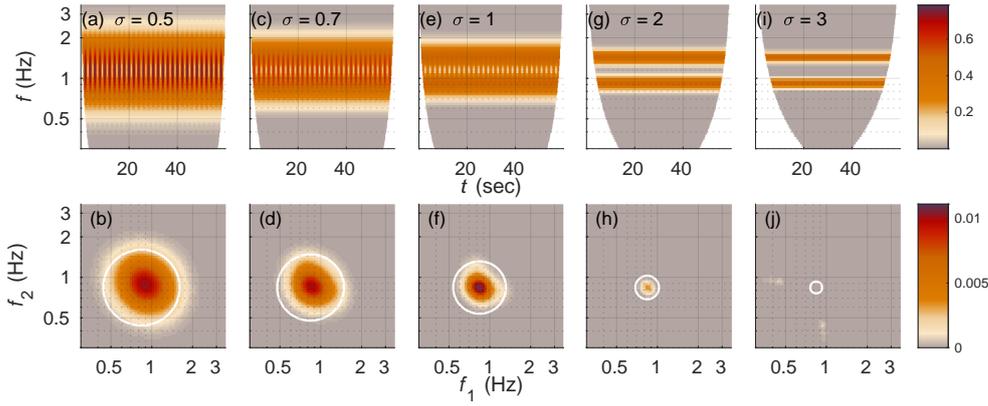
Figure 4.13: Wavelet transforms and wavelet autobispectral representation integrated over the interval I_0 for different σ values for the sum of two sinusoidal components from Eq. (4.20). The values of $|W_{\psi_\sigma,x}(f,t)|$ and $|b^{I_0}_{\psi_\sigma,xxx}|$ are shown in upper and lower row respectively. I^0 indicates integration over the interval $[20,40]$ s. In the lower row the colorbar has the units of s. The parameters are $\nu_1 = 0.9, \nu_2 = 1.4$. The white circle is centred around $(0.84, 0.84)$ and its radius is chosen empirically such that it covers most of the blur. In principles, no peak should appear, nevertheless too low σ values lead to occurrence of spurious peaks. The values of the integrals, which can be found in the main text, are very low, when compared with those from Fig. 4.5; nevertheless they are non-zeros.

frequency. The signal from Eq. (3.5) is investigated. Ideally, knowing the dynamics *a priori*, one would like to represent it as a infinitely thin, sharp-localised "line" in time and frequency. Nevertheless, due to Heisenberg-Gabor uncertainty principle, it is not possible. Therefore for finite-time signal, the autobispectrum will probably always indicate non-zero values – the modulated sine will interfere with itself. As discussed in Sec. 3.5.2, four regimes can be identified. The structure of the wavelet autobispectrum depends, similarly to the regime, on two parameters, $\sigma f_m/f_0$ and k. Here, the effect of non-zero coupling indicated by the autobispectra of the sinusoidal component with varying frequency is measured quantitatively. Fig. 4.14 shows the wavelet transforms $|W_{\psi_\sigma,x}(f,t)|$ and Fig. 4.15 the respective autobispectra $|b^I_{\psi_\sigma,xxx}|$ of the signal from Eq. (3.5), with $f_0 = 0.13$ Hz, $f_m = 0.008$ Hz. The parameters σ and k are varied. The simulation time was $T = 1200$ s, and the sampling frequency $F_s = 20$ Hz. The *nv* was selected using Eq. (3.23), with $N_p = 6$. The autobispectra presented in Fig. 4.15 were averaged over the period $[T/2 - 1/f_m, T/2 + 1/f_m]$ s. Here averaging, as opposed to integration over time as in time-varying signal from Fig. 4.11, was applied – this enables the comparison of the values with the "instantaneous" bispectrum. Various structures from a single blur to harmonically located peaks are present in the autobispectra. Those peaks do not reflect the "real" coupling but are simply the effect of Heisenberg-Gabor uncertainty principle. Fig. 4.16 illustrates the effect quantitatively, by showing the bispectra from Fig. 4.15 integrated over frequency-frequency space as a function of σ and k. Expectedly, the bigger the amplitude variability k and the better the localisation in time, the smaller the obtained coupling. The self-coupling, as measured by autobispectrum, within a signal without the time variability, is not affected by

the change of σ. Initially it is not clear how to compare the structures present in the autobispectrum for low σ (first column in Fig. 4.15) and high σ; however the quantitative comparison of both indicated the smaller values for low σ. The values of the integrals are shown in Fig. 4.16.
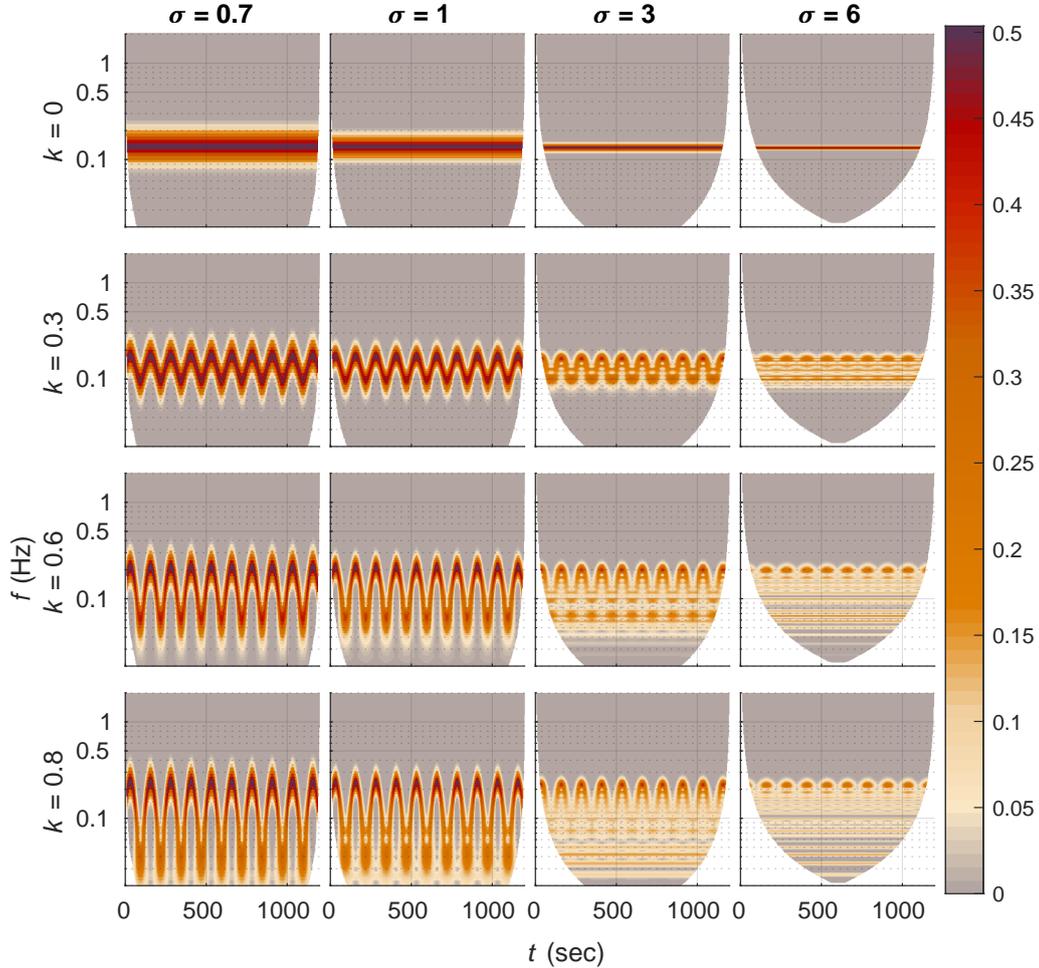
Figure 4.14: Wavelet transforms $\left|W_{\psi_\sigma, x}(f, t)\right|$ of the signal from Eq. (3.5), with $f_0 = 0.13$ Hz, $f_m = 0.008$. The parameters σ and k are varied. Four regimes described in Sec. 3.5.2 can be observed. Fig. 4.15 presents corresponding autobispectra.

4.6.3   Spurious coupling due insufficient frequency resolution

This section illustrates the uncertainty principle in practice: insufficient frequency resolution σ for fixed frequency components and the opposite, insufficient time localisation for the time-varying signals, may result in finding coupling that is spurious in nature. The bispectral density allows one to measure this effect quantitatively, and thus may enhance intuition and help identifying whether the measured coupling actually reflects the real properties of the underlying dynamics.
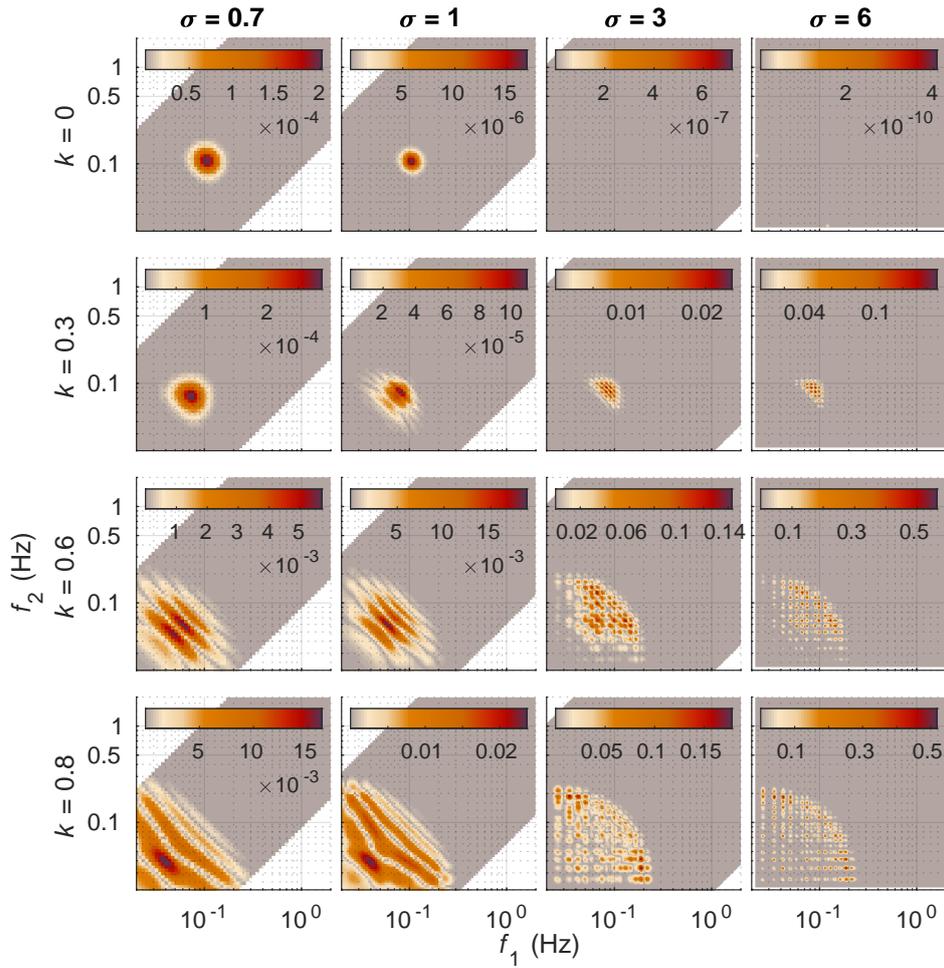
Figure 4.15: Autobispectra $|b^I_{\psi_\sigma,xxx}(f_1, f_2)|$ of the signal from Eq. (3.5), with $f_0 = 0.13$ Hz, $f_m = 0.008$ averaged over the period $[T/2 - 1/f_m, T/2 + 1/f_m]$ s. The parameters σ and k are varied. Corresponding wavelet transforms are presented in Fig. 4.14. Various structures from a single blur to harmonically located peaks are present in the autobispectra. The quantitative effect is presented in Fig. 4.16.

4.7 Surrogates

In this section an application of surrogates in bispectral analysis is discussed. The peaks observed in real data require robust testing. The use of surrogates combined with bicoherence analysis was proposed in [131] and further developed by [151, 218]. The proposed method was applied exclusively to bicoherence to detect quadratic phase coupling (QPC). Another approach was presented in [95], where a threshold obtained from surrogates was applied to bicoherence. The first application of surrogates to bispectrum were presented in [141].

In this section selected types of surrogates, namely Fourier (FT), time-shifted (tshift) and wavelet (WIAAFT), described in Sec. 3.7, are applied in the analysis of
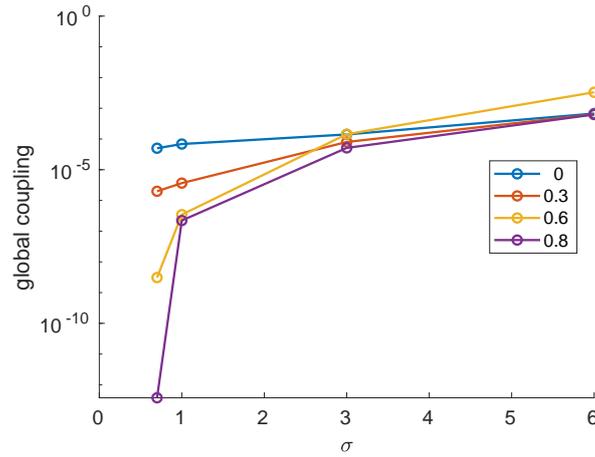
Figure 4.16: Global coupling, measured as autobispectra from Fig. 4.15 integrated over frequency-frequency space as a function of σ. Each colour corresponds to different value of k indicated by the legend. Coupling obtained for small σ is smaller than for bigger σ - this effect is particularly visible for larger values of k. Signals with larger time variability require better time localisation.

the bispectrum of phase-coupled oscillators introduced in Sec. 4.5.2. Fig. 4.17 illustrates the application of the surrogates to wavelet-bispectral representation of a linear superposition of two Kuramoto nonlinear oscillators. In (a-c) the autobispectra averaged over time intervals $I_0 = [233.33, 266.67]$ sec, $\frac{1}{T_{I_0}}|b_{\psi_\sigma,xxx}^{I_0}(f_1, f_2)|$, of the signals of uncoupled, Eq. (4.16), phase-coupled, Eq. (4.17) and phase-coupled with time-varying basic frequency, Eq. (4.18) are presented respectively. In each case, the first column shows the original bispectrum. The subsequent columns show bispectra after values obtained from surrogates are subtracted. In each case the subtracted value is 95th percentile obtained from 50 surrogates.

The lower part of the figure, (d-f) shows respective autobispectra, of the signals similar to (a-c) but with added measurement noise. The noise is the realisation of so-called pink noise, for $T = 500$ s and sampling frequency $F_s = 50$ Hz. The noise was generated using Gaussian noise MATLAB generator, randn(), then the amplitude spectrum in the Fourier domain was multiplied by $\sqrt{f}$, where f corresponds to the frequency. The standard deviation was set to $\kappa = 1$. Regardless of the noise level the results are qualitatively the same. Bispectral peaks are not significant in case of FT in uncoupled and phase coupled oscillators, (Fig. 4.17(a,b,d,e), second column), where the null hypothesis that the data were generated by a linear stochastic process with Gaussian increments cannot be rejected. Similarly, the null hypothesis is not rejected in case of tshift surrogates, (Fig. 4.17(a,b,d,e), third column). Here, the null hypothesis of two processes with arbitrary linear or nonlinear structure but without nonlinear interdependence or significant linear cross-correlation is tested. Only WIAAFT indicates some of the peaks in the correct positions, (Fig. 4.17(a,b,d,e), forth column). Nevertheless the peak $(\tilde{\nu}_2, \tilde{\nu}_2)$ was not significant in any case. The asymmetry in different "treatment" of $(\tilde{\nu}_1, \tilde{\nu}_1)$ and $(\tilde{\nu}_2, \tilde{\nu}_2)$ does not depend on the number

of surrogates (what is shown later in Fig. 4.18). The effect is probably due to the parameters choice and the fact that on wavelet transform the window of the frequency centred around $2\tilde{\nu}_2$ has a bigger spread than centred around $2\tilde{\nu}_1$ on the linear axis. Therefore, the frequency $2\tilde{\nu}_2$ is more likely to coincide with the other higher harmonics. This is another issue, that one needs to take into account when combining the linear nature of bispectral analysis with logarithmic nature of wavelet transform used to generate the surrogates. In case of coupled oscillators when one of them is time-varying, (Fig. 4.17(c,f)), all the surrogates perform similarly, indicating as significant the time-varying peak.

Fig. 4.18 illustrates the bispectrum of linear superposition of uncoupled nonlinear phase oscillators and different number of WIAAFT surrogates. 95th percentile of the n surrogates was subtracted from the original bispectrum. Increasing the number of surrogates does not change the result. In the case where the number of surrogates where not fulfilling the formula $K = m/\alpha - 1$ the percentile was calculated as a linear interpolation of the vector of surrogate data.

4.8 Summary

This chapter introduces the bispectral density which was the first tool to provide a quantitative interpretation of results obtained using the wavelet bispectrum over time-frequency-frequency space. The bispectral density allows for investigation of the time-varying dynamics. Sec. 4.5 provides numerical examples and discusses some of the limitations of the applicability. In Sec. 4.6 the practicalities of uncertainty principles are discussed and finally Sec. 4.7 displays the most appropriate surrogate techniques. Even the most appropriate surrogates tested were not able to detect all the peaks. The most reasonable approach is probably the quantitative bispectral analysis before applying any surrogates.
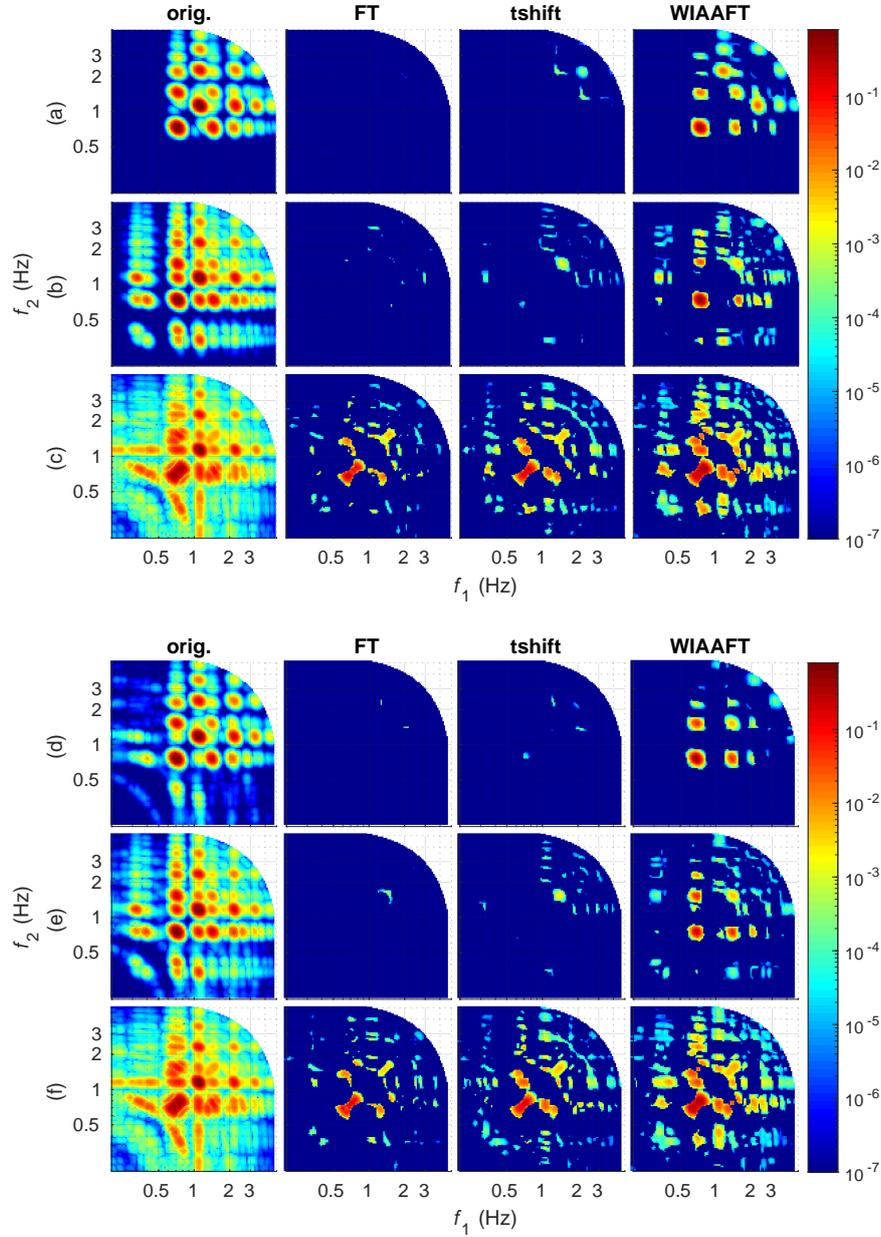
Figure 4.17: Wavelet-bispectral representation of a linear superposition of two Kuramoto nonlinear oscillators without and with measurement noise and use of surrogates. The autobispectra $\frac{1}{T_{I_0}}|b^{I_0}_{\psi_\sigma,xxx}(f_1,f_2)|$ averaged over time intervals $I_0 = [233.33, 266.67]$ sec of (a,d) the uncoupled, Eq. (4.16), (b,e) coupled, Eq. (4.17), and (c,f) coupled oscillators, where one of them has a time-varying frequency are presented. In the first column, the original representation is shown while in the consecutive columns the part remained after subtracting the 95th percentile level of the 50 surrogates. In the upper figure (a,b,c) the original signals are used, while in the lower (d,e,f) the measurement noise is added, with standard deviation $\kappa = 1$. For further details see the text. The colorbar is unitless, $\sigma = 3$.
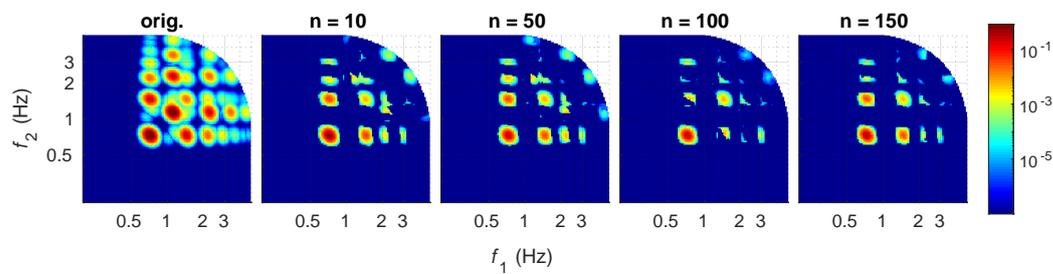
Figure 4.18: Wavelet-bispectral representation of a linear superposition of two Kuramoto nonlinear oscillators and the different number of WIAAFT surrogates. Left figure presents the wavelet-bispectral representation, as in Fig. 4.17(a), the consecutive figures wavelet-bispectral representation after subtracting 95th percentile of n WIAAFT surrogates, except the case where $n = 10$, where the power of the test is $\alpha = 0.09$. Increasing the number of surrogates, up to 150 do not improve the results compared to 10. Even though WIAAFT surrogates seem the most appropriate among tested earlier, Fig. 4.17, the surrogates were not able to detect all the peaks.

Chapter 5

Membrane potential – Wavelet and quantitative analysis

5.1 Introduction

In biophysical analysis fluctuations are often ignored or neglected because they are deemed too complicated for analysis. In particular, in the experiments using the patch-clamp technique, the membrane potential is usually clamped and hence the voltage is artificially made constant. However, because of the involvement of pumps and various ion channels, such as those for K^+, Cl^- and Na^+, fluctuations in the membrane potential result from the physiological condition of the cell. In this chapter, the free-running voltage patch-clamp recordings of the resting membrane potential of Jurkat and smooth muscle cells are analysed. The membrane potential was recorded in different extracellular concentrations, namely standard bath (SB), high K^+, low Cl^-, low Na^+; or after adding intrapipette Ca^+, or ATP, or both Ca^+ and ATP. Comparisons of the average values of the membrane potential and their standard deviations were made. The change in the average value of the membrane potential caused by alteration of the extracellular concentration can be explained by Goldman-Hodgkin-Katz equation and the change in fluctuations by Nernst equations. Later, the recordings were analysed by wavelet analysis, such as the wavelet transform to yield the time-dependent wavelet amplitude, the time-averaged wavelet power and total wavelet power. Several distinctive frequency intervals can be observed, e.g. around 0.01 and 0.3 Hz. To the best of my knowledge, this is the first study reporting the intermittent oscillations in a membrane around 8 mHz, recorded using a free-running membrane potential patch-clamp technique. Finally, possible scenarios of oscillations/fluctuations generators are suggested together with ideas for further experiments.

5.2 Previous studies

The membrane potential influences and is influenced by various cellular processes. The framework was probably initiated in a comprehensive review of cellular oscillators from the late 1970s the division of the cellular oscillators into two categories

was proposed [25]: 1) cytoplasmic and 2) membrane oscillators. The interactions between the cellular oscillators are reviewed in Chapter 2 and summarised in Fig. 2.8.

The characteristic frequencies of cardiovascular oscillations in humans span between 0.005 and 2 Hz [231, 230]. Oscillations in the membrane potential of smooth muscle cell in the context of vasomotion have been reported earlier, reviewed in [2, 1]. Reported oscillations in membrane potential had frequency 0.09 ± 0.01 Hz [182]. Authors concluded that their origins lie in rhythmically gating voltage-dependent calcium channels, that is responsible for the oscillation of intracellular calcium and thus vasomotion. It was concluded that Na^+/K^+ ATPase was not implicated in the generation of the membrane potential oscillations.

The first to investigate the spatio-temporal electrical communication in bacterial communities triggered by metabolism, were Prindle et al. [196]. Most recently, the interplay between metabolism and electrophysiology in bacterial biofilms, was addressed by introducing a spatially extended mathematical model that combines the metabolic and electrical components of the phenomenon in a discretised reaction–diffusion scheme [161].

More specifically for this work, the recordings of the membrane potential oscillations using electrophysiology techniques were previously summarised in Tab. 2.1. The most relevant findings are summarised below. Probably the first to investigate the connection between intestine electrical slow waves and Na^+/K^+ pumps was Job in 1969 [121], however it was also investigated extensively later by Connor et al. [56, 54]. They proposed an experiment to simultaneously measure mammalian intestine electrical slow waves and NADH fluorescence [55]. They found that the slow wave oscillations in the membrane potential were phase locked with the NAD/NADH ratio. The maximum ATP utilization and NADH oxidation occurs during the repolarising phase of the slow wave when sodium ions are being extruded. Their estimated change in intracellular ATP concentration which occurs during the hyperpolarisng phase of the membrane potential was 10%.

The frequency of slow wave potential fluctuations observed experimentally varied between $0.16 - 0.25$ Hz [121, 54, 56]. The main generator of the slow waves was considered to be the Na^+/K^+ pump [121, 56]. Meanwhile the glycolytic oscillator was suggested to mediate the activity of various physiological behaviours, e.g. the slow wave potential in smooth muscles [54], bursting electrical activity in Aplysia neurons [45], and insulin release from the islet cells of the pancreas [57], or excitation-contraction coupling in heart cells [187]. Metabolic oscillations *in vivo* reported more recently can be divided into three distinctive metabolic sub-bands: metabolic oscillator-1 ($5 - 9$ mHz), metabolic oscillator-2 ($2.5 - 5$ mHz) and metabolic oscillator-3 ($1.5 - 2.5$ mHz) [225]. The NADH/ATP oscillations reported earlier have a frequency around 0.1 mHz [190].

In part of the experiment analysed here, additional ATP was added into the

pipette. An effect of the intracellular ATP concentration manipulation on the membrane potential and *vice versa* reported in the literature can be summarised as following. The application of ATP to locus Coeruleus neurons was reported to cause a depolarising response in membrane potential associated with an increase in the firing rate of spontaneous action potential [138]. Mimura et al. investigated the dependence of the membrane potential on the intracellular ATP concentration of *Nitellopsis obtusa* plant cells [172]. They observed that when cells had less negative potential at lower intracellular ATP, the membrane potential could reach the threshold for excitation. At zero intracellular ATP, the membrane was not excitable. This agrees with the earlier finding of Shimmen and Tazawa [221], who concluded that although ATP is essential for the membrane excitation, the excitability can be maintained at very low ATP levels (10-50 μM). Stimulation of the electrogenic pumps by respiration and photosynthesis may result from an increase in the intracellular concentrations of ATP [172], however, several authors have reported that changes in the activity of the electrogenic pumps do not parallel the changes in the intracellular ATP [129, 127]. Ataullakhanov and Vitvitsky defended a point that the cell stabilizes its energy charge by adjusting the rate of ATP synthesis to the state of energy demand [12]. Metabolic needs can fluctuate on the order of seconds or persist for prolonged periods; therefore adaptation is needed [169]. For example, in the heart, ATP is rapidly metabolized and the ATP pool can turnover more than 6 times per minute [111]; at such rates if consumption remains constant, a 10% decrease in ATP production would halve ATP levels in less than one minute. Therefore cells must have the ability to immediately sense and respond to perturbations in the energy state [169].

The majority of the analysis presented here is focused on the membrane potential of Jurkat cells. The detailed description of the membrane transport that may contribute in this experiment is presented in Sec. 2.8. The explicit Ca^{2+} and ATP influence on membrane transport in Jurkat cell is discussed.

Here, the free-running voltage patch-clamp recordings of the resting membrane potential of Jurkat cells and smooth muscle cell *in vitro* are analysed using wavelet analysis, means and standard deviations. The similar analyses of the same recordings from Jurkat cells was done independently in [192, 67]. Each Jurkat cell was classified into one of three groups, based on their dominant permeability, prior to the recordings. Subtle oscillations in membrane potential around 0.01 and 0.3 Hz are observed in the time-averaged wavelet transform. A few other individual cell-dependent bands can be indicated. The smooth muscle cell membrane potential, recorded with perforated patch-clamp technique revealed a characteristic 0.008 Hz oscillatory pattern that coincided with membrane potential hyperpolarisation, below -120 mV. Consecutively, the role of alteration of extracellular K^+, Na^+ and Cl^-

ions or addition of intracellular Ca^{2+} and ATP or on the averaged membrane potential and its fluctuations is investigated. The effect of changing the extra/intracellular content on the fluctuations depends on the dominant permeability. The average membrane potential and its fluctuations can be modified in two ways. First, by alteration of the extracellular concentrations of the ions K^+, Na^+ and Cl^-: thus bringing the Nernst potentials of three dominant ions closer (decrease) or further (increase in fluctuations). Secondly, by addition of the intracellular content: in this experiment Ca^{2+} depolarises the membrane potential, meanwhile Ca^{2+} and ATP together hyperpolarise it, compared to the standard intrapipette solution; the effect of fluctuations depends on the dominant ion channel types (and the Nernst potential of the dominant ion).

5.3 Materials and Methods

5.3.1 Experiments

Two experiments were conducted: 1) the recordings of the membrane potential of Jurkat cells with the free-running membrane potential whole-cell patch-clamp technique done by S. Patel, as a part of his PhD research [192] and 2) the recording of a membrane potential of a smooth muscle cell with the free-running membrane potential perforated whole-cell patch-clamp technique done by me, as a part of my industrial training in Unversity of Aarhus, under the supervision of Assoc. Prof. V. Matchkov.

Jurkat cells

All necessary experimental information included here is taken directly from the PhD thesis [192]. More technical details about cell handling and preparation can be found there. Jurkat E6.1 cells, a widely used human T-lymphocyte cell line, purchased from the American Type Culture Collection (ATCC) were used as a model of T-lymphocytes.

Solutions The standard bath solution contained (in mM): 6 KCl, 150 NaCl, 1 MgCl$_2$, 2 CaCl$_2$, 10 Hepes, 10 glucose. In high K$^+$ additionally 54 potassium gluconate, in low Na$^+$ 150 sodium gluconate while in low Cl$^-$ 140 chloride choline. The intrapipette solution contained (in mM): 120 KCl, 20 NaCl, 10 Hepes, 11 EGTA, in elevated Ca^{2+} additionally 1 μM CaCl$_2$ was added. The calculated ionic concentrations are presented in Tab. 5.3a. The solutions were made by adding each of the constituents from stock solutions prepared in advance. The bath solutions were made up to 450ml with dH$_2$O. The pH of the solutions was adjusted to 7.4 with NaOH and then dH$_2$O was added to make the total volume of 500 ml. The intracellular solution was made to a final volume of 100 ml but the pH was adjusted to 7.2 with KOH. The concentration of CaCl$_2$ in elevated Ca^{2+} solution is the free concentration of Ca^{2+}. The intracellular solution was frozen in aliquots of 1 ml and kept until used in the experiment.

Cell handling and measurement On the day of experimentation, 200 μl of cells were removed from the culture flask and kept at room temperature. 50 μl of the cell suspension was then placed on 35 mm culture dishes for patching. The cells were left for 5 minutes to settle and loosely attach to the bottom of the culture dish, before the perfusion system was switched on. The cells were kept on the culture dish for a maximum of 60 minutes. The standard procedure was applied to achieve whole-cell patch-clamp. The cytosolic solution and the intracellular pipette solution were allowed to equilibrate for 10 minutes before measurement. The membrane voltage recordings were made in current clamp mode ($I = 0$), using standard setup

Axopatch 200B. The osmolarity of the solutions was between 280 and 310 mOsm (measured using a Vapro osmometer). The experiment consisted of two parts:

- alteration of extracellular bath, increasing the concentration of K^+, decreasing Na^+, or decreasing Cl^-, (Tab. 5.3a) with respect to physiological conditions. Each recording consists of at least 7.5 min in each experimental conditions: standard bath (SB) or non standard bath (non-SB). The same cells were used in SB and non-SB, here 58 cells were analysed in two different experimental conditions. 116 recordings were analysed.

- addition of intracellular substances, namely adding Ca^{2+}, ATP or both, (Tab. 5.3b). The cells measured in standard and in non-standard intrapipette conditions were different. 129 recordings were analysed.

Initially the cells were divided into three cohorts, based on the dominant ion permeability for K^+, Cl^-, Na^+ ions, measured as a maximum membrane potential shift in a response to alteration of the extracellular concentration of K^+, Cl^-, Na^+ ions respectively. Another criterium was the averaged membrane potential value, which depends on the permeability to particular ions given the Goldman-Hodgkin-Katz equation.

Smooth muscle cell

This dataset was recorded using the perforated patch-clamp technique. The recordings of the membrane potential of six cells were initially collected, however five experiments failed before 10 min, probably due to loosing the gigaseal, namely the averaged values of the membrane potential suggested the leak of the extracellular solution into the pipette. The cultured smooth muscle cell was used in the experiment. The extracellular solution used during the experiment contained (in mM): 135 NaCl, 6 KCl, 10 Hepes (Na^+), 1 $MgCl_2$, 0.1 $CaCl_2$. The intrapipette solution contained (in mM): 10 Hepes (K^+), 10 BAPTA, 102 KCl, 10 NaCl, 1 $CaCl_2$, 1.44 $MgCl_2$. The solutions were made by adding each of the constituents from the stock solutions prepared in advance. The bath solutions were made up to 450ml with dH_2O. The pH of the solutions was adjusted to 7.4 with NaOH and then dH_2O was added to make the total volume of 500 ml. The intracellular solution was made to a final volume of 200 ml and the pH was adjusted to 7.4 with KOH.

An amphotericin B stock solution was prepared earlier and kept frozen in the darkness at a concentration of 60 mg/mL in dimethyl sulfoxide (DMSO) until the day of the experiment. The final concentration of amphotericin B was prepared by ultrasonicating the 10 μL stock amphotericin B in 1 mL interpipette solution. Pipettes were tip-dipped in amphotericin-free solution for several seconds and backfilled with freshly mixed amphotericin intracellular solution. This procedure was applied to simplify achieving the gigaseal. Standard procedure was then applied to achieve the cell attached mode, perforated cell was obtained several minutes later

when amphotericin B formed the pores in the cellular membrane. The recording was carried on for about 70 minutes in one cell.

Figure 5.1: Experimental setup for patch-clamp experiment used during the internship in Aarhus to collect the recordings of the membrane potential.

5.3.2 Preprocessing

The original time series were recorded with sampling frequency 20 kHz. All datasets used in analysis were downsampled to 20 Hz, using the moving average filter described in Sec. 3.3.2, and de-trended, using the build-in MATLAB, `detrend` function, that removes the best straight-line fit from the data.

5.3.3 Statistical analysis

The exact numbers of cells analysed are shown in Tab. 5.1. A total of 116 of successful Jurkat cells recordings in the experiment with alteration of the extracellular content and 129 in the experiment where Ca^{2+} or/and ATP was added to the pipette were analysed. No statistical comparisons were possible in the experiment with the smooth muscle cell. All the comparisons between the membrane potentials (MP) and the fluctuations, measured as standard deviations (σ) were made with the two-sided Wilcoxon rank sum test (unpaired, where the cells were different, like in comparison of different intracellular solutions) or the Wilcoxon signed-rank test (paired, where the cells were the same, as when altering the extracellular solution). Probability $p \leq 0.05$ was considered significant and led to a rejection of the null hypothesis that the two groups come from the same distribution. Note that here σ corresponds to the standard deviations, not wavelet frequency resolution. For clarification, the

units of mV beside σ imply the standard deviation as opposed to wavelet frequency resolution, also abbreviated as σ, that is dimensionless.

5.3.4 Equilibrium potential

To estimate the equilibrium potential for each K^+, Cl^-, Na^+ ion the Nernst potential was used introduced earlier in Eq. (2.1). The temperature was considered to be $T = 293$ K.

5.3.5 Wavelet analysis

Wavelet analysis is introduced and defined in Sec. 3.5.2. Here, additionally, the time-averaged wavelet power (TAWP) is defined as

$$\text{TAWP}(f) = \frac{1}{t_2 - t_1} \int_{t_1}^{t_2} \rho^I_{\psi,x,x}(f, \tau) d\tau, \tag{5.1}$$

where t_1 and t_2 indicate the time interval of interest, and $\rho^I_{\psi,x,x}$ wavelet energy density as defined in Eq. (3.16). Moreover the averaged wavelet power (AWP) is used, defined as

$$\text{AWP}(f_1, f_2) = \int_{f_1}^{f_2} \text{TAWP}(f) df, \tag{5.2}$$

where f_1 and f_2 indicate the frequency interval of interest. In all analysis the log-normal wavelet is used, defined in Sec. 3.5.2.

Parameter choice Frequency resolution σ, as discussed earlier in Sec. 3.5.2, is a compromise between the optimal localisation in time and the resolution in frequency. Because the low frequency activity is of particular interest, (low from perspective of the length of available recordings), the wish is to preserve as much of the data as possible after removing the cone of influence (discussed in Sec. 3.5.2). Therefore, according to criterium given by Eq. (3.21), one should select σ as low as possible. The $\sigma = 0.5$ was selected. As explained earlier, for the log-normal wavelet, approximately 0.95 of the wavelet integral captures $4 \times \sigma = 2$ cycles of oscillations. This σ is on the border of obtaining meaningful results, however it allows preservation of as much of the low frequency range as possible. The lowest frequency f_1 selected in AWP analysis (Eq. (5.2)) is given by the Eq. (3.21), with $m = 3$. 3 cycles of the oscillations are considered here as a minimal and sufficient to draw any conclusions about the oscillations. For 10 min-long time series this translates to the minimum frequency $f_1 = 8.3$mHz. The highest frequency under consideration in AWP was $f_2 = 3$ Hz.

5.4 Results

The results are organised in the following manner:

intra	K^+	Cl^-	Na^+
i	5	3	8
Ca^{2+}	6	5	0
ATP	7	6	3
Ca^{2+}ATP	6	5	4

(a) First part, 58×2 datasets

intra	SB (high K^+)	SB (low Cl^-)	SB (low Na^+)
i	7(7)	3(4)	6(6)
Ca^{2+}	7(7)	7(8)	0(0)
ATP	7(7)	6(7)	3(3)
Ca^{2+}ATP	6(8)	6(6)	4(4)

(b) Second part, 129 datasets

Table 5.1: Number of cells in each part of experiment (each cohort). In the first part (a), the same cells were measured in two extracellular solutions, while in the second part (b) different cells were measured in different intracellular solutions.

ion	SB (mV)	non-SB (mV)
K^+	-75.64	-17.50
Cl^-	-3.69	79.53
Na^+	50.87	-17.50

(a) Jurkat

ion	(mV)
K^+	-73.89
Cl^-	-5.07
Na^+	63.77

(b) Smooth muscle

Table 5.2: Nernst potentials in the whole-cell (Jurkat cells) and the perforated whole-cell (smooth muscle cell) patch-clamp experiments.

ion	SB	low Cl^-	low Na^+	high K^+
K^+	6	6	6	60
Cl^-	162	6	162	162
Ca^{2+}	2	2	2	2
Na^+	150	150	10	150
Mg^{2+}	1	1	1	1

(a) External bath (mM)

ion	i	Ca^{2+}	ATP	Ca^{2+} + ATP
K^+	120	120	120	120
Cl^-	140	140	140	140
Ca^{2+}	10^{-5}	10^{-3}	10^{-5}	10^{-3}
Na^+	20	20	20	20
ATP	0	0	4	4

(b) Intrapipette (mM)

Table 5.3: Ions concentrations in the solutions in the experiment using the whole-cell patch-clamp.

ion	out	in
K^+	6	112
Cl^-	143	117
Na^+	125	10

Table 5.4: Extracellular and intracellular ionic concentrations (mM) in the smooth muscle cell experiment

- First, in Sec. 5.4.1, the effect of changing the extracellular concentrations are presented. This includes the analysis of the same cells in both standard and non-standard extracellular conditions and standard intrapipette solutions. Alteration of the extracellular concentrations significantly changed the membrane potential (where at least 4 datasets were available). The effect of the change of extracellular concentration on the fluctuations depends whether the 3 Nernst potentials were brought closer or further apart. If further – an increase was observed, if closer – a decrease.

- Secondly, in Sec 5.4.2, the effect of different extracellular concentrations is shown after adding Ca^{2+}, or ATP, or both to the intrapipette solution. The aim of this section is to illustrate if and how intrapipette Ca^{2+} and/or ATP change the effects observed in the standard pipette.

- Sec. 5.4.2 illustrates the effect of adding Ca^{2+} and/or ATP in the pipette. Adding intrapipette Ca^{2+} depolarises the membrane, while adding both Ca^{2+} and ATP hyperpolarises it compared to standard intrapipette solution. Additional ATP does not bring any systematic changes.

- Sec. 5.4.3 presents the time-averaged wavelet power from all the datasets. This analysis aims at characterising the frequency bands of the spectral peaks. Given the intracellular pipette solution, each cell was analysed in both standard and non-standard extracellular solutions to separate the inter-cell variability from the actual external effect caused by the change in concentration. Oscillations could be grouped into two bands centred around 0.01 and 0.3 Hz but their presence depends more on a particular cell rather than on the extracellular or intracellular solutions.

- Sec. 5.4.4 shows the analysis of the membrane potential of a smooth muscle cell of the length 70 minutes recorded with perforated patch-clamp technique. The time series very clearly reveals the oscillatory component around 8 mHz, occurring in several time localised events, accompanied by strong membrane potential hyperpolarisation: there the membrane potential dropped below -120mV. Spectral peaks in several other bands, e.g. 2 mHz can be observed.

5.4.1   Alteration of the extracellular concentrations in standard pipette

Figs. 5.2 and 5.3 summarise the idea of the first part of the experiment: namely motivation to investigate fluctuations, and separation into cohorts based on the dominant ion permeability. Fig. 5.2 presents the 0.5 min recordings of fluctuating membrane potential. Recordings under the same ionic concentrations lasted between 8 and 12 min in total. For each cohort the membrane potentials were recorded in two different extracellular concentrations. Different cells manifested different sensitivity to different ionic concentrations. The division into cohorts was rather heuristic. Each cell was assigned to one group. For a few cells the membrane potential was recorded under multiple conditions. Fig. 5.3 presents the membrane potential (MP) recorded in low Na^+, standard bath (SB) and high K^+, together with the respective amplitudes of wavelet transform $|W(f,t)|$ and time-averaged wavelet power (TAWP). The figure illustrates that the averaged value of the membrane potential and its fluctuations depend on the extracellular concentrations of K^+ and Na^+. Deviating the concentrations from the standard bath (in the specific direction discussed later) decreases the fluctuations, at the same time makes some of the frequency bands more prominent, e.g. low Na^+ decreased the spectral peak around 0.01 Hz and 0.07 Hz relative to the other frequencies, while high K^+ made the peak around 0.05 Hz more pronounced. Fig. 5.4 shows the membrane potential recordings (MP) of the example cell from the Cl^- cohort, amplitudes of their wavelet transforms $|W(f,t)|$ and time-averaged wavelet powers (TAWP) under standard bath and low Cl^- conditions. Low Cl^- did

not substantially change the fluctuations in the membrane potential but reduced the spectral power between 0.007–0.05 Hz, thus making the power spectrum flatter.

Fig. 5.5 illustrates how the alteration of the extracellular content influences the averaged membrane potentials and their fluctuations under standard intrapipette conditions. The averaged membrane potential (MP) and standard deviation (σ) values for K^+, Cl^- and Na^+ cohorts are shown in the consecutive rows. Modifying the extracellular concentrations shifts the Nernst potentials, as indicated. Alteration of the extracellular concentrations changes the average membrane potentials and standard deviations significantly in the majority of cases. However, no concussion can be drawn for Cl^-, as only 3 datasets were available. The changes in fluctuations are in the direction indicated by the changes from the distance from Nernst potentials.
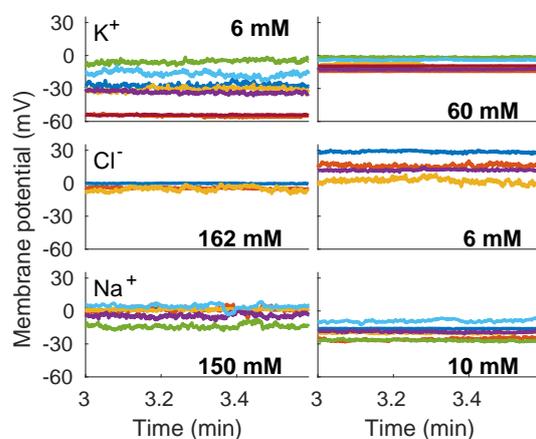
Figure 5.2: The membrane potential is not clamped but naturally fluctuates around its average value. Recordings of the membrane potential of the Jurkat cells measured with the free-running voltage whole-cell patch-clamp technique. The cells were divided into three cohorts K^+, Cl^-, Na^+, based on the dominant permeability. In the left column: standard extracellular bath (SB), in the right: altered the dominant ion concentration, as written in bold. In each row the same colour represents the same individual cell. For each concentration recordings were made for at least 8 min; 0.5 min is shown.

5.4.2 Alteration of the extracellular concentrations given the intracellular Ca^{2+} and ATP

In the second part of the experiment intracellular Ca^+ or ATP, or both Ca^+ and ATP were added to the pipette. Here, the focus of the analysis is to investigate how alteration of the extracellular ions influences the dynamics of the membrane potential, given the non-standard intrapipette solution, either with Ca^+ or ATP or both. Figs. 5.6-5.8 illustrate the representative membrane potential (MP) of the cell from each cohort (K^+, Cl^-, Na^+) with intracellular Ca^+, or ATP, or both Ca^+ and ATP, in the consecutive figures respectively. In each come the corresponding wavelet transforms, $W(f,t)$, and time-averaged wavelet power, TAWP are also shown.

Fig. 5.9 shows the quantitative effect of an alteration in the extracellular solutions on the averaged wavelet power (AWP) and the membrane potential (MP) for each cell individually, with successful recordings in both SB and non-SB. Increasing the extracellular K^+ made the membrane potential less negative and decreased the AWP. Moreover high K^+ decreased the variance in the MP, which seems not to be the case for Cl^- and Na^+. Decreasing the extracellular Cl^- increased the membrane potential (by making it either less negative or even positive) for all concentrations and
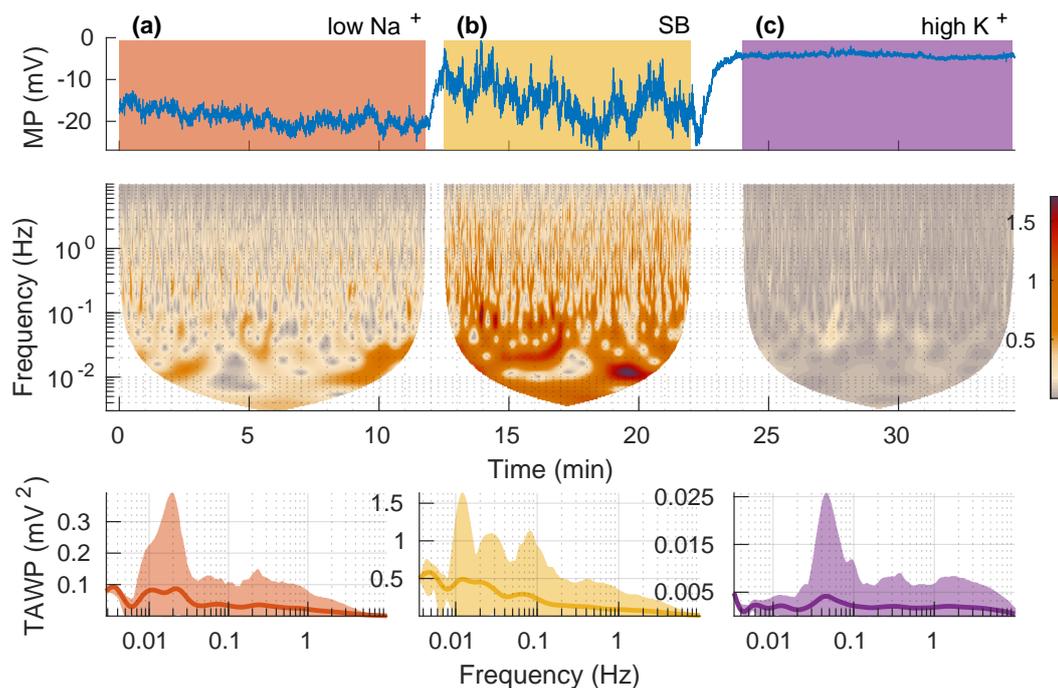
Figure 5.3: Alteration of extracellular concentrations influences the dynamics of the membrane potential. The membrane potential, MP (upper), amplitude of the wavelet transform, $|W(f,t)|$ (middle) and the time-averaged wavelet power TAWP, (lower row) are shown. The cellular membrane potential of the same cell recorded under three conditions: low Na^+, SB and high K^+. Both low Na^+ and high K^+ extracellular concentrations reduce the fluctuations, low Na^+ is making the membrane potential more negative while high K^+ makes it less negative. The amplitude of the wavelet transform, $|W(f,t)|$ is given in units of mV. The shaded areas on TAWP correspond to the 5th and 95th percentiles. TAWP indicates that most of the wavelet power is cumulated in low frequencies (≤ 0.04 Hz). The wavelet power below 0.02 Hz, relative to the higher frequencies, is strongly pronounced in SB. Note the different y-axis scales that emphasise the difference in fluctuation intensities under different experimental conditions, in particular the decrease in fluctuations when increasing the extracellular K^+, compared to standard bath conditions.
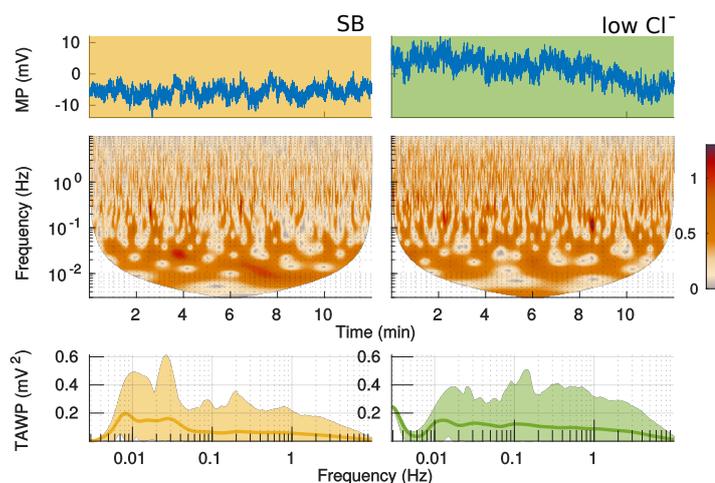
Figure 5.4: The membrane potential MP of the example cell from the Cl^- cohort, amplitudes of their wavelet transform, $|W(f,t)|$ and the time-averaged wavelet power (TAWP) in standard bath and low Cl^- conditions and standard intracellular solution. Low Cl^- did not substantially change the fluctuations in the membrane potential but reduced the power around 0.007–0.05 Hz, thus making the power spectrum flatter.

increased the AWP (17 out of 19 datasets). Decreasing the extracellular Na^+ made the membrane potentials less positive or more negative, or in other words decreased

Figure 5.5: The change in the extracellular concentrations influences the averaged membrane potential and its fluctuations. The averaged membrane potential, MP on the vertical axis and standard deviation, σ on horizontal axis for the K^+, Cl^- and Na^+ cohorts in the consecutive rows. Circles correspond to the standard extracellular bath while stars to the non-standard conditions. Each semi-transparent marker corresponds to a different cell and opaque one to the median for each group. The vertical lines indicate the Nernst potentials for standard conditions (dashed), and the non-standard bath (dash-dotted), for K^+ in blue, Cl^- in orange and Na^+ in green. Alteration of the extracellular concentrations changes the average membrane potentials and standard deviations significantly in the majority of cases. For Cl^- where only 3 datasets are available, therefore reliable conclusions cannot be drawn. The changes in fluctuations are proportional to the distance from the Nernst potentials.

them (13 out of 15 datasets) and decreased the AWP (11 out of 15).

Now the observations made based on Figs. 5.6-5.8 are presented. The focus is on the distribution of the time-averaged wavelet power across different frequencies, rather than quantitative wavelet power comparison that was done earlier.

In the Ca^{2+} pipette, Fig. 5.6

- Low extracellular Cl^- enhances the oscillations around 0.3 Hz (Fig. 5.6, bottom-right, especially visible in TAWP). This observation was made in 3 out of 5 datasets (Fig. 5.13(b), second row).

- High extracellular K^+ does not substantially change the distribution of the wavelet power across the frequencies. Any changes in the shape of the spectrum were very subtle and incoherent across the cells.

In the ATP pipette, Fig. 5.7

- No robust and consistent changes are observed in the wavelet power distribution across the frequencies caused by increasing the concentration of the K^+ nor by deceasing Cl^-.

- The variance of TAWP in all 3 datasets in low Na^+ is smaller than in SB.

In the combined Ca^{2+} and ATP pipette, Fig. 5.8 No robust and consistent changes are observed in the wavelet power distribution across the frequencies caused by increasing the concentration of the K^+ nor by decreasing the concentration of the Na^+ or Cl^-.
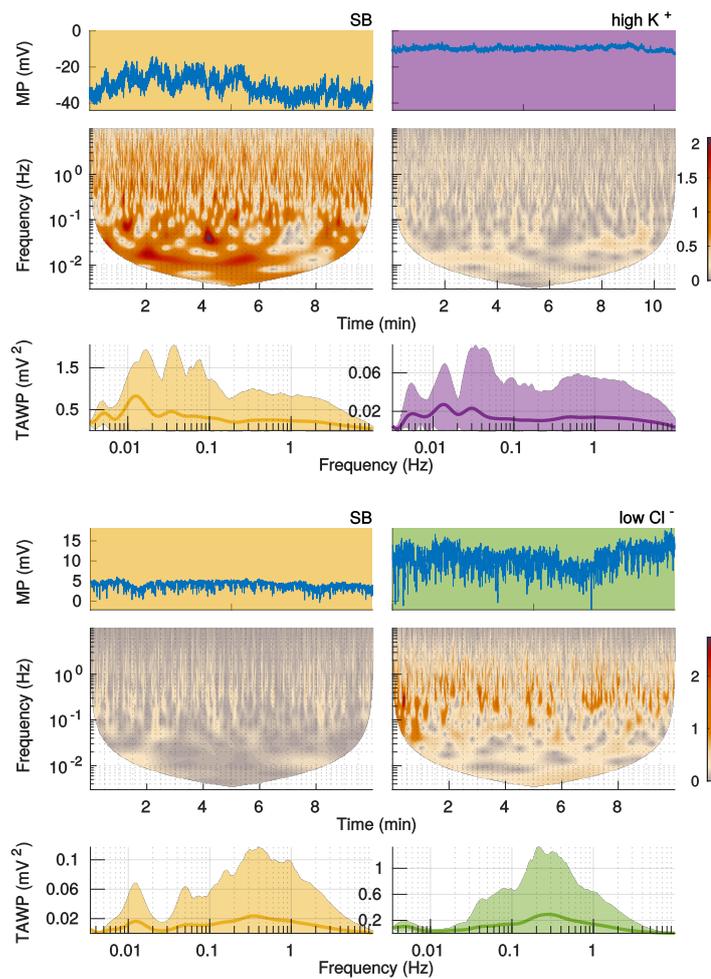
Figure 5.6: The membrane potential dynamics of the selected representatives from the K^+ and Cl^- cohorts with intracellular Ca^{2+} in two different extracellular conditions. Each panel illustrates the time series, the amplitude of the wavelet transform, and the time-averaged wavelet power (TAWP) under SB and non-standard conditions. In each panel recordings for SB and non-SB come from the same cell. The shaded areas correspond to the 5th and 95th percentiles of TAWP. The upper panel shows results from representative cell from the K^+ cohort, while the lower refers to the Cl^- cohort. The recordings with intracellular Ca^{2+} in the Na^+ cohort were not successful. In the Cl^- cohort the oscillatory component around 0.2 Hz can be observed, note the scale in the low Cl^- solution. In the SB in both cohorts the oscillatory component between $0.01 - 0.02$ Hz can be identified. In high K^+ the whole spectrum not only drops by an order of magnitude but the 0.01 Hz component becomes less distinctive.
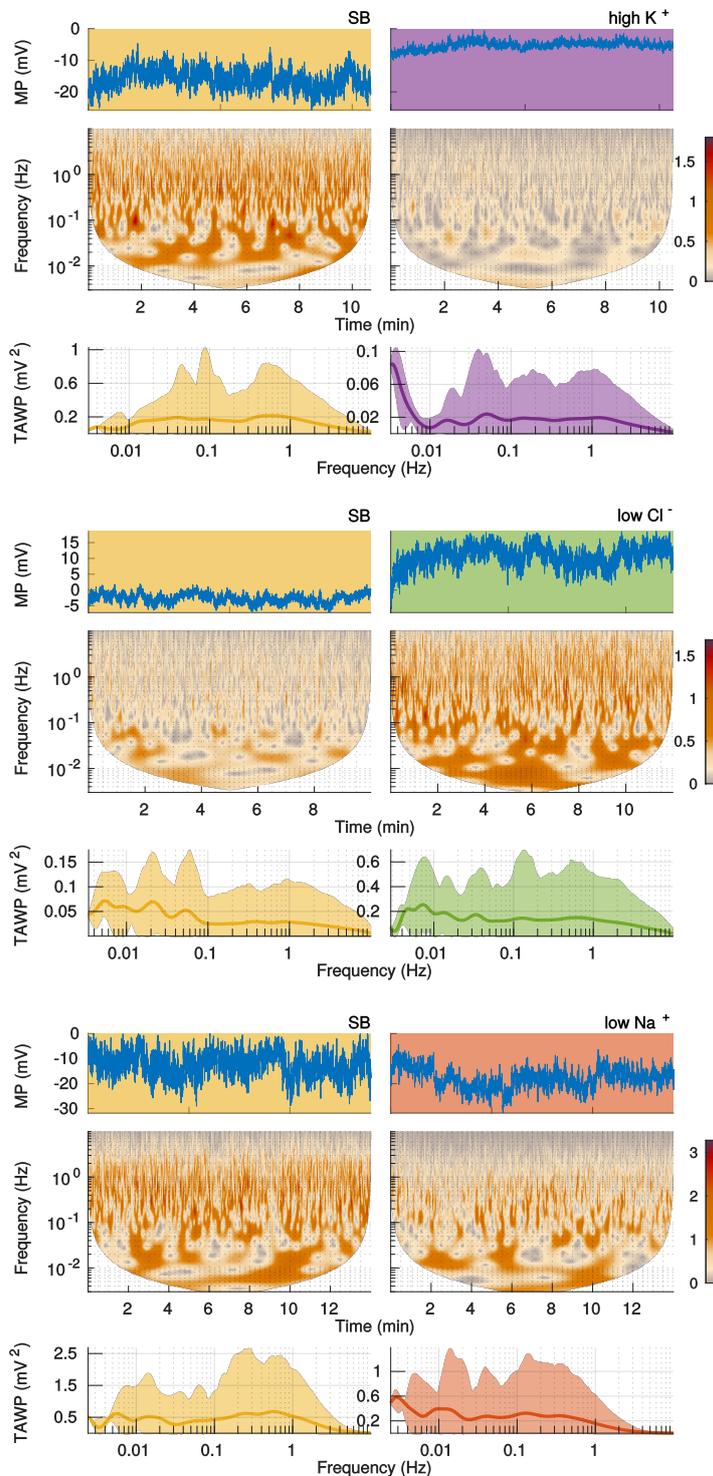
Figure 5.7: The membrane potential dynamics of the selected representatives from the K^+, Cl^- and Na^+ cohorts with intracellular ATP in two different extracellular conditions. Each panel illustrates the time series, the amplitude of the wavelet transform, and the time-averaged wavelet power (TAWP) under SB and non-standard conditions. In each panel recordings for SB and non-SB come from the same cell. The shaded areas correspond to the 5th and 95th percentiles of TAWP. The panels show results from the representative cell from the K^+ (the upper), Cl^- (the middle), and the Na^+ cohort (the lower). In the SB, in the K^+ cohort, the spectrum is relatively flattened. The whole power spectrum is one order of magnitude smaller under high K^+ concentration compared to SB; and small bumps around the frequencies of 0.01 and 0.05 Hz are visible. For the other cells from this experiment the pronounced frequencies are cell dependent. Under low Cl^- concentration the general intensity of fluctuations increases, but the peaks visible in SB become less distinctive. In the representative cell from the Na^+ cohort the fluctuations are slightly smaller in low Na^+ solution, thus TAWP is slightly lower.
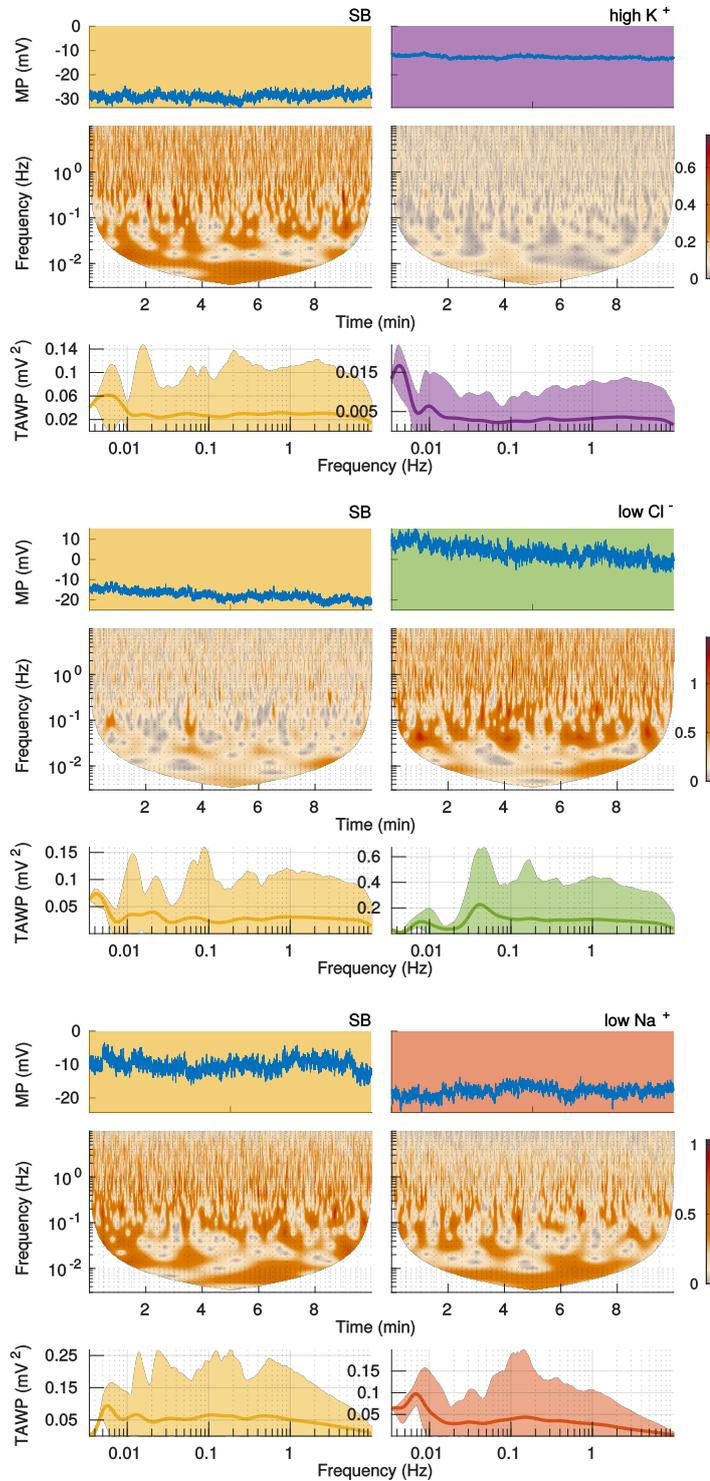
Figure 5.8: The membrane potential dynamics of the representatives from the K^+, Cl^- and Na^+ cohorts with added intracellular Ca^{2+} and ATP in two different extracellular conditions. Each panel illustrates the time series, the amplitude of the wavelet transform, and the time-averaged wavelet power (TAWP) under SB and non-standard conditions. In each panel recordings for SB and non-SB come from the same cell. The shaded areas correspond to the 5th and 95th percentiles of TAWP. The upper panel shows results from the representative cell from the K^+ cohort, middle Cl^-, while the lower refers to the Na^+ cohort. Considering the reliable frequencies range (> 8.3 mHz, the wavelet power spectra in the representative cell from the K^+ and Na^+ are relatively flattened. In the Cl^- cohort, low Cl^- solution, the peak around 0.04 Hz is visible, nevertheless this peak is not pronounced in most of the other cases for the same concentrations.
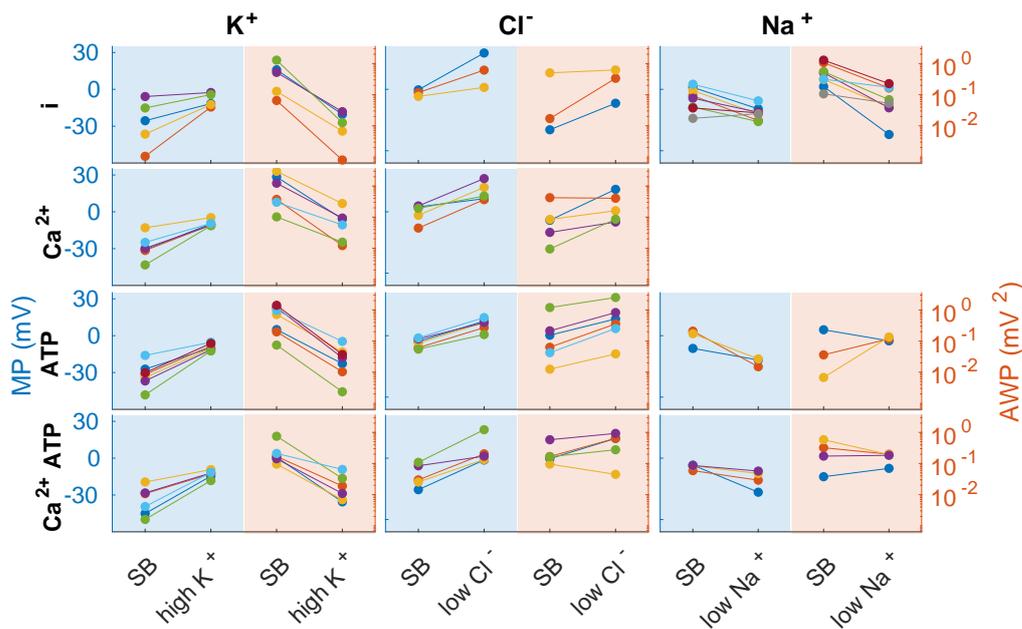
Figure 5.9: The change in the extracellular concentrations influences the averaged membrane potential and its fluctuations, measured as the averaged wavelet power for individual cells. The membrane potential (MP, blue background, left axis) and the averaged wavelet power (AWP, orange background, right axis) for the datasets with successful recordings in both SB and non-SB. In each subplot (left and right sides) a particular colour represents the same cell. Increasing the extracellular K^+ made the membrane potentials less negative and decreased the AWP in all the datasets. Decreasing the extracellular Cl^- made the membrane either less negative or even positive, or in other words increased it in all datasets and increased the AWP (17 out of 19 datasets). Decreasing the extracellular Na^+ made the membrane potentials less positive or more negative, or in other words decreased it (13 out of 15 datasets) and decreased the AWP (11 out of 15).

The effect of different intrapipette solutions with Ca^{2+} or ATP or both

In this part, the effect of adding Ca^+, or ATP, or both Ca^+ and ATP, with respect to standard intrapipette solution is illustrated. Figs. 5.10, 5.11 and 5.12 show the results of comparisons of the time-averaged wavelet power in different intracellular solutions and the *p*-values of the comparisons for the K^+, Cl^- and Na^+ cohorts respectively. In K^+, Fig. 5.10, and Cl^- Fig. 5.11, different intrapipette solutions had no significant effect on the TAWP. In the Na^+ cohort, Fig. 5.12, TAWP is significantly bigger in the ATP pipette, compared to the standard ((a), SB, left); however there were only 3 cells in the ATP group. Wavelet power for a frequency of 0.02 Hz was bigger for the standard pipette compared with Ca^{2+} ATP; and the opposite effect was observed in the low Na^+ bath ((b), low Na^+, right) for a frequency of 0.03 Hz, namely there is greater power in the Ca^{2+} ATP pipette compared to a standard solution. However, the significant frequency ranges are very narrow compared to the frequency resolution (width of the window in frequency domain). This makes the robust conclusions impossible.

Fig. 5.13 presents the averaged wavelet power, AWP, integrated over 8.3 mHz −

3 Hz for the K^+, Cl^- and Na^+ cohorts, SB and non-SB for different intrapipette solutions marked with colours: standard–i, Ca^{2+}, ATP, Ca^{2+} and ATP. The number of cells in each group spans from 3 to 8. In the SB and Cl^- cohort the AWP is significantly lower in the Ca^{2+} pipette than in the combined Ca^{2+} ATP. In the SB Na^+ the AWP is significantly lower with ATP inside, compared to the standard intrapipette solution. Note, however, that the results were obtained with only 3 datasets in ATP group.

Fig. 5.14 shows the effect of different intrapipette solutions on the membrane potential and fluctuations measured as a) averaged wavelet power and b) standard deviations. The averaged wavelet power (AWP) was integrated over $8.3 \, \text{mHz} - 3 \, \text{Hz}$. Standard deviation ($\sigma$) is shown as a function of the membrane potential for the K^+, Cl^- and Na^+ cohorts and SB and non-SB for different intrapipette solutions: standard–i, Ca^{2+}, ATP, Ca^{2+} and ATP. The integrated AWP captures the activity between 8.3 mHz and 3 Hz, while the standard deviations capture the activity between $1/T \simeq 1.7 \, \text{mHz}$ up to 10 Hz. 7 significant changes summarised below can be identified.

Intracellular Ca^{2+}

- Increased intracellular Ca^{2+} did not result in any significant change in fluctuations measured either as AWP or σ compared to standard pipette.

- For high intracellular K^+ concentration the membrane potential is significantly more negative when both Ca^+ and ATP were added, compared to the case when only ATP was added in the pipette.

Intracellular ATP

- In the SB in the Na^+ cohort, the AWP was significantly lower in the ATP pipette than in standard one (comparison made with only 3 datasets).

- In the SB in the Cl^- cohort, the AWP and σ in the combined Ca^{2+} and ATP pipette was significantly lower than in the pipette with increased Ca^{2+}.

- In the combined Ca^{2+} and ATP pipette the standard deviation was significantly smaller than in the pipette with elevated Ca^{2+} in SB, in the K^+ cohort but the opposite effect was observed in SB, in the Cl^- cohort.

- In high K^+ and in Cl^- the membrane potential was significantly depolarised in the pipette with elevated Ca^{2+} in comparison to the combined Ca^{2+} and ATP pipette.

Intracellular Ca^{2+} and ATP

- In low extracellular Na^+ in the combined Ca^{2+} ATP pipette σ was significantly bigger than in standard intrapipette solution.

(a) standard vs Ca^{2+}

(b) standard vs ATP

(c) standard vs Ca^{2+}ATP
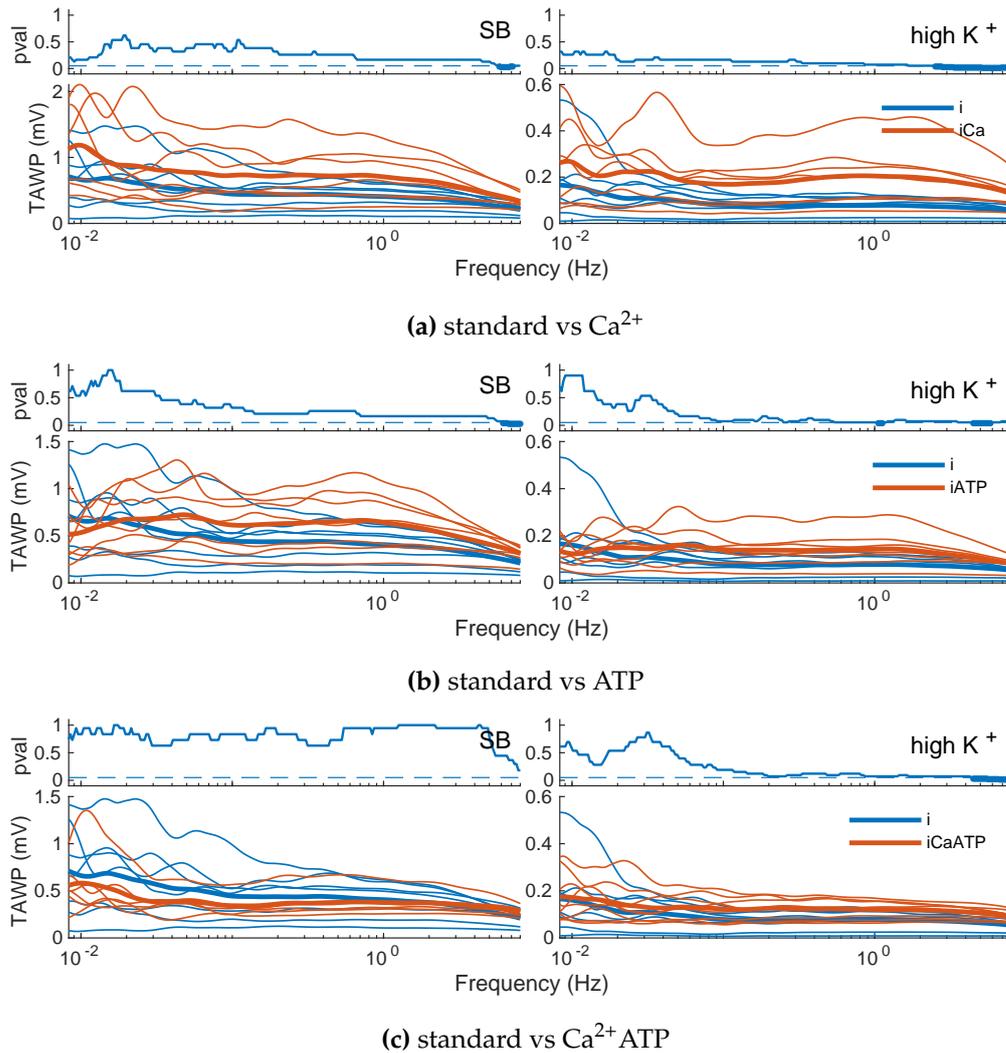
Figure 5.10: The effect of different intrapipette solutions on the time-averaged wavelet power (TAWP) for the K^+ cohort. Consecutive rows present the comparison of two different intrapipette solutions marked with different colours, a) standard vs Ca^{2+}, b) standard vs ATP, c) standard vs combined Ca^{2+} and ATP. The left column presents the results in the standard bath (SB), and the right one in the high K^+ concentration. In each panel the upper plot shows the probability value, pval. In most of the cases different intrapipette solutions had no significant effect on the TAWP.

Summary In this part the results for different intrapipette solutions of Ca^{2+}, ATP and both Ca^{2+} and ATP are presented. The consistent change, present for all the cohorts, was the effect on the average value of the membrane potential. The most negative (the most hyperpolarised) membrane potentials were observed with the Ca^{2+} and ATP pipette (in 5 out of 6 cases) and the least negative or even positive (the most depolarised) was the membrane potential observed for the Ca^{2+} pipette. The differences between the Ca^{2+} and the Ca^{2+} and ATP pipettes were significant in 3 out of 6 cases. No significant changes were observed when ATP alone was added. When it comes to fluctuations, the opposite effect was observed in the SB in the K^+ and Cl^- cohorts. In the K^+ cohort, the fluctuations in the Ca^{2+} pipette were bigger

(a) standard vs Ca^{2+}

(b) standard vs ATP

(c) standard vs Ca^{2+}ATP
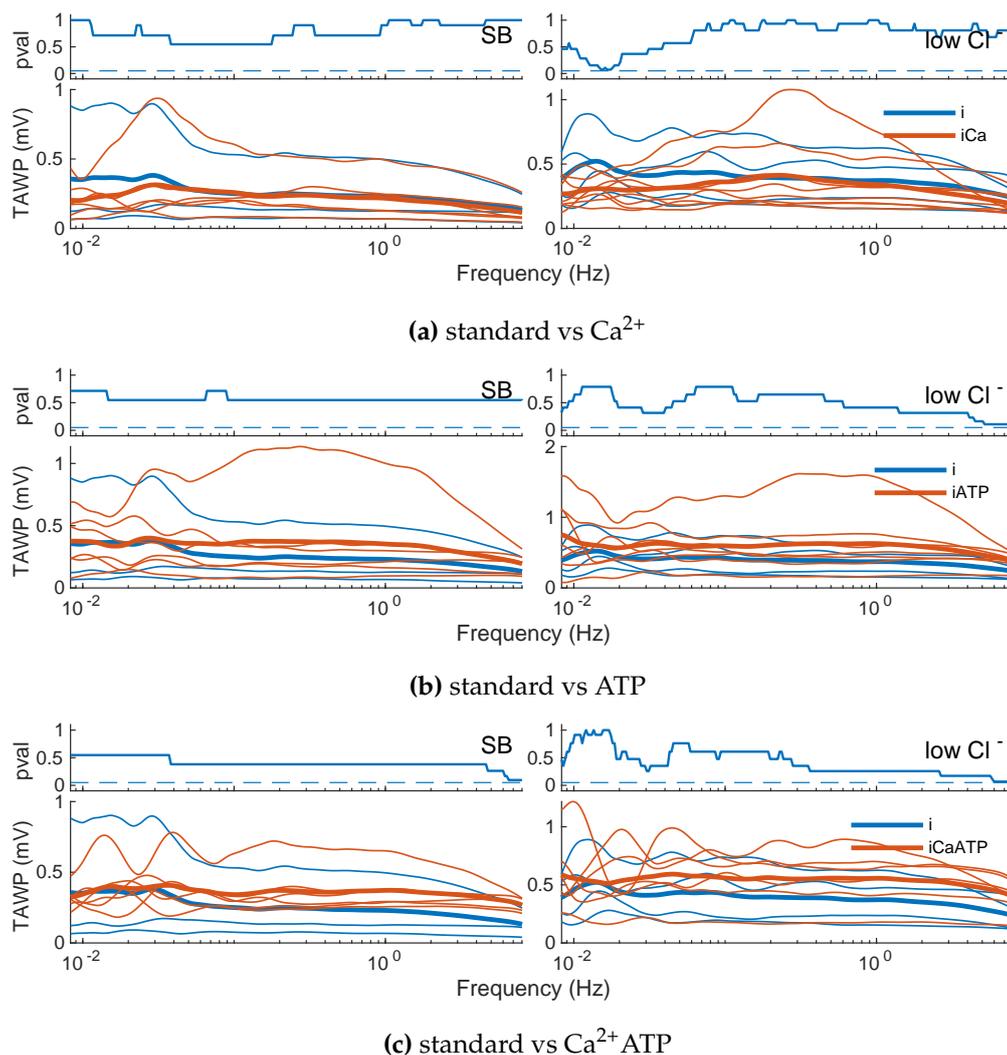
Figure 5.11: The effect of different intrapipette solutions on the time-averaged wavelet power (TAWP) for Cl^- cohort. Consecutive rows present the comparison of two different intrapipette solutions, marked with different colours, a) standard vs Ca^{2+}, b) standard vs ATP, c) standard vs combined Ca^{2+} and ATP. The left column presents the results in standard (SB), and the right one in low Cl^- bath solutions. In each panel the upper plot shows the probability value, pval. Different intrapipette solutions had no significant effect on the TAWP.

than in the combined Ca^{2+} and ATP pipette (significant for the SB, tendency for the high K^+ bath), while in the Cl^- cohort quite the opposite was found (significant in SB, tendency in low Cl^- bath). The spread of median values, both membrane potentials and the AWP, is relatively small in the K^+ cohort, compared to the Cl^- cohort.

(a) standard vs ATP

(b) standard vs Ca^{2+} ATP
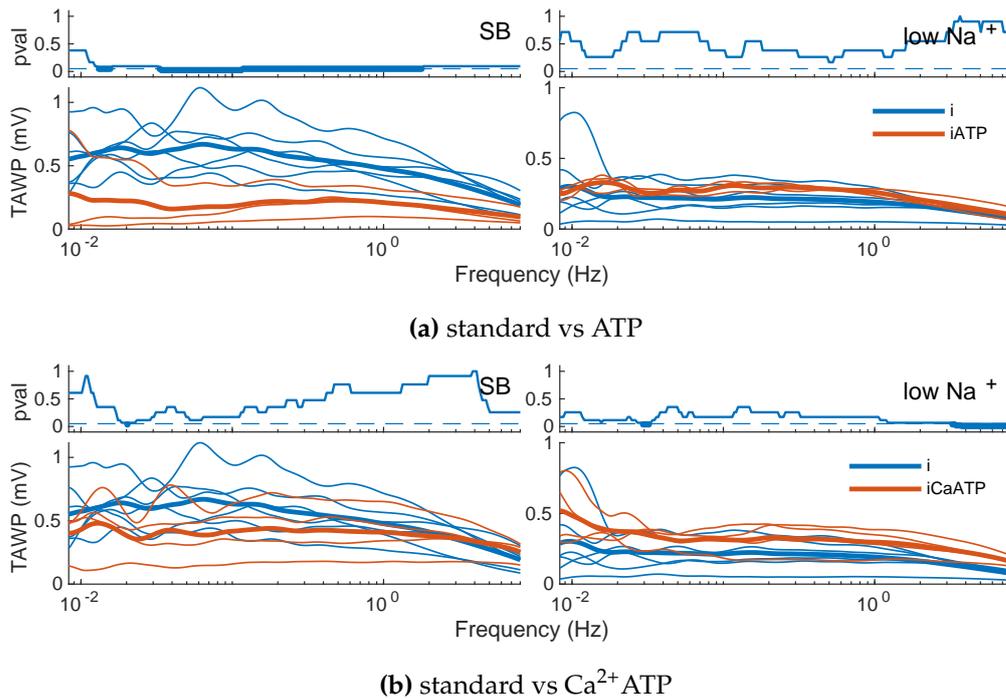
Figure 5.12: The effect of different intrapipette solutions on the time-averaged wavelet power (TAWP) for the Na^+ cohort. Consecutive rows present the comparison of two different intrapipette solutions, marked with different colours, a) standard vs Ca^{2+}, b) standard vs ATP, c) standard vs combined Ca^{2+} and ATP. The left column presents the results in the standard (SB), and the right one in the low Na^+ bath solutions. In each panel the upper plot shows the probability value, pval. TAWP is significantly bigger in ATP pipette compared with the standard one (a), SB, left), however there were only 3 cells in ATP group; and (b), SB, left) wavelet power for a frequency 0.02 Hz was bigger is standard pipette compared with Ca^{2+} ATP; and the opposite effect was observed in low Na^+ bath (b), low Na^+, right) for frequency 0.03 Hz, namely greater power in the combined Ca^{2+} and ATP pipette compared to the standard solution. However, the frequency ranges are very narrow compared to the frequency resolution. This makes the robust conclusions impossible.
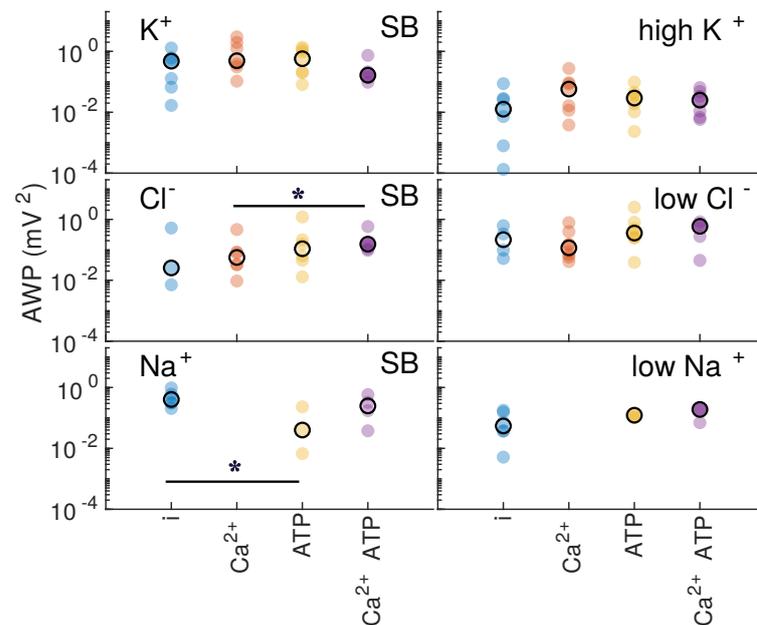
Figure 5.13: The averaged wavelet power (AWP) integrated over $8.33 \text{ mHz} - 3 \text{ Hz}$ for the K^+, Cl^- and Na^+ cohorts (in rows) and SB and non-SB in columns for different intrapipette solutions marked with colours: standard (i), Ca^{2+}, ATP and combined Ca^{2+} and ATP. Each semi-transparent dot represents a different cell. The black circles indicate the median values in each group. The significant values are marked with bars and stars. In the SB and the Cl^- cohort the AWP was significantly lower in the Ca^{2+} pipette than in the Ca^{2+} and ATP. In the SB and the Na^+ cohort the AWP is significantly smaller with additional ATP inside, when compared to standard intrapipette solution. Note, however, that the results are based on only 3 recordings.
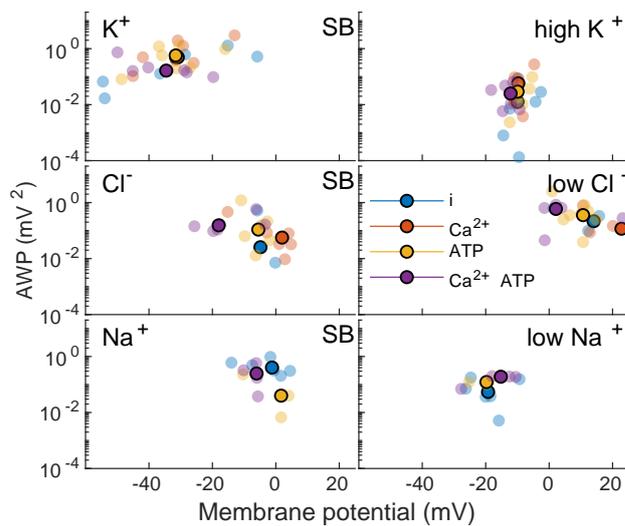
(a)
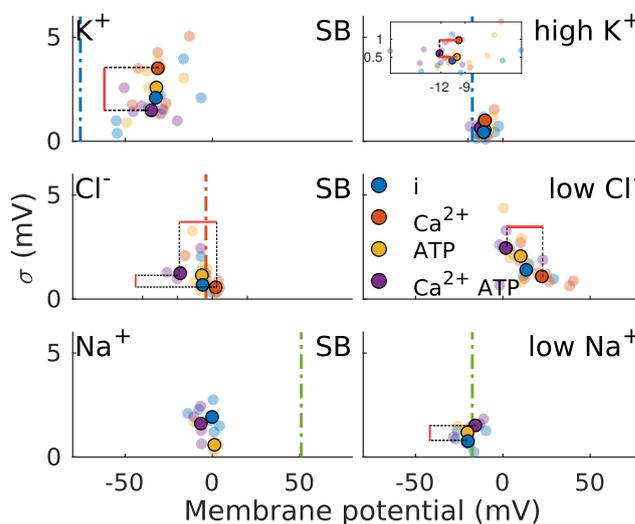
(b)

Figure 5.14: The effect of different intrapipette solutions on the membrane potential and fluctuations measured as a) averaged wavelet power and b) standard deviations. On the vertical axis (a) averaged wavelet power (AWP) integrated over $8.33 \text{ mHz} - 3 \text{ Hz}$, (b) standard deviations (σ). On the horizontal axis the membrane potentials for the K^+, Cl^- and Na^+ cohorts (in rows) and SB and non-SB in columns. Different intrapipette solutions are marked with colours: standard i, Ca^{2+}, ATP, Ca^{2+} and ATP. Each semi-transparent dot represents different cell, and the opaque circles the median values in each group. (a) The significant comparisons of AWPs are marked in Fig. 5.13: the only significant difference that contained a minimum of 4 datasets was in the SB, the Cl^- cohort: the AWP was significantly lower in Ca^{2+} pipette than in combined Ca^{2+} and ATP. (b) The significant differences are marked with continuous red bars, horizontal in membrane potentials and vertical in standard deviations. 7 significant changes can be observed (see the main text for the details). The dash-dotted vertical lines indicate Nernst potentials of the dominant ions, K^+ (blue), Cl^- (orange) and Na^+ (green).

5.4.3   Particular frequency bands

In this part the collective results of the time-averaged wavelet power (TAWP) computations are presented. Only the cells with successful recordings in both SB and non-SB are shown. Here, particular attention is paid to the distribution of power across the frequencies, rather than the total power, that is discussed in Sec. 5.4.1, and in Fig. 5.9. Fig. 5.15 presents the time averaged wavelet power (TAWP) in all three cohorts: (a) K^+, (b) Cl^-, (c) Na^+. The peaks are clustered around different frequencies 0.01 Hz, 0.03–0.1 Hz and 0.1–0.5 Hz. However, the presence and the exact positions of the peaks is cell dependent, rather then forced by any particular external factor.

| **(a)** K^+ cohort | **(b)** Cl^- cohort | **(c)** Na^+ cohort |
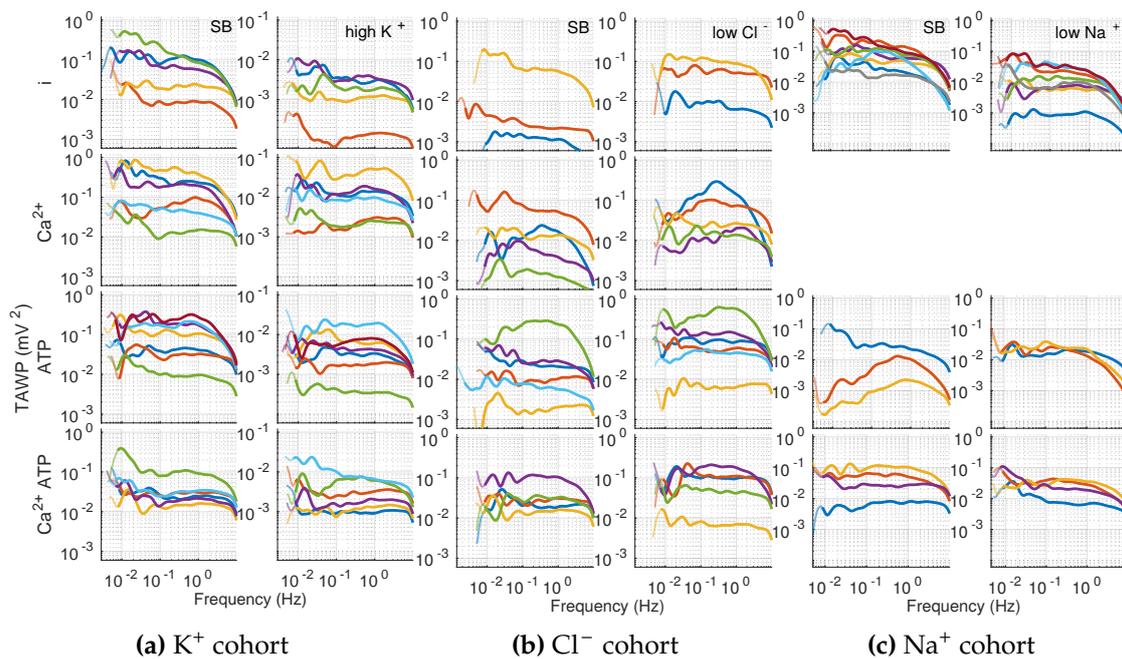
Figure 5.15: Time averaged wavelet power (TAWP) of all three cohorts: (a) K^+, (b) Cl^-, (c) Na^+. In each cohort, given the same intracellular solution, the lines in the same colour correspond to the same cell, in different intracellular solutions, to the different cells. The opaque parts of TAWP correspond to the frequencies where a sufficient length of recording was available, enabling to analyse at least 3 cycles. The transparent ones, presented for an informative purpose, where between 1 and 3 cycles of oscillations were available. Occurrence and the exact positions of the peaks are cell dependent rather then forced by any particular external factor. Oscillations could be clustered in three bands around 8.7 mHz–0.02 Hz, 0.03–0.1 Hz and 0.1–0.5 Hz.

5.4.4 Perforated patch-clamp – smooth muscle cell

In this section the recording of the membrane potential using the free-running voltage perforated whole-cell patch-clamp technique is analysed. Fig. 5.16 illustrates the membrane potential (MP), the amplitude of the wavelet transform $|W(f,t)|$ and the time-averaged wavelet power (TAWP) of a smooth muscle cell for two different frequency resolutions, σ. The intermittent line indicates -74 mV, the Nernst potential for K^+. The membrane potential exhibits strongly non-stationary behaviour. After initial 10 min it drops below the Nernst potential for K^+, then its average value stays relatively constant at the very negative value for about 30 min. This is followed by the slow drift of the membrane potential towards less negative values for about next 20 min. The fluctuations cease with time. The wavelet analysis reveals several components of the membrane potential oscillations. Particularly strong is intermittent activity around 8 mHz, appearing in a time-localised manner around 4, 11, 27 and 38 min lasting between 3-6 min each. The occurrence of the oscillations seems to be accompanied by a decrease in the membrane potential. Higher frequency oscillations, e.g. 0.03, 0.05 or 0.09 Hz exhibit a similar time-localised behaviour.
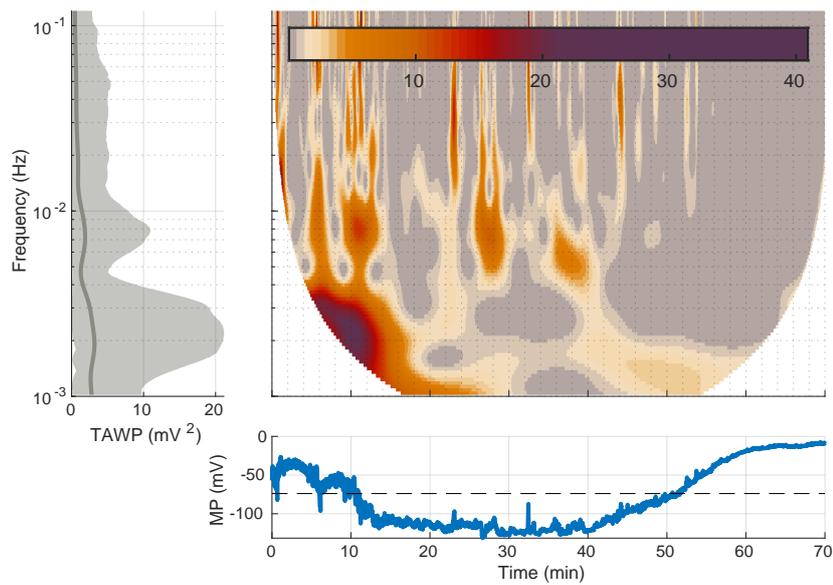
(a) $\sigma = 0.5$
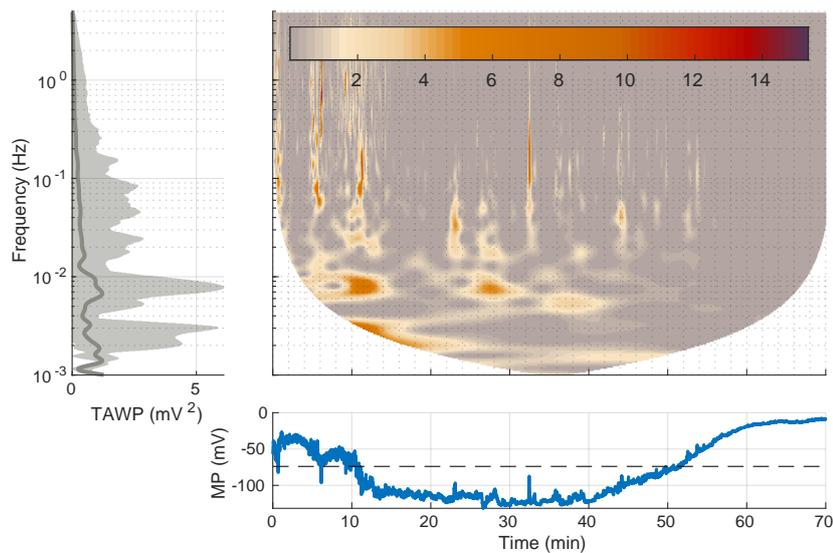
(b) $\sigma = 2$

Figure 5.16: Recordings of the free-running voltage with the perforated whole-cell patch-clamp technique applied to a smooth muscle cell, the amplitude of its wavelet transform $|W(f,t)|$ and time-averaged wavelet power (TAWP) with two different wavelet frequency resolutions, a) $\sigma = 0.5$ and b) $\sigma = 2$. The intermittent line corresponds to the K^+ Nernst potential (for pipette and extracellular bath solutions). The average MP goes far below the passive transport limit, which is the Nernst potential for K^+ (-74 mV). The grey, shaded area indicates clear intermittent activity at around 8 mHz, particularly visible in (b). Particularly well time-localised in (a), peaks appear around 4, 11, 27 and 38 min and last between 3-6 min each. There is a tendency for the frequency to decrease, and eventually the oscillations disappear at around 45 min. The occurrence of the peaks is always accompanied by a decrease in membrane potential and the decline with the slow drift of the membrane potential towards less negative values. Better frequency localisation and an adjusted frequency scale allow for better identification of higher frequency components, e.g. 0.03, 0.05 or 0.09 Hz appearing intermittently.

5.5 Discussion

The fluctuations and oscillations in the membrane potential of Jurkat cells and a smooth muscle cell were analysed. The oscillations appear intermittently. Therefore it is reasonable that temporal dynamics is explicitly considered, as opposed to the approach used earlier [47]. On the shorter time scales, the free-running membrane potential of T cells and its responses to various stimuli were also studied in the early 1990s [160]. However, to my knowledge, the free-running membrane potential has not been studied on the longer time scales, using time-frequency representations. The discussion is structured in a following way: in Sec. 5.5.1 the effect of alteration of the extracellular concentrations is discussed, in Sec. 5.5.2 the effect of intracellular Ca^{2+} and ATP is considered. Finally, in Sec. 5.5.3 the oscillations in the membrane potential of smooth muscle cell are discussed.

5.5.1 Alteration of the extracellular concentrations

Alteration of the extracellular concentrations in standard pipette

In the first part of the experiment (results presented in Sec. 5.4.1) the extracellular concentrations were modified. The membrane potentials of the same cells were analysed in both standard and non-standard extracellular conditions and standard intrapipette solutions. Alteration of the extracellular concentrations significantly changed the membrane potential (where at least 4 datasets were available). The direction of the change in the average value of the membrane potential caused by alteration of the extracellular concentration is consistent with the one predicted by Goldman-Hodgkin-Katz equation. Tab. 5.5 shows the relative values of permeabilities p, calculated using GHK equation and the averaged values of the membrane potential in two experimental conditions. The analysis shows that $p_K > p_{Cl} > p_{Na}$. Positive values of permeability exist in each case except in the K^+ cohort, where the Na^+ permeability was slightly negative $\simeq -0.01$, so that 0 was later assumed. The values of permeabilities were assumed identical for SB and non-SB, which is most likely not the case in reality. However, importantly, regardless of the cohort, always $p_K > p_{Cl} > p_{Na}$. The Jurkat cells in this experiment can undoubtedly be considered K^+ dominant, as pointed out in [39, 70]; nevertheless the other permeabilities should not be ignored.

In an earlier study, an increase in the extracellular K^+ was reported to increase the cellular volume and depolarise the membrane [270]. Altering the extracellular concentration shifts the Nernst potential, as indicated by Fig. 5.5. Increasing the concentration of K^+ or decreasing the concentration of Na^+ brings all the Nernst potentials closer together, and thus decreases the currents and correspondingly the fluctuations in the membrane potential. Reducing the passive ionic flow, would intuitively be expected to reduce the burden on active transport, that tries to maintain

the concentrations gradients. Active transport works on timescales longer than passive transport [77]. The effect of different impact on different timescales can to some extent be observed in the time-averaged wavelet power, as shown in Fig. 5.3. In addition to there being a decrease in the amplitude of fluctuations in general, the power spectrum peak around 0.01 Hz present in the standard conditions, decreases relative to the others, when decreasing the driving force for passive transport of K^+ or Na^+.

The experiment with chloride is very interesting. Lowering the extracellular Cl^-, not only shifts the Nernst potential further apart from the ones of K^+ and Na^+, as can be seen in Fig. 5.5, but also changes the direction of the chloride current from Cl^- influx into the cell for SB to Cl^- efflux out of the cell for low Cl^-. The chloride current is expected to increase and consequently so are the fluctuations. While in case of K^+ and Na^+ an uptake mechanism is straightforward, e.g. Na^+/K^+ pumps, in the case of chloride the situation may be less clear. Chloride transport is mostly involved in volume regulation, see Fig. 2.2. Lowering the extracellular concentration of Cl^- increases the efflux of Cl^-, and thus a decrease in the cellular volume should be expected [270], together with an increase in the membrane potential. This, in return, would activate the transporters involved in the volume regulations. On the other hand, one would expect activation of the mechanism bringing Cl^- back. One of the chloride uptake mechanisms is the $Na^+/K^+/2Cl^-$ co-transporter, NKCC1, transporting Na^+, K^+ and $2\,Cl^-$ into the cell. The transport stays electroneutral. However, it contributes to the total flux, and thus fluctuations in the membrane potential. In this experiment a general membrane potential depolarisation and an increase in the fluctuations can be observed, Fig. 5.9.

cohort	p_K	p_{Cl}	p_{Na}	SB V_m (mV)	non-SB V_m (mV)
K^+	1	0.51	0.00	-24.4	-11.0
Cl^-	1.03	1	0.84	-2.6	15.7
Na^+	1.72	1.30	1	-6.2	-19.5

Table 5.5: The relative values of permeabilities for K^+, Cl^- and Na^+ calculated using the Goldman–Hodgkin–Katz equation and the median of the membrane potential averages from the SB and non-SB experiments. The values of permeabilities were assumed identical for SB and non-SB, which is most likely not the case in reality. However, the model shows the possible values of permeabilities to reproduce the averaged values of the membrane potential. Regardless of the cohort, always $p_K > p_{Cl} > p_{Na}$. This confirms the dominant K^+ permeability.

Alteration of the extracellular concentrations given the intracellular Ca^{2+} and ATP

The quantitative effect of the alteration of the extracellular solutions on the membrane potential and its fluctuations, measured as the AWP is similar in the cases of standard and non-standard pipette, summarised in Fig. 5.9. In the Ca^{2+} pipette, the oscillations around 0.3 Hz in the dataset presented in Fig. 5.6 are slightly enhanced

by low Cl^-. Low Cl^- depolarises the membrane and possibly membrane depolarisation could be considered as one potential mechanism to enhance these oscillations – what will be discussed later, in Sec. 5.5.2 again. In the ATP pipette, the variance of the TAWP, among all three datasets, in low Na^+ is smaller than in SB. Nevertheless, robust conclusions require larger number of recordings on different cells in this group. In 2 out of 3 datasets, the oscillations around 0.3 Hz appear present in the SB, disappear in low Na^+. In the SB the membrane potential has a value above 0 mV and becomes negative in low Na^+: this could be potentially related to the oscillations cessation. No robust and consistent changes are observed in the wavelet power distribution across the frequencies caused by increasing the concentration of K^+ nor by decreasing the concentration of Na^+ or Cl^-.

5.5.2 The effect of different intrapipette solutions with Ca^{2+} or ATP or both Ca^{2+} and ATP

Ca^{2+} pipette In the Ca^{2+} pipette, and Cl^- cohort the oscillations around 0.3 Hz can be identified, as presented in Fig. 5.6. This can be to some extent observed in the other datasets too. The oscillatory frequency of Ca^{2+} oscillations can vary from tens of Hz in neurons to tens of mHz in non-excitable cells [31]. Ca^{2+} is also known to rather oscillate with a very specific frequency dependent on the function of these oscillations, spanning from 0.1 mHz to 100 Hz [224], and elongated periods of its elevated concentration are dangerous [23, 24]. Ca^{2+} is known to have an inhibitory effect on the sodium pump [34] and metabolism [237]. The oscillations were not visible in the K^+ cohort. The oscillatory bursts are either the effect of depolarisation of the membrane potential with elevated intracellular Ca^{2+} or/and additional transporters. Cells with dominating Cl^- permeability may additionally posses Ca^{2+}–activated chloride channels [22]. Nevertheless, in all the experiments intrapipette Ca^{2+} depolarised the membrane and in the Na^+ cohort, where the membrane potential was relatively high compared to the other cohorts, the experiment failed. Fig. 5.17 summarises the contribution of Ca^{2+} to the transport in Jurkat cells. The effect of the membrane potential depolarisation is dominant in the experiment – one possible explanation is Na^+/K^+ pumps blocking by intracellular Ca^{2+} [34, 237, 35]. Blocking of K_v channels by Ca^{2+} [33], is possibly stronger than activating K_{Ca} by Ca^{2+} (see Sec. 2.8.1) since otherwise, a decrease in the membrane potential would be observed. The intrapipette Ca^{2+} concentration (1000nM) was greater than 300nM reported as the effective saturation threshold for K_{Ca} channels [39]. However, figuring out the exact mechanism of the membrane potential depolarisation and generating the oscillations in the membrane potential in this experiment will require additional recordings with blocked K_{Ca} channels and Na^+/K^+ pumps.

ATP pipette Fig. 5.18 presents the effect of ATP in Jurkat cells. No substantial effect neither on the membrane potential nor on the fluctuations was observed in ATP pipette compared to the standard one.
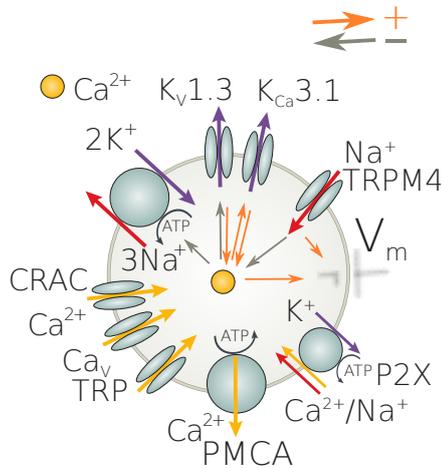
Figure 5.17: Ca^{2+} transport in Jurkat cells, independent of T cell activation. The positive (+) interaction are marked with orange, inhibitory (-) with grey. Interactions are either direct or indirect via membrane potential, by changing the driving force for Ca^{2+} (TRPM4, K_v, K_{Ca}). Ca^{2+} can enter the cell via CRAC channels, Ca_v but also by TRP (to smaller extent). All of those channels cause the depolarisation and further reduction in the driving force for Ca^{2+} entry. On the one hand depolarisation enhances the opening of K_v channels and increases the driving force for K^+, but on the other hand Ca^{2+} was reported to block them [33]. Intracellular Ca^{2+} was also reported to block Na^+/K^+ pumps [34, 237, 35]. The effect of blocking K_v channels and Na^+/K^+ pumps can be one possible explanation to depolarisation caused by intracellular Ca^{2+}. Ca^{2+} can be removed from the cell at the expense of ATP molecule via PMCA. For further details of the membrane transport in Jurkat cell see Sec. 2.8.

Ca^{2+} and ATP pipette The averaged membrane potential of the cells with intracellular Ca^{2+} and ATP was most hyperpolarised compared to any other intrapipette solution in all the cohorts in 5 out of 6 experiments available. The effect on the fluctuations may depend on the direction of shift from the Nernst potential of the dominant ion – in the K^+ cohort the fluctuations decrease, while in Cl^- they increase. The addition of ATP seems to not only overcome the Ca^{2+} effect of depolarisation, but also additionally to hyperpolarise the membrane. This can be explained by expelling Ca^{2+} at the expense of available ATP and consequently leading to decrease in the membrane potential. This hypothesis can be further tested in the experiment with blocking PMCA.
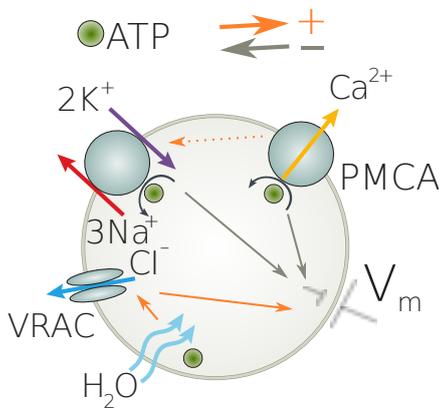
Figure 5.18: ATP involvement in Jurkat cells. ATP, by causing a rise in osmotic pressure, facilitates water entry to the cell [209, 39, 150]. As the water enters the cell, the cell's volume increases, activating further the VRAC channels and efflux of Cl^- ions. This leads to membrane potential depolarisation. ATP enables functioning of the Na^+/K^+ and PMCA pumps (both are fuelled by ATP) – both of them lead to decrease in the membrane potential, effectively transporting one positive ion out of the cell; see Tab. 2.2. Activating additional transporters would be expected to increase the total flux across the membrane and consequently increase the fluctuations.

5.5.3 The oscillations in the membrane potential

This work reports intermittent oscillations in the frequency around 0.008 Hz present in membrane potential recorded with the perforated patch-clamp technique, Fig. 5.16. Interestingly, oscillations in the free-running membrane potential do not last continuously but rather appear intermittently. Increase in the low frequency activity is typically accompanied by a decrease in the membrane potential. The membrane potential reaches very low values below -120 mV – much lower than the Nernst potential for K^+, namely -74 mV. Therefore it must be maintained by active transport, e.g. Na^+/K^+ pumps that utilise the ATP. There was no glucose in the extracellular solutions, therefore it would be expected that the intracellular ATP/ADP ratio dropped within few minutes, see Fig. 5.19. On the other hand, the intracellular concentration of ATP was reported to be saturating for Na^+/K^+ pumps activity [244]. No available glucose means a lack of the natural molecule to initiate metabolic reactions for over 1 h of the recordings (and preparation before). The origin of the very negative membrane potential (below K^+ Nernst potential) and the fact it was maintained for over 40 min without any extracellular glucose, and the origin of the oscillatory pattern require further investigations and more datasets. Other oscillations with frequency around 0.3 Hz appear mostly when the membrane is depolarised, and/or Ca^{2+} or ATP pipette. The effect is visible mostly in the Cl^- cohort, see Fig. 5.15. Earlier analysis of the membrane potential of T cells using the Fourier transform [47] did not report any oscillations around this frequency.

5.5.4 Models of the membrane potential and metabolism interactions

Metabolism and the membrane potential may interact in the various ways described in Chapter 2 and summarised in Fig. 2.8. The most straightforward way is to consider Na^+/K^+ pumps as a direct link between metabolism and the membrane potential. In this experiment the possible scenarios of interactions are:

1. **ATP is fully available.** The pumps are not limited by the availability of ATP and function according to their own rhythm which could possibly have some preferred frequencies. This scenario is present in the experiment with intrapipette ATP. The comparisons of the time-averaged wavelet power for standard and ATP intrapipette solutions did not show any statistically significant differences in any of the frequency bands that were considered. The results are shown in Figs. 5.10(b), 5.11(b) 5.12(a). There are three possibilities: either the intrapipette ATP does not change the fluctuations nor TAWP, or intrapipette ATP was not fully available for the cell in the experiment with an increased concentration of ATP, or ATP was fully available in standard pipette experiment.

2. Another possibility is that **the low availability of ATP limits the Na^+/K^+ pumping rate.** This means that the pumps follow the dynamics of ATP. Intracellular ATP can be either produced in a periodic way, for example by following
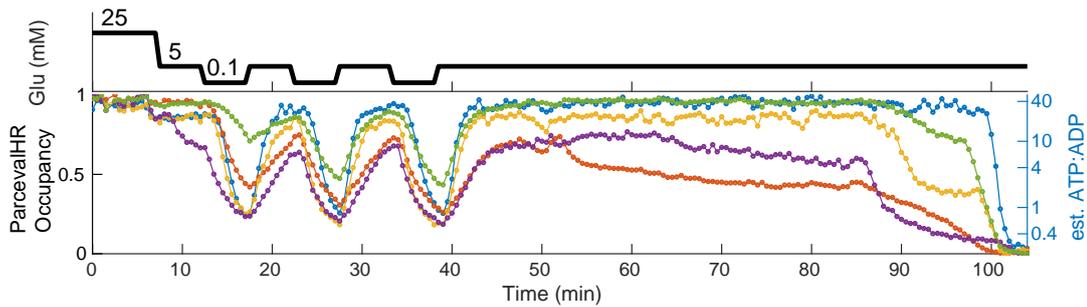
Figure 5.19: Availability of glucose strongly influences the intracellular ATP/ADP ratio. The upper plot presents the externally adjusted dynamics of the glucose in time and the lower plot shows ParcevalHR sensor occupancy that allows one to estimate ATP:ADP ratio. PercevalHR is an optimized genetically encoded fluorescent biosensor, that senses the ATP:ADP ratio [240]. Each colour represents recording from different astrocyte cell. Circles correspond to measurement points. The data show that drop in the extracellular glucose concentration may result in drop of ATP/ADP ratio even 100 times only in few minutes. Data adapted from [240], for the exact details see the paper and Fig. 3. I am sincerely grateful to Prof. Gary Yellen for sharing the data together with his useful suggestions.

the metabolic frequency (glycolytic or mitochondrial oscillations [142, 9, 136, 137]), or with the fluctuations without any particular frequency preference. In the first case the periodic hyperpolarisation in the membrane potential will be observed. This can clearly be observed in the recordings of the smooth muscle cell (SMC) membrane potential. To support this hypothesis, the limited availability of glucose was reported to decrease the frequency of ATP/NADH oscillations [190]. In the SMC experiment, where the extracellular glucose was not available, one can observe the tendency of the membrane potential oscillations around 8 mHz to decrease and eventually disappear. In the latter scenario, where ATP does not follow any particular frequency, no clear membrane hyperpolarisation events would be present. This scenario is possible in the Jurkat cells experiment, where 10 mM of extracellular glucose was available. According to the results of [240], presented in Fig. 5.19, a concentration of 10 mM is sufficient to avoid the big drops in ATP/ADP ratio.

3. **The intracellular ATP is not available at all.** The pumps are not functioning and only passive transport is present. This scenario can only be investigated by for example investigating the effect of blocking the pumps with ouabain [90] and/or the metabolism with oligomycin [195] on the membrane potential.

5.6 Summary

This work is the first to investigate the dynamics of the free-running membrane potential of non-excitable cells over a time series of at least 8 min with a method explicitly addressing the temporal variability – the wavelet transform. Oscillations present in the membrane potential appear in the intermittent regime and may easily be overlooked when not taking temporal behaviour into account. This work reports oscillations in the membrane potential of the frequency around 0.008 Hz, strongly visible in the dataset recorded with a perforated patch-clamp technique. In this experiment no extracellular glucose was available, therefore the possibility to obtain ATP was prevented by glucose exhaustion in a cell. Oscillations in the membrane potential mentioned before may be the result of a residual amount of glucose being available. In a living cell the membrane potential is continually perturbed by the changes in the extracellular concentrations. An important motivation in this work was to investigate how those changes influence the natural fluctuations in the membrane potential. In the Jurkat cell experiment the extracellular concentrations were changed – the direction of the change in the membrane potential is consistent with the GHK equation, $p_K > p_{Cl} > p_{Na}$, and the effect on the magnitude of fluctuations depends on whether the three Nernst potentials were brought closer or further apart. It is expected that bringing them closer will decrease the total current and therefore the fluctuations, and this is confirmed in the experiment. As the Nernst potentials were separated further from each other, one would expect that the total intensity of fluctuations in the membrane potential increased, and again this is observed experimentally. Interestingly, intracellular Ca^{2+} depolarised the membrane compared to any other intrapipette solutions as opposed to Ca^{2+} and ATP that make the membrane hyperpolarised.

5.7 Ideas for future work

In addition to all aforementioned ideas there are many additional avenues for future research. In particular, one should address the problem of the dynamical interactions between the membrane potential and metabolism. The three scenarios presented in Sec. 5.5.4 should be carefully investigated. Ideally, the interior of the cell should be kept intact to preserve mitochondria for further production of ATP. Note that this may not apply to cancer cells or red blood cells because they obtain their ATP through glycolysis. Therefore, the use of the perforated patch clamp technique instead of the whole-cell patch-clamp would allow the organelles to stay inside the cell. Possibly, the use of cell lines that are close to the natural human cells, rather than cancer (immortalised) cells could give a better understanding of a *living cell*. The following modifications in the free-running voltage experiment may shed new light on the problem:

- The question of putting the cell under stress-conditions or perturbing it should be precisely addressed. One possibility to achieve this is by altering the concentration in the opposite direction; rather than bringing the Nernst potentials closer, to separate them further apart (the opposite what was done in the K^+ and Na^+ experiments analysed here). Consequently the passive flow of ions will increase, thus possibly increasing the burden on the Na^+/K^+ pump and ATP demand. This perturbation could be a factor enhancing the coupling between metabolism and the membrane potential and could show how the dynamics of metabolism is reflected in the membrane potential. Possibly, the dynamics of the membrane potential would resemble that observed in the smooth muscle cell experiment.

- Another idea is to monitor simultaneously the dynamics of the membrane potential and the ATP/ADP ratio with perforated patch-clamp and fluorescence methods. Manipulating the amount of glucose allows one to influence the ATP/ADP ratio, which will further possibly influence the membrane potential. The intracellular fluctuations in the ATP/ADP ratio that are present under a fixed glucose concentration are most probably impossible to measure accurately with fluorescence methods due to the instrumental fluctuations. However, altering the extracellular glucose concentration may give measurable changes in ATP/ADP ratio, as shown in Fig. 5.19.

- Another option is to investigate the influence of temperature on the dynamics of the membrane potential. Temperature is known to have a strong effect on metabolism [82, 49, 183]. The effect of the temperature on the passive transport in the membrane potential is much smaller.

- A very important way of reducing the bias due to variability among different cells in the experiment with different intrapipette solutions would be using the pipette perfusion system [258]. This would allow one to directly investigate the effect of changing the intrapipette solution on each cell, which is not possible in the current data.

- Address explicitly the question: "how does the free-running membrane potential dynamics depend on time?", by having possibly the same group size recorded in standard conditions first and non-standard after and vice versa or repeating sufficiently long recordings several time without changing the conditions.

- Another future direction is to investigate the effect of blocking or slowing down/speeding up the Na^+/K^+ pumps, as described in [244] on the dynamics of the membrane potential. It would allow one to investigate whether the intermittent oscillations around 8 mHz are due to the activity of the pumps; in case they disappear after adding the blocker, this would favour the hypothesis that the pumps are responsible for generating the rhythm.

- An interesting insight may be also gained by the experimenting with red blood cells, as they obtain their energy entirely by glycolysis and do not posses mitochondria. Nevertheless, the earlier experiments with red blood cells using the patch clamp technique were reported to be unsuccessful [125].

Chapter 6

Membrane potential – Time-reversibility and bispectral analysis

6.1 Abstract

When investigating the dynamics of the time series, a natural step is to look for nonlinearities or higher order coupling between the signals or between the different timescales of the same signal. In the previous chapter the membrane potential recordings were analysed using wavelet transform in order to search for the oscillations. This chapter makes one step forward and uses the same recordings to search for nonlinearities. The fact that the data are univariate narrows down the possible choice of the methods. Here, the two types of nonlinearities were investigated: time-irreversibility (that implies nonlinearity) and nonlinearity present in the dynamical coupling between different oscillatory modes. To measure the first one, α that introduced in Sec. 3.3.1 was used. In order to investigate the latter one, bispectral analysis developed in Chapter 4 was applied.

The analysis of time-reversibility indicated that on timescales faster than 10 ms, the recordings indicated significant time-irreversibility. Moreover the majority of α values were positive which correspond to a steeper increase and smoother decrease in the time series.

Wavelet bispectral analysis allows for investigating coupling with relatively close frequencies. The general motivation in the experiment analysed here was understanding how metabolism may reflect in the dynamics of the membrane potential. That is why the low frequencies (<0.5 Hz) were of the main interest in the bispectral analysis. Many recordings indicated possible coupling/nonlinearity involving frequencies from the range 0.02–0.05 Hz. In majority of significant pairs one of the frequencies is within a range 0.04–0.05 Hz, and the other 0.1–0.4 Hz.

6.2   Introduction

Various cellular rhythms and their possible links to the membrane potential were reviewed in Chapter 2 and summarised in Fig. 2.8. Tab. 2.1 reviews the oscillations in the membrane potential recorded with electrophysiology techniques. Moreover, other coupling types were reported, e.g. between neurons and glia cells [6], cytosolic and mitochondrial calcium oscillations [206]. The particular role of feedback-loops in cellular oscillators has been stressed [88, 130, 181, 251]. The importance of coupling was also discussed in the context of electronic-neural cell interfaces, where strong coupling causes oscillation death [189]. Spontaneous membrane potential oscillations with a frequency spanning from 0.017 to 0.15 Hz measured with an electrophysiology method were reported in L cells [183, 184]. As a possible generator, the authors suggested metabolic processes: cyanide completely abolished the oscillators, moreover the oscillations were strongly dependent on temperature. More recently, the dynamics of oscillatory metabolism in β cells were investigated using fluorescence imaging, simultaneously with recording the membrane potential bursting using the perforated patch-clamp technique [167]. The authors reported that the Ca^{2+} entry into β-cells stimulates the rate of mitochondrial metabolism, accounting for the depletion of glycolytic intermediates during each oscillatory burst.

This work is the first to seek evidence for nonlinearities and higher-order coupling/interactions in the recording of the free-running membrane potential by using the time-reversibility measure and bispectral analysis. The recordings of the membrane potential indicated significant time-irreversibility on the timescales faster than 10 msec. Moreover, the majority of the significant values were positive, what indicates a relatively steeper increase, compared to a decrease in the time series on these timescales.

Bispectral analysis allows the inference of information from a single time series. However, without additional experiments, one can only guess the rhythms involved in creating the bispectral peaks. Many recordings indicated possible coupling/nonlinearity involving frequencies from the range 0.02–0.05 Hz. In majority of significant pairs one of the frequencies is within a range 0.04–0.05 Hz, and the other 0.1–0.4 Hz. However, the results should be considered with caution, because even the application of surrogates does not always guarantee the correct results, as discussed in Sec. 4.6.

6.3   Methods

6.3.1   Cells

Experimental details are described in Chapter 5. In this chapter the membrane potential of Jurkat cells (JC) from K^+ cohort in standard bath and standard intrapipette solutions, where at least 10 min was available (6 cells) and smooth muscle cell (SMC,

1 cell), as described in Sec. 5.3.1 were analysed. This subset of recordings was considered as the closest representative to the natural cell. In the time-reversibility analysis all the cohorts (i.e. K^+, Na^+ and Cl^-) in standard bath conditions and standard intrapipette solutions were analysed.

6.3.2 Preprocessing

The original time series were recorded with sampling frequency 20 kHz. All datasets used in analysis, except the time-reversibility analysis, were downsampled to 20 Hz, using the moving average filter described in Sec. 3.3.2, and de-trended, using the build-in MATLAB, `detrend` function, that removes the best straight-line fit from the data. The time series used for calculating time-reversibility were de-trended, then the IAAFT surrogates were generated, and later the original time series together with the surrogates were downsampled to the desired frequency Fs_{down}, used as a parameter. Reversing the operations of downsampling and generating the surrogates reduced the computational burden.

6.3.3 Time-reversibility

A very simple and powerful method to detect the nonlinearity is the test for time-reversibility, introduced earlier in Sec. 3.3.1 and initially defined in Eq. (3.6). The additional modification used in this chapter is

$$\alpha_{rev} = \frac{1}{N} \sum_{n=1}^{N-1} (s_{n+1} - s_n)^3 \times Fs^3. \tag{6.1}$$

In this section, α_{rev} is investigated as a function of sampling frequency Fs. Additional multiplication of α_{rev} by Fs^3 gives the numerical estimate of a third power of a first derivative on the timescale of $dt = 1/Fs$.

Parameter choice   As pointed out in [213], the timescale for time-reversibility α, Eq. (3.6), is an adjustable parameter that requires careful selection. Here, no prior assumptions about the dynamics were made. For each dataset, originally sampled with Fs = 20kHz, the signals were first de-trended and the end-points matched (as described in [141]). Then 39 IAAFT surrogates were generated and downsampled to the desired frequency Fs_{down} using a moving average filter. 8 values of the downsampling frequency were selected from the range 10 to 20 kHz. Values of α estimated from data that exceeded the extrema of the values estimated from surrogates were considered significant.

6.3.4 Wavelet analysis

Wavelet analysis is introduced and defined in Sec. 3.5.2.

6.3.5   Bispectral density

In this chapter the autobispectral density of the signal x averaged over time interval I is defined as

$$b^I_{\psi,xxx}(f_1, f_2) := \frac{1}{I} \int_I b_{\psi,xxx}(f_1, f_2, t)\, dt, \tag{6.2}$$

where $b_{\psi,xxx}$ is a bispectral density, as defined in Eq. (4.12), f_1, f_2 are frequencies, ψ wavelet function, t time. WIAAFT surrogates, described in Sec. 3.7.1, were applied.

Biamplitude and biphase

Following the idea introduced in [115], additionally biamplitude and biphase are introduced. The time-dependent autobiamplitude of a signal x is defined as

$$\mathbb{b}_{f_1,f_2}(t) = |b_{xxx}(f_1, f_2, t)|. \tag{6.3}$$

Here, $b_{\psi,xxx}$ is a bispectral density, as defined in Eq. (4.12), f_1, f_2 a frequency pair, t time, $|.|$ denotes the absolute value. The time-dependent autobiphase of a signal x is defined as

$$\Phi_{f_1,f_2}(t) = \text{unwrap}(\arg(b_{xxx}(f_1, f_2, t))). \tag{6.4}$$

Here, $\arg(.)$ denotes the argument of a complex number, and "unwrap" is an unwrapping function. If the biphase constant for several periods of the slower frequency, this indicates phase coupling [115]. However, it is not clear *how constant is constant?*. Therefore, an additional measure – minimum range of the biphase values R is introduced

$$R(i) = \min_{t_1} \left(\max_{|t_2-t_1| \leq iT_1} (\Phi_{f_1,f_2}(t_1) - \Phi_{f_1,f_2}(t_2)) \right). \tag{6.5}$$

Here, assuming that $f_1 \leq f_2$, then $T_1 = 1/f_1$ and i is the number of cycles of the oscillations of f_1. $\Phi_{f_1,f_2}(t)$ represents the biphase, and t is time. In other words $R(i)$ is the measure of the minimal range that the biphase values occupy given the number of cycles of slower frequency. The values obtained from the recordings are compared with the WIAAFT surrogates.

6.3.6   Parameter choice

Choice of a suitable frequency resolution for the wavelet transform (σ) was discussed in Chapter 5 and set to 0.5. Nevertheless, this choice is far from optimal for bispectral analysis. On the one hand having a lower σ allows one to investigate lower frequencies, but on the other it biases the results of bispectral analysis when frequency triplets ($f_1, f_2, f_1 + f_2$) are considered, as shown in Eq. (4.21). The equation was originally derived for fixed frequency components, yet the formula including frequency triplets is applied in a general case. So $\sigma = 3$ was selected. This is considered to be a relatively good compromise between frequency resolution and

time localisation, as discussed in Secs. 4.6.1 and 4.6.2, for signals with frequencies ranging from 0.02 to 0.2 Hz for time series of the length 10 min (JC) and from 0.005 to 0.2 Hz for 60 min (SMC). In order to allow for tracing the dynamics that generated the time-averaged bispectra, wavelet transforms using the same $\sigma = 3$ are also presented. Time windows of length 2 min were selected for the bispectral analysis of Jurkat cells and 10 min for smooth muscle cell. This allows one for having at least 2 cycles of the lowest possible frequency 0.02 Hz for JC, and around 3 cycles of 0.005 Hz for SMC. However, other choices of σ may also be justified.

The choice of the bispectral peaks that were further used for biphase/biamplitude analysis was rather heuristic. The bispectral peaks were considered significant, where the value of bispectral density exceeded the level indicated by the surrogates. Since there were very many values exceeding the threshold, only the peaks with the biggest integrals around them were selected. They may not be the unique ones corresponding to the meaningful coupling.

6.4 Results

This section is structured as follows: first, the results of time-reversibility analysis are presented in Sec. 6.4.1. The majority of the datasets indicated time-irreversibility on timescales faster than 10 milliseconds and the positive α values. Sec. 6.4.2 shows the bispectral analysis of Jurkat and smooth muscle cells.

6.4.1 Time-reversibility

This subsection presents the results of the analysis of time-reversibility (the method is described in detail in Sec. 3.3.1). Fig. 6.1 illustrates time-reversibility α in three cohorts (in consecutive rows) as a function of downsampling frequency Fs_{down}. The positive and negative values of alpha are separated: in the right and left column respectively. 39 IAAFT surrogates were used to indicate the minimum and maximum: the values exceeding extrema were considered significant. The majority of the significant values of α were observed on the timescales faster than 10 msec (downsampling frequency greater than 100 Hz). Fig. 6.2 illustrates the total number of significant values of α and its median value for each Fs_{down}. To indicate significant values 39 IAAFT surrogates were generated. Very few significant values were present for Fs_{down} smaller than 20 Hz. The majority of the α values were positive, except some cases in the Na^+ cohort, where also negative values were observed.

Fig. 6.3 shows an example of the membrane potential time series, presented on the timescales where α values were significant. The upper figure shows the histogram of $((s_{n+1} - s_n) \times Fs)^3$ values (which corresponds to α before an averaging). The maximum of the histogram corresponds to a positive α value, which is associated with a steeper increase and a relatively smoother decrease in the time series. The majority of values are cumulated around the mean value, however there are non-zero values in the tails of the distribution.
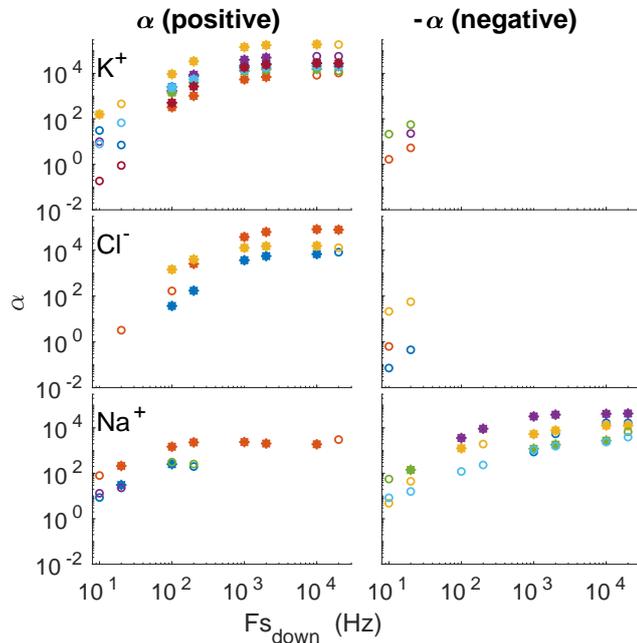
Figure 6.1: The membrane potential indicates time-irreversibility on short timescales. Time-reversibility α in three cohorts (in consecutive rows) is shown as a function of downsampling frequency Fs_{down}. The positive and negative values of alpha are separated: in the right and left column respectively. 39 IAAFT surrogates were used to indicate the minimum and maximum - significant values of α are marked with bold stars. Each colour indicates a different cell. As mentioned in Sec. 3.3.1, the time-irreversibility implies nonlinearity. The majority of the significant values of α are positive and appears on the timescales faster than 10 msec ($Fs_{down} \geq 100$ Hz), which coincides with the timescales of the order of few milliseconds.
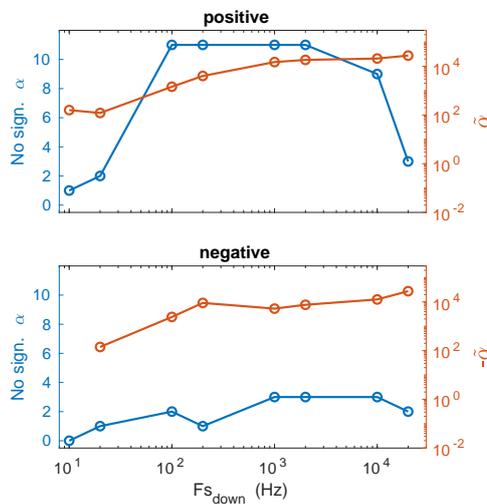
Figure 6.2: Time-reversibility for standard extracellular and intracellular solutions in three cohorts as functions of downsampling frequency Fs_{down}. There were 16 cells in total. The left axis (blue) illustrates the total number of significant values of α for each value of downsampling frequency Fs_{down}. Positive and negative values of α (or $-\alpha$, where α was negative) are presented in upper and lower plot correspondingly. The right axis shows the median value of α for the significant values only for each Fs_{down}. The number of significant values is rising with increasing Fs_{down}. For Fs_{down} greater than 100 Hz more than half of the cells indicate time-irreversibilty and positive α values, therefore implying nonlinearity on timescales faster than 10 milliseconds.

6.4.2   Bispectral analysis

Jurkat cells

Figs. 6.4, 6.7, 6.10, 6.13, 6.16, 6.19 show the analysis of six consecutive cells from the K^+ cohort in the standard bath using standard intrapipette solutions. Each figure consists of the time-averaged wavelet bispectral density, the windowed wavelet bispectral density, the 95th percentile of 19 WIAAFT surrogates, the amplitude of
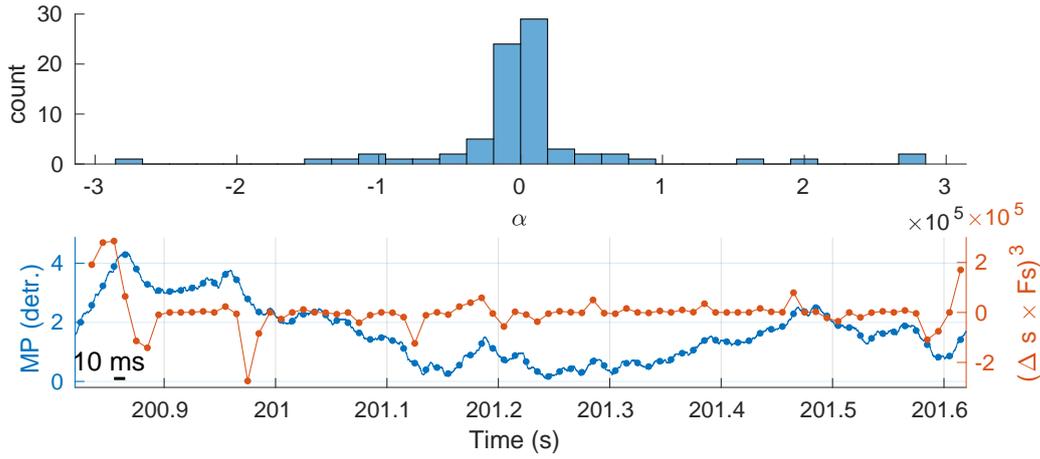
Figure 6.3: Example of a time series of the membrane potential, presented on the timescale of where α values were significant. The upper figure presents the histogram of $((s_{n+1} - s_n) \times \mathrm{Fs})^3$ values (marked in orange on the lower plot) for a segment of the time series downsampled to 100 Hz presented on the lower plot. The maximum of the histogram corresponds to a positive α value, which is associated with a steeper increase and relatively smoother decrease in the time series. The lower plot presents a segment of the membrane potential recording, with the markers placed every 10 msec on the left axis, and the corresponding value of $((s_{n+1} - s_n) \times \mathrm{Fs})^3$ on the right axis in orange.

the wavelet transform and the original dataset. For each cell the significant peaks were individually selected – the values of the integrals and the corresponding frequency pairs are presented in Tab. 6.1. Figs. 6.5, 6.8, 6.11, 6.14, 6.17 and 6.20 show the analysis of the time-dependent biamplitudes and biphases for each of the significant pair, together with the bispectrum and amplitude of the wavelet transform. In order to measure what *constant* means in terms of the dynamics of the biphases, the minimal range as defined in Eq. (6.5) together with WIAAFT surrogate testing was applied. Figs. 6.6, 6.9, 6.12, 6.15, 6.18, 6.21 show a minimal span, as a function of a number of cycles of the slower frequency. Fig. 6.25(a) shows the significant pairs of frequencies for all the analysed cells, significantly constant biphases, together with the membrane potential. There is no discernible trend, neither in the frequencies pairs, nor in the membrane potential. One observation can be made that the cells with the less negative membrane potential have more fluctuations and also significant bispectral peaks within the frequency range 0.02–0.05 Hz. The majority of the values with constant biphases are, where the lower frequency was not smaller than 0.04 Hz. This may be a bias introduced by an insufficient length of the time series for low frequencies, as discussed in [18].

Figure 6.4: Wavelet bispectral density for several time intervals with WIAAFT surrogates, the amplitude of wavelet transform and original time series for the recordings of membrane potential of cell 1. (a) Wavelet-bispectral density, $|b^I_{\psi,xxx}(f_1, f_2)|$, averaged over time 10 min; (b) 95th percentile of 19 WIAFFT; (c) wavelet-bispectral density after subtracting the surrogates; (d) wavelet bispectral density average over 2 min windows; (e) amplitude of wavelet transform (mV); (f) membrane potential, (mV). Upper colourbar has a units of mV^3 and relates to all the bispectra in the figure while the lower has a dimension of mV and relates to all the wavelet transform. The circles mark selected peaks that were significant, the values of their numerical integral can be found in the main text.

Figure 6.5: Wavelet bispectral density, the time-averaged wavelet power, wavelet transform, time-dependent biamplitudes and biphases for significant peaks, and original time series of the membrane potential of cell 1. (a) Wavelet autobispectral density, as defined in Eq. (6.2). Circles indicate the significant bispectral peaks, as explained in Fig. 6.4. Black circle corresponds to a pair (0.39, 0.05) Hz, and blue to (0.179, 0.044) Hz. (b) Time-averaged wavelet transform. Grey area indicate the values of wavelet power between 5th and 95th percentiles. Vertical lines indicate the frequency triplets $(f_1, f_2, f_1 + f_2)$ that generated the peaks in the bispectrum. Frequency triplets only to small extent coincide with the peaks in TAWP. (c) Amplitude of wavelet transform. Time-dependent (d) biamplitude, as defined in Eq. (6.3), (e) biphase, as defined in Eq. (6.4). The values of biamplitudes (d) change in time. For both pairs they are the lowest between 4-6 min of the recording. For a visual guideline in (f) grey, dashed lines in are drawn every 2π, and dots on the biphase appear once every period of the slow frequency. Biphases of both pairs of frequencies are relatively constant – several cycles of oscillations of the lowest frequency stays within 2π range. For a further analysis of the biphase see Fig. 6.6. (e) Original recording of the membrane potential.
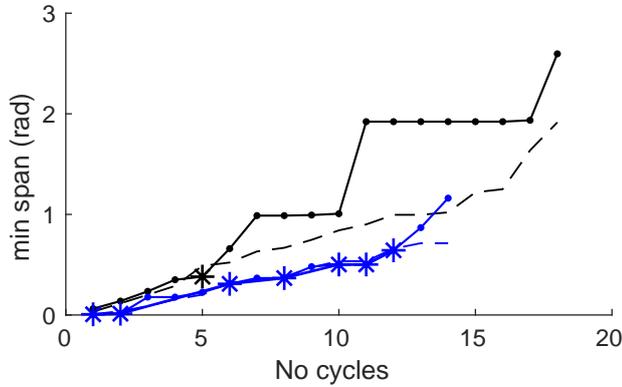
Figure 6.6: Minimal range/span of biphases as a number of cycles of lower frequency, as defined in Eq. (6.5) of the cell 1. Black curve corresponds to a pair (0.05, 0.39) Hz, and blue to (0.044, 0.179) Hz as shown in Fig. 6.5. Intermittent lines indicate the 5th percentile of 19 WIAAFT surrogates. Stars correspond to the significantly smaller values of the biphases. A biphase of a pair (0.044, 0.179, blue) Hz has significantly smaller range than the surrogates, up to 12 cycles of oscillations. A pair (0.05, 0.39) Hz – black, is significantly more constant for 5 cycles.
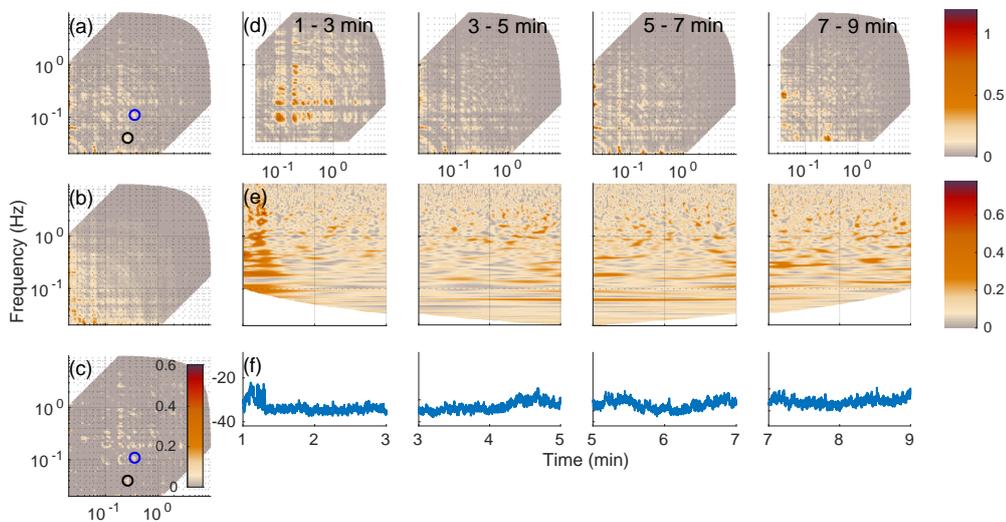
Figure 6.7: Wavelet bispectral density for several time intervals with WIAAFT surrogates, the amplitude of wavelet transform and original time series for the recordings of membrane potential of cell 2. Analysis analogous to the one presented in Fig. 6.4 for cell 2 (a) Wavelet-bispectral density, $|b_{\psi,xxx}^I(f_1, f_2)|$, averaged over time 10 min; (b) 95th percentile of 19 WIAFFT; (c) wavelet-bispectral density after subtracting the surrogates; (d) wavelet bispectral density average over 2 min windows; (e) amplitude of wavelet transform (mV); (f) membrane potential, (mV). Upper colourbar has a units of mV^3 and relates to all the bispectra in the figure while the lower has a dimension of mV and relates to all the wavelet transform. The circles mark selected peaks that were significant, the values of their numerical integral can be found in the main text.
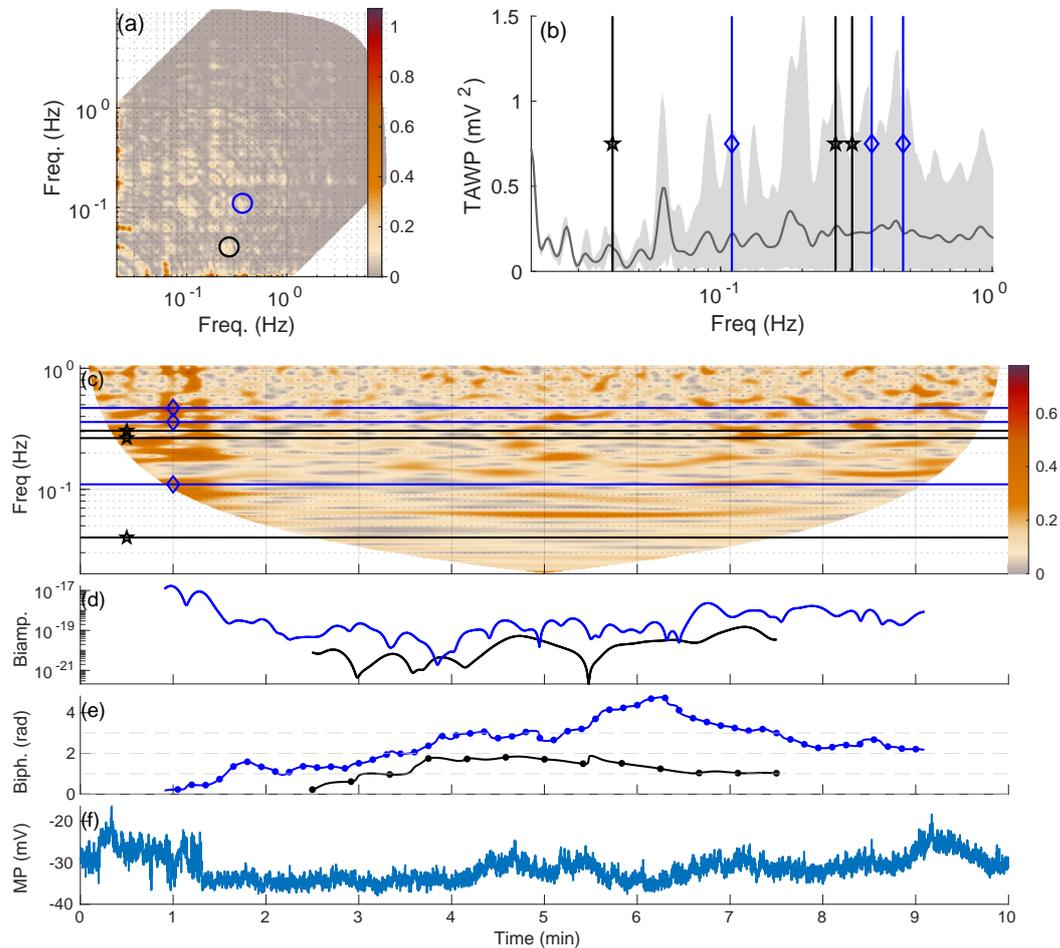
Figure 6.8: Wavelet bispectral density, the time-averaged wavelet power, wavelet transform, time-dependent biamplitudes and biphases for significant peaks, and original time series of the membrane potential of cell 2. (a) Wavelet autobispectral density, as defined in Eq. (6.2). Marked circles indicate the significant bispectral peaks, as explained in Fig. 6.7. Black circle corresponds to a pair (0.265, 0.04) Hz, and blue to (0.36, 0.11) Hz. (b) Time-averaged wavelet transform. Grey area indicate the values of wavelet power between 5th and 95th percentiles. Vertical lines indicate the frequency triplets $(f_1, f_2, f_1 + f_2)$ that generated the peaks in the bispectrum. (c) Amplitude of wavelet transform. Time-dependent (d) biamplitude, as defined in Eq. (6.3), (e) biphase, as defined in Eq. (6.4). The values of biamplitudes (d) change in time. High biamplitude of a pair (0.36, 0.11) Hz – blue, seems to coincide with the instability of the membrane potential around the first minute of the recording. For a visual guideline in (f) grey, dashed lines in are drawn every 2π, and dots on the biphase appear once every period of the slow frequency. Biphases of both pairs of frequencies are relatively stable – several cycles of oscillations of the lowest frequency stays within 2π range. For further analysis see Fig. 6.9. (e) Original recording of the membrane potential.
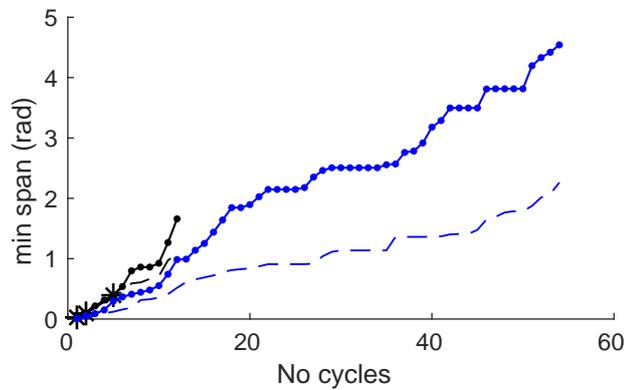
Figure 6.9: Minimal range/span of biphases as a number of cycles of lower frequency, as defined in Eq. (6.5) of the cell 2. Black curve corresponds to a pair (0.04, 0.265) Hz, and blue to (0.11, 0.36) Hz, as shown in Fig. 6.8. Intermittent lines indicate the 5th percentile of 19 WIAAFT surrogates. Stars correspond to the significantly smaller values of the biphases. The span of the biphase of a pair (0.04, 0.265, black) for 1, 2, 5 cycles is significantly smaller than the surrogates level. No significant differences in the biphase of (0.11, 0.36) Hz.
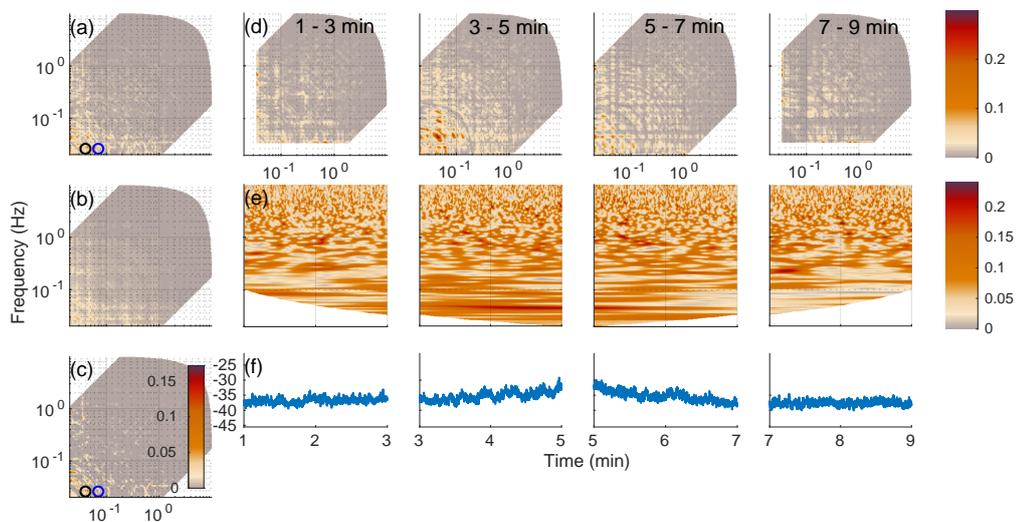
Figure 6.10: Wavelet bispectral density for several time intervals with WIAAFT surrogates, the amplitude of wavelet transform and original time series for the recordings of membrane potential of cell 3. Analysis analogous to the one presented in Fig. 6.4 for cell 1. (a) Wavelet-bispectral density, $|b^I_{\psi,xxx}(f_1, f_2)|$, averaged over time 10 min; (b) 95th percentile of 19 WIAFFT; (c) wavelet-bispectral density after subtracting the surrogates; (d) wavelet bispectral density average over 2 min windows; (e) amplitude of wavelet transform (mV); (f) membrane potential, (mV). Upper colourbar has a units of mV^3 and relates to all the bispectra in the figure while the lower has a dimension of mV and relates to all the wavelet transform. The circles mark selected peaks that were significant, the values of their numerical integral can be found in the main text.

Figure 6.11: Wavelet bispectral density, the time-averaged wavelet power, wavelet transform, time-dependent biamplitudes and biphases for significant peaks, and the original time series of the membrane potential of cell 3. (a) Wavelet autobispectral density, as defined in Eq. (6.2). Marked circles indicate the significant bispectral peaks, as explained in Fig. 6.4. Black circle corresponds to a pair (0.040, 0.026) Hz, and blue to (0.070, 0.026) Hz. (b) Time-averaged wavelet transform. Grey area indicate the values of wavelet power between 5th and 95th percentiles. Vertical lines indicate the frequency triplets $(f_1, f_2, f_1 + f_2)$ that generated the peaks in the bispectrum. (c) Amplitude of the wavelet transform. Time-dependent (d) biamplitude, as defined in Eq. (6.3), (e) biphase, as defined in Eq. (6.4). For a visual guideline in (f) grey, dashed lines are drawn every 2π, and dots on the biphase appear once every period of the slow frequency. The individual analysis of the biphases is presented in Fig. 6.12. However, for both biphases only three cycles were available. (e) Original recording of the membrane potential.
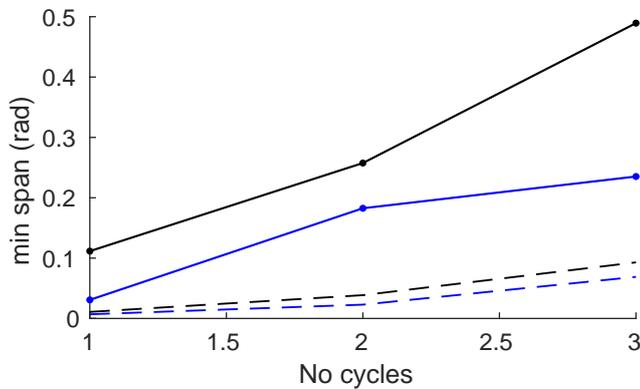
Figure 6.12: Minimal range/span of biphases as a number of cycles of lower frequency, as defined in Eq. (6.5) of the cell 3. Black curve corresponds to a pair (0.026, 0.040) Hz, and blue to (0.026, 0.070) Hz, as shown in Fig. 6.11. Intermittent lines indicate the 5th percentile of 19 WIAAFT surrogates. Stars correspond to the significantly smaller values of the biphases. No significant differences between the data and the surrogates in any of frequency pairs. However, there were only 3 cycles available.
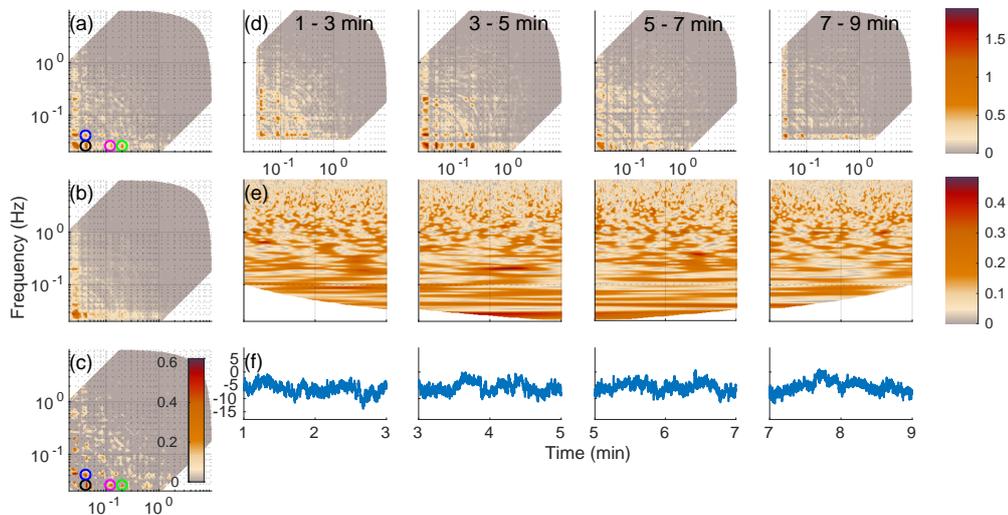
Figure 6.13: Wavelet bispectral density for several time intervals with WIAAFT surrogates, the amplitude of the wavelet transform and original time series of the recordings of membrane potential of cell 4. Analysis analogous to the one presented in Fig. 6.4 for cell 1 (a) Wavelet-bispectral density, $|b^I_{\psi,xxx}(f_1, f_2)|$, averaged over time 10 min; (b) 95th percentile of 19 WIAFFT; (c) wavelet-bispectral density after subtracting the surrogates; (d) wavelet bispectral density average over 2-min windows; (e) amplitude of wavelet transform (mV); (f) membrane potential, (mV). Upper colourbar has a units of mV^3 and relates to all the bispectra in the figure while the lower has a dimension of mV and relates to all the wavelet transform. The circles mark selected peaks that were significant, the values of their numerical integral can be found in the main text.

Figure 6.14: Wavelet bispectral density, the time-averaged wavelet power, wavelet transform, time-dependent biamplitudes and biphases for significant peaks, and original time series of the membrane potential of cell 4. (a) Wavelet autobispectral density, as defined in Eq. (6.2). Marked circles indicate the significant bispectral peaks, as explained in Fig. 6.4. Black circle corresponds to a pair (0.026, 0.041) Hz, blue (0.041, 0.041) Hz, magenta (0.026, 0.12) Hz, green (0.026, 0.2) Hz. (b) Time-averaged wavelet transform. Grey area indicate the values of wavelet power between 5th and 95th percentiles. Vertical lines indicate the frequency triplets $(f_1, f_2, f_1 + f_2)$ that generated the peaks in the bispectrum. (c) Amplitude of the wavelet transform. Time-dependent (d) biamplitude, as defined in Eq. (6.3), (e) biphase, as defined in Eq. (6.4). For a visual guideline in (f) grey, dashed lines are drawn every 2π, and dots on the biphase appear once every period of the slow frequency. A biphase of a pair (0.041, 0.041) Hz, blue, stays within very narrow range, less than π for all the 12 cycles available. However, significance analysis is presented in Fig. 6.15. (e) Original recording of the membrane potential.
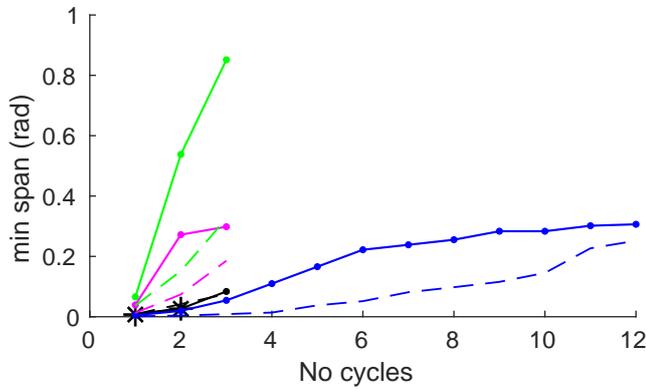
Figure 6.15: Minimal range/span of biphases as a number of cycles of lower frequency, as defined in Eq. (6.5) of the cell 4. Black curve corresponds to a pair (0.026, 0.041) Hz, blue (0.041, 0.041) Hz, magenta (0.026, 0.12) Hz, green (0.026, 0.2) Hz. Intermittent lines indicate the 5th percentile of 19 WIAAFT surrogates. Stars correspond to the significantly smaller values of the biphases. All the biphases stay within narrow range, e.g. (0.041, 0.041) Hz, blue, stays within a range $\leq 0.8\pi$ for all 12 cycles available. However the values are not significantly different from surrogates. The only significant values of a span are for at most 2 cycles (black), therefore no conclusions are drawn.
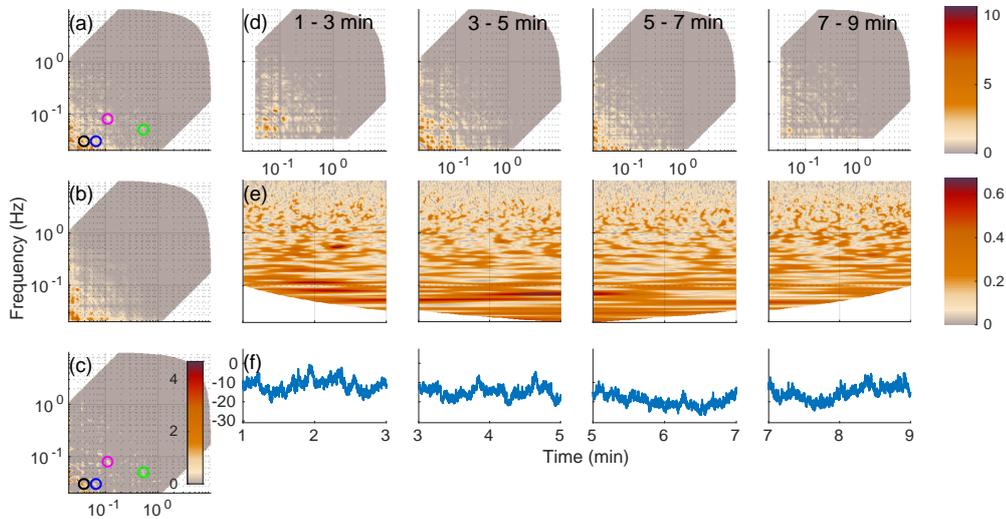
Figure 6.16: Wavelet bispectral density for several time intervals with WIAAFT surrogates, the amplitude of wavelet transform and original time series for the recordings of the membrane potential of cell 5. Analysis analogous to the one presented in Fig. 6.4 for cell 1. (a) Wavelet-bispectral density, $|b^I_{\psi,xxx}(f_1, f_2)|$, averaged over time 10 min; (b) 95th percentile of 19 WIAFFT; (c) wavelet-bispectral density after subtracting the surrogates; (d) wavelet bispectral density average over 2 min windows; (e) amplitude of wavelet transform (mV); (f) membrane potential, (mV). Upper colourbar has a units of mV^3 and relates to all the bispectra in the figure while the lower has a dimension of mV and relates to all the wavelet transform. The circles mark selected peaks that were significant, the values of their numerical integral can be found in the main text.

Figure 6.17: Wavelet bispectral density, the time-averaged wavelet power, wavelet transform, time-dependent biamplitudes and biphases for significant peaks, and original time series of the membrane potential of cell 5. (a) Wavelet autobispectral density, as defined in Eq. (6.2). Marked circles indicate the significant bispectral peaks, as explained in Fig. 6.4. Black circle corresponds to a pair (0.030, 0.039) Hz, blue (0.030, 0.066) Hz, magenta (0.080, 0.110) Hz, green (0.050, 0.530) Hz. (b) Time-averaged wavelet transform. Grey area indicate the values of wavelet power between 5th and 95th percentiles. Vertical lines indicate the frequency triplets $(f_1, f_2, f_1 + f_2)$ that generated the peaks in the bispectrum. (c) Amplitude of the wavelet transform. Time-dependent (d) biamplitude, as defined in Eq. (6.3), (e) biphase, as defined in Eq. (6.4). For a visual guideline in (f) grey, dashed lines in are drawn every 2π, and dots on the biphase appear once every period of the slow frequency. Significance analysis of the biphases is presented in Fig. 6.18. (e) Original recording of the membrane potential.
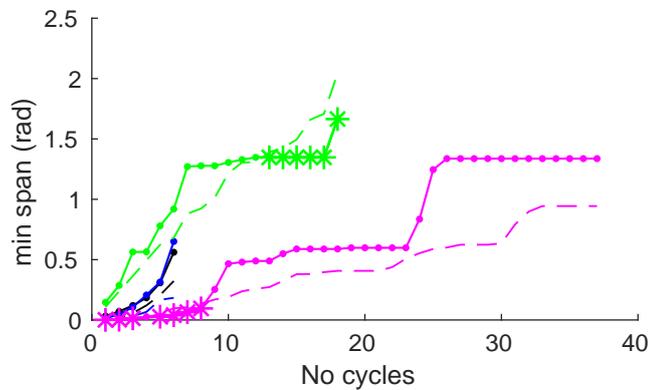
Figure 6.18: Minimal span of biphases as a number of cycles of lower frequency, as defined in Eq. (6.5) of the cell 5. Black curve corresponds to a pair (0.030, 0.039) Hz, blue (0.030, 0.066) Hz, magenta (0.080, 0.110) Hz, green (0.050, 0.530) Hz. Intermittent lines indicate the 5th percentile of 19 WIAAFT surrogates. Stars correspond to the significantly smaller values of the biphases. A biphase of a pair (0.080, 0.110) Hz, magenta, cover significantly smaller range for 1-3 and 5-8 cycles and biphase of a pair (0.05, 0.53) Hz, green, for 13-18 cycles.
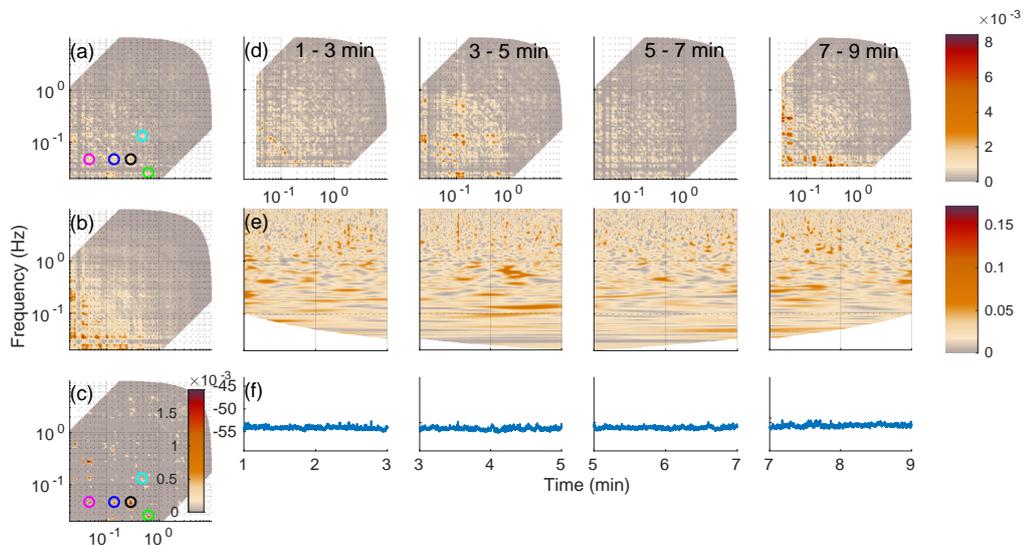
Figure 6.19: Wavelet bispectral density for several time intervals with WIAAFT surrogates, the amplitude of wavelet transform and original time series for the recordings of the membrane potential of cell 6. Analysis analogous to the one presented in Fig. 6.4 for cell 1. (a) Wavelet-bispectral density, $|b^I_{\psi,xxx}(f_1, f_2)|$, averaged over time 10 min; (b) 95th percentile of 19 WIAFFT; (c) wavelet-bispectral density after subtracting the surrogates. No significant peaks in bispectrum were present; (d) wavelet bispectral density average over 2 min windows; (e) amplitude of wavelet transform (mV); (f) membrane potential, (mV). Upper colourbar has a units of mV^3 and relates to all the bispectra in the figure while the lower has a dimension of mV and relates to all the wavelet transform. The circles mark selected peaks that were significant, the values of their numerical integral can be found in the main text.
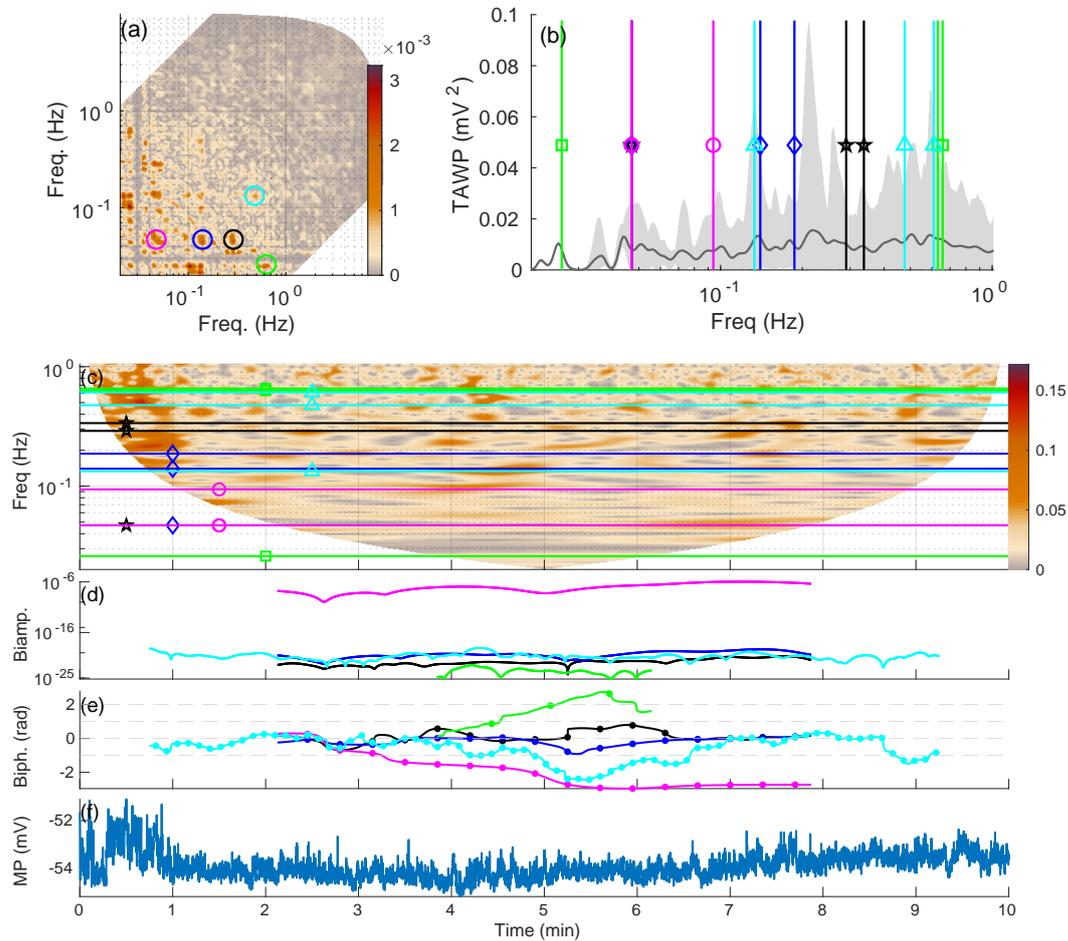
Figure 6.20: Wavelet bispectral density, the time-averaged wavelet power, wavelet transform, time-dependent biamplitudes and biphases for significant peaks, and original time series of the membrane potential of cell 6. (a) Wavelet autobispectral density, as defined in Eq. (6.2). Marked circles indicate the significant bispectral peaks, as explained in Fig. 6.4. Black circle corresponds to a pair (0.047, 0.290) Hz, blue (0.047, 0.140) Hz, magenta (0.047, 0.047) Hz, green (0.026, 0.631) Hz, and cyan (0.133, 0.476) Hz. (b) Time-averaged wavelet transform. Grey area indicate the values of wavelet power between 5th and 95th percentiles. Vertical lines indicate the frequency triplets $(f_1, f_2, f_1 + f_2)$ that generated the peaks in the bispectrum. (c) Amplitude of the wavelet transform. Time-dependent (d) biamplitude, as defined in Eq. (6.3), (e) biphase, as defined in Eq. (6.4). For a visual guideline in (f) grey, dashed lines in are drawn every 2π, and dots on the biphase appear once every period of the slow frequency. Significance analysis of the biphases is presented in Fig. 6.21. (e) Original recording of the membrane potential.
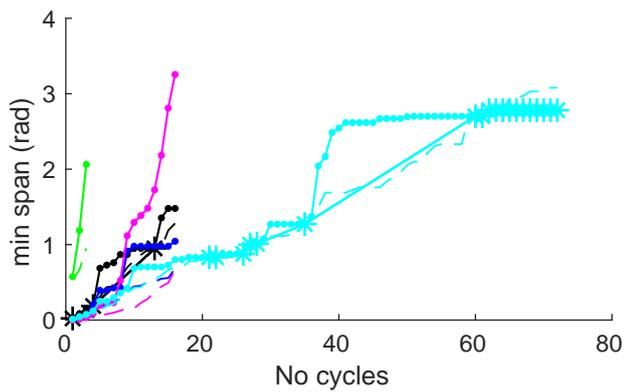
Figure 6.21: Minimal span of biphases as a number of cycles of lower frequency, as defined in Eq. (6.5) of the cell 6.   Black line corresponds to a pair (0.047, 0.290) Hz, blue (0.047, 0.140) Hz, magenta (0.047, 0.047) Hz, green (0.026, 0.631) Hz, and cyan (0.133, 0.476) Hz.   Intermittent lines indicate the 5th percentile of 19 WIAAFT surrogates. Stars correspond to the significantly smaller values of the biphases. A biphase of a pair (0.047, 0.290) Hz, black, covered significantly smaller range for 4 and 13 cycles and biphase of a pair (0.133, 0.476) Hz, cyan, for 21–28 and 60–72 cycles.

Smooth muscle cell

Fig. 6.22 shows the analysis of the recording of the membrane potential of a smooth muscle cell. Similar to Fig. 6.4 previously presented for JC, Fig. 6.22 consists of the time-averaged wavelet bispectral density, the windowed wavelet bispectral density, the 95th percentile of 19 WIAAFT surrogates, the amplitude of the wavelet transform and the original dataset. For each of the significant peaks – the corresponding frequencies and the values of the integrals are presented in Tab. 6.2. Fig. 6.23 shows the analysis of the time-dependent biamplitudes and biphases for each of the significant pair, together with the bispectrum and amplitude of the wavelet transform. The minimal range as defined in Eq. (6.5) together with WIAAFT surrogate testing was applied. Fig. 6.24 shows a minimal span, as a function of a number of cycles of the slower frequency. Fig. 6.25(b) shows the summary of the significant pairs of frequencies and significantly constant biphases. Numerical values of the integrals associated with peaks in the bispectrum of the SMC are much bigger than those in the JC bispectrum.
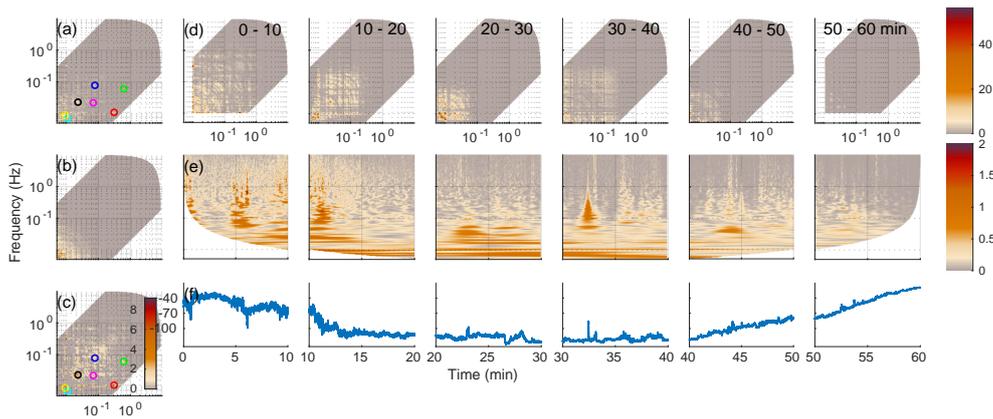
Figure 6.22: Wavelet bispectral density for several time intervals with WIAAFT surrogates, the amplitude of wavelet transform and original time series for the recordings of the membrane potential of a smooth muscle cell. (a) Wavelet-bispectral density, $|b^I_{\psi,xxx}(f_1, f_2)|$, averaged over time 10 min; (b) 95th percentile of 19 WIAFFT; (c) wavelet-bispectral density after subtracting the surrogates; (d) wavelet bispectral density average over 10 min windows; (e) amplitude of wavelet transform (mV); (f) membrane potential, (mV). Upper colourbar is has a units of mV^3 and relates to all the bispectra in the figure while the lower has a dimension of mV and relates to all the wavelet transform. The circles mark selected peaks that were significant, the values of their numerical integral can be found in the main text.
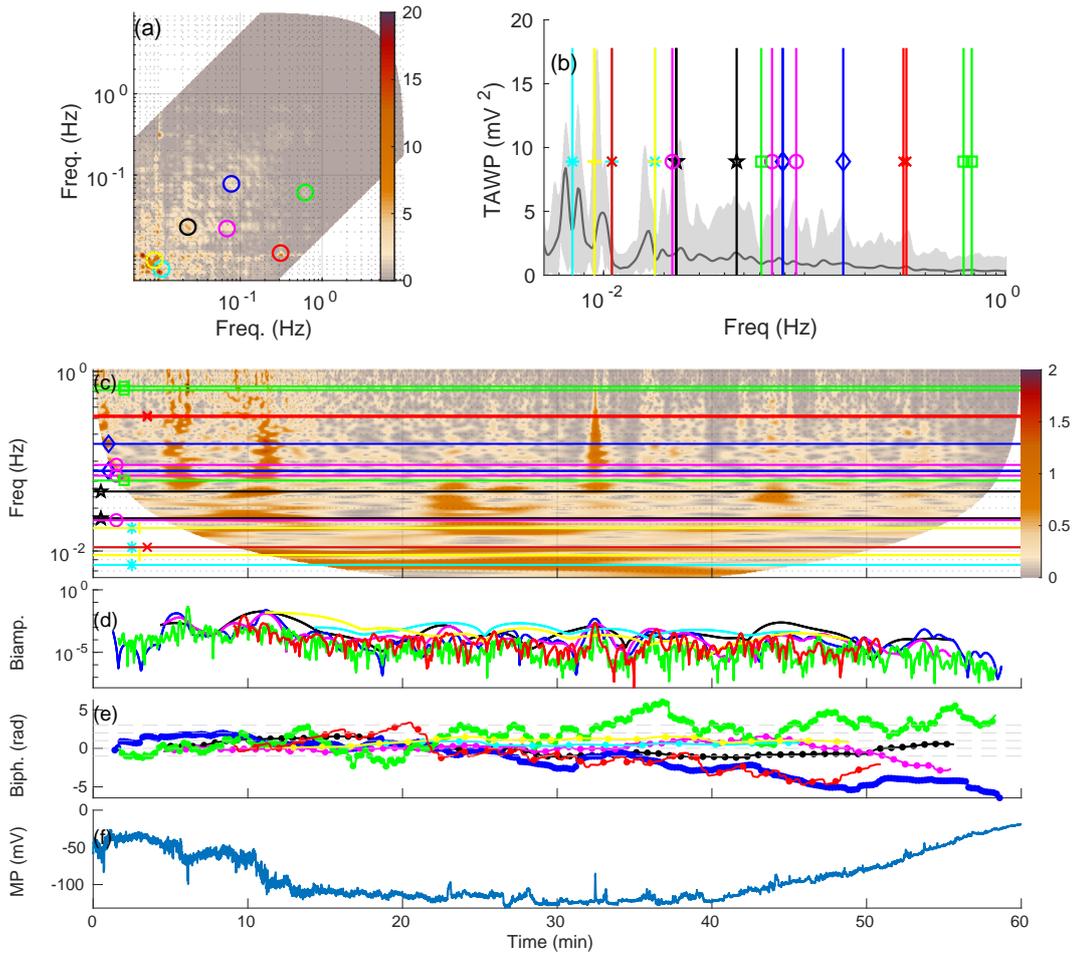
Figure 6.23: Wavelet bispectral density, the time-averaged wavelet power, wavelet transform, time-dependent biamplitudes and biphases for significant peaks, and original time series of the membrane potential of cell 1. (a) Wavelet autobispectral density, as defined in Eq. (6.2). Circles indicate the significant bispectral peaks, as explained in Fig. 6.22. For the exact values of frequencies see the main text. (b) Time-averaged wavelet transform. Grey area indicate the values of wavelet power between 5th and 95th percentiles. Vertical lines indicate the frequency triplets $(f_1, f_2, f_1 + f_2)$ that generated the peaks in the bispectrum. Frequency triplets only to small extent coincide with the peaks in TAWP. (c) Amplitude of wavelet transform. Time-dependent (d) biamplitude, as defined in Eq. (6.3), (e) biphase, as defined in Eq. (6.4). For a visual guideline in (f) grey, dashed lines in are drawn every 2π, and dots on the biphase appear once every period of the slow frequency. Biphases of both pairs of frequencies are relatively constant – several cycles of oscillations of the lowest frequency stays within 2π range. For a further analysis of the biphase see Fig. 6.24. (e) Original recording of the membrane potential.

cell	MP (mV)	I_{black}	I_{blue}	$I_{magenta}$	I_{green}	I_{cyan}
1	-28.6	$0.011e^{-0.182\pi i}$	$0.0067e^{0.073\pi i}$	-	-	-
2	-31.4	$0.008e^{0.085\pi i}$	$0.008e^{0.623\pi i}$	-	-	-
3	-36.5	$0.002e^{-0.057\pi i}$	-	-	-	-
4	-5.9	$0.032e^{-0.411\pi i}$	$0.021e^{0.989\pi i}$	$0.019e^{-0.151\pi i}$	$0.014e^{0.110\pi i}$	-
5	-15.2	$0.144e^{-0.615\pi i}$	$0.060e^{0.626\pi i}$	$0.047e^{0.222\pi i}$	$0.020e^{0.264\pi i}$	-
6	-53.9	$0.0001e^{0.195\pi i}$	$0.0001e^{0.065\pi i}$	$0.0001e^{0.586\pi i}$	$3.15 \times 10^{-5}e^{-0.515\pi i}$	$3.38 \times 10^{-5}e^{-0.0232\pi i}$

Table 6.1: The numerical values of the integrals around the peaks marked in Figs. 6.4–6.19(a) (before subtracting the surrogates). The greatest values of the integrals can be attributed to the cells with the least negative membrane potentials, e.g. -5.9, -15.2 mV.
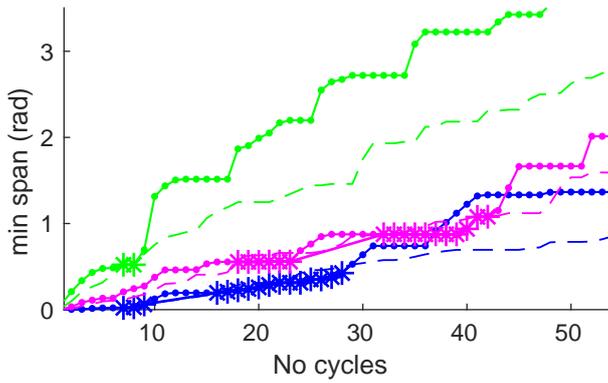
Figure 6.24: Minimal range/span of biphases as a number of cycles of lower frequency, as defined in Eq. (6.5) of the SMC. For transparency, only biphases that covered significantly smaller range are shown. Blue curve corresponds to a pair (0.078, 0.078) Hz, magenta to (0.069, 0.022) Hz and green to (0.620, 0.061) Hz as shown in Fig. 6.5. Intermittent lines indicate the 5th percentile of 19 WIAAFT surrogates. Stars correspond to the significantly smaller values of the biphases.

I_{black}	$0.3057e^{0.343\pi i}$
I_{blue}	$0.185e^{-0.465\pi i}$
$I_{magenta}$	$0.155e^{0.054\pi i}$
I_{green}	$0.061e^{-0.800\pi i}$
I_{cyan}	$0.385e^{0.405\pi i}$
I_{yellow}	$0.648e^{0.316\pi i}$
I_{red}	$0.130e^{-0.735\pi i}$

Table 6.2: The numerical values of the integrals around the peaks marked in Fig. 6.22(a) (before subtracting the surrogates). The average value of the membrane potential was around -90 mV.

(a) Jurkat cells   **(b)** Smooth muscle cell
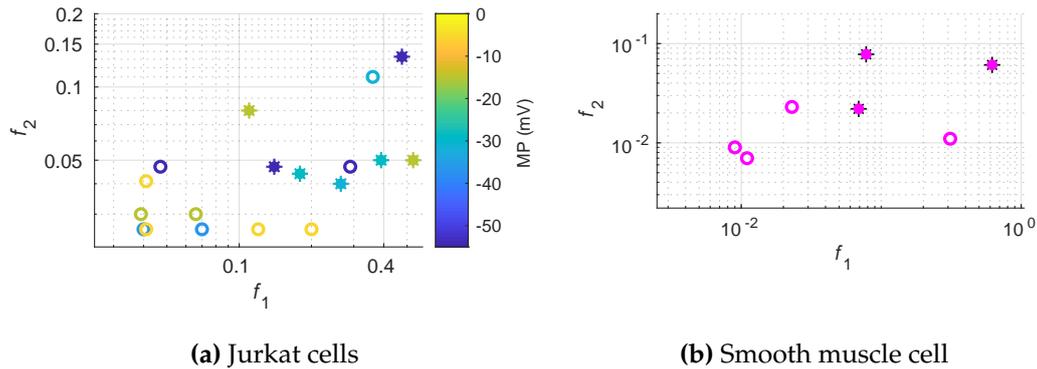
Figure 6.25: All significant pair of frequencies in the bispectrum for all the analysed cells. Asterisk (corona) markers correspond to the pairs of frequencies whose biphases covered significantly smaller range than the surrogates for at least 5 cycles of the slower frequency. The colours correspond to the value of the average values of the membrane potential. Majority of the values with significantly stable biphases, are where the lower frequency was not smaller than 0.04 Hz. Insignificance in the other cases may be an effect of insufficient length of the time series. The average values of the membrane potential for smooth muscle cell (b) was -90.0mV.

6.5   Discussion

6.5.1   Time-reversibility

On the timescales faster than 10 msec, the null hypothesis of the dynamics being time-reversible is rejected in the majority of the datasets. Time-irreversibility implies nonlinearity. Nonlinearity on the fast timescales will be expected from the kinetic-like dynamics of the membrane potential, proposed by Hodgkin & Huxley [100]. The majority of α values were positive, what is associated with a relatively steeper increase, and smoother decrease of the consecutive values. An example of this type of dynamics on timescales of 10 msec can be observed in the recordings of the K_v current in T lymphocytes using whole-cell patch clamp [39]. Very few significant values were present on timescales slower than 10 msec. To my knowledge, this work is first to seek evidence for time-irreversibility in recordings of the membrane potential.

This work is the first one to present analysis of the free running membrane potential in Jurkat cells, using bispectral analysis. Introduced in Chapter 4, bispectral density together with surrogate testing was applied to the recordings of the membrane potential. The proof of concept of application of the bispectral analysis (including bispectral density) to real data is presented.

The majority of the datasets indicated significant peaks in the bispectrum, suggesting possible higher order coupling or nonlinerities, etc. on the timescales around 0.026 – 0.4 Hz, yet the exact values are subjected to intercellular variability. It is not clear what may be causing it. The majority of the time series did not indicate significant time-irreversibility on these timescales. Therefore if dynamics is nonlinear, then time-reversible.

In majority of significant pairs one of the frequencies is within a range 0.04–0.05 Hz, and the other 0.1–0.4 Hz. The first one falls within a range 0.017–0.15 Hz of reported earlier frequency of oscillations in the membrane potential of in L cells recorded with electrophysiology techniques [183, 184]. Authors suggested cellular metabolism as a possible origin of those oscillations, because of very high sensitivity to temperature. However, in this experiment, one can only guess the possible origin.

Another cluster of significant frequencies can be indicated around 0.02–0.03 Hz, however the biphases did not occupy significantly different range than the surrogates. This can be due to insufficient number of cycles for this range. Frequencies 0.02 and 0.04 Hz may represent the harmonics of the same nonlinear oscillations.

Longer time series will be needed to investigate the frequency 0.0038 Hz reported more recently in the dynamics of the membrane potential of β cells recorded with patch clamp technique and metabolic oscillations recorded with fluorescence methods [167]. This is particularly so, when it comes to bispectral analysis.

Larger numerical values of the integrals associated with peaks in the bispectrum of the SMC compared to the JC are an effect of bigger fluctuations (measured as standard deviation).

6.6 Summary

This work is the first one to seek evidences for nonlinearities and higher-order coupling in the recording of the free-running membrane potential by using the time-reversibility measure and bispectral analysis. The analysis indicated time-irreversibility on the short timescales, precisely shorter than 10 msec and nonlinerities/coupling on longer timescales, precisely 0.026 – 0.4 Hz using bispectral analysis. Interestingly, the type of nonlinearity on the longer timescales did not indicate time-irreversibility.

This chapter presents an application of the bispectral analysis to the recordings of the membrane potential. The results represent a proof of concept for the application of the bispectral analysis (including bispectral density) to real data. Many recordings indicated possible coupling/nonlinearity. However, the results should be considered with caution, because even an application of surrogates does not always guarantee the correct results, as discussed in Sec. 4.6.

Chapter 7

Concluding remarks

7.1 Conclusions

The work presented in this thesis aims at improving the understanding of the nature of the continuous membrane potential fluctuations in biological cells. To achieve this, initially, the origin of the membrane potential is explained – seen as a consequence of osmotic adjustments. Later, the most important cellular processes that may affect the membrane potential, independent of the cell function, are reviewed – these include cellular metabolism, the cell cycle, the regulation of cell volume, pH, and Ca^{2+} oscillations. This way of looking at the membrane potential allows one to gain a new perspective, taking into account the importance of interactions that are of a crucial importance for the living organisms.

Subsequently, the dynamical systems are introduced; they represent the living organisms. The dynamical systems motivate the development of new methods for time series analysis. The latter are categorised with respect to their domain: time, frequency, or time-frequency. Here, the particular importance is assigned to the wavelet transform and the practicalities of its application to various signals. This creates the background for later introduction of the bispectral density – the first tool allowing for quantitative, not merely qualitative, interpretation of the results of wavelet bispectrum analysis over time-frequency-frequency space. This allows one for an investigation of the time-varying dynamics and therefore becomes a well-suited method for analysing the biomedical signals. Practical issues, especially the selection of the frequency resolution, are also discussed. This allows one to translate this framework to more general applications. The pointed culprits show that even an application of surrogates does not always guarantee correct results and can also be misleading.

In the next chapters, namely 5 and 6, the dynamics of the free-running membrane potential of non-excitable cells is investigated. The major focus in biophysics nowadays is centred around neuroscience and neurons. Here, the importance of understanding at more basic level, namely the non-excitable cells, is stressed. To highlight the importance of interactions, the temporal variability of the membrane potential was analysed with the wavelet transform. Many recordings of the membrane potential indicated intermittent oscillations that may be missed when looking

at the time-averaged wavelet power. It is probably the first set of work to report oscillations in the membrane potential around 0.01 Hz, that vary in time, recorded with the patch-clamp technique. These appear intermittently, and are strongly visible in the dataset recorded with the perforated patch-clamp technique. The fluctuating nature of the membrane potential gives a great motivation to perform the experiments where the membrane potential is not clamped.

Fluctuations in the free-running membrane potential can be modified in two ways: by altering the extracellular concentrations and thus shifting the Nernst potential for one ion or by adding Ca^{2+}, or both Ca^{2+} and ATP. Ca^{2+} was observed to depolarise the membrane and Ca^{2+} and ATP together to hyperpolarise it. The possible mechanisms are discussed in the chapter. Interestingly, intracellular Ca^{2+} depolarised the membrane compared to any other intrapipette solutions as opposed to Ca^{2+} and ATP together that make the membrane hyperpolarised. ATP was found not to have any significant effect neither on the membrane potential nor its fluctuations. This part shows how one can manipulate the average value of the membrane potential and its fluctuations. This may happen at the expense of putting the cell under stress, which is discussed in the chapter for various experimental conditions.

In the next chapter the evidences for nonlinearity in the recordings of the membrane potential are presented. The time series indicated time-irreversibility on the timescales shorter than 10 msec estimated directly from the signals. On the slower timescales no significant time-irreversibility was present, however the bispectral analysis indicated the signature of nonlinearities/coupling type that could be detected using bispectral analysis, on the timescales $0.026 - 0.4$ Hz. The values are subjected to time and intercellular variability. The bispectrum seems to evolve over time – this can be seen in the bispectra averaged over 2-min/10-min windows. Results from this part is a very important step on the way to built a realistic model of the dynamics of the membrane potential.

7.2   Original contribution and future work

The original contributions of the thesis are listed below

1. The recordings of the free-running membrane potential are analysed with wavelet transform. This work reports the intermittent oscillations, around 0.008 Hz (subjected to time-variability) in the membrane potential recorded with the free-running voltage for the perforated whole-cell patch-clamp configuration. The oscillations were, to a lesser extent, visible in Jurkat cells recorded with the whole-cell patch-clamp. Another activity around frequencies 0.03, 0.05 or 0.09 Hz appearing intermittently, can also be observed. These results motivate the need for explicit consideration of time-variability when designing and analysing the experiments.

2. It was concluded that the fluctuations in the free-running membrane potential can be modified in two ways: by altering the extracellular concentrations and thus shifting the Nernst potential for one ion or by adding Ca^{2+} or both Ca^{2+} and ATP. Ca^{2+} was observed to depolarise the membrane and Ca^{2+} and ATP together to hyperpolarise it. The possible mechanism are discussed in Chapter 5. It was concluded that adding intracellular ATP has no significant effect neither on the membrane potential nor its fluctuations (where at least 4 datasets were available). This part of the work explains how one can manipulate the magnitude of fluctuations in the membrane potential. Possible mechanisms of putting the cell under stress conditions are also discussed.

3. The new method based on the wavelet bispectral density – the first tool allowing for quantitative, not merely qualitative, interpretation of the results of wavelet bispectrum analysis over time-frequency-frequency space, was introduced – work jointly with J. Newman and A. Stefanovska. The method is well-suited for investigating the time-varying dynamics. The practical issues and parameters selection discussed in the thesis allows one to translate the framework to analyse more general signals.

4. The signature of nonlinearities was found in the recordings of the membrane potential. On the timescales shorter than 10 msec the time series indicated time-irreversibility and relatively steeper increase compared to a decrease. Meanwhile, on the longer timescales (0.026 – 0.4 Hz) wavelet-bispectral analysis indicated the possible nonlinearities or higher order couplings in the recordings of the membrane potential. This results are the important step on the way to create realistic model on the dynamics of the membrane potential.

Various suggestions for further experimental work are proposed in Sec. 5.7 to test the scenarios proposed in Sec. 5.5.4.

In the case of wavelet-bispectral analysis one possibility is to develop the method, possibly based on the ridge extraction procedure, mentioned in 3.5.3. This could allow one to track temporal variability in the bispectrum over frequency-frequency space, in addition to biphases. In the current form only the values averaged over the time window are considered. The bispectral density allows one to integrate over the peaks that could be further tracked in time. Another option is to quantitatively investigate various types of coupling. Possible direction for a future work is elaborating on the question "what do the bispectral peaks mean?" in terms of the bispectral density integral values, e.g. the values of the integrals obtained when investigating the phase-amplitude coupling are much bigger than values in phase coupled oscillators with time-varying basic frequencies.

Appendix A

Membrane potential

A.1 Changes in the concentration and MP

The following simple scenario is assumed: of ions of one type crossing the membrane, and causing a change in the membrane potential. The order of magnitude of the change in the concentration of this ion is now estimated as a function of the change in the membrane potential. The estimations are made for the whole volume of the spherical cell, under the assumption of uniform charge and concentration distribution, which in reality is not exactly true, but this is discussed later. The change in the membrane potential, ΔV, can be written as

$$\Delta V = \frac{\Delta Q}{C_{tot}} = \frac{ze\Delta N}{C_m \times 4\pi r^2},$$
(A.1)

where ΔQ is the charge difference, C_{tot} the total membrane capacitance, C_m the membrane capacitance for the area unit, δN the number of ions crossing the membrane, r the cellular radius, z the ion valence, and e the elementary change.

The change in the concentration, Δc, can be written as

$$\Delta c = \frac{\Delta N}{N_A w} = \frac{3C_m}{zFr \times 10^3}\Delta V,$$
(A.2)

where N_A is Avogadro's number, w is the cellular volume, in dm^3, and F is the Faraday constant. Assuming that $C_m = 10^{-2}F/m^2$, $r = 6\mu m$, and $F = 9.64 \times 10^4$, we obtain $\Delta c \simeq 5 \times 10^{-8} \times \Delta V$, where the units of c are mM, and of V are mV. This justifies the assumption of intracellular electroneutrality, usually made in most quantitative treatments of the membrane potential. This means, that there is no measurable charge excess on either side of the membrane. In spite of the fact, that there is an electric potential difference across the membrane due to charge separation, there is no actual significant difference in the global concentration of positive and negative ions across the membrane, as estimated above. This is because the charge affects the electrochemical potential hugely greater than affects the concentration. Therefore an infinitesimal change in concentration creates a large change in electric potential. The solutions on either side of the membrane remain electrically neutral, and the small excess charge accumulates near the interface. The region in which there is a

charge imbalance is called the Debye layer, and is on the order of a few nanometers thick [126].

Appendix B

Signal analysis

B.1 Frequency modulated signal expansion

In this section a signal with periodically varying basic frequency is transformed to a form where no time-variability is present. The following signal, as earlier defined in Eq. (3.5), is considered:

$$S = \sin(\phi)$$
$$S = \sin\left(\omega_0 t - \frac{\omega_0}{\omega_m} k \cos(\omega_m t)\right).$$
(B.1)

When $k \neq 0$, after applying a Taylor expansion and formulas for $\cos^{2n} x$ and $\cos^{2n+1} x$ one obtains:

$$S = \sin(\boldsymbol{\omega}_0 t) \sum_{n=0}^{\infty} \frac{1}{2n!} \left(\frac{\omega_0}{\omega_m} k\right)^{2n} \left[\frac{1}{2^{2n}} \binom{2n}{n} + \frac{1}{2^{2n-1}} \sum_{m=0}^{n-1} \binom{2n}{m} \cos(2(n-m)\boldsymbol{\omega}_m t)\right] -$$
$$- \cos(\boldsymbol{\omega}_0 t) \sum_{n=0}^{\infty} \frac{1}{(2n+1)!} \left(\frac{\omega_0}{\omega_m} k\right)^{2n+1} \left[\frac{1}{4^n} \sum_{m=0}^{2n+1} \binom{2n+1}{m} \cos((2n+1-2m)\boldsymbol{\omega}_m t)\right]$$
(B.2)

In this form one can see that, first of all, the sum is infinite, and secondly it contains only terms of the form
$A \sin(\omega_0 t) \cos(2(n-m)\omega_m t) - B \cos(\omega_0 t) \cos((2n+1-2\hat{m})\omega_m t)$,
for $\omega_m > 0$; the frequencies present in the signal do not "cover" the range $< \omega_0 - k, \omega_0 + k >$.

B.2 Justification for the use of lognormal wavelet

This section shows how the parameter σ relates quantitatively to the frequency resolution and time localisation of the wavelet transform for lognormal wavelet – adapted from [177].

First, an approach to quantification of time localisation and frequency resolution for windowed Fourier transforms is defined. Given an even function w, probably the most standard way to quantify the time localisation and frequency resolution of

the associated windowed is, inversely, by the Heisenberg uncertainty properties of w. Given a window function w, and writing $\|w\|_2 := \int_{-\infty}^{\infty} w(t)^2 \, dt = \int_{-\infty}^{\infty} \hat{w}(f)^2 \, df$,

- the *Heisenberg time uncertainty* of w is defined by

$$
\epsilon_{\text{time}}(w) = \left(\frac{\int_{-\infty}^{\infty} t^2 w(t)^2 \, dt}{\|w\|_2} \right)^{\frac{1}{2}};
$$

- and the *Heisenberg frequency uncertainty* of w is defined by

$$
\epsilon_{\text{freq}}(w) = \left(\frac{\int_{-\infty}^{\infty} f^2 \hat{w}(f)^2 \, df}{\|w\|_2} \right)^{\frac{1}{2}}.
$$

Here, $\hat{w}$ is a Fourier transform of w, t corresponds to time, and f to frequency. Now for any $\tau > 0$ let f_τ be the probability density function of the normal distribution of mean zero and variance τ^2. The squared Heisenberg uncertainties of the Gaussian function f_τ are given by

$$
\epsilon_{\text{time}}(f_\tau)^2 = \tfrac{1}{2}\tau^2 \quad \text{and} \quad \epsilon_{\text{freq}}(f_\tau)^2 = \frac{1}{8\pi^2\tau^2}.
$$

The product $\epsilon_{\text{time}}(f_\tau)\epsilon_{\text{freq}}(f_\tau)$, called the *Heisenberg area* or the *Heisenberg time-frequency uncertainty* of f_τ, is equal to $\frac{1}{4\pi}$ (independently of τ). This is the lowest possible value for the Heisenberg time-frequency uncertainty of a window function, and is uniquely obtained by Gaussian windows [123, Sec. 2.2].

Now the concept of Heisenberg uncertainties is translated to wavelets. Given a wavelet ψ, with given κ and $\|\psi\|_2 := \int_{-\infty}^{\infty} |\psi(r)|^2 \, dr$, and with admissibility constant $C_\psi := \int_{-\infty}^{\infty} \hat{\psi}(e^r)^2 \, dr$,

- the *Heisenberg time uncertainty* of $\boldsymbol{\psi}$ is defined by

$$
\epsilon_{\text{time}}(\psi) = \kappa \left(\frac{\int_{-\infty}^{\infty} r^2 |\psi(r)|^2 \, dr}{\|\psi\|_2} \right)^{\frac{1}{2}};
$$

- the *Heisenberg linear frequency uncertainty* of $\boldsymbol{\psi}$ is defined by

$$
\epsilon_{\text{linfreq}}(\psi) = \kappa^{-1} \left(\frac{\int_0^{\infty} (r - \kappa)^2 \hat{\psi}(r)^2 \, dr}{\|\psi\|_2} \right)^{\frac{1}{2}};
$$

- and the *Heisenberg logarithmic frequency uncertainty* of ψ is defined by

$$
\epsilon_{\text{freq}}(\psi) = \left(\frac{\int_{-\infty}^{\infty} (r - \log\kappa)^2 \hat{\psi}(e^r)^2 \, dr}{C_\psi} \right)^{\frac{1}{2}}
$$

.

The logarithmic-frequency approach in the definition of $\epsilon_{\text{freq}}(\psi)$ is very natural for wavelets, due to the inherently logarithmic nature of frequency resolution for the wavelet transform.

Let ψ_σ be the lognormal wavelet as defined in Sec. 3.5.2. One can compute (via Plancherel's theorem) that

$$\epsilon_{\text{time}}(\psi_\sigma)^2 \;=\; \tfrac{1}{2}\sigma^2 + \tfrac{1}{16\pi^2}.$$

This is only slightly more than the classical Heisenberg time uncertainty of a Gaussian window with variance σ^2, namely by $\tfrac{1}{2}\sigma^2$. The Heisenberg logarithmic frequency uncertainty of ψ_σ is (essentially by definition) the same as the classical Heisenberg frequency uncertainty of a Gaussian window with variance σ^2; that is,

$$\epsilon_{\text{freq}}(\psi_\sigma)^2 \;=\; \frac{1}{8\pi^2\sigma^2}.$$

Finally, one can compute that

$$\epsilon_{\text{linfreq}}(\psi_\sigma)^2 \;=\; e^{\frac{1}{2\pi^2\sigma^2}} - 2e^{\frac{3}{16\pi^2\sigma^2}} + 1.$$

For σ not too small, this is very close to $\frac{1}{8\pi^2\sigma^2}$.

B.3   Wavelet 2nd and 3rd order spectra normalisation

The following section conveys an intuitive understanding of how to find the correct normalisation for the wavelet 2nd and 3rd order spectra - note that this is not a proof.

B.3.1   2nd order spectrum

Wavelet cross-spectrum of signal x, y and wavelet function ψ can be expressed

$$\int_{\mathbb{R}^2} \frac{W_{\psi,x}(f,t)\overline{W_{\psi,y}(f,t)}}{f} d(f,t) = \int_{\mathbb{R}^2} \frac{\hat{x}(\xi)\hat{\phi}(\frac{\xi}{f})\overline{\hat{y}(\xi)}\hat{\phi}(\frac{\xi}{f})}{f} d(\xi,f), \qquad \text{(B.3)}$$

after changing the variables $r = \frac{\xi}{f}$, we obtain

$$\int_{\mathbb{R}} \left(\hat{x}(\xi)\overline{\hat{y}(\xi)} \int_{\mathbb{R}} \frac{\hat{\psi}(r)^2}{r} dr \right) d\xi = C_\psi \int_{\mathbb{R}} \left(\hat{x}(\xi)\overline{\hat{y}(\xi)} \right) d\xi \qquad \text{(B.4)}$$

B.3.2   3rd order spectrum

After applying the same intuition to the 3rd order spectra, we obtain

$$\int_{\mathbb{R}^3} \frac{W_{\psi,x}(f_1,t)W_{\psi,y}(f_2,t)\overline{W_{\psi,z}(f_1+f_2,t)}}{f_1 f_2} \, d(f_1,f_2,t)$$

$$= \int_{\mathbb{R}^4} \frac{\hat{x}(\xi_1)\hat{\psi}(\frac{\xi_1}{f_1})\hat{y}(\xi_2)\hat{\psi}(\frac{\xi_2}{f_2})\overline{\hat{z}(f_1+f_2)}\hat{\psi}(\frac{\xi_1+\xi_2}{f_1+f_2})}{f_1 f_2} \, d(f_1,f_2,\xi_1,\xi_2)$$

$$= \int_{\mathbb{R}^2} \left(\mathcal{B}_{xyz}(\xi_1,\xi_2) \int_{\mathbb{R}^2} \frac{\hat{\psi}(\frac{\xi_1}{f_1})\hat{\psi}(\frac{\xi_2}{f_2})\hat{\psi}(\frac{\xi_1+\xi_2}{f_1+f_2})}{f_1 f_2} \, d(f_1,f_2) \right) d(\xi_1,\xi_2).$$

If the term $\frac{f_1+f_2}{\xi_1+\xi_2}$ were instead $\frac{f_1}{\xi_1} + \frac{f_2}{\xi_2}$, then after the change of variables $r_i = \frac{f_i}{\xi_i}$ ($i = 1,2$) would cause the above expression to simplify but the combination of logarithmic-frequency nature of the wavelet transform with the linear-frequency sum involved in bispectral analysis creates difficulties in finding the normalisation independent of the frequencies.

Bibliography

[1]   C. Aalkjaer, D. Boedtkjer, and V. Matchkov. "Vasomotion – what is currently thought?" In: *Acta. Physiol.* 202.3 (2011), pp. 253–269.

[2]   C. Aalkjaer and H. Nilsson. "Vasomotion cellular background for the oscillator and for the synchronization of smooth muscle cells". In: *Br. J. Pharmacol.* 144.5 (2005), pp. 605–616.

[3]   P. S. Addison. *The Illustrated Wavelet Transform Handbook: Introductory Theory and Applications in Science, Engineering, Medicine and Finance.* Bristol: IOP Publishing, 2002.

[4]   B. Alberts, D. Bray, K. Hopkin, A. Johnson, J. Lewis, M. Raff, K. Roberts, and P. Walter. *Essential Cell Biology. Third Edition.* New York, Abingdon: Garland Science, 2010.

[5]   M. R. Allen and L. A. Smith. "Monte Carlo SSA: Detecting irregular oscillations in the presence of colored noise". In: *J. Clim.* 9.12 (1996), pp. 3373–3404.

[6]   V. Alvarez-Maubecin, F. García-Hernández, J. T. Williams, and E. J. Van Bockstaele. "Functional coupling between neurons and glia". In: *Neurosci. J.* 20.11 (2000), pp. 4091–4098.

[7]   J. Anderson, I. Lampl, I. Reichova, M. Carandini, and D. Ferster. "Stimulus dependence of two-state fluctuations of membrane potential in cat visual cortex". In: *Nat. Neurosci.* 3.6 (2000), p. 617.

[8]   R. G. Andrzejak, A. Kraskov, H. Stogbauer, F. Mormann, and T. Kreuz. "Bivariate surrogate techniques: Necessity, strengths, and caveats". In: *Phys. Rev. E* 68.6 (2003), p. 066202.

[9]   M. A. Aon, S. Cortassa, E. Marbán, and B. O'Rourke. "Synchronized whole cell oscillations in mitochondrial metabolism triggered by a local release of reactive oxygen species in cardiac myocytes". In: *J. Biol. Chem.* 278.45 (2003), pp. 44735–44744.

[10]   C. M. Armstrong. "The Na/K pump, Cl ion, and osmotic stabilization of cells". In: *Proc. Natl. Acad. Sci. U.S.A.* 100.10 (2003), pp. 6257–6262.

[11]   F. M. Ashcroft and P. Rorsman. "K-ATP channels and islet hormone secretion: new insights and controversies". In: *Nat. Rev. Endocrinol.* 9.11 (2013), p. 660.

[12]   F. I. Ataullakhanov and V. M. Vitvitsky. "What determines the intracellular ATP concentration". In: *Biosci. Rep.* 22.5-6 (2002), pp. 501–511.

[13]   D. E. Atkinson and G. M. Walton. "Adenosine triphosphate conservation in metabolic regulation rat liver citrate cleavage enzyme". In: *J. Biol. Chem.* 242.13 (1967), pp. 3239–3241.

[14]   R. Averdunk and T. Günther. "Characterization of the concanavalin A-induced increase in lymphocyte cell membrane permeability by furosemide". In: *Immunobiology* 157.4-5 (1980), pp. 358–364.

[15]   R. Averdunk and T. Günther. "Effect of concanavalin A on Ca^{2+} binding, Ca^{2+} uptake and the Ca^{2+} ATPase of lymphocyte plasma membranes". In: *Biochem. Biophys. Res. Commun.* 97.3 (1980), pp. 1146–1153.

[16]   A. Badou, M. K. Jha, D. Matza, W. Z. Mehal, M. Freichel, V. Flockerzi, and R. A. Flavell. "Critical role for the β regulatory subunits of CaV channels in T lymphocyte function". In: *Proc. Natl. Acad. Sci. U.S.A.* 103.42 (2006), pp. 15529–15534.

[17]   M. Balasubramanyam, M. Kimura, A. Aviv, and J. P. Gardner. "Kinetics of calcium transport across the lymphocyte plasma membrane". In: *Am. J. Physiol., Cell Physiol.* 265.2 (1993), pp. C321–C327.

[18]   A. Bandrivskyy, A. Bernjak, P. V. E. McClintock, and A. Stefanovska. "Wavelet phase coherence analysis: Application to skin temperature and blood flow". In: *Cardiovasc. Engin.* 4.1 (2004), pp. 89–93.

[19]   T. P. Barnett, L. C. Johnson, P. Naitoh, N. Hicks, and C. Nute. "Bispectrum analysis of electroencephalogram signals during waking and sleeping". In: *Science* 172.3981 (1971), pp. 401–402.

[20]   W. Bechtel and A. A. Abrahamsen. "Thinking dynamically about biological mechanisms: Networks of coupled oscillators". In: *Found. Sci.* 18.4 (2013), pp. 707–723.

[21]   M. R. Bennett, W. L. Pang, N. A. Ostroff, B. L. Baumgartner, S. Nayak, L. S. Tsimring, and J. Hasty. "Metabolic gene regulation in a dynamically changing environment". In: *Nature* 454.7208 (2008), p. 1119.

[22]   J. Berg, H. Yang, and L. Y. Jan. "Ca^{2+}-activated Cl^- channels at a glance". In: *J. Cell Sci.* 125.6 (2012), pp. 1367–1371.

[23]   M. J. Berridge, M. D. Bootman, and P. Lipp. "Calcium-a life and death signal". In: *Nature* 395.6703 (1998), p. 645.

[24]   M. J. Berridge, P. Lipp, and M. D. Bootman. "The versatility and universality of calcium signalling". In: *Nat. Rev. Mol. Cell Biol.* 1.1 (2000), p. 11.

[25]   M. J. Berridge and P. E. Rapp. "A comparative survey of the function, mechanism and control of cellular oscillators". In: *J. Exp. Biol.* 81.1 (1979), pp. 217–279.

[26] R. Binggeli and R. C. Weinstein. "Membrane potentials and sodium channels: hypotheses for growth regulation and cancer formation based on changes in sodium channels and gap junctions". In: *J. Theor. Biol.* 123.4 (1986), pp. 377–401.

[27] D. J. Blackiston, K. A. McLaughlin, and M. Levin. "Bioelectric controls of cell proliferation: ion channels, membrane voltage and the cell cycle". In: *Cell Cycle* 8.21 (2009), pp. 3527–3536.

[28] B. Boashash and B. Ristic. "Polynomial time–frequency distributions and time-varying higher order spectra: application to the analysis of multicomponent FM signals and to the treatment of multiplicative noise". In: *Signal Process.* 67.1 (1998), pp. 1–23.

[29] A. Boiteux, A. Goldbeter, and B. Hess. "Control of oscillating glycolysis of yeast by stochastic, periodic, and steady source of substrate: a model and experimental study". In: *Proc. Natl. Acad. Sci. U.S.A.* 72.10 (1975), pp. 3829–3833.

[30] A. Boiteux and B. Hess. "Oscillations in glycolysis, cellular respiration and communication". In: *Faraday Symp. Chem. Soc.* Vol. 9. Royal Society of Chemistry. 1974, pp. 202–214.

[31] M. J. Boulware and J. S. Marchant. "Timing in cellular Ca^{2+} signaling". In: *Curr. Biol.* 18.17 (2008), R769–R776.

[32] M. Breakspear, M. Brammer, and P. A. Robinson. "Construction of multivariate surrogate sets from nonlinear data using the wavelet transform". In: *Physica D* 182.1 (2003), pp. 1–22.

[33] P. Bregestovski, A. Redkozubov, and A. Alexeev. "Elevation of intracellular calcium reduces voltage-dependent potassium conductance in human T cells". In: *Nature* 319.6056 (1986), p. 776.

[34] A. Breier, Z. Sulova, and A. Vrbanova. "Ca^{2+}-induced inhibition of sodium pump: noncompetitive inhibition in respect of magnesium and sodium cations". In: *Gen. Physiol. Biophys.* 17 (1998), pp. 179–188.

[35] A. M. Brown and V. L. Lew. "The effect of intracellular calcium on the sodium pump of human red cells." In: *J. Physiol.* 343.1 (1983), pp. 455–493.

[36] A. Bruns. "Fourier-, Hilbert- and wavelet-based signal analysis: are they really different approaches?" In: *J. Neurosci. Methods* 137.2 (2004), pp. 321–332.

[37] A. H. Bui and J. S. Wiley. "Cation fluxes and volume regulation by human lymphocytes". In: *J. Cell Biol.* 108.1 (1981), pp. 47–54.

[38] G. Buzsáki, C. A. Anastassiou, and C. Koch. "The origin of extracellular fields and currents – EEG, ECoG, LFP and spikes". In: *Nat. Rev. Neurosci.* 13.6 (2012), p. 407.

[39] M. D. Cahalan and K. G. Chandy. "The functional network of ion channels in T lymphocytes". In: *Immunol. Rev.* 231.1 (2009), pp. 59–87.

[40] M. D. Cahalan, K. G. Chandy, T. E. DeCoursey, and S. Gupta. "A voltage-gated potassium channel in human T lymphocytes." In: *J. Physiol.* 358.1 (1985), pp. 197–237.

[41] Y. Cao, A. Lopatkin, and L. You. "Elements of biological oscillations in time and space". In: *Nat. Struct. Mol. Biol.* 23.12 (2016), p. 1030.

[42] W. A Catterall, I. M. Raman, H. P. C. Robinson, T. J. Sejnowski, and O. Paulsen. "The Hodgkin-Huxley heritage: from channels to circuits". In: *J. Neurosci.* 32.41 (2012), pp. 14064–14073.

[43] F. A. Chandra, G. Buzi, and J. C. Doyle. "Glycolytic oscillations and limits on robust efficiency". In: *Science* 333.6039 (2011), pp. 187–192.

[44] K. G. Chandy, T. E. DeCoursey, M. D. Cahalan, and S. Gupta. "Electroimmunology: the physiologic role of ion channels in the immune system". In: *J. Immunol.* 135.2 (1985), 787S–791S.

[45] R. A. Chaplain. "Metabolic regulations of the rhythmic activity in pacemaker neurons. II. Metabolically induced conversions of beating to bursting pacemaker activity in isolated Aplysia neurons". In: *Brain Res.* 106.2 (1976), pp. 307–319.

[46] T. W. S. Chow and F. Gou. "Three Phase Induction Machines Asymmetrical Faults Identification Using Bispectrum". In: *IEEE Trans. Energy Convers.* 10 (4 1995), pp. 688–693.

[47] A. M. Churilla, W. A. Gottschalke, L. S. Liebovitch, L. Y. Selector, A. T. Todorov, and S. Yeandle. "Membrane potential fluctuations of human T-lymphocytes have fractal characteristics of fractional Brownian motion". In: *Ann. Biomed. Eng.* 24.1 (1995), pp. 99–108.

[48] D. E. Clapham. "Calcium signaling". In: *Cell* 131.6 (2007), pp. 1047–1058.

[49] A. Clarke. "Is there a universal temperature dependence of metabolism?" In: *Funct. Ecol.* 18.2 (2004), pp. 252–256.

[50] P. T. Clemson and A. Stefanovska. "Discerning non-autonomous dynamics". In: *Phys. Rep.* 542.4 (2014), pp. 297–368.

[51] Wikimedia Commons. *File:Hodgkin-Huxley.svg*. [Online; accessed 4-November-2019]. 2018. URL: https://commons.wikimedia.org/w/index.php?title=File:Hodgkin-Huxley.svg&oldid=302668993.

[52] C. D. Cone and C. M. Cone. "Induction of mitosis in mature neurons in central nervous system by sustained depolarization". In: *Science* 192.4235 (1976), pp. 155–158.

[53] C. D. Cone Jr. "Section of biological and medical sciences: electroosmotic interactions accompanying mitosis initiation in sarcoma cells in vitro". In: *Trans. N. Y. Acad. Sci.* 31.4 Series II (1969), pp. 404–427.

[54] J. A. Connor. "On exploring the basis for slow potential oscillations in the mammalian stomach and intestine". In: *J. Exp. Biol.* 81.1 (1979), pp. 153–173.

[55] J. A. Connor, D. L. Kreulen, and C. L. Prosser. "Relation between oxidative metabolism and slow rhythmic potentials in mammalian intestinal muscle". In: *Proc. Natl. Acad. Sci. U.S.A.* 73.11 (1976), pp. 4239–4243.

[56] J. A. Connor, C. L. Prosser, and W. A. Weems. "A study of pace-maker activity in intestinal smooth muscle". In: *J. Physiol.* 240.3 (1974), pp. 671–701.

[57] B. E. Corkey, K. Tornheim, J. T. Deeney, M. C. Glennon, J. C. Parker, F. M. Matschinsky, N. B. Ruderman, and M. Prentki. "Linked oscillations of free Ca^{2+} and the ATP/ADP ratio in permeabilized RINm5F insulinoma cells supplemented with a glycolyzing cell-free muscle extract." In: *J. Biol. Chem.* 263.9 (1988), pp. 4254–4258.

[58] C. Diks, J. C. Van Houwelingen, F. Takens, and J. DeGoede. "Reversibility as a criterion for discriminating time series". In: *Phys. Lett. A* 201.2-3 (1995), pp. 221–228.

[59] R. E. Dolmetsch and R. S. Lewis. "Signaling between intracellular Ca^{2+} stores and depletion-activated Ca^{2+} channels generates $Ca^{2+}i$ oscillations in T lymphocytes". In: *J. Gen. Physiol.* 103.3 (1994), pp. 365–388.

[60] E. Donnadieu, G. Bismuth, and A. Trautmann. "Calcium fluxes in T lymphocytes." In: *J. Biol. Chem.* 267.36 (1992), pp. 25864–25872.

[61] E. Donnadieu and A. Trautmann. "Is there a Na^+/Ca^{2+} exchanger in macrophages and in lymphocytes?" In: *Pflugers Arch.* 424.5-6 (1993), pp. 448–455.

[62] J. A. Draghi, T. L. Parsons, G. P. Wagner, and J. B. Plotkin. "Mutational robustness can facilitate adaptation". In: *Nature* 463.7279 (2010), p. 353.

[63] G. Dumermuth, P. J. Huber, B. Kleiner, and T. Gasser. "Analysis of the interrelations between frequency bands of the EEG by means of the bispectrum a preliminary study". In: *Clin. Neurophysiol.* 31.2 (1971), pp. 137–148.

[64] L. N. M. Duysens and J. Amesz. "Fluorescence spectrophotometry of reduced phosphopyridine nucleotide in intact cells in the near-ultraviolet and visible region". In: *Biochim. Biophys. Acta* 24 (1957), pp. 19–26.

[65] T. Epstein, L. Xu, R. J. Gillies, and R. A. Gatenby. "Separation of metabolic supply and demand: aerobic glycolysis as a normal physiological response to fluctuating energetic demands in the membrane". In: *Cancer & Metabolism* 2.1 (2014), p. 7.

[66] C. M. Fanger, S. Ghanshani, N. J. Logsdon, H. Rauer, K. Kalman, J. Zhou, K. Beckingham, K. G. Chandy, M. D. Cahalan, and J. Aiyar. "Calmodulin mediates calcium-dependent activation of the intermediate conductance KCa channel, IKCa1". In: *J. Biol. Chem.* 274.9 (1999), pp. 5746–5754.

[67] M. Farout. "The interaction between metabolism and the plasma membrane potential, and intracellular pH". PhD thesis. Lancaster University, 2019.

[68] S. M. Felber and M. D. Brand. "Factors determining the plasma-membrane potential of lymphocytes". In: *Biochem. J.* 204.2 (1982), pp. 577–585.

[69] S. Feske, Y. Gwack, M. Prakriya, S. Srikanth, S. H. Puppel, B. Tanasa, P. G. Hogan, R. S. Lewis, M. Daly, and A. Rao. "A mutation in Orai1 causes immune deficiency by abrogating CRAC channel function". In: *Nature* 441.7090 (2006), p. 179.

[70] S. Feske, H. Wulff, and E. Y. Skolnik. "Ion channels in innate and adaptive immunity". In: *Annu. Rev. Immunol.* 33 (2015), pp. 291–353.

[71] M. L. Fidelman, S. H. Seeholzer, K. B. Walsh, and R. D. Moore. "Intracellular pH mediates action of insulin on glycolysis in frog skeletal muscle". In: *Am. J. Physiol., Cell Physiol.* 242.1 (1982), pp. C87–C93.

[72] D. J. Field. "Relations between the statistics of natural images and the response properties of cortical cells". In: *J. Opt. Soc. Am. A* 4.12 (1987), pp. 2379–2394.

[73] M. Flinck, S. H. Kramer, and S. F. Pedersen. "Roles of pH in control of cell proliferation". In: *Acta Physiol.* 223.3 (2018), e13068.

[74] J. R. Fonollosa and C. T. Nikias. "Wigner higher order moment spectra: definition, properties, computation and application to transient signal analysis". In: *IEEE Trans. Signal Process.* 41.1 (1993), p. 245.

[75] S. P. Fraser, J. K. J. Diss, L. J. Lloyd, F. Pani, A.-M. Chioni, A. J. T. George, and M. B. A. Djamgoz. "T-lymphocyte invasiveness: control by voltage-gated Na^+ channel activity". In: *FEBS Lett.* 569.1-3 (2004), pp. 191–194.

[76] Nicolis G. and Prigogine I. *Self-organization in Nonequilibrium Systems*. New York: Wiley, 1977.

[77] D. C. Gadsby. "Ion channels versus ion pumps: the principal difference, in principle". In: *Nat. Rev. Mol. Cell Biol.* 10.5 (2009), p. 344.

[78] R. F. Galán, G. B. Ermentrout, and N. N. Urban. "Efficient estimation of phase-resetting curves in real neurons and its significance for neural-network modeling". In: *Phys. Rev. Lett.* 94 (15 2005), p. 158101.

[79] R. Gallager. *Course materials for 6.450 Principles of digital communications I*. MIT OpenCourseWare. Downloaded 12.08.2019. 2006. URL: http://ocw.mit.edu.

[80]   Z. Ge. "Significance testing for wavelet bicoherence and its application in analyzing nonlinearity in turbulent shear flows". In: *Phys. Rev. E* 81.5 (2010), p. 056311.

[81]   A. Ghosh and B. Chance. "Oscillations of glycolytic intermediates in yeast cells". In: *Biochem. Biophys. Res. Commun.* 16.2 (1964), pp. 174–181.

[82]   J. F. Gillooly, J. H. Brown, G. B. West, V. M. Savage, and E. L. Charnov. "Effects of size and temperature on metabolic rate". In: *science* 293.5538 (2001), pp. 2248–2251.

[83]   R. Glaser. *Biophysics, An Introduction, Second Edition*. Berlin Heidelberg: Springer-Verlag, May 2012.

[84]   L. Glass. "Synchronization and rhythmic processes in physiology". In: *Nature* 410.6825 (2001), pp. 277–284.

[85]   M. D. Godfrey. "An Exploratory Study of the Bi-Spectrum of Economic Time Series". In: *J. R. Stat. Soc. Ser. C Appl. Stat.* 14 (1 1965), pp. 48–69.

[86]   A. Goldbeter. "Computational approaches to cellular rhythms". In: *Nature* 420.6912 (2002), p. 238.

[87]   A. Goldbeter. "Modulation of the adenylate energy charge by sustained metabolic oscillations". In: *Febs Lett.* 43.3 (1974), pp. 327–330.

[88]   A. Goldbeter, C. Gérard, D. Gonze, J.-C. Leloup, and G. Dupont. "Systems biology of cellular rhythms". In: *FEBS lett.* 586.18 (2012), pp. 2955–2965.

[89]   D. E. Goldman. "Potential, impedance, and rectification in membranes". In: *J. Gen. Physiol.* 27.1 (1943), pp. 37–60.

[90]   A. Gorman and M. F. Marmor. "Long-term effect of ouabain and sodium pump inhibition on a neuronal membrane". In: *J. Physiol.* 242.1 (1974), pp. 49–60.

[91]   S. Grinstein and S. J. Dixon. "Ion transport, membrane potential, and cytoplasmic pH in lymphocytes: changes during activation". In: *Physiol. Rev.* 69.2 (1989), pp. 417–481.

[92]   S. Grinstein, A. Dupre, and A. Rothstein. "Volume regulation by human lymphocytes. Role of calcium." In: *J. Gen. Physiol.* 79.5 (1982), pp. 849–868.

[93]   S. Grinstein, J. D. Goetz, and A. Rothstein. "$22Na^+$ fluxes in thymic lymphocytes. I. Na^+/Na^+ and Na^+/H^+ exchange through an amiloride-insensitive pathway." In: *J. Gen. Physiol.* 84.4 (1984), pp. 565–584.

[94]   S. Grissmer, A. N. Nguyen, and M. D. Cahalan. "Calcium-activated potassium channels in resting and activated human T lymphocytes. Expression levels, calcium dependence, ion selectivity, and pharmacology". In: *J. Gen. Physiol.* 102.4 (1993), pp. 601–630.

[95] K. Gurley, T. Kijewski, and A. Kareem. "First- and higher-order correlation detection using wavelet transforms". In: *Journal of Engineering Mechanics* 129.2 (2003), pp. 188–201.

[96] H. Haken. "Cooperative phenomena in systems far from thermal equilibrium and in nonphysical systems". In: *Rev. Mod. Phys.* 47 (1975), pp. 67–121.

[97] H. Haken. *Synergetics, An Introduction.* Berlin: Springer, 1983.

[98] S. C. Hartsel, C. Hatch, and W. Ayenew. "How does amphotericin B work?: Studies on model membrane systems". In: *J. Liposome Res.* 3.3 (1993), pp. 377–408.

[99] K. Hasselmann, W. Munk, and G. MacDonald. "Bispectra of ocean waves". In: *Time Series Analysis.* New York: Wiley, 1963, pp. 125–139.

[100] A. L. Hodgkin and A. F. Huxley. "A quantitative description of membrane current and its application to conduction and excitation in nerve". In: *J. Physiol.* 117.4 (1952), pp. 500–544.

[101] A. L. Hodgkin and A. F. Huxley. "Currents carried by sodium and potassium ions through the membrane of the giant axon of Loligo". In: *J. Physiol.* 116.4 (1952), pp. 449–472.

[102] A. L. Hodgkin and A. F. Huxley. "The components of membrane conductance in the giant axon of Loligo". In: *J. Physiol.* 116.4 (1952), pp. 473–496.

[103] A. L. Hodgkin and A. F. Huxley. "The dual effect of membrane potential on sodium conductance in the giant axon of Loligo". In: *J. Physiol.* 116.4 (1952), pp. 497–506.

[104] A. L. Hodgkin, A. F. Huxley, and B. Katz. "Measurement of current-voltage relations in the membrane of the giant axon of Loligo". In: *J. Physiol.* 116.4 (1952), pp. 424–448.

[105] W. Huang, C. Lu, Y. Wu, S. Ouyang, and Y. Chen. "Identification and functional characterization of voltage-gated sodium channels in lymphocytes". In: *Biochem. Biophys. Res. Commun.* 458.2 (2015), pp. 294–299.

[106] P. Huber, B. Kleiner, T. Gasser, and G. Dumermuth. "Statistical methods for investigating phase relations in stationary stochastic processes". In: *IEEE Trans. Audio Electroacoust.* 19 (1 1971), pp. 78–86.

[107] D. Iatsenko, A. Bernjak, T. Stankovski, Y. Shiogai, P. J. Owen-Lynch, P. B. M. Clarkson, P. V. E. McClintock, and A. Stefanovska. "Evolution of Cardio-Respiratory Interactions with Age". In: *Phil. Trans. R. Soc. Lond. A* 371.1997 (2013), p. 20110622.

[108] D. Iatsenko, P. V. E. McClintock, and A. Stefanovska. "Linear and synchrosqueezed time-frequency representations revisited: Overview, standards of use, resolution, reconstruction, concentration, and algorithms". In: *Digit. Signal Proc.* 42 (2015), pp. 1 –26.

[109]   D. Iatsenko, P. V. E. McClintock, and A. Stefanovska. "On the extraction of instantaneous frequencies from ridges in time-frequency representations of signals". In: *Signal Proc.* 125 (2016), pp. 290–303.

[110]   D. Iatsenko, A. Stefanovska, and P. V. E. McClintock. "Nonlinear mode decomposition: a noise-robust, adaptive, decomposition method". In: *Phys. Rev. E.* 92 (2015), p. 032916.

[111]   W. E. Jacobus. "Respiratory control and the integration of heart high-energy phosphate metabolism by mitochondrial creatine kinase". In: *Annu. Rev. Physiol.* 47.1 (1985), pp. 707–725.

[112]   B. Jagadeesh, C. M. Gray, and D. Ferster. "Visually evoked oscillations of membrane potential in cells of cat visual cortex". In: *Science* 257.5069 (1992), pp. 552–554.

[113]   E. Jakobsson. "Interactions of cell volume, membrane potential, and membrane transport parameters". In: *Am. J. Physiol., Cell Physiol.* 238.5 (1980), pp. C196–C206.

[114]   J. Jamšek, A. Stefanovska, and P. V. E. McClintock. "Nonlinear cardio-respiratory interactions revealed by time-phase bispectral analysis". In: *Phys. Med. Biol.* 49.18 (2004), pp. 4407–4425.

[115]   J. Jamšek, A. Stefanovska, and P. V. E. McClintock. "Wavelet bispectral analysis for the study of interactions among oscillators whose basic frequencies are significantly time variable". In: *Phys. Rev. E* 76 (2007), p. 046221.

[116]   J. Jamšek, A. Stefanovska, P. V. E. McClintock, and I. A. Khovanov. "Time-phase bispectral analysis". In: *Phys. Rev. E* 68.1 (2003), p. 016201.

[117]   J. Jamšek, M. Paluš, and A. Stefanovska. "Detecting couplings between interacting oscillators with time-varying basic frequencies: Instantaneous wavelet bispectrum and information theoretic approach". In: *Phys. Rev. E* 81.3 (2010), p. 036207.

[118]   C. Jarzynski. "Diverse phenomena, common themes". In: *Nat. Phys.* 11.2 (2015), p. 105.

[119]   T. J. Jentsch. "VRACs and other ion channels and transporters in the regulation of cell volume and beyond". In: *Nat. Rev. Mol. Cell Biol.* 17.5 (2016), p. 293.

[120]   M. K. Jha, A. Badou, M. Meissner, J. E. McRory, M. Freichel, V. Flockerzi, and R. A. Flavell. "Defective survival of naive CD8+ T lymphocytes in the absence of the $\beta3$ regulatory subunit of voltage-gated calcium channels". In: *Nat. Immunol.* 10.12 (2009), p. 1275.

[121]   D. D. Job. "Ionic basis of intestinal electrical activity". In: *Am. J. Physiol.-Legacy Content* 217.5 (1969), pp. 1534–1541.

[122]   L. A. Kadir, M. Stacey, and R. Barrett-Jolley. "Emerging roles of the membrane potential: action beyond the action potential". In: *Front. Physiol.* 9 (2018).

[123]   G. Kaiser. *A Friendly Guide to Wavelets*. Boston: Birkhäuser, 1994.

[124]   R. S. Kass and R. W. Tsien. "Fluctuations in membrane current driven by intracellular calcium in cardiac Purkinje fibers". In: *Biophys. J.* 38.3 (1982), pp. 259–269.

[125]   A. R. Kay and M. P. Blaustein. "Evolution of our understanding of cell volume regulation by the pump-leak mechanism". In: *J. Gen. Physiol.* 151.4 (2019), pp. 407–416.

[126]   J. P. Keener and J. Sneyd. *Mathematical Physiology. I: Cellular Physiology, Second Edition*. Vol. 1. Springer, 2009.

[127]   D. W. Keifer and R. M. Spanswick. "Activity of the electrogenic pump in Chara corallina as inferred from measurements of the membrane potential, conductance, and potassium permeability". In: *Plant Physiol.* 62.4 (1978), pp. 653–661.

[128]   C. J. Keylock. "A wavelet-based method for surrogate data generation". In: *Physica D: Nonlinear Phenomena* 225.2 (2007), pp. 219–228.

[129]   M. Kikuyama, T. Hayama, S. Fujii, and M. Tazawa. "Relationship between light-induced potential change and internal ATP concentration in tonoplast-free Chara cells". In: *Plant and Cell Physiol.* 20.6 (Sept. 1979), pp. 993–1002.

[130]   J.-R. Kim, Y. Yoon, and K.-H. Cho. "Coupled feedback loops form dynamic motifs of cellular networks". In: *Biophys J.* 94.2 (2008), pp. 359–365.

[131]   T. Kim, E. J. Powers, W. M. Grady, and A. Arapostathis. "A novel QPC detector for the health monitoring of rotating machines". In: *Instrumentation and Measurement Technology Conference Proceedings, 2007. IMTC 2007. IEEE*. IEEE. 2007, pp. 1–6.

[132]   H. Knutsson, C.-F. Westin, and G. Granlund. "Local multiscale frequency and bandwidth estimation". In: *Proceedings of 1st International Conference on Image Processing*. Vol. 1. IEEE. 1994, pp. 36–40.

[133]   E. Komatsu and D. N. Spergel. "Acoustic signatures in the primary microwave background bispectrum". In: *Phys. Rev. D* 63.6 (2001), p. 063002.

[134]   B. Kralemann, A. Pikovsky, and M. Rosenblum. "Detecting triplet locking by triplet synchronization indices". In: *Phys. Rev. E* 87 (5 2013), p. 052904.

[135]   D. Kugiumtzis. "Test your surrogate data before you test for nonlinearity". In: *Phys. Rev. E* 60.3 (1999), p. 2808.

[136]   F. T. Kurz, M. A. Aon, B. O'Rourke, and A. A. Armoundas. "Spatio-temporal oscillations of individual mitochondria in cardiac myocytes reveal modulation of synchronized mitochondrial clusters". In: *Proc. Natl. Acad. Sci.* 107.32 (2010), pp. 14315–14320.

[137] F. T. Kurz, M. A. Aon, B. O'Rourke, and A. A. Armoundas. "Wavelet analysis reveals heterogeneous time-dependent oscillations of individual mitochondria". In: *Am. J. Physiol. Heart Circ. Physiol.* 299.5 (2010), H1736–H1740.

[138] T. Kuwahata. "Effects of adenosine and ATP on the membrane potential and synaptic transmission in neurons of the rat locus coeruleus". In: *The Kurume Med. J.* 51.2 (2004), pp. 109–123.

[139] J. P. Lachaux, A. Lutz, D. Rudrauf, D. Cosmelli, M. Le van Quyen, J. Martinerie, and F. Varela. "Estimating the time-course of coherence between single-trial brain signals: an introduction to wavelet coherence". In: *Clin. Neurophysiol.* 32.3 (2002), pp. 157–174.

[140] I. Lampl, I. Reichova, and D. Ferster. "Synchronous membrane potential fluctuations in neurons of the cat visual cortex". In: *Neuron* 22.2 (1999), pp. 361–374.

[141] G. Lancaster, D. Iatsenko, A. Pidde, V. Ticcinelli, and A. Stefanovska. "Surrogate data for hypothesis testing of physical systems". In: *Physics Reports* (2018).

[142] G. Lancaster, Y. F. Suprunenko, K. Jenkins, and A. Stefanovska. "Modelling chronotaxicity of cellular energy metabolism to facilitate the identification of altered metabolic states". In: *Sci. Rep.* 6 (2016), p. 29584.

[143] F. Lang, J. Madlung, J. Bock, U. Lükewille, S. Kaltenbach, K. S. Lang, C. Belka, C. A. Wagner, H. J. Lang, E. Gulbins, and A. Lepple-Wienhues. "Inhibition of Jurkat-T-lymphocyte Na^+/H^+-exchanger by CD95 (Fas/Apo-1)-receptor stimulation". In: *Pflügers Arch.* 440.6 (2000), pp. 902–907.

[144] P. Launay, H. Cheng, S. Srivatsan, R. Penner, A. Fleig, and J. P. Kinet. "TRPM4 regulates calcium oscillations after T cell activation". In: *Science* 306.5700 (2004), pp. 1374–1377.

[145] P. Launay, A. Fleig, A. L. Perraud, A. M. Scharenberg, R. Penner, and J. P. Kinet. "TRPM4 is a Ca^{2+}-activated nonselective cation channel mediating cell membrane depolarization". In: *Cell* 109.3 (2002), pp. 397–407.

[146] M. Le Van Quyen, J. Foucher, J. P. Lachaux, E. Rodriguez, A. Lutz, J. Martinerie, and F. J. Varela. "Comparison of Hilbert transform and wavelet methods for the analysis of neuronal synchrony". In: *J. Neurosci. Methods* 111.2 (2001), pp. 83–98.

[147] Z. Levnajić and A. Pikovsky. "Network reconstruction from random phase resetting". In: *Phys. Rev. Lett.* 107 (3 2011), p. 034101.

[148] R. S. Lewis. "Calcium signaling mechanisms in T lymphocytes". In: *Annu. Rev. Immunol.* 19.1 (2001), pp. 497–521.

[149] R. S. Lewis and M. D. Cahalan. "Mitogen-induced oscillations of cytosolic Ca^{2+} and transmembrane Ca^{2+} current in human leukemic T cells." In: *Cell Regul.* 1.1 (1989), pp. 99–112.

[150] R. S. Lewis, P. E. Ross, and M. D. Cahalan. "Chloride channels activated by osmotic stress in T lymphocytes." In: *J. Gen. Physiol.* 101.6 (1993), pp. 801–826.

[151] X. Li, D. Li, L. J. Voss, and J. W. Sleigh. "The comodulation measure of neuronal oscillations with general harmonic wavelet bicoherence and application to sleep analysis". In: *NeuroImage* 48.3 (2009), pp. 501–514.

[152] A. H. Lichtman, G. B. Segel, and M. A. Lichtman. "Calcium transport and calcium-ATPase activity in human lymphocyte plasma membrane vesicles." In: *J. Biol. Chem.* 256.12 (1981), pp. 6148–6154.

[153] M. A. Lichtman, A. H. Jackson, and W. A. Peck. "Lymphocyte monovalent cation metabolism: cell volume, cation content and cation transport". In: *J. Cell. Physiol.* 80.3 (1972), pp. 383–396.

[154] J. M. Lilly and S. C. Olhede. "Generalized Morse wavelets as a superfamily of analytic wavelets". In: *IEEE Trans. Signal Process.* 60.11 (2012), pp. 6036–6041.

[155] C.-N. Liu, M. Michaelis, R. Amir, and M. Devor. "Spinal nerve injury enhances subthreshold membrane potential oscillations in DRG neurons: relation to neuropathic pain". In: *J. Neurophysiol.* 84.1 (2000), pp. 205–215.

[156] J. Liu, A. Prindle, J. Humphries, M. Gabalda-Sagarra, M. Asally, D. D. Lee, S. Ly, J. Garcia-Ojalvo, and G. M. Süel. "Metabolic co-dependence gives rise to collective oscillations within biofilms". In: *Nature* 523.7562 (2015), p. 550.

[157] P. Machamer, L. Darden, and C. F. Craver. "Thinking about mechanisms". In: *Philos. Sci.* 67.1 (2000), pp. 1–25.

[158] I. H. Madshus. "Regulation of intracellular pH in eukaryotic cells." In: *Biochem. J.* 250.1 (1988), pp. 1–8.

[159] S. Mallat. *A Wavelet Tour of Signal Processing, 3rd edn.* Burlington: Academic Press, 2008.

[160] V. A. Maltsev. "Oscillating and triggering properties of T cell membrane potential". In: *Immunol. Lett.* 26.3 (1990), pp. 277–282.

[161] R. Martinez-Corral, J. Liu, A. Prindle, G. M. Süel, and J. Garcia-Ojalvo. "Metabolic basis of brain-like electrical signalling in bacterial communities". In: *Philos. Trans. Royal Soc. B* 374.1774 (2019), p. 20180382.

[162] T. Matsuoka and J. Ulrych. "Phase estimation using the bispectrum". In: *Proc. IEEE* 72 (10 1984).

[163] J. H. McDonald. *Handbook of biological statistics*. Vol. 2. Sparky House Publishing Baltimore, MD, 2009.

[164] A. D. C. Mecknight. "Principles of cell volume regulation". In: *Renal Physiol. Biochem.* 3.5 (1988), pp. 114–141.

[165] S. Meignen, T. Oberlin, P. Depalle, P. Flandrin, and S. McLaughlin. "Adaptive multimode signal reconstruction from time-frequency representations". In: *Philos. Trans. Royal Soc. A* 374.2065 (2016), p. 20150205.

[166] I. Mellman, R. Fuchs, and A. Helenius. "Acidification of the endocytic and exocytic pathways". In: *Annu. Rev. Biochem.* 55.1 (1986), pp. 663–700.

[167] M. J. Merrins, C. Poudel, J. P. McKenna, J. Ha, A. Sherman, R. Bertram, and L. S. Satin. "Phase analysis of metabolic oscillations and membrane potential in pancreatic islet β-cells". In: *Biophys. J.* 110.3 (2016), pp. 691–699.

[168] A. Messiah and J. Potter. *Quantum Mechanics*. Quantum Mechanics. North-Holland, 1961.

[169] C. M. Metallo and M. G. Vander Heiden. "Understanding metabolic regulation and its influence on cell physiology". In: *Mol. cell* 49.3 (2013), pp. 388–398.

[170] B. P. van Milligen, E. Sanchez, T. Estrada, C. Hidalgo, B. Brañas, B. Carreras, and L. Garcia. "Wavelet bicoherence: a new turbulence analysis tool". In: *Phys. Plasmas* 2.8 (1995), pp. 3017–3032.

[171] R. Milo and Phillips R. *Cell Biology by the numbers. Draft*. New York, Abingdon: Garland Science, 2015.

[172] T. Mimura, T. Shimmen, and M. Tazawa. "Dependence of the membrane potential on intracellular ATP concentration in tonoplast-free cells of Nitellopsis obtusa". In: *Planta* 157.2 (1983), pp. 97–104.

[173] P. Mitchell. "Coupling of phosphorylation to electron and hydrogen transfer by a chemi-osmotic type of mechanism". In: *Nature* 191.4784 (1961), pp. 144–148.

[174] A. Mokeichev, M. Okun, O. Barak, Y. Katz, O. Ben-Shahar, and I. Lampl. "Stochastic emergence of repeating cortical motifs in spontaneous membrane potential fluctuations in vivo". In: *Neuron* 53.3 (2007), pp. 413–425.

[175] W. Moody Jr. "Effects of intracellular H^+ on the electrical properties of excitable cells". In: *Annu. Rev. Neurosci.* 7.1 (1984), pp. 257–278.

[176] M. Moser, M. Frühwirth, R. Penter, and R. Winker. "Why life oscillates – from a topographical towards a functional chronobiology". In: *Cancer Causes Control* 17.4 (2006), pp. 591–599.

[177] J. Newman, A. Pidde, and A. Stefanovska. "Defining the Wavelet Bispectrum". resubmitted to Applied and Computational Harmonic Analysis. 2020.

[178] C. L. Nikias and J. M. Mendel. "Signal processing with higher-order spectra". In: *IEEE Signal Process. Mag.* 10.3 (1993), pp. 10–37.

[179] C. L. Nikias and A. P. Petropulu. *Higher-Order Spectra Anlysis: A Nonlinear Signal Processing Framework*. Englewood Cliffs: Prentice-Hall, 1993.

[180] T. Ning and J. D. Bronzino. "Bispectral analysis of the rat EEG during various vigilance states". In: *IEEE Trans. Biomed. Eng.* 36 (4 1989), pp. 497–499.

[181] B. Novák and J. J. Tyson. "Design principles of biochemical oscillators". In: *Nat. Rev. Mol. Cell Biol.* 9.12 (2008), pp. 981–991.

[182] H. Oishi, A. Schuster, M. Lamboley, N. Stergiopulos, J.-J. Meister, and J.-L. Bény. "Role of membrane potential in vasomotion of isolated pressurized rat arteries". In: *Life Sci.* 71.19 (2002), pp. 2239–2248.

[183] Y. Okada, Y. Doida, G. Roy, W. Tsuchiya, K. Inouye, and A. Inouye. "Oscillations of membrane potential in L cells". In: *J. Membr. Biol.* 35.1 (1977), pp. 319–335.

[184] Y. Okada, G. Roy, W. Tsuchiya, Y. Doida, and A. Inouye. "Oscillations of membrane potential in L cells". In: *J. Membr. Biol.* 35.1 (1977), pp. 337–350.

[185] K. Omilusik, J. J. Priatel, X. Chen, Y. T. Wang, H. Xu, K. B. Choi, R. Gopaul, A. McIntyre-Smith, H. S. Teh, R. Tan, et al. "The CaV1.4 calcium channel is a critical regulator of T cell receptor signaling and naive T cell homeostasis". In: *Immunity* 35.3 (2011), pp. 349–360.

[186] S. N. Orlov, A. A. Platonova, P. Hamet, and R. Grygorczyk. "Cell volume and monovalent ion transporters: their role in cell death machinery triggering and progression". In: *Am. J. Physiol., Cell Physiol.* 305.4 (2013), pp. C361–C372.

[187] B. O'Rourke, B. M. Ramza, and E. Marban. "Oscillations of membrane current and excitability driven by metabolic oscillations in heart cells". In: *Science* 265.5174 (1994), pp. 962–966.

[188] V. C. Özalp, T. R. Pedersen, L. J. Nielsen, and L. F. Olsen. "Time-resolved measurements of intracellular ATP in the yeast Saccharomyces cerevisiae using a new type of nanobiosensor". In: *J. Biol. Chem.* 285.48 (2010), pp. 37579–37588.

[189] I. Ozden, S. Venkataramani, M. A. Long, B. W. Connors, and A. V. Nurmikko. "Strong coupling of nonlinear electronic and biological oscillators: Reaching the 'amplitude death' regime". In: *Phys. Rev. Lett.* 93.15 (2004), p. 158102.

[190] A. Papagiannakis, B. Niebel, E. C. Wit, and M. Heinemann. "Autonomous metabolic oscillations robustly gate the early and late cell cycle". In: *Mol. Cell* 65.2 (2017), pp. 285–295.

[191] C. Y. Park, P. J. Hoover, F. M. Mullins, P. Bachhawat, E. D. Covington, S. Raunser, T. Walz, K. C. Garcia, R. E. Dolmetsch, and R. S. Lewis. "STIM1 clusters and activates CRAC channels via direct binding of a cytosolic domain to Orai1". In: *Cell* 136.5 (2009), pp. 876–890.

[192] S. Patel. "The role of membrane potential dynamics in cell behaviours: invastigating the membrane potantial dynamics in the Jurkat and HMEC-1 cell lines using the continuous wavelet transform". PhD thesis. Division of Biomedical and Life Sciences, Lancaster University, 2015.

[193] R. J. Paul, M. Bauer, and W. Pease. "Vascular smooth muscle: aerobic glycolysis linked to sodium and potassium transport processes". In: *Science* 206.4425 (1979), pp. 1414–1416.

[194] A. Pikovsky, M. Rosenblum, and J. Kurths. *Synchronization – A Universal Concept in Nonlinear Sciences*. Cambridge: Cambridge University Press, 2001.

[195] L. A. Pinna, M. Lorini, V. Moret, and N. Siliprandi. "Effect of oligomycin and succinate on mitochondrial metabolism of adenine nucleotides". In: *Biochim. Biophys. Acta – Bioenergetics* 143.1 (1967), pp. 18–25.

[196] A. Prindle, J. Liu, M. Asally, S. Ly, J. Garcia-Ojalvo, and G. M. Süel. "Ion channels enable electrical communication in bacterial communities". In: *Nature* 527.7576 (2015), p. 59.

[197] Y. Qin, B. Tang, and Y. Mao. "Adaptive signal decomposition based on wavelet ridge and its application". In: *Signal Process.* 120 (2016), pp. 480–494.

[198] Z. Qiu, A. E. Dubin, J. Mathur, B. Tu, K. Reddy, L. J. Miraglia, J. Reinhardt, A. P. Orth, and A. Patapoutian. "SWELL1, a plasma membrane protein, is an essential component of volume-regulated anion channel". In: *Cell* 157.2 (2014), pp. 447–458.

[199] R. Quian Quiroga, A. Kraskov, T. Kreuz, and P. Grassberger. "Performance of different synchronization measures in real data: A case study on electroencephalographic signals". In: *Phys. Rev. E* 65.4 (2002), p. 041903.

[200] D. Raju, O. Sauter, and J. B. Lister. "Study of nonlinear mode coupling during neoclassical tearing modes using bispectrum analysis". In: *Plasma Phys. Controlled Fusion* 45.4 (2003), p. 369.

[201] P. E. Rapp. "Atlas of cellular oscillations". In: *J. Exp. Biol.* 81 (1979), pp. 281–306.

[202] P. E. Rapp. "Why are so many biological systems periodic?" In: *Prog. Neurobiol.* 29.3 (1987), pp. 261–273.

[203] C. Räth, M. Gliozzi, I. E. Papadakis, and W. Brinkmann. "Revisiting algorithms for generating surrogate time series". In: *Phys. Rev. Lett.* 109.14 (2012), p. 144101.

[204] T. J. Rink, R. Y. Tsien, and T. Pozzan. "Cytoplasmic pH and free Mg^{2+} in lymphocytes." In: *J. Cell Biol.* 95.1 (1982), pp. 189–196.

[205] J. P. Roach, A. Pidde, E. Katz, J. Wu, N. Ognjanovski, S. J. Aton, and M. R. Zochowski. "Resonance with subthreshold oscillatory drive organizes activity and optimizes learning in neural networks". In: *Proc. Natl. Acad. Sci. U.S.A.* 115.13 (2018), E3017–E3025.

[206] L. D. Robb-Gaspers, G. A. Rutter, P. Burnett, G. Hajnóczky, R. M. Denton, and A. P. Thomas. "Coupling between cytosolic and mitochondrial calcium oscillations: role in the regulation of hepatic metabolism". In: *Biochim. Biophys. Acta – Bioenergetics* 1366.1-2 (1998), pp. 17–32.

[207] H. M. Rosenberg, B. B. Shank, and E. C. Gregg. "Volume changes of mammalian cells subjected to hypotonic solutions in vitro: Evidence for the requirement of a sodium pump for the shrinking phase". In: *J. Cell Biol.* 80.1 (1972), pp. 23–32.

[208] M. Rosenblum, A. Pikovsky, J. Kurths, C. Schäfer, and P. A. Tass. "Phase synchronization: from theory to data analysis". In: *Handbook of Biological Physics*. Vol. 4. Elsevier, 2001, pp. 279–321.

[209] P. E. Ross, S. S. Garber, and M. D. Cahalan. "Membrane chloride conductance and capacitance in Jurkat T lymphocytes during osmotic swelling." In: *Biophys. J.* 66.1 (1994), p. 169.

[210] F. Sachs and M. V. Sivaselvan. "Cell volume control in three dimensions: Water movement without solute movement". In: *J. Gen. Physiol.* 145.5 (2015), pp. 373–380.

[211] F. Sagués, J. M. Sancho, and J. García-Ojalvo. "Spatiotemporal order out of noise". In: *Rev. Mod. Phys.* 79.3 (2007), p. 829.

[212] B. Schack, H. Witte, M. Helbig, Ch. Schelenz, and M. Specht. "Time-variant non-linear phase-coupling analysis of EEG burst patterns in sedated patients during electroencephalic burst suppression period". In: *Clin. Neurophysiol.* 112.8 (2001), pp. 1388–1399.

[213] T. Schreiber and A. Schmitz. "Discrimination power of measures for nonlinearity in a time series". In: *Phys. Rev. E* 55.5 (1997), p. 5443.

[214] T. Schreiber and A. Schmitz. "Improved surrogate data for nonlinearity tests". In: *Phys. Rev. Lett.* 77.4 (1996), pp. 635–638.

[215] T. Schreiber and A. Schmitz. "Surrogate time series". In: *Physica D* 142.3-4 (2000), pp. 346–382.

[216] E. Schrödinger. *What is Life? The Physical Aspect of the Living Cell*. Cambridge University Press, 1944.

[217] J. T. C. Schwabedal and A. Pikovsky. "Effective phase dynamics of noise-induced oscillations in excitable systems". In: *Phys. Rev. E* 81.4 (2010), p. 046218.

[218] C. G. Scully, N. Mitrou, B. Braam, W. A. Cupples, and K. H. Chon. "Detecting interactions between the renal autoregulation mechanisms in time and space". In: *IEEE Trans. Biomed. Eng.* 64.3 (2017), pp. 690–698.

[219] L. W. Sheppard, A. Stefanovska, and P. V. E. McClintock. "Detecting the harmonics of oscillations with time-variable frequencies". In: *Phys. Rev. E* 83 (2011), p. 016206.

[220] L. W. Sheppard, A. Stefanovska, and P. V. E. McClintock. "Testing for time-localised coherence in bivariate data". In: *Phys. Rev. E* 85 (2012), p. 046205.

[221] T. Shimmen and M. Tazawa. "Control of membrane potential and excitability of Chara cells with ATP and Mg^{2+}". In: *J. Membr. Biol.* 37.1 (1977), pp. 167–192.

[222] J. C. Sigl and N. G. Chamoun. "An introduction to bispectral analysis for the electroencephalogram". In: *J. Clin. Monit.* 10.6 (1994), pp. 392–404.

[223] F. J. Sigworth. "The variance of sodium current fluctuations at the node of Ranvier". In: *J. Physiol.* 307.1 (1980), pp. 97–129.

[224] E. Smedler and P. Uhlén. "Frequency decoding of calcium oscillations". In: *Biochim. Biophys. Acta* 1840.3 (2014), pp. 964–969.

[225] S. Smirni, A. D. McNeilly, M. P. MacDonald, R. J. McCrimmon, and F. Khan. "In-vivo correlations between skin metabolic oscillations and vasomotion in wild-type mice and in a model of oxidative stress". In: *Sci. Rep.* 9.1 (2019), p. 186.

[226] S. C. Song, J. A. Beatty, and C. J. Wilson. "The ionic mechanism of membrane potential oscillations and membrane resonance in striatal LTS interneurons". In: *J. Neurophysiol.* 116.4 (2016), pp. 1752–1764.

[227] A. Spicher, W. J. Miloch, L. B. N. Clausen, and J. I. Moen. "Plasma turbulence and coherent structures in the polar cap observed by the ICI-2 sounding rocket". In: *J. Geophys. Res. A* 120.12 (2015).

[228] T. Stankovski, A. Duggento, P. V. E. McClintock, and A. Stefanovska. "Inference of time-evolving coupled dynamical systems in the presence of noise". In: *Phys. Rev. Lett.* 109 (2012), p. 024101.

[229] T. Stankovski, T. Pereira, P. V. E. McClintock, and A. Stefanovska. "Coupling functions: Universal insights into dynamical interaction mechanisms". In: *Rev. Mod. Phys.* 89.4 (2017), p. 045001.

[230] A. Stefanovska. "Coupled oscillators: Complex but not complicated cardiovascular and brain interactions". In: *IEEE Eng. Med. Bio. Magazine* 26.6 (2007), pp. 25–29.

[231] A. Stefanovska and M. Bračič. "Physics of the human cardiovascular system". In: *Contemp. Phys.* 40.1 (1999), pp. 31–55.

[232] W. D. Stein. "The sodium pump in the evolution of animal cells". In: *Philos. Trans. Royal Soc. B* 349.1329 (1995), pp. 263–269.

[233] J. Stelling, U. Sauer, Z. Szallasi, F. J. Doyle III, and J. Doyle. "Robustness of cellular functions". In: *Cell* 118.6 (2004), pp. 675–685.

[234] E. A. Stern, A. E. Kincaid, and C. J. Wilson. "Spontaneous subthreshold membrane potential fluctuations and action potential variability of rat corticostriatal and striatal neurons in vivo". In: *J. Neurophysiol.* 77.4 (1997), pp. 1697–1715.

[235] S. H. Strogatz. *Nonlinear Dynamics And Chaos*. Boulder: Westview Press, 2015.

[236] S. H. Strogatz. *Sync: The Emerging Science of Spontaneous Order*. New York: Hyperion, 2003.

[237] Z. Sulova, F. Vyskocil, T. Stankovicova, and A. Breier. "Ca^{2+}-induced inhibition of sodium pump: effects on energetic metabolism of mouse diaphragm tissue." In: *Gen. Physiol. Biophys.* 17.3 (1998), pp. 271–283.

[238] S. Sundelacruz, M. Levin, and D. L. Kaplan. "Role of membrane potential in the regulation of cell proliferation and differentiation". In: *Stem Cell Rev. Rep.* 5.3 (2009), pp. 231–246.

[239] A. Swami, G. B. Giannakis, and G. Zhou. "Bibliography on higher-order statistics". In: *Signal Process.* 60.1 (1997), pp. 65–126.

[240] M. Tantama, J. R. Martínez-François, R. Mongeon, and G. Yellen. "Imaging energy status in live cells with a fluorescent biosensor of the intracellular ATP-to-ADP ratio". In: *Nat. Commun.* 4 (2013), p. 2550.

[241] S. A. Taplidou and L. J. Hadjileontiadis. "Nonlinear analysis of wheezes using wavelet bicoherence". In: *Comput. Biol. Med.* 37.4 (2007), pp. 563–570.

[242] J. Theiler, S. Eubank, A. Longtin, B Galdrikian, and J.D. Farmer. "Testing for nonlinearity in time series: the method of surrogate data". In: *Physica D* 58.1–4 (1992), pp. 77–94.

[243] J. Theiler and D. Prichard. "Constrained-realization Monte-Carlo method for hypothesis testing". In: *Physica D* 94.4 (1996), pp. 221–235.

[244] A. G. Therien and R. Blostein. "Mechanisms of sodium pump regulation". In: *Am. J. Physiol., Cell Physiol.* 279.3 (2000), pp. C541–C566.

[245] A. N. Thompson, D. J. Posson, P. V. Parsa, and C. M. Nimigean. "Molecular mechanism of pH sensing in KcsA potassium channels". In: *Proc. Natl. Acad. Sci. U.S.A.* 105.19 (2008), pp. 6900–6905.

[246] M. Timme. "Revealing network connectivity from response dynamics". In: *Phys. Rev. Lett.* 98.22 (2007), p. 224101.

[247] I. T. Tokuda, S. Jain, I. Z. Kiss, and J. L. Hudson. "Inferring Phase Equations from Multivariate Time Series". In: *Phys. Rev. Lett.* 99 (6 2007), p. 064101.

[248] E. Toledo, S. Akselrod, I. Pinhas, and D. Aravot. "Does synchronization reflect a true interaction in the cardiorespiratory system?" In: *Med. Eng. & Phys.* 24.1 (2002), pp. 45–52.

[249] C. Torrence and G. P. Compo. "A practical guide to wavelet analysis". In: *Bull. Am. Meteorol. Soc.* 79.1 (1998), pp. 61–78.

[250] C. Torrence and P. J. Webster. "Interdecadal changes in the ENSO – monsoon system". In: *J. Clim.* 12.8 (1999), pp. 2679–2690.

[251] T. Y.-C. Tsai, Y. S. Choi, W. Ma, J. R. Pomerening, C. Tang, and J. E. Ferrell. "Robust, tunable biological oscillations from interlinked positive and negative feedback loops". In: *Science* 321.5885 (2008), pp. 126–129.

[252] R. W. Tsien, R. S. Kass, and R. Weingart. "Cellular and subcellular mechanisms of cardiac pacemaker oscillations". In: *J. Exp. Biol.* 81.1 (1979), pp. 205–215.

[253] M. Ui. "A role of phosphofructokinase in pH-dependent regulation of glycolysis". In: *Biochim. Biophys. Acta* 124.2 (1966), pp. 310–322.

[254] B. P. van Milligen, C. Hidalgo, and E. Sánchez. "Nonlinear phenomena and intermittency in plasma turbulence". In: *Phys. Rev. Lett.* 74 (3 1995), pp. 395–398.

[255] M. G. Vander Heiden, L. C. Cantley, and C. B. Thompson. "Understanding the Warburg effect: the metabolic requirements of cell proliferation". In: *Science* 324.5930 (2009), pp. 1029–1033.

[256] J. A. H. Verheugen, M. Oortgiesen, and H. P. M. Vijverberg. "Veratridine blocks voltage-gated potassium current in human T lymphocytes and in mouse neuroblastoma cells". In: *J. Membr. Biol.* 137.3 (1994), pp. 205–214.

[257] F. K. Voss, F. Ullrich, J. Münch, K. Lazarow, D. Lutter, N. Mah, M. A. Andrade-Navarro, J. P. von Kries, T. Stauber, and T. J. Jentsch. "Identification of LRRC8 heteromers as an essential component of the volume-regulated anion channel VRAC". In: *Science* 344.6184 (2014), pp. 634–638.

[258] W. Walz, A. A. Boulton, and G. B. Baker. *Patch-Clamp Analysis: Advanced Techniques*. 35. Springer Science & Business Media, 2002.

[259] C.-Z. Wang, H. Yano, K. Nagashima, and S. Seino. "The Na^+-driven Cl^-/HCO_3^- exchanger cloning, tissue distribution, and functional characterization". In: *J. Biol. Chem.* 275.45 (2000), pp. 35486–35490.

[260] K. A. Webster. "Evolution of the coordinate regulation of glycolytic enzyme genes by hypoxia". In: *J. Exp. Biol.* 206.17 (2003), pp. 2911–2922.

[261] G. Widman, T. Schreiber, B. Rehberg, A. Hoeft, and C.E. Elger. "Quantification of depth of anesthesia by nonlinear time series analysis of brain electrical activity". In: *Phys. Rev. E* 62.4 (2000), p. 4898.

[262] F. Wilcoxon. "Individual Comparisons by Ranking Methods". In: *Biometr. Bull.* 1.6 (1945), pp. 80–83.

[263] J. S. Wiley, N. Kraft, and I. A. Cooper. "The binding of ouabain to normal and chronic lymphocytic leukemic lymphocytes". In: *Blood* 54.5 (1979), pp. 994–1000.

[264] C. J. Wilson and Y. Kawaguchi. "The origins of two-state spontaneous membrane potential fluctuations of neostriatal spiny neurons". In: *J. Neurosci.* 16.7 (1996), pp. 2397–2410.

[265] H. A. Wilson and T. M. Chused. "Lymphocyte membrane potential and Ca^{2+}-sensitive potassium channels described by oxonol dye fluorescence measurements". In: *J. Cell Phys.* 125.1 (1985), pp. 72–81.

[266] A. T. Winfree. "Biological rhythms and the behavior of populations of coupled oscillators". In: *J. Theor. Biol.* 16.1 (1967), pp. 15–42.

[267] T. Dudok de Wit and V. V. Krasnosel'skikh. "Wavelet bicoherence analysis of strong plasma turbulence at the Earth's quasiparallel bow shock". In: *Phys. Plasmas* 2.11 (1995), pp. 4307–4311.

[268] T. Yada and Y. Okada. "Electrical activity of an intestinal epithelial cell line: hyperpolarizing responses to intestinal secretagogues". In: *J. Membr. Biol.* 77.1 (1984), pp. 33–44.

[269] N.-C. Yao, S. Neshyba, and H. Crew. "Rotary Cross-Bispectra and Energy Transfer Functions Between Non-Gaussian Vector Processes I. Development and Example". In: *J. Phys. Oceanogr* 5 (1974), pp. 164–172.

[270] F. Yellin, Y. Li, V. K. A. Sreenivasan, B. Farrell, M. B. Johny, D. Yue, and S. X. Sun. "Electromechanics and volume dynamics in nonexcitable tissue cells". In: *Biophys. J.* 114.9 (2018), pp. 2231–2242.

[271] S. P. Yu and D. W. Choi. "Ions, cell volume, and apoptosis". In: *Proc. Natl. Acad. Sci. U.S.A.* 97.17 (2000), pp. 9360–9362.

[272] S. L. Zhang, Y. Yu, J. Roos, J. A. Kozak, T. J. Deerinck, M. H. Ellisman, K. A. Stauderman, and M. D. Cahalan. "STIM1 is a Ca^{2+} sensor that activates CRAC channels and migrates from the Ca^{2+} store to the plasma membrane". In: *Nature* 437.7060 (2005), p. 902.

[273] P. D. Zieve, M. Haghshenass, and J. R. Krevans. "Intracellular pH of the human lymphocyte". In: *Am. J. Physiol., Cell Physiol.* 212.5 (1967), pp. 1099–1102.